Hydrodynamics of astrophysical winds driven by scattering in spectral lines

Achim Feldmeier

Habilitation thesis in Astrophysics
Potsdam University, June 2001

Meinen Eltern

Instead of a quote

Abstract. Line driven winds are accelerated by the momentum transfer from photons to a plasma, by absorption and scattering in numerous spectral lines. Line driving is most efficient for ultraviolet radiation, and at plasma temperatures from 10^4 K to 10^5 K. Astronomical objects which show line driven winds include stars of spectral type O, B, and A, Wolf-Rayet stars, and accretion disks over a wide range of scales, from disks in young stellar objects and cataclysmic variables to quasar disks. It is not yet possible to solve the full wind problem numerically, and treat the combined hydrodynamics, radiative transfer, and statistical equilibrium of these flows. The emphasis in the present writing is on wind hydrodynamics, with severe simplifications in the other two areas. I consider three topics in some detail, for reasons of personal involvement. 1. *Wind instability*, as caused by Doppler de-shadowing of gas parcels. The instability causes the wind gas to be compressed into dense shells enclosed by strong shocks. Fast clouds occur in the space between shells, and collide with the latter. This leads to X-ray flashes which may explain the observed X-ray emission from hot stars. 2. *Wind runaway*, as caused by a new type of radiative waves. The runaway may explain why observed line driven winds adopt fast, critical solutions instead of shallow (or breeze) solutions. Under certain conditions the wind settles on overloaded solutions, which show a broad deceleration region and kinks in their velocity law. 3. *Magnetized winds*, as launched from accretion disks around stars or in active galactic nuclei. Line driving is assisted by centrifugal forces along co-rotating poloidal magnetic field lines, and by Lorentz forces due to toroidal field gradients. A vortex sheet starting at the inner disk rim can lead to highly enhanced mass loss rates.

Zusammenfassung. Liniengetriebene Winde werden durch Impulsübertrag von Photonen auf ein Plasma bei Absorption oder Streuung in zahlreichen Spektrallinien beschleunigt. Dieser Prozess ist besonders effizient für ultraviolette Strahlung und Plasmatemperaturen zwischen 10^4 K und 10^5 K. Zu den astronomischen Objekten mit liniengetriebenen Winden gehören Sterne der Spektraltypen O, B und A, Wolf-Rayet-Sterne sowie Akkretionsscheiben verschiedenster Größenordnung, von Scheiben um junge Sterne und in kataklysmischen Veränderlichen bis zu Quasarscheiben. Es ist bislang nicht möglich, das vollständige Windproblem numerisch zu lösen, also die Hydrodynamik, den Strahlungstransport und das statistische Gleichgewicht dieser Strömungen gleichzeitig zu behandeln. Die Betonung liegt in dieser Arbeit auf der Windhydrodynamik, mit starken Vereinfachungen in den beiden anderen Gebieten. Wegen persönlicher Beteiligung betrachte ich drei Themen im Detail. 1. *Windinstabilität* durch Doppler*de-shadowing* des Gases. Die Instabilität bewirkt, dass Windgas in dichte Schalen komprimiert wird, die von starken Stoßfronten begrenzt sind. Schnelle Wolken entstehen im Raum zwischen den Schalen und stoßen mit diesen zusammen. Dies erzeugt Röntgen*flashes*, die die beobachtete Röntgenstrahlung heißer Sterne erklären können. 2. *Wind runway* durch radiative Wellen. Der *runaway* zeigt, warum beobachtete liniengetriebene Winde schnelle, kritische Lösungen anstelle von Brisenlösungen (oder *shallow solutions*) annehmen. Unter bestimmten Bedingungen stabilisiert der Wind sich auf masseüberladenen Lösungen, mit einem breiten, abbremsenden Bereich und Knicken im Geschwindigkeitsfeld. 3. *Magnetische Winde* von Akkretionsscheiben um Sterne oder in aktiven Galaxienzentren. Die Linienbeschleunigung wird hier durch die Zentrifugalkraft entlang korotierender poloidaler Magnetfelder und die Lorentzkraft aufgrund von Gradienten im toroidalen Feld unterstützt. Ein Wirbelblatt, das am inneren Scheibenrand beginnt, kann zu stark erhöhten Massenverlustraten führen.

Contents

§1 INTRODUCTION[1]

Why line driven winds? The study of winds from astronomical objects started with Parker's work on the solar wind in 1958, one of the landmark theories in astronomy. At present, four important types of hydrodynamic winds are known in astronomy: the thermal wind from Sun; dust driven winds from red supergiants; line driven winds from blue stars and accretion disks; and magnetocentrifugal winds from accretion disks, either around stars or in quasars.

Thermal winds are accelerated by gas pressure in a hot corona. Parker's breakthrough idea was that the solar wind can be described as a transsonic hydrodynamic flow, instead of a discrete particle flux. Dusty winds are driven by continuum radiation pressure acting on dust grains in a relatively cool environment. Line driven winds are also driven by radiation pressure, yet, in numerous ultraviolet spectral lines. Finally, magnetocentrifugal winds are launched from accretion disks, via centrifugal forces acting along poloidal field lines, or Lorentz forces caused by the toroidal field.

By contrast to geological winds which are essentially horizontal flows caused by pressure gradients and the Coriolis force, the above four astronomical winds directly oppose gravity, and carry away mass and momentum from the central object. For line driven winds, both the mass loss rate, $\dot{M}$, and the momentum rate, $\dot{M}v_\infty$ (with terminal wind speed v_∞), are large. These winds are therefore important in two respects:

Stellar evolution. Hot, massive stars lose a large fraction of their initial mass through winds, and the winds control stellar evolution. Unfortunately, the phases of strongest mass loss, the LBV (luminous blue variable) and Wolf-Rayet phase, are not well understood, and empirical formulae have to be used in evolutionary calculations. The LBV phase may be characterized by the star reaching its Eddington limit (radiation pressure on electrons larger than gravity; Langer et al. 1999).

Star formation. Hot stars often reside in environments rich of gas and dust. The stellar wind enriches the interstellar medium with metals and triggers (bursts of) star formation (Leitherer et al. 1999). Figure 1 shows an aspect of this process which was recently discovered. Shown is a Hubble Space Telescope image, where radiation from an O7 main sequence star may prevent planet formation. The stellar wind is seen blowing off matter from the protoplanetary accretion disk.

We add more reasons why the hydrodynamics of line driven winds is an important and interesting new research area.

Spectroscopy. Fundamental parameters of hot stars like radius and mass can be derived from quantitative spectroscopy of spectral lines forming in their winds (Pauldrach, Hoffmann, & Lennon 2001; Kudritzki & Puls 2000; Hamann & Koesterke 1998a; Hillier & Miller 1998). Most importantly, the star's luminosity follows from the wind-momentum luminosity relation (Kudritzki, Lennon, & Puls 1995). In the near future, hot, massive stars may compete with Cepheids as primary distance indicators. Wind hydrodynamics affects spectral line formation and therefore quantitative spectroscopy in a fundamental way. Observed spectral line features which

---

[1] Only some key references are cited in the introduction.

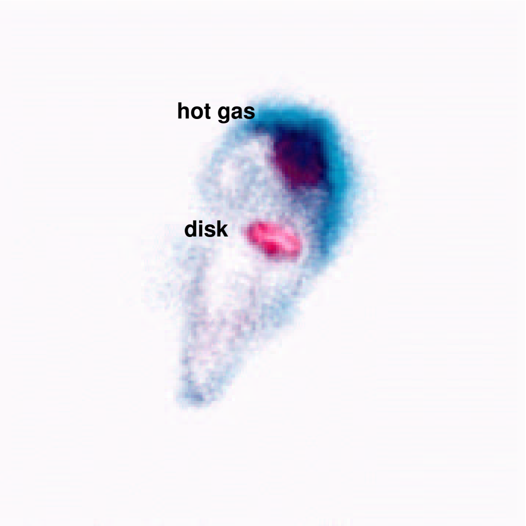

Figure 1: **NASA press release, April 26, 2001.** "*Hubble Watches Planetary Nurseries Being Torched by Radiation from Hot Star.* Planet formation is a hazardous process. This snapshot, taken by HST, shows a dust disk around an embryonic star in the Orion Nebula being 'blowtorched' by a blistering flood of ultraviolet radiation from the region's brightest star. Within these disks are the seeds of planets. Evidence suggests that dust grains in the disk are already forming larger particles, which range in size from snowflakes to gravel. But these particles may not have time to grow into full-fledged planets because of the relentless 'hurricane' of radiation from the nebula's hottest star, Theta 1 Orionis C. In the picture, the disk is oval near the center. Radiation from the hot star is heating up the disk, causing matter to dissipate. A strong 'stellar wind' is propelling the material away from the disk."

are indicators for time-dependent flow features are (we mention only the terms, without going into explanations): black troughs, discrete absorption components, enhanced electron scattering wings, bowed variation contours, variable blue edges, and discrete emission components.

New force. Line driving is a new hydrodynamic force, and defines a new class of 'radiating fluids'. In astrophysics, radiation hydrodynamics is of similar importance as magnetohydrodynamics. The unique quality about line driving is 'Doppler tuning'. Each spectral line can absorb photons in a narrow frequency band only, its width being determined by the thermal speed of ions. After a minute acceleration of the gas by the line force, the Doppler-shifted spectral line can absorb at bluer frequencies, from the 'fresh' stellar continuum. The ratio of terminal to thermal speed, which is roughly the maximum Mach number, Ma, of the flow, is therefore of order the width of the UV frequency band divided by the line width: $\mathrm{Ma} > 100$! By contrast, flows driven by continuum absorption of radiation, the solar wind, and MHD flows (if the Mach number with respect to Alfvén waves is considered) have $\mathrm{Ma} \leq 10$ in their accelerating regions.

New waves. Actually, $\mathrm{Ma} \leq 10$ also holds for line driven winds, with respect to a new type of line driven or *Abbott* waves (Abbott 1980). These waves are discussed controversially in the literature, and a strict proof of their existence is still missing. They may play a central role in the ubiquitous 'discrete absorption components' observed in unsaturated P Cygni line profiles (Cranmer & Owocki 1996); and they may drive line driven winds towards a unique, critical solution.

Range of objects. The importance of line driving is also clear from a list of astronomical objects which share this flow type. Line driven winds occur in O and B stars (Lucy & Solomon 1970), Wolf-Rayet stars (Lucy & Abbott 1993; Gayley, Owocki, & Cranmer 1995; Hamann & Koesterke 2000), central stars of planetary nebula (Koesterke & Hamann 1997), and in A supergiants (Kudritzki et al. 1999). The latter are the *optically* brightest stars, and are central in extragalactic distance determination. A relatively new idea is that line driven winds are launched from *accretion disks.* Relevant cases span a huge range, reaching from active galactic nuclei (quasars and Seyfert galaxies; Weymann, Turnshek, & Christiansen 1985) to cataclysmic variables (white dwarfs with a late-type, main-sequence companion; Heap et al. 1978) and young stellar objects (bright B protostars; Drew, Proga, & Stone 1998).

Interaction of line and magnetic driving. Line driven winds from magnetized accretion disks may show an intricate interplay of three driving forces: the radiative, Lorentz, and centrifugal force. The assistance of line driving may help to overcome problems encountered with pure magnetocentrifugal driving. This should be relevant for accretion disks in quasars and young stellar objects, where magnetic fields and radiation fields are strong.

After this general motivation, and before we go over to more detailed discussions in the main text, we give an overview of the results and ideas treated in the following.

Wind instability and X-ray emission. Line driven winds are subject to a new radiation-hydrodynamics instability (Lucy & Solomon 1970). If a fluid parcel experiences a small, positive velocity perturbation, it gets Doppler-shifted out of the absorption shadow of gas lying closer to the radiation source (the photosphere). It sees more light and experiences stronger driving, hence, is further accelerated: an amplification cycle results, termed *de-shadowing* instability. Since the flow is highly supersonic, perturbations are expected to quickly grow into shocks.

In an important paper, Owocki, Castor, and Rybicki (1988; OCR from now) calculated for the first time the unstable flow structure numerically, along a 1-D, radial ray assuming spherical symmetry. The initially smooth flow is transformed into a sequence of dense shells. Since the shells are accelerated outwards, they are Rayleigh-Taylor unstable and should fragment. In linear approximation, the de-shadowing instability has no lateral component (Rybicki, Owocki, & Castor 1990), and one may expect that the R-T debris maintains a relatively large, lateral scale. However, this is presently mere speculation, since 2-D simulations are lacking due to computational limitations. The fragmented shells are separated radially by broad regions of rarefied, steeply accelerating gas. The thin, fast gas is eventually decelerated in strong reverse shocks on the inner, starward (or disk) facing rim of the shells. The shells propagate outwards at a speed similar to that of smooth, stationary flow. Figure 2 shows the evolved wind structure. The origin of X-ray emission in cloud-shell collisions is also indicated in this sketch.

The detection of X-rays from early-type stars was one of the major discoveries of the EINSTEIN satellite (Seward et al. 1979; Harnden et al. 1979). For O stars, the

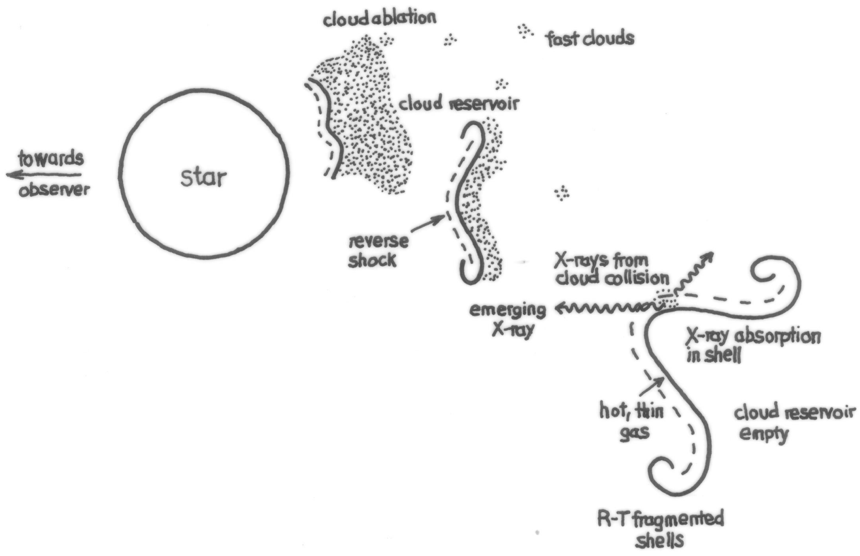

Figure 2: Expected structure of an unstable, line driven wind. Dense shells fragment via Rayleigh-Taylor instability. Fast clouds collide with the shell fragments, creating X-ray flashes.

ratio of X-ray and total luminosity is $L_x/L_{\mathrm{bol}} \sim 10^{-7\pm1}$. X-ray temperatures are 10^6 to $10^{7.5}$ Kelvin, two or three orders of magnitude above photospheric temperatures. Early-type stars have no envelope convection zones and are thus quite different from solar-type stars with convection zones, magnetic fields, and hot coronae. It is generally believed that the X-ray emission from hot stars originates in their winds, possibly in shocks which result from de-shadowing instability.

While this idea is consistent with many observational facts, especially the absence of K-shell absorption edges, theoretical modeling encounters severe problems. In a phenomenological model of strong forward shocks in the wind (Lucy 1982b), L_x was found to be a factor of 100 smaller than derived from EINSTEIN data (Cassinelli & Swank 1983). The same problem occured for the hydrodynamic wind models of OCR, which show an X-ray flux deficiency by factors of 10 to 100 (Hillier et al. 1993).

Instead of a continuous X-ray emission from quasi-steady wind shocks, we propose X-rays flashes of short duration. These flashes occur when fast wind clouds collide with a dense, cold shell. The clouds are created via turbulent ablation from a ‘mildly’ dense gas reservoir lying ahead of the overdense, highly compressed shells. At the wind base, roughly one half of the upstreaming gas is quickly compressed into shells. The remaining gas is available for cloud formation at larger heights in the wind. The clouds are accelerated through empty intershell space, until they collide with the next outer shell. Time averaged X-ray spectra synthesised from these models match ROSAT observations well. Variations between individual snapshots are large, however, in contrast to the observed constancy of X-ray fluxes.

Since the clouds are of turbulent origin, we speculate that their lateral scale is much smaller than that of shell fragments. In future 2-D modeling, X-ray flux constancy may be achieved via angle averaging over independent, radial wind rays, each with its own cloud-shell collisions taking place.

Wind runaway caused by Abbott waves. After the discussion in Chapter 2 of *localized* flow features due to de-shadowing instability, we turn in Chapter 3 to the *global* solution topology of steady, line driven winds. The question we pose is: why do line driven winds from stars and accretion disks adopt a unique, critical solution? In a first attempt to answer this question, we suppress de-shadowing instability by adopting the simplifying *Sobolev approximation* in the line force. Future work has to unify both aspects, global and local. (A relevant question could then be: can local, unstable flow structure provide the seed perturbations required for global solution transformation?)

In their fundamental work on line driven winds, Castor, Abbott, and Klein (1975; CAK from now) showed that the stationary Euler equation has an infinite number of possible solutions. They come in two classes, 'shallow' and 'steep'. Steep solutions are supersonic, and cannot connect to the subsonic wind base. Shallow solutions fail to reach large radii, as they cannot perform the required spherical expansion work. CAK concluded that the wind adopts the unique, critical solution which starts shallow and ends steep, switching smoothly between the classes at some critical point. This defines the critical or CAK solution.

Evidence mounts that the argument given by CAK is too restrictive. The question arises whether the CAK solution is still unique if discontinuities are allowed for in *derivatives* of flow quantities (i.e., kinks). Is the CAK solution a dynamical attractor in the sense of mechanical system theory? And how does the transition between shallow and the critical solution occur?

Radiative or Abbott waves are the key to answer these questions. We show that shallow solutions are sub-abbottic, and Abbott waves propagate inwards towards the photosphere from any point in the wind. Numerical wind simulations published so far assume pure outflow boundary conditions, which apply if all characteristics leave the mesh. The standard argument is that the outer boundary is highly supersonic, at $\mathrm{Ma} > 100$. Instead, we see now that $\mathrm{Ma} < 1$ for Abbott waves along shallow solutions. We show that, by chosing outflow boundary conditions, the numerical scheme is forced to relax to a super-abbottic solution. If the wind is sub-abbottic (yet, supersonic), outflow boundary conditions cause numerical runaway.

Abbott waves define the characteristics of line driven winds, and as such have to be included in the Courant time step, to prevent numerical runaway. This has not be done so far. Accounting for Abbott waves in the Courant time step and applying non-reflecting Riemann conditions at the outer boundary, we find that the numerical scheme converges to shallow solutions from a wide class of initial conditions.

Will line driven winds in nature adopt a shallow solution? We suggest that this is not the case, and identify a new, physical runaway which drives shallow solutions towards the critical one. This runaway depends on new and strange dispersion properties of Abbott waves: negative velocity gradients propagate downstream and outwards, as opposed to upstream propagating, positive velocity gradients. This asymmetry causes systematic evolution of the wind towards larger speeds. The runaway stops when a critical point forms in the flow, and prevents waves to penetrate downwards to the wind base. This is the case for the CAK solution.

A new solution type occurs with generalized critical points. If the wind is perturbed in the sub-abbottic region below the CAK critical point, runaway does not stop on the CAK solution. Instead, the wind becomes *overloaded.* A new critical point forms, showing up as a *kink* in the velocity law at which the wind starts to decelerate. This is a direct consequence of overloading, since super-CAK mass loss rates cannot be *accelerated* through the CAK critical point. Increasing the overloading further, negative flow speeds result, and a steady solution is no longer possible. Shocks and shells form in the wind, and propagate outwards. There is some observational evidence suggesting that the wind of the LBV star P Cygni has indeed a broad, decelerating region.

Winds from accretion disks. The last, forth chapter also deals with a simple Sobolev line force, however, in a more complicated flow geometry. Observations indicate that line driven winds are launched by the ultraviolet radiation field in certain types of accretion disks. For example, P Cygni line profiles from broad absorption line quasars show terminal speeds of 10% the speed of light (Turnshek 1984). The flow is rather massive, with mass fluxes of order one solar mass per year in luminous quasars. Both facts are suggestive of a line driven wind. However, the ionizing radiation from the central source poses a serious problem. Wind gas which is not highly compressed or shielded from this radiation becomes fully ionized, and line driving stalls. Shielding could be provided by a cold disk atmosphere. The wind is launched vertically from the disk, reaches large speeds already within the atmosphere, and escapes on ballistic orbits after being exposed to the central radiation (Shlosman et al. 1985). Alternatively, dense regions of hot, ionized gas (of unspecified origin) may occur between the central source and the wind (Murray et al. 1995). This gas may block ionizing X-rays, but could be transparent to UV radiation. The flow is again launched vertically by local disk radiation, but quickly bends over and makes a shallow angle with the disk when irradiated by the central source. Numerical simulations show that the shielding region may consist of highly-ionized, failed wind (Proga, Stone, & Kallman 2000). Strong observational support that winds from broad absorption line quasars are driven by resonance line scattering comes from "the ghost of Lyα" (Arav 1996).

While very fascinating, line driven quasar winds are still a matter of debate. On the other hand, observational evidence for line driven disk winds in cataclysmic variables (CVs) is unambiguous (Heap et al. 1978; Krautter et al. 1981). These systems consist of a white dwarf and a late-type, main sequence companion. The latter fills its Roche lobe and feeds an accretion disk onto the white dwarf. Observed P Cygni line profiles clearly indicate a biconical outflow from the disk, not a spherical outflow from the white dwarf itself (Vitello & Shlosman 1993). In Chapter 4, we discuss numerical simulations and a semi-analytical model for CV winds. We encounter a two-dimensional eigenvalue problem, for mass loss rates and wind tilt angles with the disk. The derived mass loss rates are much smaller than was hitherto expected. We discuss why the latter expectations were overestimates. Still, a large discrepancy remains, and it is not yet clear why CV disk winds are so efficient in nature. Possibly,

magnetic fields assist line driving. This leads over to the last topic of this writing, magnetized winds.
Magnetocentrifugal winds could occur in young stellar objects and in quasars. In the classical model of Blandford & Payne (1982; see Fig. 3 for a realistic scenario), outflow occurs along poloidal magnetic field lines. If the magnetic pressure in the disk corona is much larger than gas pressure, the field lines co-rotate with the disk. The field lines act as lever arms and, at inclination angles < 60 degrees with the disk, flung the gas outwards. Above the Alfvén point, ram pressure dominates magnetic pressure in the wind. The gas parcels start to conserve angular momentum, and lack behind the disk rotation. The poloidal field gets wound-up into a toroidal field. Hoop stresses of the latter confine the centrifugal outflow to bipolar jets, and jets are indeed often found associated with young stellar objects (Eisloeffel et al. 2000). There is a large body of literature on the theory of magnetocentrifugal disk winds. Some key references include: Pudritz & Norman (1983; 1986), Königl (1989), and Heyvaerts & Norman (1989). An excellent review is Königl & Pudritz (2000).

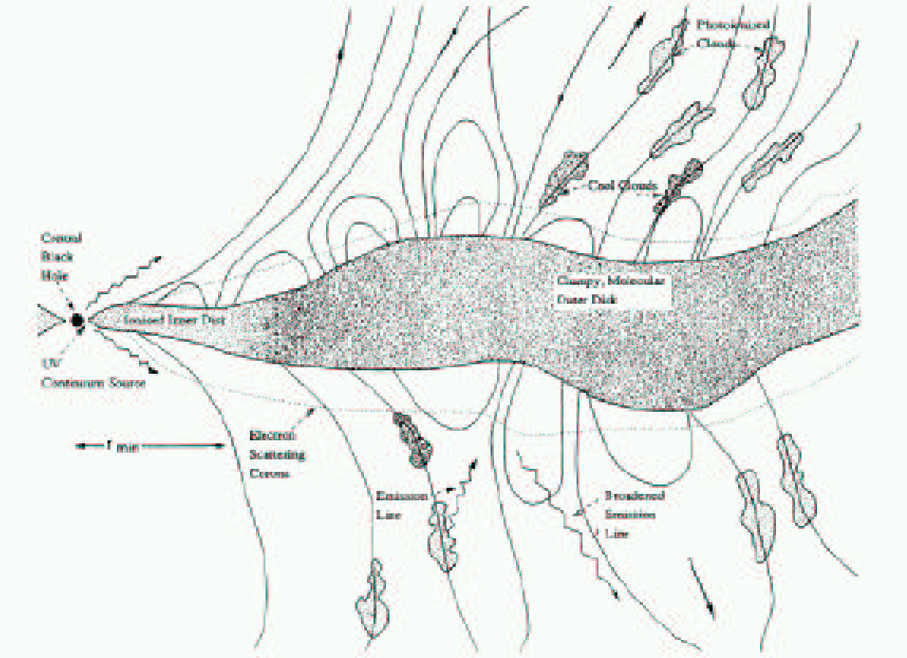

Figure 3: Realistic scenario for a magnetocentrifugal wind from a quasar disk. Gas clouds are centrifugally driven outwards along sufficiently inclined, co-rotating magnetic field lines. From Emmering, Blandford, & Shlosman (1992).

Recently, Drew, Proga, & Stone (1998) suggested that line driving could assist magnetocentrifugal driving in *bright* young stellar objects (young B stars). The cold accretion disk is assumed to be illuminated by the hot central star, and either scatters the incident UV radiation or is itself heated to temperatures resulting in strong UV emission. The disk radiation field launches a flow. The terminal speed of line driven winds scales with the escape speed at their base, and is much smaller from outer disk regions than from the central star. This scenario could therefore explain the small observed outflow speeds from certain objects.

At the end of Chapter 4, we present explorative 2-D simulations of magnetized line driven winds. The resulting flow dynamics above accretion disks with small Eddington factor is rather intricate. For realistic magnetic field strengths, mass loss rates may be dramatically increased. We find that dominant magnetic driving is *not* via the centrifugal force along poloidal field lines, but via the Lorentz force caused by toroidal field gradients. This scenario, complementary to the Blandford & Payne model, was proposed by Contopoulos (1995). Still, we find that the poloidal field is mandatory for increased mass loss. A vortex sheet forms in the poloidal wind velocity and magnetic field, and carries the toroidal field to such heights that it can assist in driving the enhanced mass loss through the critical point (the 'bottleneck' of the flow).

Much work remains to be done on magnetized line driven winds, in order to understand the relevant physics and rule out numerical artefacts. This is the reason why no paper or preprint on this subject is appended to the present writing.

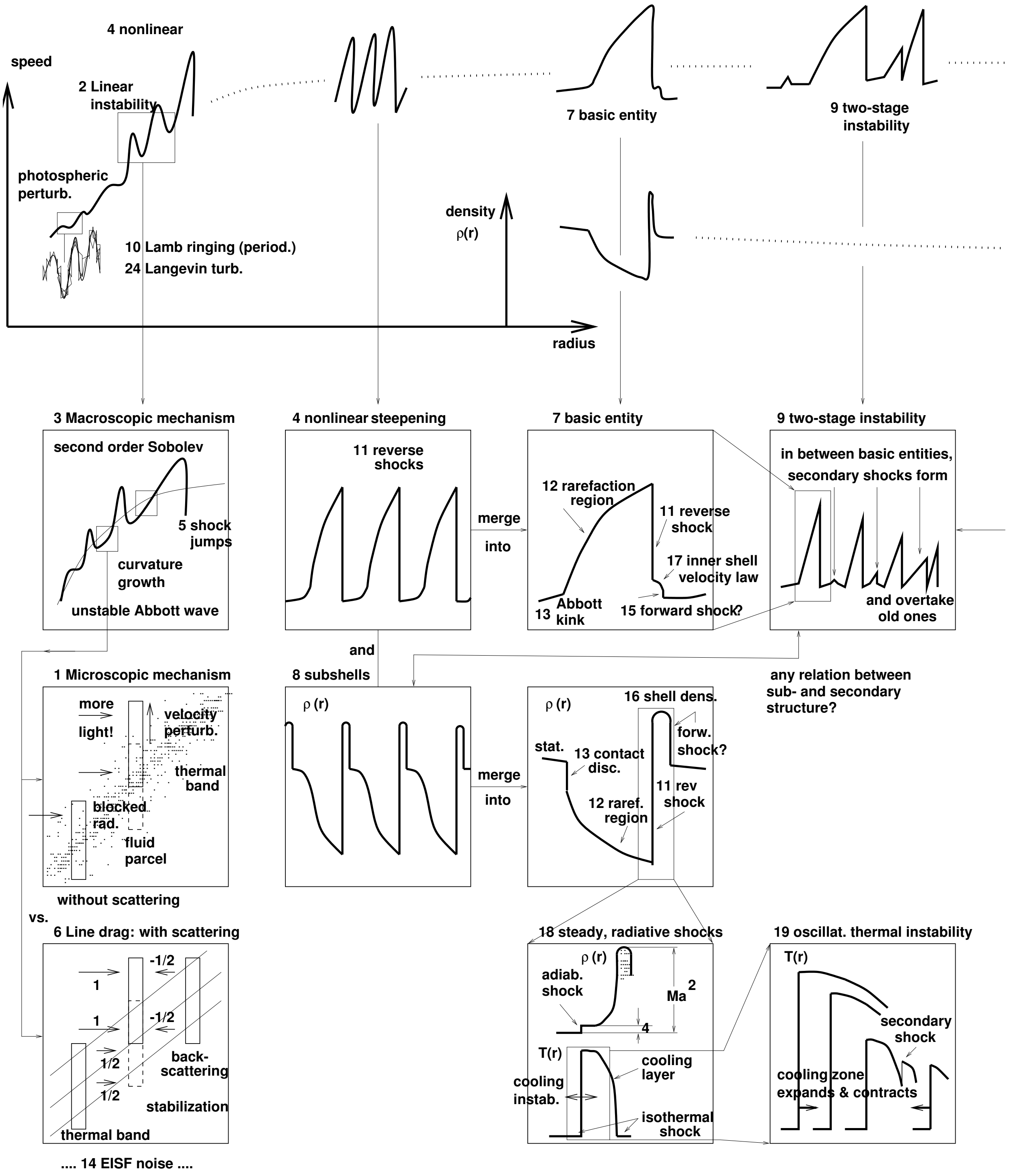
4 nonlinear
speed
2 Linear instability
photospheric perturb.
10 Lamb ringing (period.)
24 Langevin turb.
7 basic entity
9 two-stage instability
density ρ(r)
radius
3 Macroscopic mechanism
second order Sobolev
5 shock jumps
curvature growth
unstable Abbott wave
4 nonlinear steepening
11 reverse shocks
merge into
7 basic entity
12 rarefaction region
11 reverse shock
17 inner shell velocity law
13 Abbott kink
15 forward shock?
9 two-stage instability
in between basic entities, secondary shocks form
and overtake old ones
and
1 Microscopic mechanism
more light!
velocity perturb.
thermal band
blocked rad.
fluid parcel
without scattering
vs.
8 subshells
ρ (r)
merge into
ρ (r)
16 shell dens.
stat.
13 contact disc.
forw. shock?
11 rev shock
12 raref. region
any relation between sub- and secondary structure?
6 Line drag: with scattering
1
-1/2
1
-1/2
1/2
1/2
back-scattering
stabilization
thermal band
.... 14 EISF noise ....
18 steady, radiative shocks
ρ (r)
adiab. shock
Ma 2
4
T(r)
cooling layer
cooling instab.
isothermal shock
19 oscillat. thermal instability
T(r)
secondary shock
cooling zone expands & contracts

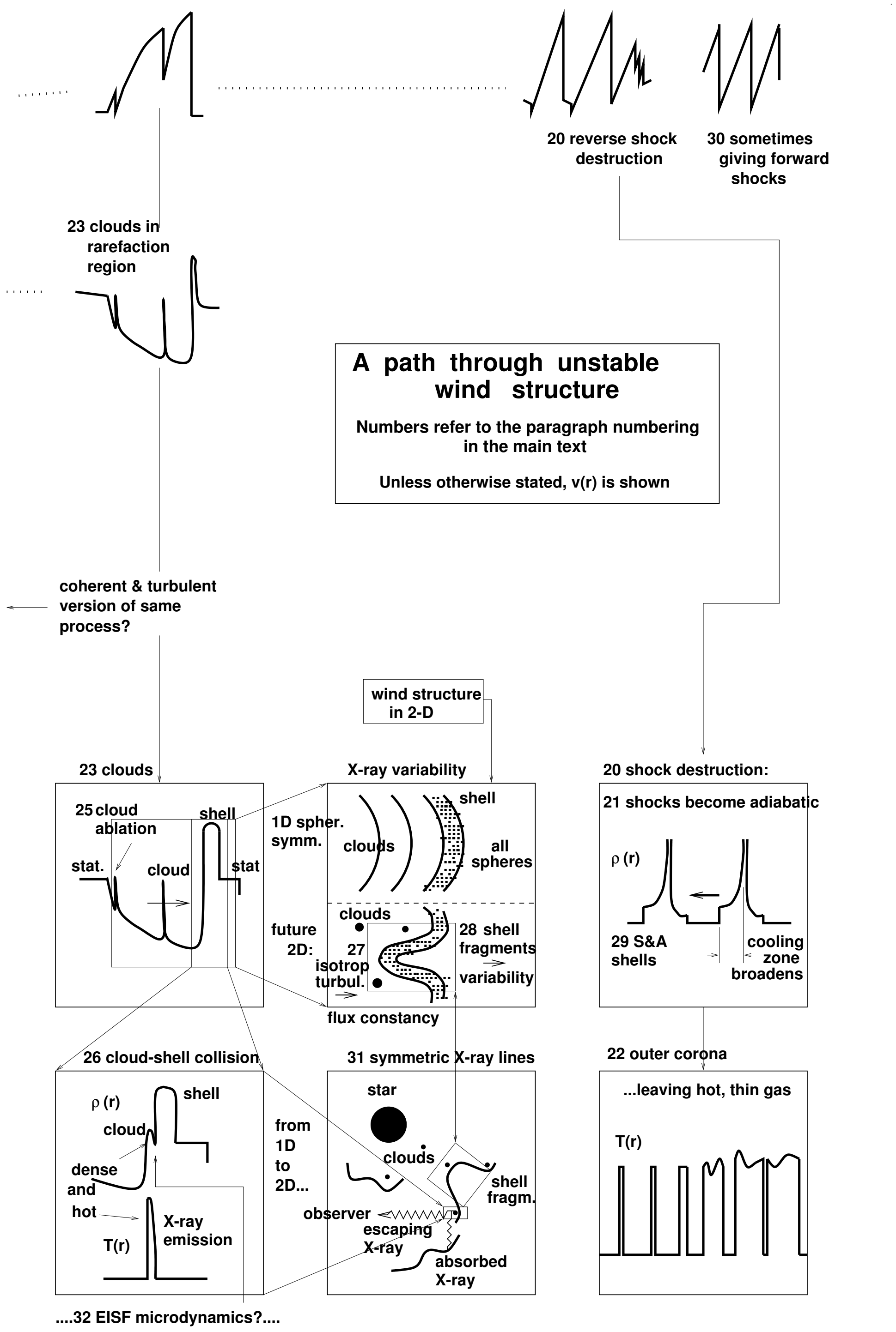

A path through unstable wind structure

Numbers refer to the paragraph numbering in the main text

Unless otherwise stated, v(r) is shown

§2 Pure absorption line force. Sobolev approximation

For one line. Line driven winds stand and fall with the formulation of the radiative force. The force due to momentum transfer by absorption and re-emission of photons in spectral lines is termed 'line force' from now. The basic problem in calculating the line force is the inclusion of scattering in the wind. The absorbed radiation determines together with particle collisions the ionization degree and occupation numbers of the plasma, which in turn determine the emitted radiation field. For a stationary and smooth flow, the feedback between radiative transfer and statistical equilibrium of the gas can be solved using ALI techniques (Cannon 1973; Scharmer 1981; Hamann 1985). However, coupling the radiative transfer and thermal equilibrium to time-dependent hydrodynamics over $\approx 10^5$ time steps (instead of '1' for stationary winds) and for ≈ 5000 spatial grid points in a highly non-monotonic velocity law (instead of 50 for smooth flow) is not yet possible. Hydrodynamic simulations have to severely approximate the radiative transfer and thermal equilibrium of the wind. The line force from all driving lines (between 10 and 10^5) is calculated from the force on a single line via a power law line distribution function with two parameters (Castor, Abbott, & Klein 1975; CAK in the following). For dense O supergiant winds, these parameters are constrained within relatively narrow margins (Gayley 1995; Puls, Springmann, & Lennon 2000). The radiative transfer in the remaining, 'generic' spectral line is further simplified. In Chapter 2, we consider pure line absorption and a simplified approach to scattering. In Chapters 3 and 4, Sobolev approximation is used.

The force which acts on a gas absorbing radiation of intensity I is derived in the textbooks by Chandrasekhar (1950) and Mihalas (1978). To avoid angle integrals at the present step, we consider a radial, spherically symmetric flow with coordinate r, which is accelerated by absorption (no scattering) of radiation from a point source located at $r = 0$. The line force per mass, g_l, is

$$g_l(r) = g_t(r) \int_{-\infty}^{\infty} dx\, \phi(x - v(r)/v_{\rm th}) e^{-\tau(x,r)}, \tag{1}$$

where τ is the line optical depth,

$$\tau(x,r) = \int_0^r dr' \kappa(r') \phi(x - v(r')/v_{\rm th})) \tag{2}$$

and

$$g_t(r) = \kappa \Delta\nu_D F_{\nu_0}(r)/c \tag{3}$$

is the radiative acceleration if the line were optically thin, $\tau \ll 1$. A Doppler profile function is assumed, $\phi(x) = \pi^{-1/2} \exp(-x^2)$, with normalized frequency variable $x = (\nu - \nu_0)/\Delta\nu_D$. Here, ν_0 is the line frequency and $\Delta\nu_D = \nu_0 v_{\rm th}/c$ the Doppler width of the line, with c the speed of light. For simplicity, the thermal speed $v_{\rm th}$ is assumed to be constant. The radial wind velocity is given by v, and $v/v_{\rm th}$ in the profile function accounts for Doppler shifts. In an accelerating wind, ions can absorb 'blue' photons, $\nu > \nu_0$, in the line transition ν_0, since they appear redshifted. Finally, F_ν is the radiative flux per frequency interval $d\nu$ at frequency ν, and κ is the mass absorption coefficient of the line, in units cm^2 per gram. For line transitions to the ground state (resonance lines) and to metastable levels, which both dominate the line force, κ is to a good approximation constant, as shall be assumed in all the following.

In hydrodynamic wind simulations of the de-shadowing instability, eqs. (1) and (2) have to be calculated as they stand, by explicit quadrature over dr and dx (and over angle; Owocki, Castor, & Rybicki 1988; Owocki 1991; paper [1]). The r and x integrals are time consuming, since high spatial and frequency resolution is required: the thermal band has to be resolved in both r and x. The thermal speed of metal ions is a few km/s in hot star winds, whereas the terminal wind speed is thousand km/s and larger. Hence, thousands of frequency and spatial grid points are required. The angle integral, on the other hand, is cheap for stellar wind simulations with a high degree of symmetry. A one- or two-ray quadrature may be sufficient. This is no longer true for winds above accretion disks, due to the radial temperature stratification of the disk and the complicated flow geometry (Proga, Stone, & Drew 1998; [6]).

Sobolev approximation. In Sobolev approximation, the profile function ϕ is replaced by a Dirac δ function: the wind is assumed to accelerate so steeply that a spectral line is Doppler-shifted into resonance with a photon over a narrow spatial range only. This region is called a resonance or Sobolev zone. The quantities ρ, κ and dv/dr are assumed to be constant over the Sobolev zone. By definition, v increases by a few thermal speeds over the zone.

Radiative transfer takes place then on a 'microscopic' scale within the zone, hydrodynamics (i.e., changes in ρ and dv/dr) on a 'macroscopic' scale (Rybicki & Hummer 1978). The fact that the wind speed v is neither a truly microscopic nor macroscopic variable causes some difficulties in our understanding of radiative waves and critical points in line driven flows [10]. A characteristic analysis in Chapter 3 shows that in Sobolev approximation, dv/dr and not v is a fundamental hydrodynamic quantity besides ρ.

To calculate the line force in Sobolev approximation from a point source of radiation, substitute $r \rightarrow \tilde{x}$ in the optical depth (2), where $\tilde{x} = x - v(r)/v_{\rm th}$. This is allowed for monotonic $v(r)$, and gives

$$\tau(\tilde{x}) = \tau_0\,\Phi(\tilde{x}), \tag{4}$$

where $\Phi(\tilde{x}) = \int_{\tilde{x}}^{\infty} dy\,\phi(y)$, and $\tau_0 = \rho\kappa v_{\rm th}/(dv/dr)$ is the total optical depth of the Sobolev resonance zone. The line force at r is caused by lines which absorb at r, hence $\tilde{x}(r) = 0$ and $\tau_0 = \tau_0(r)$. Furthermore, $\tilde{x} \equiv \infty$ is assumed at the wind base. Substituting $x \rightarrow \Phi$ in the line force integral (1) gives

$$g_l(r) = g_t(r) b(r), \qquad \text{with} \qquad b(r) = \frac{1 - e^{-\tau_0}}{\tau_0} \tag{5}$$

the so-called 'photon escape probability.' For $\tau \ll 1$ and $\tau \gg 1$, the line force scales as κ and $\rho^{-1}dv/dr$, respectively.
The expression (5) holds also for the Sobolev force when line scattering is included, and the diffuse radiation field is fore-aft symmetric, i.e., the latter does then not contribute to the line force. We will apply a Sobolev force in Chapters 3 and 4. In Chapter 2, we consider the more complicated SSF and EISF forces, which are extensions of the general force (1) to the case of line scattering, using ingredients from Sobolev approximation to calculate the radiative source function.

Force from all lines. To calculate the line force from thousands of spectral lines, the CAK line distribution function is used throughout. By assumption, there is no wind-velocity induced line overlap, and each photon is scattered in one line at most. The CAK line distribution function is given by

$$N(\nu, \kappa) = \frac{1}{\nu}\,\frac{1}{\kappa_0}\,\left(\frac{\kappa_0}{\kappa}\right)^{2-\alpha}, \tag{6}$$

introducing two parameters, κ_0 and α, where $0 < \alpha < 1$. Integrating (1) over ν and κ using (6), the total line force becomes (we keep the symbol g_l from the single line force),

$$g_l(r) = \frac{\Gamma(\alpha)\kappa_0^{1-\alpha}v_{\rm th}}{c^2}\,F(r)\int_{-\infty}^{\infty} dx\,\frac{\phi(x - v(r)/v_{\rm th})}{\eta^\alpha(x, r)}, \tag{7}$$

where Γ is the Gamma function, F is the frequency integrated flux, and we introduced $\eta \equiv \tau/\kappa$ (constant κ for each line), with τ calculated from (2). Inserting instead for a moment the Sobolev optical depth (4), one finds for the total line force in Sobolev approximation,

$$g_l(r) = \frac{\Gamma(\alpha)\kappa_0 v_{\rm th}}{(1-\alpha)c^2}\,F(r)\,\tau_0(r)^{-\alpha}, \tag{8}$$

where we redefined $\tau_0 = \kappa_0\rho v_{\rm th}/(dv/dr)$ (in order to avoid adding another subscript 0 to τ_0). Precise values for κ_0 (or, equivalently, the CAK parameter k) and α must be obtained from a detailed NLTE treatment of the wind. For the present purposes, some universal estimates are sufficient. Puls et al. (2000) derive $\alpha = 2/3$ from Kramers' opacity law for hydrogen-like ions; this value should apply for dense winds. In thin winds, $\alpha \leq 1/2$ (Pauldrach et al. 1994). The absorption coefficient κ_0 corresponds roughly to the strongest line in the flow, $\kappa_0 = \mathrm{O}(10^8\ \mathrm{cm}^2\,\mathrm{g}^{-1})$ in dense winds. Alternatively, κ_0 can be expressed in terms of an effective oscillator number Q (Gayley 1995),

$$\frac{\kappa_0 v_{\rm th}}{\sigma_e c} = Q\Gamma(\alpha)^{-\frac{1}{1-\alpha}}, \tag{9}$$

where σ_e is the absorption coefficient for Thomson scattering on electrons. In a fully ionized hydrogen plasma, $\sigma_e = 0.4\ \mathrm{cm}^2/\mathrm{g}$. For O supergiant winds, $Q \approx 2000$ (Gayley 1995), from which κ_0 can be calculated.

§3 Scattering in SSF and EISF approximation

First time-dependent hydrodynamic simulations of unstable O star winds by Owocki et al. (1988) assumed a pure absorption line force like that in (1,2) since the deshadowing instability vanishes in Sobolev approximation. This led to certain unexpected results, most notably, that the time-averaged wind does not adopt the CAK solution, but a steeper solution. (The stationary CAK solution is treated in Chapter 3. Until then, it suffices to know that this solution is unique, has a maximum mass loss rate, and a critical point which is not the sonic point.) The defects of the pure absorption model are still not fully understood (see Owocki & Puls 1999 for new insights), but they vanish when line scattering is included. (The diffuse force scales $\sim v_{\rm th}/v$, and vanishes only in Sobolev approximation.) Hence, we turn to a simplified treatment of scattering now.

In the 'smooth source function' or SSF method (Owocki 1991), a purely local radiative source function from Sobolev aproximation is assumed. The principal idea goes back to Hamann (1981a), and was adopted in the SEI method of Lamers, Cerruti-Sola, & Perinotto (1987). The remaining 'formal solution' of radiative transfer is no more complex than for pure line absorption. Especially, the optical depth for photons which are backscattered to the photosphere is by symmetry related to the optical depth for photospheric photons. No extra integrals are required in the SSF method, and the computational costs are practically the same as for pure absorption. The SSF method accounts for the important *line drag* effect (Lucy 1984), which stabilizes the flow via the *mean* diffuse radiation field.

The next step of sophistication beyond pure absorption and SSF is the 'escape-integral source function' or EISF method (Owocki & Puls 1996), which accounts for the *perturbed diffuse* radiation field. Already linear stability theory becomes very complex when perturbations in the diffuse radiation field are included (Owocki & Rybicki 1985). Yet, the basic idea of the EISF method is clear and straightforward: in spherical symmetry, the direct radiative force due to photon absorption in a single line is, including now angle integrals explicitly,

$$g_a(r) \sim \langle \mu I_*(\mu) b(\mu, r) \rangle. \tag{10}$$

Angle brackets indicate angle averages, μ is the cosine of the angle of a photon ray with the radial direction, $I_*(\mu)$ is the angle dependent, photospheric radiation field, and $b(\mu, r)$ is the escape probability for direction cosine μ (cf. eq. 1),

$$b(\mu, r) = \int dx\, \phi(x - \mu v(r)/v_{\rm th})\, e^{-\tau(x,\mu,r)}. \tag{11}$$

The diffuse or scattering force, on the other hand, is

$$g_s(r) \sim S(r) \langle \mu b(\mu, r) \rangle, \tag{12}$$

with isotropic source function S. For pure scattering lines in Sobolev approximation, one derives from (5) and the transfer equation (see Owocki & Rybicki 1985 for details) that

$$S(r) = \frac{\langle I_*(\mu) b(\mu, r) \rangle}{\langle b(\mu, r) \rangle}. \tag{13}$$

In the SSF method, different expressions are used for the escape probabilities in g_a, g_s and in S: in the g's, b is calculated from the actual, time-dependent flow structure; whereas in S, purely local escape probabilities for a smooth flow are used. By contrast, in the EISF method b from the actual, structured flow is used both in g and S. No quantities are introduced in EISF which did not already occur in SSF. Still, the calculational cost is much larger in EISF since *two* spatial integrals are required. In the first integral, the source function is calculated over the whole mesh, the second serves for a formal solution. Furthermore, a quadrature over frequency x is required. Owocki & Puls (1996) remark that these 3 integrals can be reduced to 2 again for a single spectral line; but not for a line ensemble.

The EISF approach allows for the first time to study phase reversal between velocity and density fluctuations as a consequence of perturbations of the diffuse radiation field. This subtle yet important effect is discussed further on page 30. The simulations discussed in detail in the next chapter were calculated using the SSF method.

CHAPTER 2. UNSTABLE WINDS

It is now believed that line driven winds from single stars show structure in all three spatial directions. In the polar ($r\theta$) plane, wind-compressed disks may (Bjorkman & Cassinelli 1993; Owocki, Cranmer, & Blondin 1994) or may not (Owocki, Cranmer, & Gayley 1996) form around rapidly rotating stars. In the equatorial ($r\phi$) plane, co-rotating interaction regions may cause 'discrete absorption components' (Cranmer & Owocki 1996) observed in non-saturated P Cygni line profiles. Most 'simply', however, already in 1-D radial flow shocks and dense shells develop due to a new hydrodynamic instability. This instability is the subject of the present chapter.

To give an overview of the field, we start with a bibliography of relevant papers. The instability mechanism is discussed, and results from linear stability analysis are summarized. Because of the complexities of line scattering, linear theory is not complete to the present day. This is not just a mathematical curiosity, but the origin of a fundamental debate. Namely, since the Green's function for the case of pure line scattering is not yet known, the nature of signal propagation in these unstable winds is – mysterious. Signal propagation plays a key role in understanding how the flow adapts to boundary conditions. The main topic of this chapter is the evolved, nonlinear wind structure found from numerical simulations, and its relation to observed X-ray emission from O stars.

§4 THE DE-SHADOWING INSTABILITY

History. A new, radiation hydrodynamics instability of line driven flows was first suggested by Lucy & Solomon (1970). The mechanism is similar to one proposed by Milne (1926) for the solar chromosphere. Approximate linear stability analysis was performed by MacGregor, Hartmann, & Raymond (1979), Carlberg (1980), and Abbott (1980). In the former two papers, unstable growth rates were derived, whereas Abbott found a new, marginally stable, radiative-acoustic wave mode. This contradiction was resolved by Owocki & Rybicki (1984), who showed that the opposing results apply on different length scales. Lucy (1984) found that the diffuse radiation field from line scattering causes a drag effect which could prevent the instability. Owocki & Rybicki (1985) derived that complete cancellation occurs only close to the photosphere. A very puzzling result was derived by Owocki & Rybicki (1986), who showed that Abbott waves do occur in absorption flows (they shouldn't), but as a pure mathematical artefact. What are the consequences for Abbott waves if scattering is included? Rybicki, Owocki, & Castor (1990) proved that wind instability occurs in flow or radiative flux direction only. In lateral direction, line drag stabilizes the flow. A linear stability analysis for Wolf-Rayet stars was performed by Owocki & Rybicki (1991) and Gayley & Owocki (1995) in diffusion approximation. They found that unstable growth rates are reduced by the multi-scattering factor. Feldmeier (1998, paper [5]) derived that the instability occurs already in Sobolev approximation, if velocity curvature terms are included. This issue of fore-aft asymmetries when crossing the Sobolev zone is addressed in papers by Lucy (1975; Sobolev vs. Newtonian derivative); Owocki & Zank (1991; radiative viscosity) Gayley & Owocki (1994; radiative heating), and Owocki & Puls (1999; source function depression). First numerical simulations of the evolved wind structure were given in breakthrough papers by Owocki, Castor and Rybicki (1988; OCR) for the case of pure line absorption, and by Owocki (1991, 1992) for line scattering in SSF approximation. Poe, Owocki, & Castor (1990) suggested that the nodal topology of the sonic point in line driven flows causes either solution degeneracy or convergence to a steep, non-CAK solution. The classical paper on steady wind solutions and the critical point topology is Castor, Abbott, & Klein (1975; CAK). The issue of solution topology is again related to the inclusion of line scattering. The *perturbed* diffuse radiation field was treated in linear analysis by Owocki & Rybicki (1985), and implemented in numerical simulations by Owocki & Puls (1996) via the EISF method. EISF simulations which clarified deeper aspects of the Sobolev approximation were performed by Owocki & Puls (1999). Phenomenological wind shock models of X-ray emission were suggested by Lucy & White (1980), Lucy (1982b), Krolik & Raymond (1985), and MacFarlane & Cassinelli (1989). The energy equation and radiative cooling in post-shock zones was included in hydrodynamic simulations of unstable winds by Feldmeier (1995, [1]), and Feldmeier, Puls, & Pauldrach (1997, [4]) suggested X-ray emission from turbulent cloud collisions. P Cygni lines from structured, unstable winds were calculated by Puls, Owocki, & Fullerton (1993) and Puls et al. (1994).

1 The microscopic mechanism.[2] The basic mechanism of the instability is as follows. Consider the velocity law $v(r)$ of a line driven wind. Because of its width of a few $v_{\rm th}$ as caused by thermal motions, $v(r)$ may be called a *thermal band.* The thickness of the thermal band is characterized by the Sobolev length, $L = v_{\rm th}/dv/dr$. This is the *natural* length scale for line driven winds. Instability occurs for perturbations with wavelength $\lambda < L$ (we shall, however, find below that $\lambda > L$ is also unstable). An arbitrary, positive velocity fluctuation $+\delta v$ Doppler-shifts a gas parcel out of the absorption shadow of gas lying closer to the star (or the accretion disk). The enhanced radiative flux on the parcel accelerates it to larger speeds and de-shadows it further. Since the single-line force scales as $g_l \sim e^{-\tau}$, the amplification cycle can be written as $\delta v \to -\delta\tau \to \delta g_l \to \delta v$.

Once the parcel got 'kicked out' of the thermal band, further de-shadowing is impossible. Carlberg (1980) concluded that the instability should *not* cause observable perturbations of the velocity law, but microscopic fluctuations of order $v_{\rm th}$ only. This is correct for short scale perturbations $\lambda < L$. We shall see below that long scale perturbations, $\lambda \gg L$, result in $\Delta v \gg v_{\rm th}$. It is therefore slightly misleading to say (as is occasionally done) that the instability generally causes short scale structure. Milne (1926) described a runaway process which he held responsible for the ejection of high-speed atoms from the static solar chromosphere. The process is so similar to the de-shadowing instability that we give a quotation from Milne's paper.

> "An atom which, due to some cause or other, begins to move outward from the sun with an appreciable velocity will begin to absorb in the violet wing of the absorption line corresponding to the same atom at rest, owing to the Doppler effect. It will

---

[2] The numbers at the start of paragraphs correspond to the numbers in the figure on pages 14 and 15.

> therefore be exposed to more intense radiation, and the atom will be accelerated outwards. It will therefore move still further out into the wing, where it will be exposed to still more intense radiation, and so on, until it eventually climbs out of its absorption line."

Note that Milne describes a plasma instability for single ions, whereas the deshadowing instability is a hydrodynamic instability for fluid parcels. The other difference is between a static atmosphere and a wind.

2 Linear instability for absorption lines. Owocki & Rybicki (1984) gave the first, full derivation of instability growth rates. For long scale perturbations $\lambda \gg L$, the *imaginary* growth rates turn into a *real* dispersion relation for Abbott waves (or, in the older literature, 'radiative-acoustic waves'). The derivation given in equations (1) to (30) of Owocki & Rybicki (1984) is very compact. Hence we refer to this paper, and quote only some results. Starting point of the derivation is the line force from a point radiation source, eqs. (1, 2). Perturbations δv enter in *both* profile functions $\phi(x)$. After substitution from spatial to frequency variables; applying Sobolev approximation for the *mean* flow; and introducing harmonic perturbations $\delta v(r) \sim \exp(ikr)$ obeying WKB approximation, one arrives at the perturbed line force (a subscript 0 refers to the mean flow),

$$\frac{\delta g_l}{\delta v} = iK\omega_0\tau_0 \int_{-\infty}^{\infty} dx\, \phi(x) e^{-\tau_0 \Phi(x)} \int_{x}^{\infty} dx' \phi(x') e^{-iK(x'-x)}. \tag{14}$$

Here, $\omega_0 = g_t/v_{\rm th}$, $\tau_0 = \kappa_0\rho_0 v_{\rm th}/(dv_0/dr)$, $K = kL$ (the wavenumber in units of the Sobolev length, L), and $\Phi(x)$ as above. The perturbed line force depends on the profile function ϕ. Using an ingenious integration trick, Owocki & Rybicki (1984) solved the double integral analytically for $\tau_0 \gg 1$, where it becomes independent of ϕ. The result is

$$\frac{\delta g_l}{\delta v} = \omega_b \frac{ik}{\chi_b + ik} \qquad (\tau_0 \gg 1), \tag{15}$$

where (introducing an opacity $\chi = \rho\kappa$),

$$\omega_b = \omega_0\, \phi(x_b), \qquad \chi_b = \chi_0\, \phi(x_b), \tag{16}$$

and the *blue edge* frequency x_b is defined by

$$\Phi(x_b) \equiv 1/\tau_0. \tag{17}$$

For short scale perturbations, $k \to \infty$ and $\delta g_l/\delta v = \omega_b$. This implies instability, since the phase shift between velocity and force perturbations is 0. In the limit $k \to 0$, on the other hand, $\delta g_l/\delta v = ik\omega_0/\chi_0$. With 90 degrees phase lag between velocity and force perturbations, this corresponds to marginally stable waves: Abbott waves. For long scale perturbations with *finite* λ, one has (slightly) unstable waves. Again from (15), the growth rate drops as $(L/\lambda)^2$ for $\lambda \gg L$.

3 Macroscopic linear instability: 2nd order Sobolev. Instead of going through the above, 'exact absorption' analysis, Abbott (1980) applied Sobolev approximation to the mean flow *and* to velocity perturbations. He finds marginally stable waves which are not affected by the instability. This is odd since we saw above that long scale waves, $\lambda \gg L$, *are* unstable, if only at reduced growth rates. But for $\lambda \gg L$, Sobolev approximation *should* apply. Indeed, instability occurs in *second order* Sobolev approximation, including curvature terms d^2v/dr^2 [5]. The second order Sobolev optical depth τ is found to be,

$$\tau(\tilde{x}, r) = \tau_0(r)\left[\Phi(\tilde{x}) + \frac{v_{\rm th}}{2v'}\left(\frac{v''}{v'}(r) - \frac{\rho'}{\rho}(r)\right)\big(\phi(\tilde{x}) - 2\tilde{x}\Phi(\tilde{x})\big)\right], \tag{18}$$

with τ_0 as before, and primes indicating spatial derivatives. Using (18) to calculate $\delta\tau$ in the perturbed line force one finds *unstable* Abbott waves, with growth rate $\sim (L/\lambda)^2$. Despite the different approximations made in the two approaches, the latter growth rates agree to within 20% with those of Owocki & Rybicki (1984).
Equation (18) offers an intuitive understanding of the wind instability at *large* perturbation wavelengths, which complements the picture of parcels being kicked out of the thermal band described earlier (see Fig. 1 in [5]). When the velocity law experiences a small *upward bend*, $v'' < 0$, the optical depth is reduced (we assume that v' averaged over the resonance zone is left unchanged). This implies an increase in line force, $g_l \sim e^{-\tau}$. The 'elevated' region is accelerated to larger speeds. This means it gets further elevated, and $-v''$ grows further. An amplification cycle $-\delta v'' \rightarrow -\delta\tau \rightarrow \delta g_l \rightarrow \delta v \rightarrow -\delta v''$ results. The corresponding argument holds for a depression $+\delta v''$.

4 Nonlinear steepening: a first look at evolved wind structure. We can already at this stage predict some features of the evolved wind structure, before going into details of hydrodynamic simulations. A depression in $v(r)$ as considered in the last paragraph will eventually cause the *mean* velocity gradient v_0' to become smaller (assumed above to be left unchanged). Since $\tau_0 \sim 1/v_0'$ increases, the blue wing frequency x_b becomes more negative, and the growth rate $\omega_b \sim \phi(x_b)$ drops steeply. The depression region will not evolve ('depress') further. Depression regions will always remain close to the stationary flow. On the other hand, elevations of the thermal band will continue to grow until the flow becomes optically thin and no further de-shadowing is possible. In the nonlinear regime, fast gas overtakes slow gas ahead of it, and the velocity law evolves a triangular sawtooth shape. The jumps in the 'shark fins' decelerate the gas, hence, are reverse shocks. The robust morphology of the wind velocity law, which shows up in most numerical simulations, is therefore: a sawtooth pattern of steep, accelerating regions and pronounced reverse shocks.

5 How large are the shock jumps? Whereas short scale perturbations $\lambda \leq L$ saturate at the microscopic level of a few $v_{\rm th}$ (Carlberg 1980), large scale perturations $\lambda \gg L$ give velocity jumps of order v_∞, the wind terminal speed. Overall, a short scale, noisy structure ($v_{\rm th}$) is superimposed on a large scale, coherent tilt of the wind velocity law [5].

6 Scattering: the line drag effect. We consider an effect which proves the fundamental importance of line scattering, and that the pure absorption line case may be a degenerate limit (Owocki & Rybicki 1986). Lucy (1984) found that line scattering, via a so-called line drag effect, may prevent wind instability! The origin of the effect is simple. A wind parcel may again experience a perturbation $+\delta v$. The parcel leaves the absorption shadow of gas lying closer to the star, leading to instability. However, the parcel experiences also a stronger, backscattered radiation field from larger heights, because it is Doppler-shifted *into resonance* with *faster* gas further out. Hence, the inward push grows. Assuming a plane-parallel atmospheric slab and that the star fills a hemisphere, and furthermore that scattering is fore-aft symmetric, one shows that the direct and diffuse force perturbations in an optically thick line cancel exactly. We leave consideration of the *outward* pointing diffuse force from gas lying at smaller height than the perturbation site to the reader.

For spherically symmetric flow, the instability growth rate is back to 50% of its pure absorption line value at one stellar radius above the photosphere, and reaches 80% of the absorption value at large radii (Owocki & Rybicki 1985). Still, the line drag effect is of great importance both numerically, preventing fast growth at the inner boundary, and in nature, with regard to the much-speculated ‘photospheric connection’, i.e., whether wind structure grows from photospheric perturbations or is wind intrinsic (Henrichs 1986; Henrichs et al. 1990).

§5 Evolved wind structure

After decades of fascinating and frustrating mathematical research on nonlinear growth of fluid instabilities (Landau equation, bifurcation, chaos & catastrophes), computers have shown a pragmatic way into evolved, unstable flow via direct, time-dependent simulations. In this and the next sections, we discuss the structure of fully developed, unstable line driven winds. To model the evolution of the instability, a standard Eulerian grid code is used. For the pure hydrodynamics part, we coded a program following the detailed, technical descriptions given in Hawley, Smarr, & Wilson (1984), Norman & Winkler (1986), Reile & Gehren (1991), Stone & Norman (1992a,b). Some of the techniques are also summarized in [1]. The applied techniques comprise: ‘consistent’ advection (Norman, Wilson, & Barton 1980) using van Leer (1977) or ‘piecewise parabolic’ interpolants (Colella & Woodward 1984) on control volumes of staggered grids; non-reflecting Riemann boundary conditions (Hedstrom 1979; Thompson 1987, 1990) ; tensor artificial viscosity (Schulz 1965); pressure predictor (Norman & Winkler 1986).

As for the radiative line force, I followed Owocki et al. (1988) which includes technical subleties like line-list cutoff; a Schuster-Schwarzschild photospheric layer to prevent unstable growth close at the inner boundary; and the strict one-sidedness of the direct force. The SSF method for treating the diffuse radiation field is described in Owocki (1991, 1992), an unpublished draft from 1990, and in Owocki & Puls (1996). Except for one workshop paper (Owocki 1999), all simulations published so far are in radial direction only, assuming spherically symmetric flow. CPU time requirements for 2-D wind instability simulations are huge. The present work is no exception, and deals with spherical symmetric simulations only.

7 The basic entity of wind structure. Figure 4 (taken from paper [1]) shows the evolved wind structure. The pronounced features are: (1) broad rarefaction regions of accelerating gas; this gas is (2) braked in strong reverse shocks, and fed into (3) narrow, dense shells. (4) The shells propagate into gas which remains close to stationary initial conditions. If forward shocks occur at all at the outer shell edges, they are weak.

As a seed perturbation for wind instability, a coherent photospheric sound wave of period 5,000 sec and pressure amplitude 1 percent is introduced at the inner boundary of the model. The wave period determines the spacing of wind shells. Namely, the perturbation wavelength in the photosphere, $\lambda = aT = 0.009\,R_*$ (with sound speed a, period T, and stellar radius R_*), is stretched in the accelerating flow by a factor $v_\infty/a = 90$. Indeed, the shell distance far out in the wind is $0.8\,R_*$, cf the figure.

8 Subshells and overtones. Figure 4 of paper [1] shows that 50 (!) overtones of the photospheric sound wave can be clearly distinguished in the wind. There is no indication of stochasticity at all in the wind, hence the structure is strictly deterministic. This is rather unexpected from glancing at the velocity law between 2 and $5\,R_*$, in which region the wind appears to be rather chaotic (not meant in the new, technical sense of the word). Up to these heights, collisions occur between multiple shells per photospheric excitation period. As noted in [1], these sub-shells are related to non-linear steepening and harmonic overtones. The dynamical details are still not clear. Figure 4 shows the mass loss rate in the wind as function of radius and time. After initial transients have died out, the wind settles to a limit cycle. Per photospheric perturbation period, three subshells are created and mutually collide with each other up to around $3\,R_*$.

9 Two-stage instability. Even for these periodic models the de-shadowing instability is sufficiently delicate that new details become visible when model parameters are varied. Figure 5 below shows a run which differs from the above one mainly by a shorter perturbation period of 1,000 seconds (besides this, it was performed 7 years later). The difference is marked. In the new model, sub-shell collisions terminate already around $2.5\,R_*$. Afterwards, the shocks decay quickly, out to $6\,R_*$. Between 7 and $9\,R_*$, *new shocks* occur, which was not the case in the old model.

How can new shocks occur after the instability went into saturation, and left a fully developed flow? What happens here is a *second* stage of the instability. We noted above that negative velocity perturbations saturate quickly, and the wind remains close to stationary initial conditions in regions ahead of pronounced shells. Looking closely at the region from 4 to $6\,R_*$ in Fig. 5, one sees a growing velocity perturbation: in the evolved wind structure, eventually the pseudo-stationary regions become unstable, too, via secondary perturbations. We expect that the latter are related to overtones. The new perturbations steepen into new shocks. The shocks accelerate, overtake and merge with the 'old' shock front from the first growth phase of the instability. This creates a single, strong shock.

10 Lamb ringing. Introducing coherent sound waves as instability seeds allows to study the ultimate fate of linear perturbations from harmonic stability analysis. But

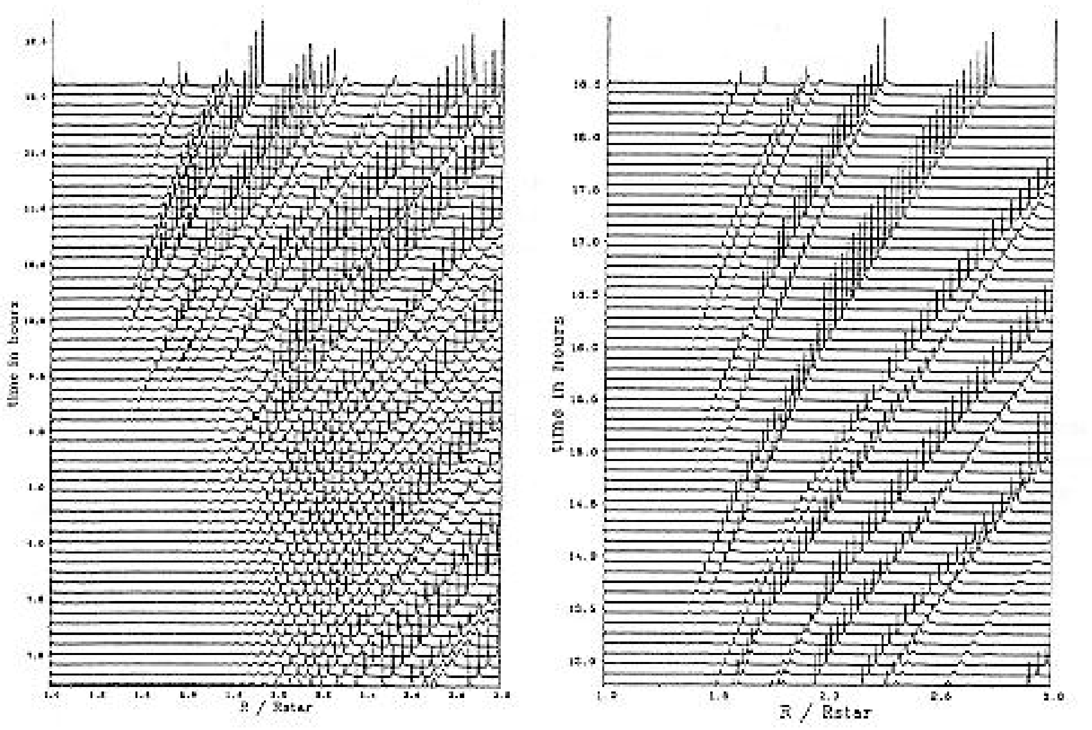

Figure 4: Wind mass loss rate as function of radius and time. After initial transients have died out, the wind settles to a limit cycle. Per photospheric excitation period, three subshells are created and mutually collide.

how relevant are coherent perturbations physically? Below we shall argue that, to understand the observed X-ray emission from hot star winds, one has to refrain from periodic, coherent perturbations and consider random ones instead. Still, relatively coherent perturbations may be expected from stellar pulsations. They cannot be modeled in 1-D simulations, where only pressure or p modes (sound waves) can be excited. Internal gravity waves or g modes cannot propagate vertically through an atmosphere, since lifting a planar atmospheric layer does not give a buoyancy force. Interestingly, coherent atmospheric perturbations do actually not require an external piston like stellar pulsations, but could be excited intrinsically in the atmosphere: an atmospheric resonance frequency exists, Lamb's *acoustic cutoff*.

As the reader may already get weary of deflections from the straight path brought about by 'unexpected' hydrodynamic effects shooting in from left and right, we add a historical note, trying to emphasize the importance of the acoustic cutoff. Lamb built on earlier work by Rayleigh (1890), who first derived the dispersion relation for sound waves in an isothermal barometric density stratification. Rayleigh failed to see the physical relevance of the frequency $\omega_a = a/2H$ defined by atmospheric parameters (a the sound speed, H the scale height). Only after the detection of a single-frequency, atmospheric response after the big Krakatao volcano eruption, Lamb realized the importance of ω_a as an atmospheric resonance. His argument

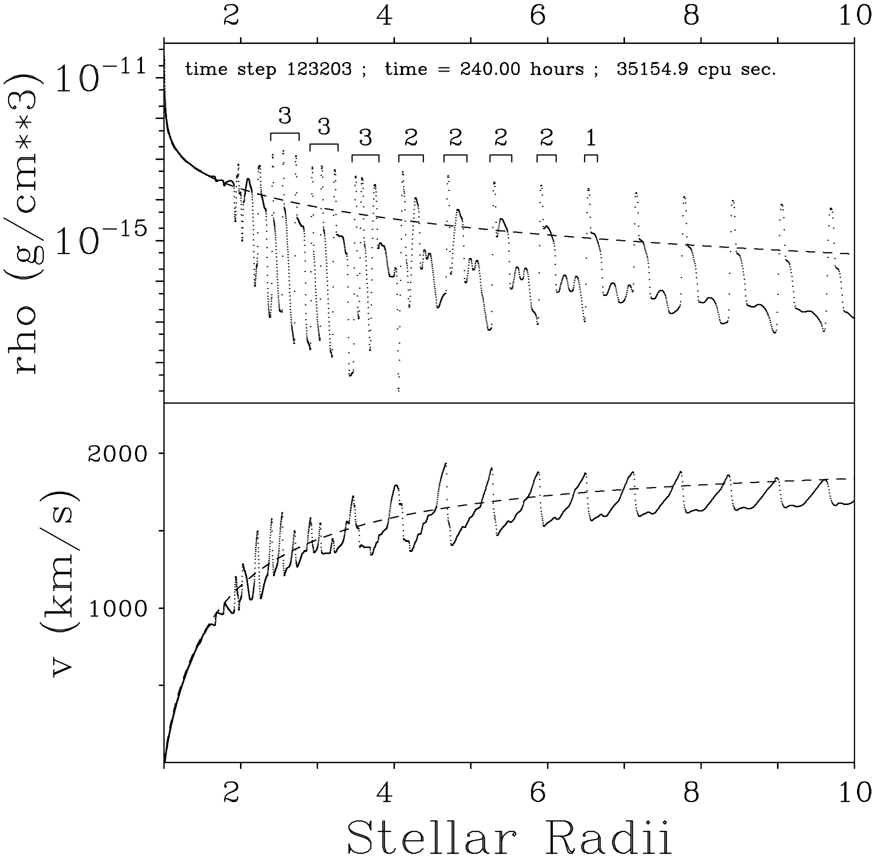

Figure 5: Snapshot of an O supergiant wind velocity law and density stratification. A periodic sound wave of 5,000 sec period is applied as photospheric seed perturbation for the de-shadowing instability. Dots show individual mesh points. The numbers in the upper panel refer to the sub-shells per excitation period. Taken from [1].

(Lamb 1908), which is far from trivial, can be found on p. 544 of his 'Hydrodynamics' (1932). Especially, he proves that in an isothermal atmosphere, a white-noise sound spectrum evolves into a one-spike spectrum, the spike located at the acoustic cutoff period. The acoustic cutoff is therefore indeed a resonance.

The acoustic cutoff was held responsible for the 5 minute oscillations of Sun (Schmidt & Zirker 1963; Meyer & Schmidt 1967). But the appropriate acoustic cutoff period is 3 to 4 min, not 5 min. Ulrich (1970) developed the alternative and correct theory that the 5 min oscillations correspond to acoustic waves trapped in a resonance cavity reaching from the deep solar interior to the top of the convection zone. This established the field of helioseismology. Deubner (1973) observed a photospheric subsignal of 3 min period, where the wave trains are correlated with the appearance of bright granules. These granules are thought to struck the photosphere from below, and excite Lamb ringing. For a review on solar 5 minute oscillations, see Stein &

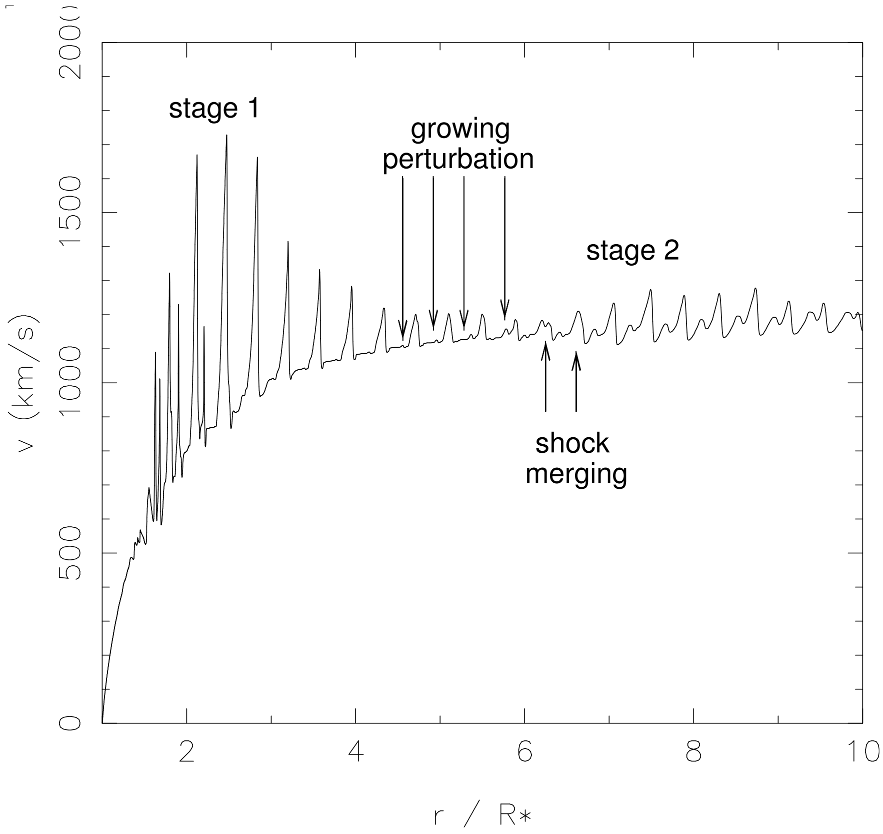

Figure 6: Snapshot of the wind velocity law, assuming a photospheric sound wave with period 1,000 sec. Two stages of unstable growth are seen. In the second stage, perturbations grow within the quasi-stationary gas ahead of dense shells, and lead to secondary shocks.

Leibacher (1974).
Simulations of line driven winds from O stars show a self-excitation of the atmosphere at the acoustic cutoff frequency. Its ‘perturbing’ influence on the outer wind structure was occasionally noted in the literature (e.g., Blondin et al. 1990), but not traced back to its physical cause. We close this excursion by expressing our belief that ‘Lamb ringing’ could be responsible for rather coherent trains of pronounced shells in hot star winds.

11 Reverse shocks. Reverse shocks occur because the instability steepens the velocity law of the wind, and the fast gas is eventually decelerated. As a reminder, we add here the distinction between reverse and forward shocks: forward shocks overtake slow gas and accelerate it. In any reference frame, the shock is faster than both the pre- and postshock gas. Forward shocks occur in explosions. Reverse shocks, on the other hand, decelerate fast gas. The shock is slower than the gas on both sides. A reverse shock occurs if a supersonic stream hits a wall or an obstacle.

12 Rarefaction regions. The rarefaction regions and reverse shocks in numerical wind simulations are quasi-stationary. Seen from a comoving frame, they change only little. Rarefaction regions can therefore, to a good approximation, be identified with (patches of) 'steep' wind solutions (Owocki, priv. comm.; Feldmeier et al. 1997c). This type of solution to the stationary Euler wind equation will be discussed in the next chapter.

If a stationary rarefaction region is to feed gas into a shell through a reverse shock, a gas source must exist. Rarefaction regions lie directly above depression regions of the velocity law (negative Abbott half waves). Here, the flow does not evolve, but maintains the initial conditions. The depression region extends inwards, to the outer edge of the next shell.

13 Contact discontinuity. Assuming a Sobolev line force and zero sound speed, a contact discontinuity separates the rarefaction and depression regions. The velocity law is continuous there but has a kink. Using terminology only introduced on page 44, the wind jumps from the critical, initial conditions to a *steep* solution. Because of subcritical mass flux in the latter, a density discontinuity occurs at the contact discontinuity. Gas cannot penetrate through a contact discontinuity, hence we are still left without gas source to feed the next outer shell.

Any discontinuity in a derivative of the fluid variables v and ρ propagates at characteristic speed (Courant & Hilbert 1968). Indeed, the contact discontinuity moves at sound speed. Yet, since $a = 0$, it moves along with the fluid. Allowing for finite sound speed instead, the 'gate opens' and the rarefaction region eats slowly into the depression. Constant mass flux is maintained through the rarefaction region. The situation is sketched in Fig. 6, which also shows earlier and later stages in the evolution of the instability. Figure 7 shows results from a numerical simulation.

14 Forward shocks and EISF noise. We come to what may at first seem a rather subtle, technical issue. The central importance of line scattering to line driven wind hydrodynamics will, as we hope, become clearer throughout the subsequent discussions. Owocki & Rybicki (1985) derived from linear stability analysis that the perturbed diffuse radiation field turns anti-correlated density and velocity fluctuations into correlated ones. Anti-correlated fluctuations steepen into reverse shocks, correlated fluctuations steepen into forward shocks. In SSF, only the mean diffuse radiation field is treated, and photospheric perturbations evolve into reverse shocks. If, on the other hand, the perturbed diffuse radiation field is included, the phase lag between velocity and density perturbations may be inverted, and strong *forward* shocks may occur instead of reverse shocks. This argument was first made by Puls (1994), and stimulated development of the EISF method.

Owocki & Puls (1999) proved from EISF simulations, which include the perturbed scattered radiation field, that forward shocks are not important in the unstable wind. EISF and SSF wind structure are essentially identical, and are both dominated by reverse shocks. The reason is that phase reversal occurs only for short scale fluctuations below the Sobolev length (Owocki & Rybicki 1985). Short scale perturbations saturate at velocity amplitudes of order v_{th} (see page 22). Correlated perturbations and forward 'shocks' (if at all) appear therefore as short scale, small amplitude noise

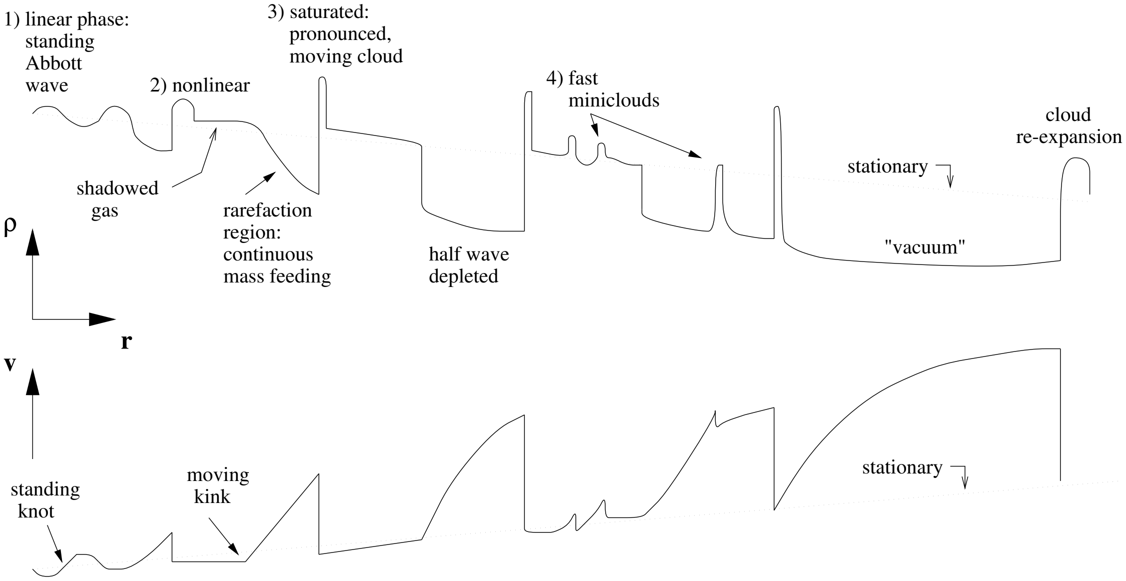

Figure 7: Evolution of winds structure from the de-shadowing instability (schematic).

superimposed on the long scale, large amplitude tilt of the thermal band leading to reverse shocks.

15 Are shells enclosed by forward shocks? Furthermore, forward shocks are *not* required to enclose the shells on their outer edges, to prevent them from expanding away. The argument is simple (Feldmeier et al. 1997c): shells are geometrically thin and consist of subsonic post-shock gas. Hence, their internal sound crossing time is small compared to the flow time, and hydrostatic equilibrium can be assumed. According to the equivalence principle, the outward directed acceleration of the shell by the line force is indistinguishable from an inward gravity binding a static atmosphere. Hence, the shells are held together without the necessity of outer forward shocks.

16 Shell densities. This same argument can be used to estimate shell overdensities with respect to smooth, stationary gas densities. The inner-shell gas expands via thermal pressure. This thermal pressure and shell acceleration define a ('gravitational') scale height, H, which measures the shell thickness. We approximate the line acceleration by $v_\infty^2/n\,R_*$, where v_∞ is the wind terminal speed and n is 'a few'; hence, $H = n\,R_* a^2/v_\infty^2$. Assuming that all gas from within a rarefaction region of average thickness $\lambda/2$ (λ being the perturbation wavelength) is fed into the shell; and that $\lambda \approx R_*$ for the longest perturbations which can still grow into saturation, the overdensity, o, of shell gas with respect to stationary wind gas becomes,

$$o \approx \frac{\lambda}{2H} = \frac{1}{2n}\left(\frac{v_\infty}{a}\right)^2 . \tag{19}$$

For $v_\infty/a \approx 100$, this is of order $\geq 10^3$, in good agreement with numerical simulations. At large radii, radiative acceleration of the shell ceases, and H grows. The

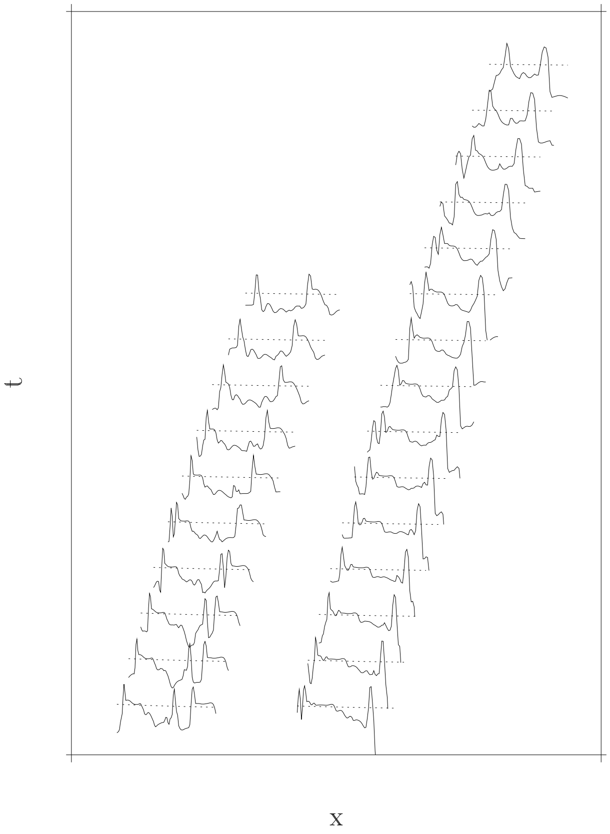

Figure 8: How the rarefaction zone eats through the mass reservoir. The plot shows subsequent snapshots of wind density (logarithmic) as function of radius (linear). No scales are given on the axes, since the same structures occur for small or large perturbation periods, at small or large separation between pronounced shells. The dotted lines show the underlying, stationary wind model. The gas reservoir ahead of dense shells is unaffected by instability, and has practically *stationary* densities.

shells should have expanded away, and the wind be homogeneous again by 30 to $100\,R_*$. This, too, agrees with numerical simulations, see Fig. 6 in [4].

17 Inner shell velocity law. At first surprisingly, the velocity law has a *negative* gradient inside shells (Owocki 1992; [3]). This is also true for *solar* wind shells (Simon & Axford 1966). The reason is that the velocity law inside the shell reflects the gas history. Gas lying close to the outer shell edge was shocked earlier than gas lying near the inner edge, close to the reverse shock. The shell velocity law is close to a stationary CAK velocity law, which means that the shell is constantly accelerated on its trajectory. With the gas velocity at the reverse shock increasing in course of time, a negative velocity gradient results inside the shell.

§6 Wind structure and line profiles

Motivation. Quantitative spectroscopy of UV and optical lines (especially of Hα, Puls et al. 1996) allows to determine mass loss rates, terminal speeds, and metal abundances of the wind. All this information (plus the stellar radius) flows into the wind-momentum luminosity relation, from which the stellar luminosity is inferred (Kudritzki et al. 1999). The premise is that hot stars will in the near future become a primary distance indicator of the same quality as Cepheids. It is therefore important to understand the influence of wind structure on line formation.

P Cygni lines from 1-D, structured wind models. Puls et al. (1993, 1994) calculated P Cygni line profiles for resonance lines from winds structured by the de-shadowing instability. Radiative transfer in the highly non-monotonic velocity law is solved for by iterating the source function, to account for multiple resonance locations (Rybicki & Hummer 1978). The resulting line profiles agree well with profiles from stationary wind models. This is at first surprising, given the 'large amount' of structure in the wind, cf. Figures 4 and 5, and Figure 8 below. The reason for the agreement is that most of the *mass* in the unstable, structured wind still follows a smooth, CAK-type velocity law. The reasoning is actually more subtle, and we refer to Puls et al. (1993) for an in-depth discussion. Some of the differences between line profiles from stationary and unstable, time-dependent wind models resemble observed variability features like black troughs, narrow absorption components (NACs), and blue edge variability.

Observed line variability, and ideas of its origin. Besides X-ray emission, which is discussed further below, the major observational evidence for pronounced flow structure in winds from hot stars comes from variability in optical and UV spectral line profiles. We give a brief, phenomenological overview of variability features. The books edited by Moffat et al. (1994) and Wolf et al. (1999) are good entry points in the large body of literature.

Of central importance are DACs (discrete absorption components), found in unsaturated P Cygni line profiles of OB stars, and so-called discrete wind emission elements, observed in flat-topped emission line profiles from W-R stars (Moffat 1994; Lépine & Moffat 1999) and O supergiants (Eversberg, Lépine, & Moffat 1998). The DACs come in company of 'bowed variation contours' or simply 'bananas' (Massa et al. 1995). DACs are pure absorption phenomena, while bananas are modulative. Bananas are explained by dense spiral-arm structures in the wind (Owocki et al. 1995; Fullerton et al. 1997), similar to CIRs (co-rotating interaction regions) in the solar wind. Their period is an even divisor (2 or 4) of the rotation period. The origin of the DACs was first supposed in the de-shadowing instability, but this was later excluded (Owocki 1994). Then CIRs were suspected as their origin, but they can only explain the much faster bananas. Hence, DACs remain enigmatic. A promising idea is that Abbott waves cause velocity plateaus in the wind which lead to enhanced absorption and DACs (Cranmer & Owocki 1996). Interestingly, velocity plateaus and not density enhancements were the first idea to explain DACs (Hamann 1980). Discrete wind emission elements, on the other hand, are thought to be caused by compressible blob turbulence. Whereas turbulence in incompressible fluids leads to an eddy cascade, supersonic or compressible turbulence leads to a shock cascade. The eddy cascade is direct, with big eddies feeding energy into small eddies. The shock cascade, on the other hand, is inverse: strong, fast shocks overtake weak, slow shocks, and merge with them into one strong and fast shock. Hence, energy is transferred from small to large scales. A connection may exist between this compressible turbulence and the wind clouds thought to be responsible for X-ray emission from hot stars. This is discussed in the following.

Wind clumping. Terminal speeds and mass loss rates are the central parameters of line driven winds. They determine the metal entrichment of the interstellar medium, and the star formation rate in starbursts. Furthermore, wind mass loss determines the evolution of hot, massive stars. And finally, knowledge of wind parameters allows to derive stellar luminosities and distances, a matter of prime importance in astronomy. Hence, reliable measurements are needed for v_∞ and $\dot{M}$. However, the mass loss rates of Wolf-Rayet stars, and probably also of O supergiants, are fundamentally affected by instability-generated flow structure. This was first realized by Hillier (1984), who introduced wind *clumpiness* to explain observed electron scattering wings of emission line profiles in Wolf-Rayet stars. The line core depends linearly on gas density, whereas the wings develop with density squared. Hence, line wings are pronounced in clumped winds. Quantitative profile fits indicate that the wind gas only fills 10 to 30 percent of the available volume around the star (Hamann & Koesterke 1998b). This leads to a reduction of mass loss rates for W-R stars by factors of 2 to 4, clearly demonstrating the importance of hydrodynamic wind structure for quantitative spectroscopy of hot stars with winds. This reduction in the formerly tremendous mass loss rates of W-R stars also opened the way to new, quantitative modeling of their winds being radiatively driven (Lucy & Abbott 1993; Springmann 1994; Gayley et al. 1995; Gräfener, Hamann, & Koesterke 2000).

§7 Including energy transfer

18 Radiative shocks. Wind shocks are *radiative* shocks, consisting of a narrow viscous layer in which the gas is heated, and a subsequent cooling zone in which the gas cools again by radiative losses. So far we assumed implicitly that radiative cooling is very efficient in the wind, and that shock cooling zones are narrow. Radiative shocks can then be viewed 'from far' as isothermal shocks, since both heating *and* cooling occurs on microscopic, unresolved length scales. In this approximation, a solution of the energy equation in the wind is not required. This is the reasoning which led OCR to undertake *isothermal* wind calculations.

However, the numerical simulations discussed above make the assumption of isothermality questionable at certain heights above the photosphere, and isothermality seems not justified a posteriori. We found that the wind gas is highly rarefied at the end of a rarefaction region, before it undergoes the reverse shock transition. Efficient radiative cooling *cannot* be assumed. To find a self-consistent wind structure including the effects of radiative cooling (possibly on long scales), Cooper & Owocki (1992) included radiative cooling in numerical wind simulations for the first time. This led to the strange, unexpected results of unresolved cooling zones, and all shocks were still isothermal. As the numerical mesh was chosen sufficiently fine to resolve cooling zones, the conclusion was that the latter got somehow *collapsed.*

Advective diffusion. We offer in this and the next paragraph two alternative explanations for cooling zone collapse. The explanations are slightly technical, and the reader primary interested in the main physical argument may want to skip two paragraphs ahead. – Owocki (1993, private communication; see also Cooper 1994) explained shock collapse by *advective diffusion.* This is a manifestation of Field's (1965) local thermal instability. Consider a propagating temperature jump, i.e., a contact discontinuity. Diffusive errors of the advection scheme spread the jump over a few grid points. The gas at intermediate temperatures cools better than hot gas: in pressure equilibrium, cold gas is denser than hot gas, giving more collisions and stronger cooling. The broadened jump is sharpened again by the different cooling rates, and thereby gets slightly shifted into the hot gas. The jump introduces new diffusive errors, and the cycle repeats. Advective diffusion should occur within the viscous shock layer, which is spread out over ≈ 3 grid points by artificial viscosity. The shock front 'eats' then through its own cooling zone. This argument assumes that errors pile up, as they indeed do at a contact discontinuity where always the same gas is located. But this is *not* the case in a shock transition, where gas passes through. A detailed calculation shows that only a slight modification of the cooling zone results from advective diffusion, but no collapse [1].

19 Oscillatory thermal instability. Besides Field's local thermal instability, a second, *global* thermal instability occurs in radiative shocks. This instability was found in numerical simulations of accretion columns onto white dwarfs (Langer et al. 1981, 1982) in magnetic (AM Her) cataclysmic variables. The linear stability analysis is due to Chevalier & Imamura (1982), and the instability mechanism is explained in detail in Langer et al. (1982), Gaetz, Edgar, & Chevalier (1988), and Wu, Chanmugam & Shaviv (1992). The instability is of oscillatory type, and causes periodic contraction and expansion of the cooling zone. The contractions are strong, and a fine grid is required to resolve them. On a coarse grid, the contracted zone drops at some point below grid resolution, and an *isothermal* shock remains [1]. Obviously, there is no thermal instability for an isothermal shock: the shock will not re-expand, and the collapse is permanent. We add as a side remark that oscillating radiative cooling zones show rich dynamics. For example, tiny condensations within the cooling zone can grow into secondary shocks and propagate through the cooling zone (Innes et al. 1987).

Altering the cooling function. We assume in the simulations below that radiative cooling is parameterized in power law form, $\Lambda = A\rho^2 T^\delta$ (units $\mathrm{erg\,s^{-1}\,cm^{-3}}$). The parameter δ is derived from fits to calculated cooling functions (Cox & Tucker 1969). Global thermal instability occurs for $\delta \leq 1/2$. We find that the above cooling zone collapse is prevented when an artificial, stable exponent $\delta > \delta_c$ is used at low temperatures, as is demonstrated in Fig. 6 of [1]. Typically, assuming $\delta = 2$ at $T < 5 \times 10^5$ K prevents cooling zone collapse in wind simulations. X-ray spectra of O stars, in which we are primarily interested, indicate temperatures between 10^6

and $10^{7.5}$ K. Hence, X-ray emission should be largely unaffected by the modified cooling function.

20 Shock destruction. How does radiative cooling influence the wind structure? What happens at intermediate and large radii in the wind, when radiative cooling ceases to be efficient in rarefied gas undergoing a reverse shock transition? Using the above method, we find in [1] that isothermality is a good approximation for O supergiant winds out to $\approx 5\,R_*$. At these radii, reverse shocks are *suddenly destroyed*, in marked contrast to their gradual decay in isothermal calculations, which continues out to $\approx 20\,R_*$. A direct comparison is made in Figures 1 and 10 of [1].

21 Shocks becoming adiabatic. The reason for shock destruction is the depletion of intershell gas. Radiative cooling becomes inefficient, and the cooling zones broaden as they become adiabatic. This drives the shock front through the rarefaction region, towards the next inner shell. Since the shock propagates into the preshock gas, the postshock temperature raises, which makes radiative cooling even more inefficient, pushing the shock *further* into the gas. Actually, this is the very mechanism of the global thermal instability of Langer et al. (1981). Eventually, the shock merges with the next inner shell (this may create forward shocks, cf. page 40). Tenuous, hot gas at temperatures $> 10^7$ K fills the whole space between shells.
Why does shock destruction occur so suddenly around $5\,R_*$? At this height, the gas reservoir ahead of a shell, which remains first at stationary conditions, is used up, i.e., was fully fed into the next outer shell. Further sub-shells – we term them 'clouds' in the following, for reasons which will become apparent – cannot occur in between shells. These clouds propagated outwards and pushed ahead of them the adiabatic shock front which tried to expand in the opposite, inward direction. Once the clouds cease, the shock front can expand freely through empty intershell space, leaving hot, thin gas.

22 Outer corona. Volume filling factors of hot gas at 10^6 to 10^7 K can almost reach unity between $5\,R_*$, the location of shock destruction, and $20\,R_*$, where hot gas has significantly cooled by adiabatic expansion [1, 4]. In winds from OB supergiants, X-ray emission from this low density gas is negligible. It is still possible that an X-ray emitting, outer corona occurs in thin winds from B stars near the main sequence. Here, the first strong wind shock can heat large fractions of the gas. UV line profiles show indeed that the cold wind vanishes before it reaches terminal speed (Lucy & White 1980; Hamann 1981b).

§8 X-RAYS AND CLOUDS

23 Clouds. The sub-shells or clouds are not quite the accidental, secondary feature as which they were treated so far (cf. secondary shock formation on page 26.) We will argue in the following that clouds are a primary agent in explaining X-rays from hot, massive stars [4]. We distinguish from now on strictly between *shells* (or shell fragments) and *clouds*. Shells (shell fragments) are instability generated, highly overdense as compared to stationary wind densities, and have probably large lateral scale even after Rayleigh-Taylor fragmentation (cf. the sketch in Figure 2). Clouds, on the other hand, are turbulence-induced, have roughly stationary wind densities, and, if turbulence is approximate isotropic, a tiny lateral scale.

Hillier et al. (1993) estimated that OCR wind models should fail by one or two orders of magnitude to produce the observed X-ray emission from hot stars. The reason is the low density of shock heated gas immediately behind the reverse shock. The gas density lies orders of magnitude below stationary wind densities. Note that X-ray emission, as a collisional process, scales with the density squared. We found in [1] that large-amplitude, periodic perturbations in the photosphere lead to chaotic wind structure, whereas strictly deterministic flow results from low-amplitude perturbations (cf. Figures 10 and 12 in [1]). We speculated, therefore, that *random* or turbulent boundary perturbations, still of small amplitude, could lead to an 'active' wind showing enhanced X-ray production. This is indeed the case, and clouds are the means of enhanced X-ray emission. For random boundary perturbations, wind clouds are prevalent, far above the level of a few 'overtone' sub-shells in models with coherent base perturbations (Figure 4). Clouds are dense and collide with shells, leading to strong X-ray emission.

24 Langevin boundary conditions. To mimic photospheric turbulence, a velocity perturbation, u, is applied on the inner simulation boundary [4]. The perturbation fulfills the Langevin equation for a continuous Markov chain, $du/dt + u/t_c = \Gamma(t)$. This equation is integrated in time-forward manner. The correlation time, t_c, is a free parameter. We choose a value not too far from the acoustic cutoff period. Γ is the stochastic force, with a white-noise correlation function. The force amplitude is the second free parameter, typically chosen at 30% the speed of sound. This is well below the limit of measured turbulent velocity dispersion in hot star atmospheres (Conti & Ebbets 1977). The power law index of this turbulence model is -2, not too different from the Kolmogorov index $-5/3$ for eddy turbulence. Some classic papers on the Langevin equation are collected in Wax (1954).

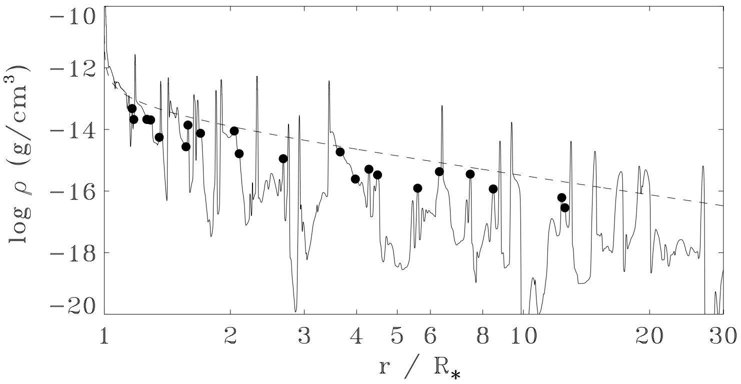

Figure 9: Clouds, marked with filled circles, in a snapshot of the density stratification in an O supergiant wind.

25 Cloud ablation. We expect that the average time interval between the passage of two dense shells is not too different from the acoustic cutoff period. Clouds, on the other hand, are excited at much shorter periods. They form in the dense gas ahead of a shell, i.e., in the decelerating part of a harmonic perturbation where unstable growth quickly saturates. The birth density of clouds is the stationary wind density, and they roughly maintain this density until collision with the next outer shell. In Fig. 8, clouds are marked explicitly in a snapshot taken from a numerical simulation. Figure 9 shows the cloud dynamics, their propagation through empty rarefaction regions between shells, and collision with the latter.

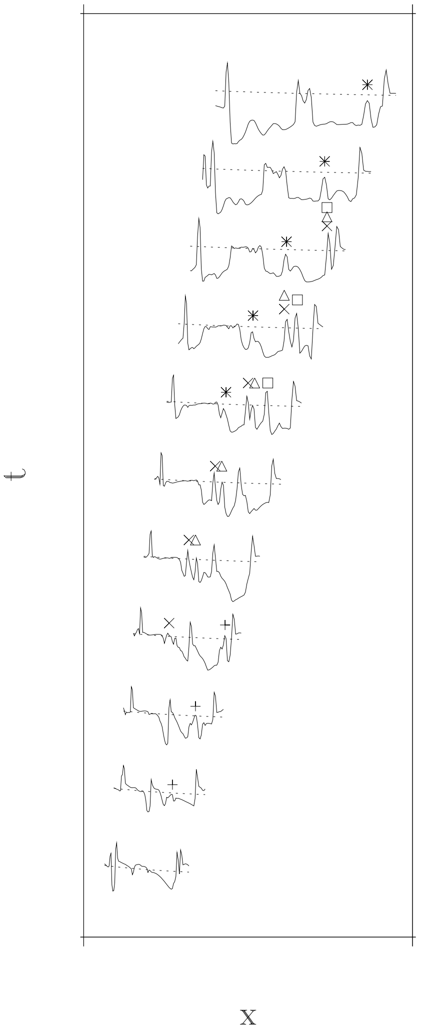

Figure 10: Clouds, marked with $+$, $\times$, $\triangle$, $\Box$, and $*$, are ablated from the gas reservoir ahead of a pronounced shell, propagate through the rarefaction region, and collide with the next outer shell. Compare with Fig. 8 on page 32.

A model case: ζ Ori. The O9 supergiant ζ Ori is a standard object for X-ray observations from O stars. Most recently, it was the first O star for which an X-ray line spectrum was taken with the CHANDRA satellite. With excellent ROSAT observations available at the time (1996), we made ζ Ori the test case for the turbulent-cloud scenario. Figure 13 in paper [4] shows a snapshot of the wind structure of ζ Ori. The X-ray spectrum from this snapshot is shown in Fig. 14 of the same paper. The spectrum is calculated using a formal integral approach on the 1-D, time-dependent wind. K-shell opacities are assumed for cold gas, Raymond-Smith emissivities for hot gas. The model flux is only a factor of 2 or 3 below the observed one, but not by factors of 10 to 100 as estimated by Hillier et al. (1993) from OCR models.

26 Cloud-shell collisions. Strangely then, Figure 15 in [4] shows that all the X-ray emission arises from a single shock at $4.5\,R_*$. The gas density in this shock lies between ±1 dex of the stationary wind density, far higher than in the rarefaction region. What happens at this location? Figure 17 in [4] shows that a collision of a fast cloud with a dense shell takes place at this time, at this radius. The figure shows also that *any* appreciable X-ray emission from the wind is due to cloud-shell collisions.

27 X-ray flux constancy. From Fig. 17 in [4] it is also evident that no more than one or two cloud collisions take place at any time. This leads to strong variability of the X-ray flux, ±1 dex around mean in spherically symmetric models. By contrast, observed X-ray flux variations for ζ Ori are a mere few percent. We expect that spherical symmetry is a very poor approximation for turbulent structures. A realistic wind model should instead consist of independent radial cones, each with its own cloud-shell collisions taking place. A few thousand such cones would guarantee the observed flux constancy.

28 X-ray variability. There are only few detections of X-ray variability so far. Berghöfer & Schmitt (1994) report on an episodic raise in the ROSAT X-ray count rate of ζ Ori. This gained wide attention, for example in the science section of the New York Times. The possible origin for the raise in count rates is the breakthrough of a dense shell through an X-ray photosphere. The event was found in one energy band only. Oskinova et al. (2001) propose observations at higher signal-to-noise, to detect different variability levels in soft and hard bands. This would allow to test certain aspects of the shock model.
Berghöfer et al. (1996) find *periodic* X-ray variability in ζ Pup, which maybe caused by absorption of X-rays in a co-rotating interaction region (a spiral arm) in the wind. Oskinova (2001, priv. comm.) finds other examples of periodic X-ray variability in ASCA observations of O stars. We recently proposed a long (180 ksec) observation of the O star ξ Per with the CHANDRA satellite, to find first signatures of X-ray *line* variability. The reason for this expectancy is that this star has amongst the shortest recurrence time scale for DACs (Kaper et al. 1999; de Jong et al. 2001).

O stars observed with ROSAT. Dedicated ROSAT observations are available for 42 stars in the spectral range from O3 to O9. These data were analyzed assuming a 2-component wind, consisting of cold, X-ray absorbing gas and a random ensemble of X-ray emitting shocks. Density and temperature stratifications of radiative cooling zones behind shocks are included in this approach (Chevalier & Imamura 1982; [3]).

These postshock stratifications allow to reduce the number of free fit parameters to the observations from 4 (Hillier et al. 1993) or 3 (Cohen et al. 1997) to 2 (see [3]). Application of a simplified version of the method is described in Kudritzki et al. (1996). We find there that the scatter in the $L_x/L_{\rm bol}$ relation for O stars is smaller than from EINSTEIN data. We currently try to decide whether this scatter is caused by a dependence of L_x on a second wind parameter, besides $L_{\rm bol}$.

29 Adiabatic shells. Paper [3] also contains an analytic treatment of outer, adiabatic shocks, whose cooling length is *not* small compared to the wind scale. We follow there a classic paper by Simon & Axford (1966) on solar wind shells.

30 Forward shocks, again. We discuss in the appendix of [3] that shock destruction as described above can be mimicked by a simple numerical test. Instead of calculating a fully structured wind model using an unstable line force, we consider multiple adiabatic shells in a flow expanding spherically symmetric, and at constant speed. The merging of reverse shocks with the next inner shell leads there to a train of *forward shocks*. Hence, it is presently not quite clear whether insufficient radiative cooling causes shock destruction or shock transformation (reverse to forward). This question is of some relevance since, for the O supergiant ζ Pup, soft X-rays originate from very large radii, far above the location of the final cloud-shell collisions (Hillier et al. 1993; Schulz et al. 2000).

Future work on X-ray emission. What determines the azimuthal scale of shell fragments and clouds? This is presently the most pressing question. The demand on computer time is huge for 2-D hydrodynamic modeling of the wind instability. One has to employ computational tricks, like using a specially designed mesh for a 3-ray radiative transfer (Owocki 1999) or 2nd order Sobolev approximation [5]. Both methods have their caveats: the specially designed mesh stretches too strongly as function of radius, and instability generated structure may 'fall between the mesh nodes'. For 2nd order Sobolev approximation, inclusion of nonlocal couplings (shadowing of one shell by another) may be impossible (Wegner 1999).

Another major question is: why are X-rays from O stars universal? Why does the intricate wind hydrodynamics and radiative transfer lead to a simple $L_x/L_{\rm bol} = 10^{-7}$? And why does universality break down for thin winds from B stars (Cassinelli et al. 1994) and for Wolf-Rayet stars (Baum et al. 1992; Wessolowski 1996; Ignace, Oskinova, & Foullon 2000)?

31 Symmetric X-ray lines. With the launch of the X-ray satellites CHANDRA and XMM, observations of X-ray lines from O stars has become possible. First observations of O stars led to the unexpected result that X-ray emission lines in ζ Ori und ζ Pup (the usual suspects) are symmetric and almost not blue-shifted (Schulz et al. 2000; Kahn et al. 2001; Waldron & Cassinelli 2001). The line width is roughly half the terminal wind speed. These results are puzzling if X-rays originate indeed in a dense wind, where one expects different optical depths for photons from the front and back hemisphere of the star, resulting in asymmetry or effective blueshift of the line profile. However, Owocki & Cohen (2001) have recently shown that even in a homogeneous wind, observed line symmetry can be partially attributed to low instrumental resolution. Even better, recent CHANDRA observations of ζ Pup

"show blue-shifted and skewed line profiles, providing the clearest evidence that the X-ray sources are embedded in the stellar wind" (Cassinelli et al. 2001).
This should be the final 'out' for coronal models of X-ray emission from O supergiants (Hearn 1972, 1973; Cassinelli & Hartmann 1977). Coronal model were practically excluded due to missing K shell absorption (Cassinelli & Swank 1983; Cohen et al. 1997) and the missing green coronal iron line (Baade & Lucy 1987). Recently, however, coronal models gained again some attention (Waldron & Cassinelli 2001). We plan to perform line-synthesis calculations in a *clumped* wind, where almost all gas is confined to narrow shell fragments. If the lateral scale of the fragments is not too small, photons from the stellar back hemisphere may escape to the observer by passing between neighboring shells (cf. Figure 2). Furthermore, on the back hemisphere one looks onto the X-ray emitting, inner rim of the shell; whereas on the front hemisphere, the shock is hidden behind a dense, absorbing shell. Both effects (lateral escape between neighboring shells; inner shell rim emission only) level off differences between the red and blue line wing.

32 Clouds and EISF structure. We add another technical remark. The turbulent wind clouds described above and in [4] have short length scales of a few mesh points only. They were calculated using the SSF method, which does not account for the perturbed diffuse radiation field. On short scales, the latter may turn anti-correlated fluctuations like clouds into correlated ones. Future EISF simulations are therefore vital to the cloud model. To achieve proper resolution of the thermal band, an adaptive mesh technique will be used.

X-rays in stationary wind models. The focus of the present work is on wind hydrodynamics, with a highly simplified treatment of NLTE (using a power-law line list; and treating *one* resonance line only) and radiative transfer (using Sobolev approximation, SSF, or EISF). The complementary viewpoint: full NLTE and radiative transfer, and assuming parameterized hydrodynamics is of central importance for quantitative spectroscopy of hot stars. Precise UV fluxes from OB stars are required to calibrate the wind momentum-luminosity relation (Kudritzki et al. 1999); to determine ionizing fluxes in H II-regions (Sellmaier et al. 1996); and for population synthesis in starbursts (Leitherer et al. 1999) and in blue galaxies at redshifts $z > 3$ (Steidel et al. 1996). In synthesising UV fluxes, the full statistical equilibrium problem of the wind is treated, however, assuming stationary flow (Pauldrach et al. 2001, and literature therein). To explain the observed 'superionization', inclusion of X-rays is still required (Pauldrach et al. 1994, MacFarlane et al. 1994). The shocks are treated in parameterized form, on a underlying, monotonic velocity law. Furthermore, inclusion of an artifically high microturbulence is necessary to reproduce observed UV line profiles (Hamann 1980). In future calculations on structured wind models, microturbulence and shock strength will no longer be independent, free parameters, but will both appear as consequence of wind hydrodynamics. Lucy (1982a, 1983) and Puls et al. (1994) showed that black troughs in saturated P Cyg profiles, so far explained by microturbulence, indeed result from an instability-generated velocity law.

High mass X-ray binaries. Neutron stars or black holes which orbit an O or B supergiant act as point-like probes in the wind. Bondi-Hoyle accretion of the supersonic wind turns the compact object into a strong X-ray source which ionizes a large volume of the wind gas. Line driving stalls in this overionized region, and a dense wake forms via the Coriolis force. The beautiful and intricate wind dynamics is discussed by Blondin et al. (1990) and Blondin, Stevens, & Kallman (1991). The presence of the dense wake can be infered from asymmetries of X-ray lightcurves at ingress and egress. For the system Vela X-1, the azimuthal extent of the wake is consistent with the observed asymmetry [2]. Kaper, Hammerschlag-Hensberge, & Zuiderwijk (1994) suggest that observed, short-term variability of X-ray lightcurves is due to fluctuations in the wind velocity as caused by the de-shadowing instability. Hence, high-mass X-ray binaries are another test case to diagnose line driven flow structure.

CHAPTER 3: RUNAWAY WINDS

§9 Solution topology

We turn now to a simpler level in our description of line driven wind hydrodynamics, and consider the simplest line force possible, in first order Sobolev approximation. The wind is then *no* longer subject to de-shadowing instability. We consider why line driven winds from stars and accretion disks adopt a unique, critical solution out of an infinite number of possible solutions, the latter falling into two classes: shallow and steep.

This unique solution is defined as follows (Castor, Abbott, & Klein 1975): it starts in the photosphere as the fastest possible, shallow solution, and crosses at some critical point smoothly and differentiably to the slowest, steep solution. From all accelerating wind solutions, this is the one with maximum mass loss rate. Shallow solutions are discarded as global wind solutions because they break down at large radii, becoming imaginary there. Steep solutions, on the other hand, are everywhere supersonic. They cannot connect to the wind base which is assumed to be subsonic, and are also discarded as global wind solutions.

There are indications that this reasoning is too restrictive (see paper [6]): (1) Shallow solutions break down around $300\,R_*$. Why then do time-dependent hydrodynamic simulations which extend out to $10\,R_*$ always adopt the critical solution, instead of remaining on shallow initial conditions? (2) Spherical expansion work, as a thermodynamic effect, scales with the gas temperature and sound speed. It is not *inherent* to line driving. (3) For line driven winds from accretion disks, neither shallow *nor* the critical solution reach infinity, because the disk flux drops off steeper than disk gravity [6]. Unavoidably, the wind has to decelerate at large heights. This is unproblematic, since the wind speed is above the local escape speed, both for the critical and for sufficiently fast, shallow solutions. (4) Once the wind is allowed to decelerate in certain regions, an initially shallow solution could jump to the decelerating branch when the speed is larger than the escape speed, and reach infinity. Wind deceleration is also discussed by Koninx (1992) and Friend & Abbott (1986), the latter authors modeling velocity laws of rotating O star winds.

A simple wind model. We consider now a simple model for line driven winds which allows to discuss the above questions in detail. The model is used in numerical simulations [8, 9, 10] to study wind runaway caused by Abbott waves. In Sobolev approximation, the line force scales as

$$\mathbf{g}_l \sim \int d\omega\, \mathbf{n}\, I_n \big(\rho^{-1}\, \partial_n v_n\big)^{\alpha}. \tag{20}$$

The integral is over solid angle, $\mathbf{n}$ is the unit direction vector, and I is the frequency-integrated intensity of the radiation field. A CAK line distribution function is assumed, and we adopt $\alpha = 1/2$ for simplicity in the following. Furthermore, the velocity gradient is taken out of the integral, assuming that the gradient of the flow speed in flow direction gives the main contribution. This is equivalent to the CAK point star approximation. Assuming 1-D, planar geometry,

$$g_l(z) \sim F\sqrt{\rho^{-1}\partial v/\partial z}, \tag{21}$$

with frequency-integrated, radiative flux F in z direction. We assume that F is constant, but $g(z)$ may be an arbitrary function. Constancy of both F and g leads to solution degeneracy for zero sound speed (Poe et al. 1990). If the disk is extended and isothermal (the latter is a bad approximation), F is indeed constant at sufficiently small z. For g we choose

$$g(z) = \frac{GM}{q^2}\frac{z/q}{1+(z/q)^2}, \tag{22}$$

which roughly resembles effective gravity (gravity minus centrifugal force) close to a thin accretion disk. M is the mass of the central object, q is the footpoint radius in the disk. Note that $g(0) = 0$. Furthermore, the sound speed is set to zero, which turns the Euler equation into an algebraic equation in vv'. Note that the Sobolev line force is independent of v_{th}, and therefore of a. The continuity and Euler equation become,

$$C \equiv \dot{\rho} + (\rho v)' = 0, \tag{23}$$

$$E \equiv \dot{v} + vv' + g - \tilde{K}\sqrt{v'/\rho} = 0. \tag{24}$$

Dots indicate temporal, primes spatial differentiation. The flux was absorbed into $\tilde{K}$. The Euler equation was divided through by GM/q^2, which means that speed is measured in units of the local Kepler speed, $\sqrt{GM/q}$, height in units of q, and time in units of a Kepler flow time through a distance q. We keep the symbols v, z, and t also for the normalized quantities. For a stationary wind, the continuity equation becomes $\rho v = \mathrm{const}$. We introduce $m = \rho v/\rho_c v_c$ and $w' = vv'$. Subscripts c refer to the critical or CAK solution, to be introduced shortly. The Euler equation turns into,

$$w' + g - K\sqrt{w'/m} = 0, \tag{25}$$

For stationary winds, m and w' replace ρ and v as fundamental hydrodynamic variables.

Shallow and steep solutions. At each z, (25) is a quadratic equation in $\sqrt{w'}$, with solutions

$$\sqrt{w'} = \frac{K \pm \sqrt{K^2 - 4gm}}{2\sqrt{m}}. \tag{26}$$

Solutions with '$-$' are termed *shallow*, solutions with '$+$' are termed *steep*. For sufficiently small m, shallow and steep solutions are globally defined. At the critical point of the critical solution, termed z_c from now, the square root vanishes, and two *globally defined* shallow and steep solutions merge. By definition, $m = 1$ for the critical solution. For $m > 1$, shallow and steep solutions become imaginary in a neigborhood of z_c. In this region, gravity g overcomes line driving $\sim K$. These failing winds are termed *overloaded* [8]. We may also allow for $v' < 0$, by introducing $\sqrt{|v'|}$ in the line force. This expresses that the Sobolev force is blind to the sign of

v'. A *single* decelerating branch results from this generalization. Figure 11 shows the 'solution topology' of the quadratic equation (25) in the zw' plane (see also Fig. 3 in CAK; Fig. 3 in Cassinelli 1979; Fig. 4 in Abbott 1980; Fig. 1 in Bjorkman 1995; and Fig. 6 in [6]).

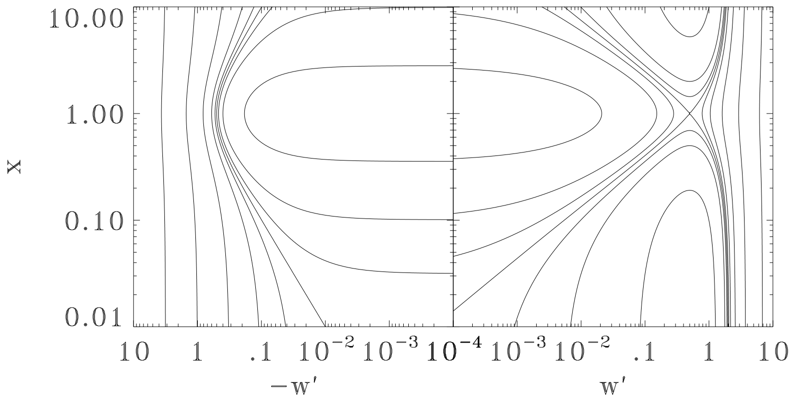

Figure 11: Solution topology of the equation of motion (25) for stationary winds. The right panel shows acceleration solutions, the left panel decelerating ones. For the latter, $\sqrt{|w'|/m}$ was assumed in the line force. Note the saddle point at $x = 1, w' = 1/2$, which is the CAK critical point for Abbott waves.

From (26), the critical point is a saddle point of E in the zw' plane (Bjorkman 1995). Note the important difference that the sonic points for the solar wind and the Lavalle nozzle are saddle points in the zv plane instead. The critical point being a saddle, the shallow solution with $m = 1$ has a discontinuity in v'' at z_c. This discontinuity is avoided by switching to the steep solution. Discontinuities in *derivatives* of the fundamental hydrodynamic variables lie on *characteristics* (Courant & Hilbert 1968). Characteristics are space-time curves along which Riemann invariants or wave amplitudes are constant, or change according to an ordinary, not a partial differential equation. Indeed, the flow becomes super-abbottic at the CAK critical point (Abbott 1980).

The constant K can be expressed in terms of flow quantities at the critical point. Setting the square root in (26) to zero gives, for $m = 1$,

$$K = 2\sqrt{g_c}, \tag{27}$$

where $g_c = g(z_c)$. Since the critical point is a saddle of E in the zw' plane, $\partial E/\partial z_c = \partial E/\partial w'_c = 0$ holds. The latter ('singularity') condition leads to $w'_c = g_c$. The former ('regularity') condition leads to $dg/dz_c = 0$, hence the critical point coincides with the gravity maximum. This reveals the role of the critical point as bottleneck of the flow. For height-dependent F, g/F^2 determines the nozzle function instead. If F *and* g are constant, the critical point degenerates, and each location z becomes critical (for zero sound speed). Inserting k and w'_c, the general, stationary wind acceleration becomes,

$$w' = \frac{g_c}{m}(1 \pm \sqrt{1 - mg/g_c})^2. \tag{28}$$

The velocity law $v(z)$ is found by (analytic or numerical) quadrature of $w' = vv'$.

§10 ABBOTT WAVES

Since Abbott waves are of central importance in the following, we derive them in three different ways: by dispersion analysis [9]; characteristic analysis [10]; and Green's function analysis [10]. The first and last are necessarily linear, but the characteristic analysis holds for arbitrary wave amplitudes. This should not mask the fundamental limitation of our approach: a derivation of Abbott waves including line scattering in any approximation (SSF, EISF) going beyond Sobolev approximation was not given so far, due to mathematical complexities.

Dispersion relation. For all wind solutions, $K = 2\sqrt{g_c}$ holds. Inserting this into the time-dependent Euler equation,

$$\dot{v} + vv' = -g + \sqrt{2\rho_c v_c \, v'/\rho}. \tag{29}$$

We consider small harmonic perturbations on a stationary wind solution ρ_0, v_0 (not necessarily the critical solution), $\rho = \rho_0 + \rho_1 \exp[i(kz - \omega t)]$, $v = v_0 + v_1 \exp[i(kz - \omega t)]$. Linearizing the continuity and Euler equation gives,

$$\left[-i\frac{\omega}{v_0'} + i\chi + 1\right] \frac{\rho_1}{\rho_0} + (i\chi - 1)\, \frac{v_1}{v_0} = 0, \tag{30}$$

$$\frac{1}{q_0}\frac{\rho_1}{\rho_0} + \left[-i\frac{\omega}{v_0'} + 1 + i\chi\left(1 - \frac{1}{q_0}\right)\right] \frac{v_1}{v_0} = 0, \tag{31}$$

where $\chi \equiv k\, v_0/v_0'$ and $q_0 = \sqrt{2m_0 w_0'}$ were introduced. Setting the determinant of the system to 0 gives the dispersion relation $\omega(k)$. In the WKB approximation, $\chi \gg 1$, the phase speed and growth rate of the downstream mode (subscript $+$) become, in the observers frame,

$$v_\phi = \mathrm{Re}(\omega_+)/k = v_0, \qquad \mathrm{Im}(\omega_+) = -\epsilon. \tag{32}$$

The small damping term $-\epsilon$ is of no further consequence. In the comoving frame, the wave speed is 0 in this zero sound speed limit: the downstream mode consists of sound waves. For the upstream or $(-)$ mode,

$$v_\phi = \mathrm{Re}(\omega_-)/k = v_0\big(1 - 1/q_0\big), \qquad \mathrm{Im}(\omega_-) = 0. \tag{33}$$

This new wave type is caused by radiation pressure, and is termed an Abbott wave (after Abbott 1980). For shallow solutions, $q_0 < 1$, and Abbott waves propagate towards smaller z: shallow solutions are the analog to solar wind breezes. For steep solutions, $q_0 > 1$, and the waves propagate towards larger z. At the critical point, $m = 1$, $w_c' = g_c$, and $q_0 = 1$, hence the critical point is a stagnation point for Abbott waves. At smaller (larger) radii, the waves propagate towards smaller (larger) z.

For shallow solutions with $m_0 \ll 1$ and $w'_0 \ll w'_c$, Abbott waves propagate inward at arbitrary large speed. Wave propagation along shallow solutions was not treated so far in the literature, as a consequence of Abbott's (as it appears now: erroneous) postulate that "a line driven wind has no analog to a solar breeze." (Abbott 1980)

Abandoning steep solutions. Steep solutions are super-abbottic everywhere, and cannot communicate with the wind base. Hence, their mass loss rate cannot converge to an eigenvalue. Numerical simulations show indeed that steep solutions are stable to almost any perturbations [9]. The perturbations are advected to the outer boundary and leave the mesh. Steep solutions are in the following of not much interest. Still, they may have physical significance, and we encountered them already before: the quasi-stationary rarefaction regions in time-dependent simulations of the de-shadowing instability are steep solution 'patches'.

Characteristic analysis. The above dispersion analysis holds for linear waves. We turn now to a characteristic analysis for arbitrary amplitudes. The equations of motion for arbitrary g are written as,

$$C(\rho, v) = \dot{\rho} + v\rho' + \rho v' = 0, \tag{34}$$

$$E(\rho, v) = \dot{v} + vv' + g(z) - 2\Gamma\sqrt{v'/\rho} = 0, \tag{35}$$

with $\Gamma \equiv \sqrt{g_c \rho_c v_c}$. C and E are brought into *advection* form without further approximation. A first-order system of partial differential equations is called *quasi-linear* if it is linear in all *derivatives* of the unknowns (ρ and v here). Usually, characteristics are defined for quasi-linear systems. Equations (34, 35) are *not* quasi-linear, due to the presence of $\sqrt{v'}$. Courant & Hilbert (1968) show that characteristic directions, a, for general, nonlinear systems are given by

$$\begin{vmatrix} -aC_{\dot{\rho}} + C_{\rho'} & -aC_{\dot{v}} + C_{v'} \\ -aE_{\dot{\rho}} + E_{\rho'} & -aE_{\dot{v}} + E_{v'} \end{vmatrix} = 0. \tag{36}$$

The symbol a, so far reserved for the sound speed, refers now to any characteristic speed. The distinction should be clear from the context. For quasi-linear systems, the matrix in (36) becomes independent of differentials $\dot{\rho}$, v', etc. For the present case, however,

$$\begin{vmatrix} -a + v & \rho \\ 0 & -a + v - \Gamma/\sqrt{\rho v'} \end{vmatrix} = 0, \tag{37}$$

or, in the observers frame,

$$a_+ = v, \qquad\qquad a_- = A = v - \frac{\Gamma}{\rho v'}, \tag{38}$$

with Abbott speed A. For small perturbations,

$$A = v\,(1 - \sqrt{g_c/mw'}) = A_0, \tag{39}$$

with A_0 from the dispersion analysis above. To bring the hydrodynamic equations into characteristic form [10], the system must be made quasi-linear, by applying the following trick (Courant & Hilbert 1968): the Euler equation is differentiated with respect to z, and a new variable $f = v'$ is introduced,

$$\dot{f} + vf' + f^2 - \frac{\Gamma}{\sqrt{f\rho}} \left(f' - f\frac{\rho'}{\rho} \right) = -g'. \tag{40}$$

This equation is linear in $\dot{f}$ and f'. The new system consists then of the continuity equation, the Euler equation (40) for f, and the defining relation $f = v'$. Rebracketing (40) and multiplying by ρ,

$$\rho\dot{f} + \rho A f' + \rho f^2 + \frac{\Gamma}{\sqrt{f\rho}} f\rho' = -\rho g'. \tag{41}$$

Replacing ρf using the continuity equation,

$$\begin{aligned} -\rho g' &= \rho\dot{f} + \rho A f' - f\dot{\rho} - \left(v - \frac{\Gamma}{\sqrt{f\rho}} \right) f\rho' \\ &= \rho\dot{f} + \rho A f' - f\dot{\rho} - Af\rho' \\ &= \rho^2 \left(\partial_t + A\partial_z \right) \frac{f}{\rho}. \end{aligned} \tag{42}$$

The characteristic (or advection) form of the Euler equation is therefore,

$$\left(\partial_t + A\partial_z \right) \frac{v'}{\rho} = -\frac{g'}{\rho}. \tag{43}$$

We assume that WKB approximation applies, i.e., that the temporal and spatial derivatives on the left hand side are individually much larger than the right hand side, hence, the latter can be neglected. In a frame moving at speed A, the function v'/ρ is then constant, and can be interpreted as a wave amplitude propagating with speed A. The Sobolev optical depth is proportional to the inverse of v'/ρ, which indicates that Abbott waves are indeed a radiative mode. Introducing $f = v'$ in the continuity equation, the latter is already in characteristic form,

$$\left(\partial_t + v\partial_z \right) \rho = -f\rho. \tag{44}$$

Since it contains no derivatives of ρ or f, $f\rho$ is an inhomogeneous term. The Riemann invariant, ρ, is no longer constant along the v characteristic: WKB approximation, which would mean $\rho'/\rho \gg v'/v$, does *not* apply. Since ρ scales with gas pressure, this mode can be identified with sound waves.

Green's function for Sobolev line force. Finally, we derive the Green's function for Abbott waves in Sobolev approximation. The Green's function gives the response of the wind to a localized, delta function perturbation in space and time, and is complementary to the harmonic dispersion analysis of Abbott (1980) and Owocki & Rybicki (1984). Since localized perturbations consist of many harmonics, a Green's function describes wave interference. This is clearly seen for water waves, whose

Green's function is known from Fresnel diffraction in optics (Lamb 1932, p. 386). For simplicity, we consider a single, optically thick line only, with Sobolev force,

$$g_l(z) = A\,\frac{\partial v(z)}{\partial z}. \tag{45}$$

Density ρ was absorbed into the constant A. We assume WKB approximation to apply (slowly varying background flow), and consider only velocity perturbations: the Abbott wave amplitude v'/ρ from characteristic analysis is not annihilated by this restriction. The linearized Euler equation for small perturbations is

$$\frac{\partial}{\partial t}\delta v(z,t) = \delta g_l(z,t) = A\,\delta v'(z,t). \tag{46}$$

The Green's function problem is posed by specifying as initial conditions,

$$\delta v(z,0) = \delta(z - z_0). \tag{47}$$

The solution is obtained by Fourier transformation with respect to z. We use the conventions, for an arbitrary function F (bars indicate Fourier transforms),

$$\bar{F}(k,t) = \int_{-\infty}^{\infty} dz\, e^{-ikz}\, F(z,t), \qquad F(z,t) = \frac{1}{2\pi}\int_{-\infty}^{\infty} dk\, e^{ikz}\, \bar{F}(k,t). \tag{48}$$

Fourier transforming (46) gives

$$\frac{\partial}{\partial t}\overline{\delta v}(k,t) = ikA\overline{\delta v}(k,t). \tag{49}$$

The right hand side was obtained by integration by parts, assuming $\delta v(-\infty,t) = \delta v(\infty,t) = 0$. This will be shown a posteriori. The solution of (49) is

$$\overline{\delta v}(k,t) = be^{ikAt}, \tag{50}$$

with constant b. Fourier transforming the initial conditions (47),

$$\overline{\delta v}(k,0) = e^{-ikz_0} = b, \tag{51}$$

hence,

$$\overline{\delta v}(k,t) = e^{ik(At-z_0)}. \tag{52}$$

Finally, Fourier transforming back to z space,

$$\delta v(z,t) = \frac{1}{2\pi}\int_{-\infty}^{\infty} dk\, e^{ikz} e^{ik(At-z_0)} = \delta(z - z_0 + At). \tag{53}$$

The delta function perturbation propagates without dispersion towards smaller z, at a speed $-A$. Also, $\delta v = 0$ at $z = \pm\infty$, as assumed above. A is the Abbott speed, as is seen by inserting a harmonic perturbation, $\delta v = \overline{\delta v}\, e^{i(\omega t - kz)}$, in (46), giving for the phase and group speed,

$$\frac{\omega}{k} = \frac{d\omega}{dk} = -A. \tag{54}$$

The result that a delta function peak propagates without dispersion at speed $-A$ could have been foreseen from the phase speed of linear Abbott waves: v_ϕ is independent of λ, hence no dispersion occurs and no wave interference between different harmonics. The Green's function, G, is defined by,

$$F(z,t) = \int dz'\, G(z-z',t)\, F(z',0), \tag{55}$$

with some arbitrary function F, implying

$$G(z,t) = \delta(z+At). \tag{56}$$

We have shown that the phase, group, characteristic and Green's function speed for Abbott waves all agree.
The situation seems clear, but isn't.

No Abbott waves for pure absorption. In a landmark paper, Owocki & Rybicki (1986) derived the Green's function for pure absorption line flows subject to the force (1,1). Taking the Sobolev limit in this Green's function, upstream propagating Abbott waves are found.
But this is impossible since, for pure absorption, photons propagate only downstream and an upstream radiative mode cannot exist. Indeed, the bridging law (Owocki & Rybicki 1984) which is used in deriving this Green's function is the sum of a delta function term, expressing de-shadowing instability, and a Heaviside function, expressing *downstream* shadowing of wind ions caused by velocity perturbations. To derive Abbott's upstream mode from this downstream-only bridging law is a contradiction.
The resolution was given by Owocki & Rybicki (1986), who demonstrated that two limits do not commute in the Green's function analysis: the Sobolev limit $\lambda \to \infty$ for long perturbation wavelengths; and the continuum limit $\sum_k \to \int dk$ in Fourier transforms of localized functions. Taking the Sobolev limit first, their eqs. (C1, C2) give the same Green's function for inward propagating Abbott waves as we derived above, $G(z,t) = \delta(z+At)$. If, instead, the continuum limit is taken first (their eqs. B10, C3, C4) and only then the Sobolev limit,

$$G(z,t) = \sum_{n=0}^{\infty} \frac{(At)^n}{n!} \left(\frac{d}{dz}\right)^n \delta(z). \tag{57}$$

Formally, this is the Taylor series expansion of a delta function, $G(z,t) = \delta(z+At)$. The paradox is burried and resolved at this point. The latter equation expresses $\delta(z+At)$, which is peaked at $z=-At$, in terms of derivatives of $\delta(z)$, which *vanish exactly* at $z=-At$ for $t>0$! The series (57) must be taken as it stands. Applying (57) to an arbitrary initial perturbation $F(z',0)$ using (55),

$$F(z,t) = \sum_{n=0}^{\infty} \frac{(At)^n}{n!} \frac{d^n F(z,0)}{dz^n}. \tag{58}$$

Hence, $F(z,t)$ is constructed from $F(z,0)$, $F'(z,0)$, $F''(z,0)$, $F'''(z,0)$, etc. *alone*, from pure initial conditions at the location z under consideration. No paradox occurs, there are no Abbott waves, only local information is used. The Abbott speed A is a mere constant, without deeper physical significance.

Including scattering. To the present author, this indicates that a bigger frame exists which contains the special case of pure absorption, and gives physical meaning to A. This is achieved when scattering is included. Indeed, numerical Green's function experiments for SSF and EISF forces show an upstream propagating Abbott front (Owocki & Puls 1999). However, due to mathematical difficulties, the Green's function for flows driven by line scattering was not derived analytically so far. And some authors doubt the physical relevance of Abbott waves and the CAK critical point at all, suggesting that they are artefacts of the Sobolev approximation (Lucy 1998). Using an ingenious argument, Lucy (1975) avoided the critical point singularity (0/0) in a numerical quadrature of the Euler equation. He used different numerical representatives for dv/dr in the advection term and in the Sobolev line force. The argument is that dv/dr in the advection term is a true differential, whereas dv/dr in the line force means the velocity difference over the finite Sobolev zone. We adopt here the standpoint: in numerical simulations which apply the Sobolev, SSF, or EISF approximation, Abbott waves must be accounted for in the Courant time step and (outer) boundary conditions. Yet, the physical relevance of Abbott waves remains to be strictly proven by a Green's function analysis including scattering.

Courant time step and outer boundary conditions. In simulations published so far, Abbott waves are not included in the Courant time step, but only sound waves are. We saw above that Abbott waves define the upstream characteristics of line driven winds. Therefore, they determine the numerical time step. If not properly accounted for, Abbott waves cause numerical runaway.

Furthermore, outflow boundary conditions are assumed in the literature on the outermost mesh point. All flow quantities are extrapolated from the interior mesh to the boundary. This is wrong for sub-abbottic shallow solutions, for which Abbott waves *enter* through the outer boundary. Applying outflow conditions may *drive* the solution to the critical one, which is super-abbottic at the outer boundary, hence consistent with outflow extrapolation [8].

To maintain shallow solutions, on the other hand, an outer boundary condition must be applied instead of extrapolation. When Abbott waves are included in the Courant time step and non-reflecting boundary conditions are used, we find that shallow solutions are numerically stable [9]. Non-reflecting boundary conditions annihilate any incoming waves (the boundary condition is: 'no waves'). Even initial conditions which depart strongly from a shallow wind, e.g., a linear velocity law, converge to a shallow solution.

We now turn the argument around: once *numerical* stability of shallow solutions is achieved, this allows to explicitly introduce flow perturbations on the interior mesh (away from boundaries) in a *controlled* way, and to study their evolution, especially stability. We find that a new runaway mechanism exists, which is caused by Abbott waves [8, 10]. In older simulations which applied outflow boundary conditions and did not account for Abbott waves in the Courant time step, this physical runaway was totally outgrown by numerical runaway, and therefore not detected.

Negative velocity gradients. The new, physical runaway occurs in regions where the wind decelerates, $v' < 0$. The Sobolev force is 'blind' to the sign of v'. All what counts is the relative Doppler shift between neighboring gas parcels, which determines the width of the Sobolev resonance zone. The Sobolev line force is then generalized to $g_l = 2\Gamma\sqrt{|v'|/\rho}$, where $\alpha = 1/2$ is still assumed. However, flow deceleration implies a non-monotonic velocity law, and multiple resonances occur. The incident light is no longer given by the photospheric flux alone, and the constants K in (25) or 2Γ above become velocity dependent. Rybicki & Hummer (1978) generalized Sobolev theory to account for non-monotonic velocity laws. While introducing interesting, non-local aspects to Abbott waves (action at a distance!), the method of Rybicki & Hummer is not analytically feasible, and we do not consider it further here. Instead, besides the purely local force $g_l \sim \sqrt{|v'|}$ we also consider $g_l \sim \sqrt{\max(v', 0)}$: all incident light is assumed here to be completly absorbed at the first resonance. The true line force should lie between these extremes.

For $g_l \sim \sqrt{|v'|}$, the Euler equation has characteristic form

$$(\partial_t + A\partial_z)\,\frac{v'}{\rho} = -\frac{g'}{\rho}, \qquad \text{where} \qquad A = v \mp \frac{\Gamma}{\sqrt{\pm\rho v'}} \tag{59}$$

is the Abbott speed in the observers frame. The upper resp. lower sign applies for $v' > 0$ resp. $v' < 0$. Therefore, if the flow switches from acceleration to deceleration, Abbott waves turn from propagating upstream (− characteristic) to propagating downstream (+ characteristic).

For $g_l \sim \sqrt{\max(v', 0)}$, the characteristic Euler equation for $v' < 0$ is,

$$(\partial_t + v\partial_z)\,\frac{v'}{\rho} = -\frac{g'}{\rho} \qquad\qquad (v' < 0). \tag{60}$$

Since the line force vanishes, this is just the ordinary Euler equation at zero sound speed. The upstream Abbott wave turns here into an upstream sound wave. Note that a reversal into a downstream (Abbott) wave does not occur. We conclude that for *both* types of line force, *regions* $v' < 0$ *cannot communicate with the base at* $z = 0$. Abbott (and sound) waves which originate in these regions propagate only outward.

§11 ABBOTT WAVE RUNAWAY

Figure 10, which is taken from [8], shows runaway of a shallow wind velocity law when a sawtooth-like perturbation of amplitude δv and period T is applied at a fixed position $z = 2$ (at one mesh point) at all times. The amplitude δv is sufficiently large that negative v' results.

The sequence of events which lead to runaway should be as follows [8, 10]: during the half-period of negative velocity perturbations, the slope $v' < 0$ is to the left (at

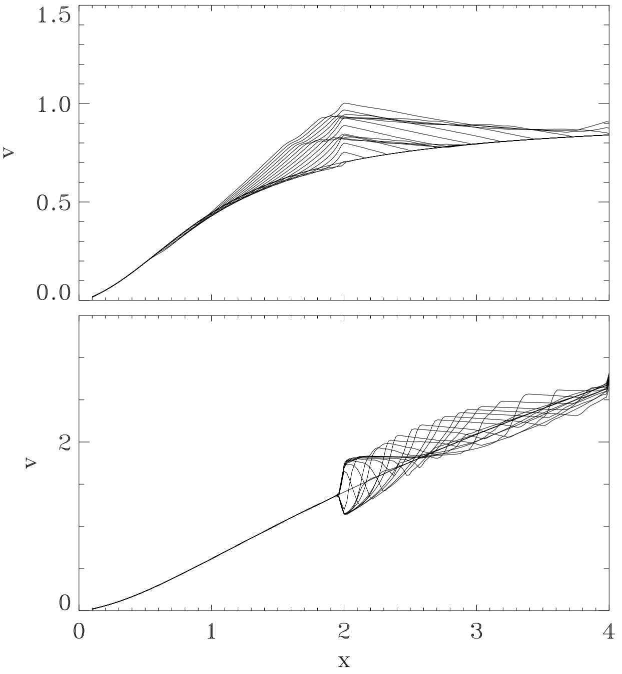

Figure 12: Abbott wave runaway for a shallow wind velocity law (upper panel), and stable Abbott wave propagation along the critical CAK solution (lower panel). The critical point lies at $x = 1$.

smaller z) of the slope $v' > 0$. Regions with $v' < 0$ propagate outwards, regions with $v' > 0$ inwards. Hence, the two slopes approach and annihilate each other, leaving an essentially unperturbed velocity law. In some more detail: the sawtooth perturbation δv is established via many small, roughly constant $dv \ll \delta v$ applied over many time steps $dt \ll T$. During the negative half wave $-\delta v$, at each time step dt, $-dv$ is applied, and largely annihilates itself during the subsequent 'advection' step of the numerical scheme. The total velocity perturbation after $T/2$ is not the perturbation amplitude δv, but roughly 0! Opposed to this, over the half-period $T/2$ when $\delta v > 0$, the slope $v' < 0$ is to the right of the slope $v' > 0$. The two slopes move apart. The gas in between gets rarefied (is 'stretched') at roughly constant speed. (This corresponds to a centered rarefaction wave.) At the next time step, dv is created atop of this region. Over the half-period $T/2$, the full perturbation amplitude δv builds up.

This is shown in the figure: the negative half wave of the sawtooth annihilates itself, leaving an unperturbed velocity law; the positive half wave is excited at the intended amplitude, and spreads upstream and downstream throughout the wind. Asymmetric evolution, or runaway, of the wind velocity towards larger speeds results over a full period. Note that the runaway is not caused by wave growth, as in a fluid instability, but by missing negative velocity perturbations to compensate for positive perturbations.

The same runaway is also found by introducing a train of sawtooth-like perturbations in the initial conditions, and let them evolve freely, without introducing further perturbations at later times. This is shown in Figure 5 of paper [10]. Neighboring slopes approach and separate in the way described above, which leads to asymmetric evolution of the wind velocity law towards larger speeds.

§12 Overloaded winds

Generalized critical points. The runaway stops when Abbott waves can no longer propagate inwards, after a critical point formed in the flow. If the perturbation source is located *above* the CAK critical point, the wind undergoes runaway until it reaches the CAK solution. The perturbation site comes to lie on the super-abbottic portion of the velocity law. Phases $v' > 0$ and $v' < 0$ of the perturbation cycle combine then to a smooth, outward-propagating Abbott wave, as shown in the figure.

The perturbation source is not required to lie at fixed z. Even when moving outwards with the local wind speed or faster, it can excite Abbott waves which propagate inwards in the observers frame, and therefore alter the whole inner flow.

For coherent perturbations below the CAK critical point, runaway does not terminate at the critical solution [8]. The perturbation site is sub-abbottic on the critical solution, and Abbott waves can further penetrate to the wind base. The wind evolves towards a velocity law which is steeper than the critical one. The wind becomes overloaded, $m > 1$. The runaway continues until a generalized (non-CAK) critical point, z_a, forms as a barrier for Abbott waves.

What are these generalized critical points, z_a? To see this, we set the (stationary) Abbott speed (39) to zero, $A_a = v_a(1 - \sqrt{g_c/mw'_a}) = 0$, giving $mw'_a = g_c$. This shows that the square root in the solution for w' in (28) vanishes, and a steep and shallow solution merge. Besides at the CAK critical point, this happens only along overloaded winds, when a shallow solution bends back towards smaller z on the steep branch. Below this location, the Euler equation has two real solutions, above it has two imaginary solutions. Physically, this means that in the proximity of the CAK critical point, which is the bottleneck of the flow, the line force can no longer balance gravity, and the wind starts to decelerate. The two *real* solution branches reappear at some height above the critical point.

Stationary overloading: kinks. Therefore, at z_a the wind jumps to the decelerating branch, $v' < 0$. In Sobolev approximation, the jump is sudden and causes a *kink* in the velocity law. Since $v' < 0$ on the decelerating branch, Abbott waves propagate outwards beyond z_a, hence z_a is a wave barrier [8].

We have arrived at the somewhat strange conclusion of a *stationary* solution with *kinks*. As mentioned before (page 30 and 45), kinks and other high-order (or weak) discontinuities of hydrodynamic variables lie on characteristics, i.e., move at characteristic speed. This is true for the present kink, which moves at characteristic Abbott speed $A_a = 0$.

Time-dependent overloading: shocks and shells again. Since z_c lies at the gravity maximum, already small super-CAK mass loss rates cause broad deceleration regions. In practice, for mass loss rates only a few percent larger than the CAK value, the deceleration regime is so broad that *negative* speeds result. Stationary solutions are then no longer possible, as upwards streaming wind gas collides with falling gas. For a periodic perturbation source in the wind, numerical simulations show the occurence of a train of shocks and shells in the wind, which still propagates outwards. This is shown in Fig. 8 of [10].

Does overloading occur in nature? The discussion so far is idealized since it assumes *coherent* perturbation sources in the wind. Perturbations with a finite life time should still lead to 'piecewise' runaway, each perturbation lifting the wind to a slightly faster, shallow solution. The wind waits on the new, stable shallow solution until the next perturbation lifts it further.

The outer wind seems to be the natural seat for runaway perturbations, since $v' < 0$ is easily excited on the outer, flat velocity law. We speculate that in nature, runaway perturbations are most prevalent above the CAK critical point and drive the wind towards the critical, not an overloaded solution [10]. In support of this we add that not even the strong de-shadowing instability leads to significant wind structure below the critical point, which could act as runaway perturbation towards an overloaded solution.

Still, there remains a slight chance that overloading occurs in real winds. Most notably, Lamers (1998, private communication) reports on a broad region in the wind of the luminous blue variable P Cygni, which is indicative of flow deceleration; and therefore, possibly, of overloading.

Instability vs. runaway. We close this chapter with a brief summary of the 'driving agents' of wind dynamics in the last two chapters: de-shadowing instability and Abbott wave runaway. The de-shadowing instability is a true fluid instability (an amplification cycle) which acts on infinitesimal velocity perturbations. Even perturbations of short duration will lead to pronounced, non-linear flow structure which is advected outwards with the wind. In Sobolev approximation, the instability occurs from second order on (including velocity curvature terms). Abbott wave runaway, on the other hand, requires finite amplitude perturbations, since $v' < 0$ is required. There is no amplification cycle, but only a kind of perturbation 'filtering' as consequence of the asymmetry of the line force with respect to the sign of v'. Negative velocity perturbations annihilate themselves, and give way to systematic flow acceleration towards the critical solution. The runaway requires persistent perturbations. Yet, it occurs already in first order Sobolev approximation.

We should also mention that the present, hydrodynamic runaway is not related to the plasma runaway caused by frictional decoupling of line driven metal ions and dragged-along protons (Springmann & Pauldrach 1992). Still, a connection may exist between these two runaways: Krticka & Kubát (2000) report that frictional decoupling in thin winds may actually be prevented by the wind jumping to a *slow* solution with shallow velocity gradient. Issues of Abbott wave propagation and multiple solution branches become again interesting in these two-component fluids.

CHAPTER 4: DISK WINDS

Line driven winds from accretion disks are a relatively new research area, with quantitative modeling starting in the mid 80ies (Shlosman et al. 1985; Weymann et al. 1985). Disk winds are fascinating because of the richness of their environments, including quasars, Seyfert galaxies, cataclysmic variables, and protostars. In these environments, high-energy particle processes, magnetic fields, coronae, jets, accretion-dominated advection, compact objects, hot boundary layers, and dust formation play important roles.
Theoretical modeling of line driven disk winds is still in its infancy. In the present chapter, we treat first a simple, analytic model [6, 7] for line driven winds from cataclysmic variables. Observational evidence for line driving is almost unequivocal in these objects. In later sections, we discuss winds from magnetized accretion disks, mainly aimed at young protostellar objects and cataclysmic variables. Here, interplay of three driving forces (centrifugal, Lorentz, and line force) leads to an intricate wind dynamics.

§13 ANALYTICAL MODEL

1-d description, flux and gravity. We set up a simplified, 1-D model for stationary, line driven winds from thin accretion disks (no self-gravity) in cataclysmic variables (CVs). These systems consist of a white dwarf and a late-type main-sequence companion, the latter filling its Roche lobe. We consider first non-magnetic systems (DQ Her class), where the accretion disk should (almost) reach the compact object. The clearest indication of line driving comes from the fact that dwarf novae develop P Cygni line profiles during outburst (Krautter et al. 1981; Klare et al. 1982; Córdova & Mason 1982). Hence, the disk radiation field and wind are causally connected.
A number of approximations is made. First, we assume that the disk is geometrically thin, a plane of zero width indeed. We assume that the basic CAK formalism (Sobolev line force; statistical line distribution function) applies for these objects. Our central assumption is that each helical wind trajectory lies in a *straight* (yet, not vertical) cone. This is sketched in Figure 13.
A realistic approximation for the temperature run with radius q in the disk is $T \sim q^{-1/2}$ (Horne & Stiening 1985; Rutten et al. 1993), slightly shallower than the famos $T \sim q^{-3/4}$ of Shakura & Sunyayev (1973). We assume that the disk is optically thick, and that the radiation field at each radius is that of a black body. The radiative flux, $\mathbf{F}$, above a disk with $T \sim q^{-1/2}$ can be derived in closed form in cylindrical coordinates [6],

$$\mathbf{F}(r,z) = (F_r, F_z) = \pi I(r,0)\, r^2 \, \frac{z}{r^2+z^2} \times \\ \left(\frac{3r^2 - z^2 - q^2}{2r\sqrt{B}} - \frac{r}{z^2+r^2} \ln C,\; \frac{3z^2 - r^2 + q^2}{2z\sqrt{B}} - \frac{z}{z^2+r^2} \ln C \right) \Bigg|_{q=r_{\rm wd}}^{r_{\rm d}}, \qquad (61)$$

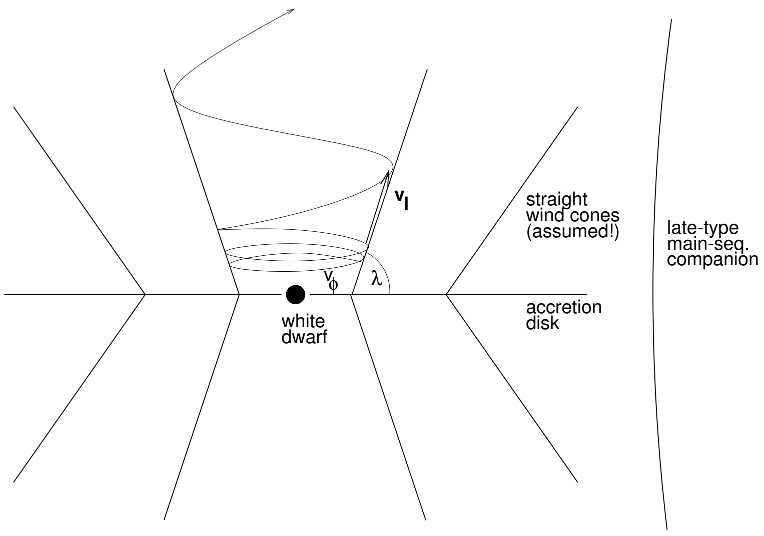

Figure 13: Flow geometry in a semi-analytic model of line driven winds from accretion disks in cataclysmic variables. The helical streamlines are assumed to lie in *straight* cones. Only the velocity component v_l along the cone is solved for. The tilt angle, λ, of the cone with the disk is a function of radius, and is derived as an eigenvalue.

where $r_{\rm wd}$ is the white dwarf radius, $r_{\rm d}$ the outer disk radius, and

$$B = (r^2 + z^2 - q^2)^2 + 4z^2q^2,$$
$$C = \frac{(z^2 - r^2)q^2 + (z^2 + r^2)^2 + (z^2 + r^2)\sqrt{B}}{q^2}. \qquad (62)$$

The flux isocontours are shown in Figures 3 and 4 of [6]. We adopt again the ('radial streaming') approximation that only velocity gradients along the flow direction are important. A qualitatively new feature of disk winds is their run of *effective* gravity with height, i.e., gravity after subtraction of the centrifugal force. In the disk plane, effective gravity is zero due to Kepler balance. Effective gravity increases linearly with height, reaches a maximum, and drops off with r^{-2} far from the disk. The exact formula is given in equation (9) of [6].

At first, it was thought that the existence of a gravity maximum makes a standard CAK critical solution for disk winds impossible, and that ionization gradients have to be included (Vitello & Shlosman 1988; [7]). The argument was that, because of zero effective gravity in the disk, a too large mass is launched. Higher up in the wind, the line force cannot carry the gas over the gravity hill, and the gas falls back to the disk. From the discussion in the last chapter we see why this argument does *not* apply. While the critical point (at finite height) is indeed the bottleneck of the flow, Abbott waves can adjust the disk (which is the wind base) to the correct, maximum possible mass loss rate.

Wind tilt angle as an eigenvalue. In the terminology of the Lavalle nozzle, the effective 'area function' along a wind ray is f^2/g, if $\alpha = 1/2$. Here, f and g are the radiative flux and effective gravity, respectively, normalized to their footpoint values in the disk. The tilt angle, λ, of the straight wind cone (with length coordinate l) with the disk midplane is found as a second eigenvalue, besides the mass loss rate. For each disk ring, the 2-D eigenvalue problem is posed as,

$$d\dot{M} = C \max_{\lambda} \min_{l} \frac{f^2}{g}. \tag{63}$$

Here, $d\dot{M}$ is the mass loss rate from the ring, and C is a constant. We search for the *maximum* mass loss rate with respect to λ, which can be driven through the bottleneck. Hence, the *minimum* must be taken with respect to l. Equation (63) defines a new *saddle* point in the $l\lambda$ plane, besides the standard CAK saddle in the lw' plane.

Isocontours of f^2/g above an accretion disk are shown in Figures 6 and 9 of [6]. Opposed to the stellar wind case, the solution topology is rather intricate here, with multiple saddles and extrema. This is a familiar situation for complicated area functions, and is also encountered when one allows for energy and momentum input at finite height in the solar wind (Holzer 1977).

We find that the accretion disk wind undergoes a rather sudden transition, at about 4 white dwarf radii in the disk, from steep tilt angles of only 10 degrees with the disk normal, to tilt angles of 30 to 40 degrees with the normal. The overall wind geometry is shown in Fig. 10 of [6]. The wind is strongly bi-conical everywhere, which is one of the main deductions from kinematic model fits to observed P Cygni line profiles (Shlosman & Vitello 1993).

Mass loss rates. The mass loss rate from the disk is obtained by integrating over all rings. For $\alpha = 1/2$, this can be written as,

$$\dot{M} = c_1(g) c_2(f)\; Q\Gamma\, \frac{L}{c^2}. \tag{64}$$

Here, L is the disk luminosity, and L/c^2 is the mass loss due to a *single*, optically thick line (the photon mass flux!), $Q \approx 2000$ is an effective oscillator strength (Gayley 1995), and Γ is the disk Eddington factor. The correction factors c_1 and c_2 account for the run of gravity and radiative flux. $c_1 = c_2 = 1$ gives the mass loss rate from a point star. For a thin accretion disk, we find in [6] that $c_1 = 3\sqrt{3}/2$. This is larger than unity since centrifugal forces assist in launching the wind. c_2 has to be calculated numerically, and is also ≥ 1.

We encounter the problem that mass loss rates from the above formula are one to two orders of magnitude smaller than values derived from P Cygni line fits ([7]; Vitello & Shlosman 1993; Knigge, Woods, & Drew 1995). Here, the values for $\dot{M}$ obtained from fitting were already revised downwards, for the following reason. In the original line fit procedure, individual disk rings were assumed to have a blackbody spectrum (as we did above). The strong Lyman continuum, however, leads then to large ionization rates, which must be balanced by large recombination rates, or large $\dot{M}$. If realistic spectra (Long et al. 1991, 1994) with suppressed (or missing) Lyman continua are used instead, $\dot{M}$ can be reduced by roughly one order of magnitude, while maintaining the ionization parameter.

Still, there remains the discrepancy noted above, between calculated and observationally deduced mass loss rates. One possible resolution of this problem is that distances and luminosities of CVs are systematically underestimated (Drew, Proga, & Oudmaijer 1999). Furthermore, the all-decisive parameter Q was so far only calculated for dense O star winds. The different spectral shapes of accretion disks, and ionization effects like the bistability jump (Pauldrach & Puls 1990) may cause larger Q values in accretion disks than in O stars. The strongest candidate, however, for resolving the discrepancy is the usual suspect: magnetic fields.

§14 NUMERICAL MODEL

The analytic model discussed so far is one dimensional, assuming straight wind cones. First time-dependent, numerical 2-D simulations of line driven winds from accretion disks were performed by Proga, Stone, & Drew (1998). Their wind rays are surprisingly straight in the polar plane (rz plane), and mass loss rates agree well with the above values. A new result from numerical simulations is the occurence of wind *streamers*. The wind above the disk is structured into alternating dense and rarefied regions. The dense streams propagate radially outwards, with a speed relative to the disk which is proportional to the local Kepler speed. During this motion, the angle between dense streamer and disk becomes ever shallower. This is shown in Fig. 14. A movie can be found at internet URL `http://www.astro.physik.uni-potsdam.de/∼afeld`). The occurence of alternating dense and rarefied regions is most probably related to mass overloading.

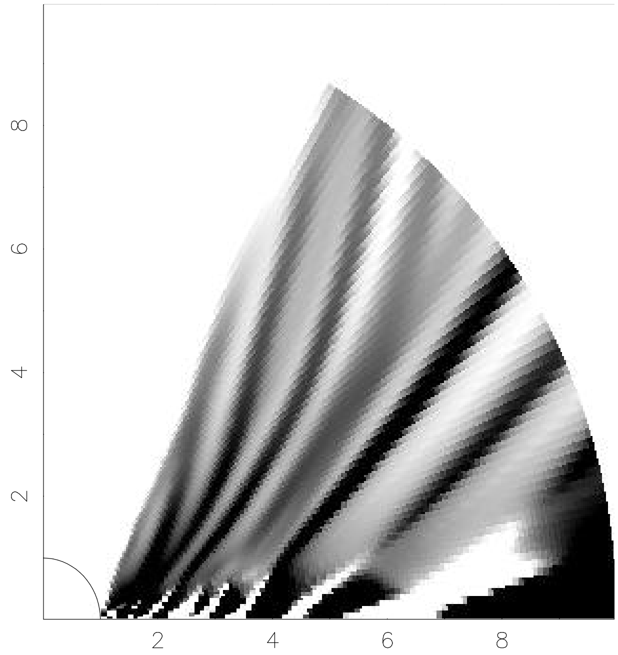

Figure 14: Dense streamers in a line driven wind above a cataclysmic variable disk (log density, dense regions in black). The white cone around the disk axis is a nearly gas free region with very fast parcels.

§15 MAGNETIZED LINE DRIVEN WINDS

We turn to accretion disks which are threaded by external magnetic fields. This could be the case in CVs (so-called polars or AM Her systems), young stellar objects (YSOs), and quasars. Our present simulations aim at the first two classes of objects only. The results are still preliminary, and much work remains to be done. The models were calculated using the publically available ZEUS 2-D MHD code (Stone & Norman 1992a,b), augmented by an own, Sobolev line force routine (Feldmeier, Drew, & Stone, in preparation).

Boundary conditions. The outcome of numerical hydrodynamic simulations depends strongly on the applied boundary conditions. We must, therefore, discuss boundary conditions in some detail. The reader interested mainly in results on disk winds may skip over the next few paragraphs, to the section entitled 'magnetized wind scenarios'.

For the present discussion, we chose again cylindrical coordinates (in the code, however, spherical coordinates are used, to avoid staircasing of the stellar surface). On the polar axis, anti-reflecting boundary conditions are used. Empirically, one finds that above the 'dark star' (both in CVs and YSOs, stellar UV fluxes are negligible), an essentially gas-free cone forms near the polar axis. The highly rarefied gas in the cone is accelerated to large speeds (a 'steep' CAK solution is adopted), and the Alfvén speed, $v_A = B/\sqrt{4\pi\rho}$, is very large in this cone. Both effects limit the Courant time step. To avoid effective stopping of the code, we let an artificial, vertical ram pressure jet originate on the star (Krasnopolsky, Li, & Blandford 1999). Along the stellar surface and the outer mesh boundary circle, inflow resp. outflow boundary conditions are chosen. Note that outflow boundary conditions are wrong close to the disk plane, below the Alfvén surface, and exert artificial forces on the wind (Ustyogova et al. 1999). Future work has to account for this.

Remains the disk itself. The inner disk structure is not resolved in our simulations (actually, zero sound speed is assumed), hence the disk is a simple, planar boundary. Given are a total of 7 hydrodynamic fields: $\rho, v_z, v_r, v_\phi, B_z, B_r, B_\phi$, minus one constraint, $\operatorname{div}\mathbf{B} = 0$. Hence, 6 wave modes result: 2 poloidal and 2 toroidal Alfvén waves, and 2 magnetosonic waves (up- and downstream mode in each case). Some of these waves are modified by the radiative line force. For simplicity, however, we keep their above names, with the one exception of the fast magnetosonic mode, which is termed a magnetoabbottic mode from now on.

By assumption, the disk shall be supersonic, subabbottic, and subalfvénic. Then 1 poloidal, 1 toroidal Alfvén mode and the slow magnetosonic mode enter the mesh from the disk, and 1 poloidal, 1 toroidal Alfvén mode and the fast magnetoabbottic mode enter the disk from the mesh. Hence, 3 extrapolations can be applied on the disk boundary, and 3 boundary conditions must be specified. For the poloidal components of the gas speed and magnetic field, we follow largely Krasnopolsky et al. (1999). Here, special care is taken to avoid kinks when magnetic field lines enter the disk. These kinks would cause artificial currents and forces. We do *not* follow Krasnopolsky et al. (1999) in case that gas falls back to the disk. In contrast to their reasoning, this should only affect the slow magnetosonic mode.

Remain the toroidal fields v_ϕ and B_ϕ. With regard to the toroidal Alfvén mode, one extrapolation and one boundary condition have to be applied. We *fix v_ϕ to be the Kepler speed.* This avoids dramatic events of sub-Keplerian gas falling towards the central object, which are encountered when v_ϕ is left free (Uchida & Shibata 1985; Stone & Norman 1994). B_ϕ is extrapolated. This causes a problem, since Lorentz force terms $\sim \partial(rB_\phi)/\partial r$ occur in the Euler equation for v_ϕ. For $B_\phi \neq 0$, v_ϕ does generally not agree with the Kepler speed. We proceed by postulating $B_\phi \sim 1/r$ in the disk (Ouyed & Pudritz 1997a,b). Whereas the latter authors leave the toroidal disk field constant at all times, we calculate, at each time step, $\bar{B}_\phi$ as average of B_ϕ on the first mesh row above the disk. Within the disk (boundary), we set $B_\phi = \bar{B}_\phi R/r$, where R is a free parameter.

This introduces an infinite signal speed, since averaging B_ϕ over the whole disk surface, at each time step, implies instantaneous couplings. Still, the above procedure works well empirically, and B_ϕ evolves smoothly in both r and z direction. By contrast, simulations assuming $B_\phi = 0$ in the disk crash.

Magnetized wind scenarios. As should be clear from this lengthy discussion, B_ϕ is of central importance in our simulations. We do not assume a magnetically dominated, co-rotating, force-free corona a priori. If a strong, line driven flow is launched from the disk, the angular-momentum conserving gas parcels may instead drag the magnetic field along, building up a strong toroidal field.

There exist two complementary, magnetocentrifugal wind scenarios. In the model of Blandford & Payne (1982), rigid poloidal field lines in a co-rotating corona act as lever arms transferring angular momentum to the gas. There act *no* Lorentz forces in the launching region of the wind. In the model of Contopoulos (1995), on the other hand, vertical gradients of a toroidal field, B_ϕ, cause non-vanishing curl (pointing towards the central object), and a Lorentz force $\mathrm{rot}\,\mathbf{B}_\phi \times \mathbf{B}_\phi$ which points vertically upwards, see Figure 15. The generation of dominant, large scale toroidal fields in disk-plus-corona simulations is treated in Miller & Stone (2000) and Elstner & Rüdiger (2000).

Model 1: a pure Lorentz wind. First, we consider a pure Contopoulos scenario. The disk has an Eddington factor of 10^{-2}, which is appropriate for CVs and YSOs. The poloidal field is set to zero. A *temporally constant*, toroidal field which drops off as r^{-1} is chosen in the disk. Note that a pure toroidal field has no Alfvén point. Physically, it is still meaningful to assume that the flow is superalfvénic, in that an initially poloidal field got wound-up, above the Alfvén point, into the toroidal field. Therefore, both *B_ϕ and v_ϕ* are now fixed in the disk. The toroidal field strength is taken from model 2: the present model 1 serves mainly as a simple reference frame for the more intricate model 2. From the calculation we find that just above the disk, the vertical Lorentz force is a few times larger than the line force. Hence, the wind is essentially magnetically launched, i.e., a Contopoulos flow. Still, the mass loss rate is almost exactly that of a *non-magnetic* model discussed in the last section. The explanation is simple: since the flow starts superalfvénic, the CAK critical point is the only flow bottleneck, and determines the mass loss rate – whatever force launches the wind.

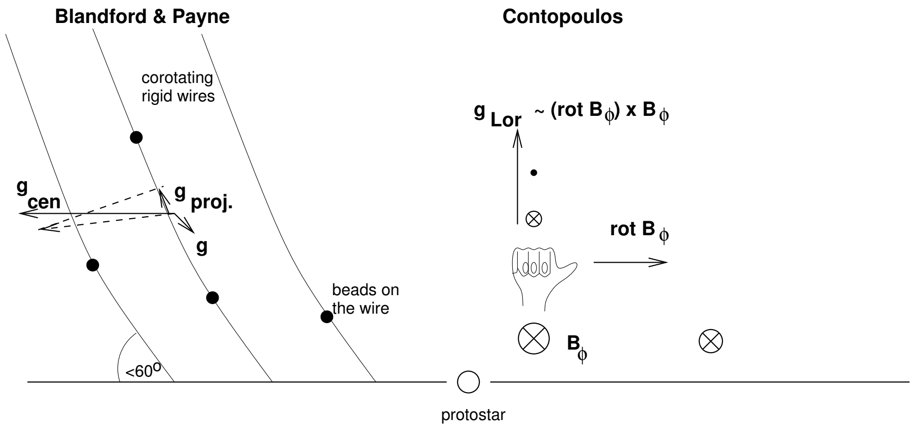

Figure 15: Two basic scenarios for magnetized disk winds, launched either by poloidal (left) or toroidal (right) magnetic fields. To apply the right-hand rule in the latter case, a constant $B_{\phi,0}$ should be added to the toroidal field, which leaves the curl unaltered.

Model 2: magnetic eddies. Next, we chose a purely line driven models from the foregoing section as initial conditions (regularly spaced, dense streamers alternating with rarefied regions). A poloidal magnetic field is switched on slowly, assuming exponential growth. The field is initially axisymmetric, $B_r = 0$. However, the field lines get tilted in time and get wound-up, creating B_z and B_ϕ components. Typically, we find toroidal fields which, at the rim where the accretion disk touches the stellar surface, are 20 times stronger than the poloidal field. For a not-too big disk, B_ϕ is still the dominant field component at the outer disk rim, only dropping off as r^{-1}. With B_ϕ dominating, one expects that the mass loss rate is still the one of model 1. Instead, it is 20 times larger!

The reason is apparently the following. In model 2, the B_ϕ bulge or wedge above the disk reaches to significantly larger heights than in model 1. The Lorentz force can assist then in overcoming the critical point, and the mass loss rate increases.

Why is the B_ϕ bulge broader in model 2? This model shows a pronounced vortex sheet in the toroidal magnetic field and gas speed, as is shown in Fig. 11. The eddies are shed-off from the disk-star rim, and carry the B_ϕ component to larger heights above the disk than in model 1. Indeed, the B_ϕ bulge extends now to the top of the spinning eddies.

The plasma gun, and other open questions. What is the origin of the vortex sheet? It is known from plasma physics that toroidal fields are often unsteady and undergo periodic cycles of field build-up and unloading. This is called a 'plasma gun'. We speculate that this is the origin of the present field eddies, too. Future work has to clarify this issue.

Other issues which shall be addressed in future work are: 1. Will a Contopoulos wind still form when a Blandford & Payne wind is launched right from model start? Instead of an initially axisymmetric field, tilt angles > 30 degrees with the disk normal shall here be assumed for the initial, poloidal field. 2. In present simulations

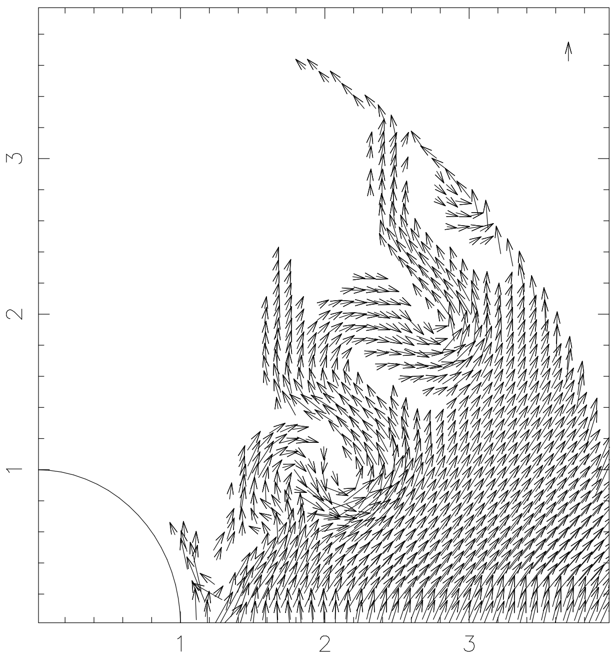

Figure 16: Eddies in the poloidal magnetic field above an accretion disk with small Eddington factor. The unit vector at the top right corresponds to 1 Gauss.

the Alfvén surface 'dives' periodically into the disk before it reaches the central star. This seems to be related to the shedding-off of magnetic eddies. 3. Riemann boundary conditions shall be applied along v_ϕ, B_ϕ characteristics, instead of the above, rather artificial boundary conditions averaging B_ϕ over the disk.
As was already mentioned, the present models are first steps only. They seem, however, to keep the basic premise that magnetic fields can lead to increased mass loss rates in disk winds. These models shall also help to clarify whether magnetic fields can provide confinement of line driven quasar winds, in order to prevent overionization by central source radiation (deKool & Begelman 1995); and whether line driving can overcome problems with launching magnetocentrifugal winds from accretion disks. The latter problems were discussed in an important paper by Ogilvie & Livio (1998).

Outlook and Acknowledgments

With the book "Foundations of Radiation Hydrodynamics" by Mihalas & Mihalas recently being added to the Dover series of classical science texts, there seems no further need to motivate "radiating fluids" (a term coined by Mihalas & Mihalas). In astrophysical hydrodynamics, radiation and magnetic fields are of similar importance.

Radiation hydrodynamics splits into two branches, according to whether the flow is driven by photon absorption in the continuum or in spectral lines. The former class includes flows with Thomson scattering on free electrons and 'dusty winds'. The latter class includes winds from hot stars and accretion disks, and is subject of the present writing. A simple, analytic approximation for the line force g_l from a point source of radiation is found by assuming a power law line list and validity of the Sobolev approximation, giving $g_l \sim F\big(\rho^{-1} dv/dr\big)^{\alpha}$, with radiative flux F and $0 < \alpha < 1$. Thus, g_l depends *non-linearly* on the velocity *gradient* dv/dr and matter density ρ, and represents a truly new, hydrodynamic force.

New waves (termed Abbott waves) and a new instability (termed de-shadowing instability) result from this new force, and are discussed in Chapters 3 and 2, respectively. Abbott waves could be responsible for shaping the velocity law of line driven winds, by causing a runaway towards the critical flow solution of Castor et al. (1975). The de-shadowing instability, on the other hand, is responsible for the formation of strong shocks and dense shells in the wind, and is probably the origin of observed X-ray emission from O stars; initial doubts after first CHANDRA X-ray line observations seem to be overcome. In Chapter 4, we gave a first glance at a rather new area in line driven wind hydrodynamics: accretion disk winds, and we discussed the interplay between radiative, Lorentz, and centrifugal forces.

What could be interesting topics for future work? With regard to the de-shadowing instability, all simulations so far are one-dimensional (with one puzzling exception), and two-dimensional hydrodynamic models are urgently missing. Line synthesis calculations using 2-D hydrodynamic models will allow to test our understanding of X-ray line formation and certain aspects of UV line variability. With regard to Abbott waves, the controversy whether they are an artefact of Sobolev theory is at present only partially overcome by post-Sobolev, numerical simulations. A strict derivation of the Green's function in presence of line scattering is missing. Finally, with regard to disk winds, some central questions are the increase in mass loss rates by combined magnetoradiative driving; magnetic flow confinement to prevent over-ionization by central source radation; and the amount of external disk viscosity caused by the wind.

With all these questions still being unanswered, line driven wind hydrodynamics appears to be a promising field for future research.

And now enough has been said (Aquinas, Sum. Theol., p. II.1, q. 114, a. 10). Almost.

It is my pleasure to thank Janet Drew in London, Wolf-Rainer Hamann in Potsdam, Rolf-Peter Kudritzki in Hawaii, Colin Norman in Baltimore, Stan Owocki in Newark, Adi Pauldrach, Joachim Puls, and Christian Reile in Munich, and Isaac Shlosman in Lexington for many stimulating discussions, at blackboards and in restaurants.

Literature

Abbreviations of journals were adopted from the Astrophysics Data System.

Abbott D.C. 1980, ApJ, 242, 1183
Arav N. 1996, ApJ, 465, 617
Baade D. & Lucy L.B. 1987, A&A, 178, 213
Baum E., Hamann W.-R., Koesterke L., & Wessolowski U. 1992, A&A, 266, 402
Berghöfer T.W. & Schmitt J. 1994, Science, 265, 1689
Berghöfer T.W., Baade D., Schmitt J., et al. 1996, A&A, 306, 899
Bjorkman J.E. 1995, ApJ, 453, 369
Bjorkman J.E. & Cassinelli J.P. 1993, ApJ, 409, 429
Blandford R.D. & Payne D.G. 1982, MNRAS, 199, 883
Blondin J.M., Kallman T.R., Fryxell B.A., & Taam R.E. 1990, ApJ, 356, 591
Blondin J.M., Stevens I.R., & Kallman T.R. 1991, ApJ, 371, 684
Cannon C.J. 1973, ApJ, 185, 621
Carlberg R.G. 1980, ApJ, 241, 1131
Cassinelli J.P. 1979, ARA&A, 17, 275
Cassinelli J.P. & Hartmann L. 1977, ApJ, 212, 488
Cassinelli J.P. & Swank J.H. 1983, ApJ, 271, 681
Cassinelli J.P., Cohen D.H., MacFarlane J.J., Sanders W.T., & Welsh B.Y. 1994, ApJ, 421, 705
Cassinelli J.P., Miller N.A., Waldron W.L., MacFarlane J.J., & Cohen D.H. 2001, ApJ, in press
Castor J.I., Abbott D.C., & Klein R.I. 1975, ApJ, 195, 157 (CAK)
Chandrasekhar S. 1950, Radiative Transfer, Dover, New York
Chevalier R.A. & Imamura J.N. 1982, ApJ, 261, 543
Cohen D.H., Cassinelli J.P., & MacFarlane J.J. 1997, ApJ, 487, 867
Colella P. & Woodward R.P. 1984, J. Comp. Phys., 54, 174
Conti P.S. & Ebbets D. 1977, ApJ, 213, 438
Contopoulos J. 1995, ApJ, 450, 616
Cooper R.G. 1994, Ph. D. thesis, Univ. Delaware
Cooper R.G. & Owocki S.P. 1992, ASPC, 22, 281
Córdova F.A. & Mason, K.O. 1982, ApJ, 260, 716
Courant R. & Hilbert D. 1968, Methoden der Mathematischen Physik II, Springer, Berlin
Cox D.P. & Tucker W.H. 1969, ApJ, 157, 1157
Cranmer S.R. & Owocki S.P. 1996, ApJ, 462, 469
deJong J.A., Henrichs H.F., & Kaper L. 2001, A&A, 368, 601
deKool M. & Begelman M. 1995, ApJ, 455, 448
Deubner F.-L. 1973, IAU Symp., 56
Drew J., Proga D., & Stone J. 1998, MNRAS, 296, L6

Drew J., Proga D., & Oudmaijer R.D. 1999, in: Variable and Non-spherical Stellar Winds in Luminous Hot Stars, eds: Wolf B., Stahl O., & Fullerton A.W., Springer, Berlin, p. 140

Eisloffel J., Mundt R., Ray T.P., & Rodriguez L.F. 2000, in: Protostars and Planets IV, eds: Mannings V., Boss A.P., & Russell S.S., Univ. of Arizona Press, Tucson, p. 815

Elstner D. & Rüdiger G. 2000, A&A, 358, 612

Emmering R.T., Blandford R.D., & Shlosman I. 1992, ApJ, 385, 460

Eversberg T., Lépine S., & Moffat A.F. 1998, ApJ, 494, 799

Feldmeier A., Norman C., Pauldrach A., et al. 1997c, ASP Conf. Ser., 128, 258

Field G.B. 1965, ApJ, 142, 531

Friend D.B. & Abbott D.C. 1986, ApJ, 311, 701

Fullerton A.W., Massa D.L., Prinja R.K., Owocki S.P., & Cranmer S.R. 1997, ApJ, 327, 699

Gaetz T.J., Edgar R.J., & Chevalier R.A. 1988, ApJ, 329, 927

Gayley K.G. 1995, ApJ, 454, 410

Gayley K.G. & Owocki S.P. 1994, ApJ, 434, 684

Gayley K.G., Owocki S.P., & Cranmer S.R. 1995, ApJ, 442, 296

Gayley K.G. & Owocki S.P. 1995, ApJ, 446, 801

Gräfener G., Hamann W.-R., & Koesterke L. 2000, ASPC, 204, 215

Hamann W.-R. 1980, A&A, 84, 342

Hamann W.-R. 1981a, A&A, 93, 353

Hamann W.-R. 1981b, A&A, 100, 169

Hamann W.-R. 1985, A&A, 148, 364

Hamann W.-R. & Koesterke L. 1998a, A&A, 333, 251

Hamann W.-R. & Koesterke L. 1998b, A&A, 335, 1003

Hamann W.-R. & Koesterke L. 2000, A&A, 360, 647

Harnden F.R., Branduardi G., Elvis M., et al. 1979, ApJ, 234, L51

Hawley J.F., Smarr L.L., & Wilson J.R. 1984, ApJS, 55, 211

Heap S.R., Boggess A., Holm A. 1978, Nature, 275, 385

Hearn A.G. 1972, A&A, 19, 417

Hearn A.G. 1973, A&A, 23, 97

Hedstrom G.W. 1979, J. Comp. Phys., 30, 222

Henrichs H. 1986, PASP, 98, 48

Henrichs H., Gies D.R., Kaper L., et al. 1990, in: Evolution in Astrophysics, IUE Astronomy in the Era of New Space Missions, p. 401

Heyvaerts J. & Norman C.A. 1989, ApJ, 347, 1055

Hillier D.J. 1984, ApJ, 280, 744

Hillier D.J., Kudritzki R.P., Pauldrach A., et al. 1993, A&A, 276, 117

Hillier D.J. & Miller D.L. 1998, ApJ, 496, 407

Holzer T.E. 1977, J. Geophys. Res., 82, 23

Horne K. & Stiening R.F. 1985, MNRAS, 216, 933

Ignace R., Oskinova L.M., & Fullon C. 2000, MNRAS, 318, 214

Innes D.E., Giddings J.R., & Falle S.A. 1987, MNRAS, 226, 67

Kahn S.M., Leutenegger M.A., Cottam J., et al. 2001, A&A, 365, L312

Kaper L., Hammerschlag-Hensberge G., & Zuiderwijk E. 1994, A&A, 289, 846

Kaper L., Henrichs H., Nichols J., & Telting J. 1999, A&A, 344, 231

Klare G., Wolf B., Stahl O., et al. 1982, A&A, 113, 76

Knigge C., Woods J.A., & Drew J.E. 1995, MNRAS, 273, 225

Koesterke L. & Hamann W.-R. 1995, A&A, 299, 503

Koesterke L. & Hamann W.-R. 1997, A&A, 320, 91

Königl A. 1989, ApJ, 342 208

Königl A. & Pudritz R.E. 2000, in: Protostars and Planets IV, eds: Mannings V., Boss A.P., & Russell S.S., Univ. of Arizona Press, Tucson, p. 759

Koninx J.P. 1992, Ph. D. thesis, Univ. Utrecht

Krasnopolsky R., Li Z.Y., & Blandford R. 1999, ApJ, 526, 631

Krautter J., Vogt N., Klare G., et al. 1981, A&A, 102, 337

Krolik J.H. & Raymond J.C. 1985, ApJ, 298, 660

Krticka J. & Kubát J. 2000, A&A, 359, 983

Kudritzki R.P., Lennon D., & Puls J. 1995, in: Science with the VLT, eds: Walsh J. & Danziger I., Springer, Berlin, p. 246

Kudritzki R.P., Palsa R., Feldmeier A., Puls J., & Pauldrach A. 1996, in: Röntgenstrahlung from the Universe, eds: Zimmermann H., Trümper J., & Yorke H., MPE Report 263, Garching, p. 9

Kudritzki R.P., Puls J., Lennon D.J., et al. 1999, A&A, 350, 970

Kudritzki & Puls J. 2000, ARA&A, 38, 613

Lamb H. 1908, Proc. Lond. Math. Soc. (1), xix, 144

Lamb H. 1932, Hydrodynamics, Dover, New York

Lamers H.J.G.L.M., Cerruti-Sola M., & Perinotto M. 1987, ApJ, 314, 726

Langer N., Garcia-Segura G., & MacLow M.M. 1999, ApJ, 520, L49

Langer S.H., Chanmugam G., & Shaviv G. 1981, ApJ, 245, L23

Langer S.H., Chanmugam G., & Shaviv G. 1982, ApJ, 258, 289

Leitherer C., Schaerer D., Goldader J.D., et al. 1999, ApJS, 123, 3

Lépine S. & Moffat A.F. 1999, ApJ, 514, 909

Long K.S., Blair W.P., Davidsen A.F., et al. 1991, ApJ, 381, L25

Long K.S., Wade R.A., Blair W.P., Davidsen A.F., & Hubeny I. 1994, ApJ, 426, 704

Lucy L.B. 1975, Memoires Societe Royale des Sciences de Liege, 8, 359

Lucy L.B. 1982a, ApJ, 255, 278

Lucy L.B. 1982b, ApJ, 255, 286

Lucy L.B. 1983, ApJ, 274, 372

Lucy L.B. 1984, ApJ, 284, 351

Lucy L.B. 1998, in: Cyclical Variability in Stellar Winds, eds: Kaper L. & Fullerton A.W., Springer, Berlin, p. 16

Lucy L.B. & Solomon P.M. 1970, ApJ, 159, 879

Lucy L.B. & White R.L. 1980, ApJ, 241, 300

Lucy L.B. & Abbott D.C. 1993, ApJ, 405, 738

MacFarlane J.J. & Cassinelli J.P. 1989, ApJ, 347, 1090

MacFarlane J.J, Cohen D.H., & Wang P. 1994, ApJ, 437, 351

MacGregor K.B., Hartmann L., & Raymond J.C. 1979, ApJ, 231, 514

Massa D., Fullerton A.W., Nichols J.S., et al. 1995, ApJ, 452, L53

Meyer F. & Schmidt H. 1967, Zeitschrift für Astrophysik, 65, 274

Mihalas D. 1978, Stellar Atmospheres, Freeman, San Francisco

Mihalas D. & Mihalas B.W. 1984, Foundations of Radiation Hydrodynamics, Dover, New York

Miller K.A. & Stone J.M. 2000, ApJ, 534, 398

Milne E.A. 1926, MNRAS, 86 459

Moffat A.F. 1994, RvMA, 7, 51

Moffat A.F., Owocki S.P., Fullerton A.W., & St-Louis N. (eds) 1994, Instability and Variability of Hot-Star Winds, Ap&SS, 221

Murray N., Chiang J., Grossman S.A., & Voit G.M. 1995, ApJ, 451, 498

Norman M.L., Wilson J.R., & Barton R.T. 1980, ApJ, 239, 968

Norman M.L. & Winkler K.H. 1986, in: Astrophysical Radiation Hydrodynamics, eds: Winkler K.H. & Norman M.L., Reidel, Dordrecht, p. 187

Ogilvie G.I. & Livio M. 1998, ApJ, 499, 329

Oskinova L.M., Ignace R., Brown J.C., & Cassinelli J.P. 2001, A&A, in press

Ouyed R. & Pudritz R.E. 1997a, ApJ, 482, 712

Ouyed R. & Pudritz R.E. 1997b, ApJ, 484, 794

Owocki S.P. 1991, in: Stellar Atmospheres: Beyond Classical Models, eds: Crivellari L., Hubeny I., & Hummer D.G., Reidel, Dordrecht, p. 235

Owocki S.P. 1992, in: Atmospheres of Early-Type Stars, eds: Heber U. & Jeffery S., Springer, Berlin, p. 393

Owocki S.P. 1994, Ap&SS, 221, 3

Owocki S.P. 1999, in: Variable and Non-spherical Stellar Winds in Luminous Hot Stars, eds: Wolf B., Stahl O., & Fullerton A.W., Springer, Berlin, p. 294

Owocki S.P. & Rybicki G.B. 1984, ApJ, 284, 337

Owocki S.P. & Rybicki G.B. 1985, ApJ, 299, 265

Owocki S.P. & Rybicki G.B. 1986, ApJ, 309, 127

Owocki S.P., Castor J.I., & Rybicki G.B. 1988, ApJ, 335, 914 (OCR)

Owocki S.P. & Rybicki G.B. 1991, ApJ, 368, 261

Owocki S.P. & Zank G.P. 1991 ApJ, 368, 491

Owocki S.P., Cranmer S.R., & Blondin J.M. 1994, ApJ, 424, 887

Owocki S.P., Cranmer S.R., & Fullerton A.W. 1995, ApJ, 453, L37

Owocki S.P. & Puls J. 1996, ApJ, 462, 894

Owocki S.P., Cranmer S.R., & Gayley K.G. 1996, ApJ, 472, L115

Owocki S.P. & Puls J. 1999, ApJ, 510, 355

Owocki S.P. & Cohen D.H. 2001, ApJ, in press
Parker E.N. 1958, ApJ, 128, 664
Pauldrach A. & Puls J. 1990, A&A, 237, 409
Pauldrach A., Hoffmann T., & Lennon M. 2001, A&A, in press
Poe C.H., Owocki S.P., & Castor J.I. 1990, ApJ, 358 199
Proga D., Stone J.M., & Drew J. 1998, MNRAS, 295, 595
Proga D., Stone J.M., & Kallman T.R. 2000, ApJ, 543, 686
Pudritz R.E. & Norman C.A. 1983, ApJ, 274, 677
Pudritz R.E. & Norman C.A. 1986, ApJ, 301, 571
Puls J., Owocki S.P., & Fullerton A.W. 1993, A&A, 276, 117
Puls J., Feldmeier A., Springmann U., Owocki S.P., & Fullerton A.W. 1994, Ap&SS, 221, 409
Puls J., Kudritzki R.P., Herrero A., et al. 1996, A&A, 305, 171
Puls J., Springmann U., & Lennon M. 2000, A&AS, 141, 23
Rayleigh J.W. 1890, Scientific Papers, vol. III, Dover, New York 1964, p. 335
Reile C. & Gehren T. 1991, A&A, 242, 142
Rutten R.G., Dhillon V.S., Horne K., Kuulkers E., & Van Paradijs J. 1993, Nature, 362, 518
Rybicki G.B. & Hummer D.G. 1978, ApJ, 219, 654
Rybicki G.B., Owocki S.P., & Castor J.I. 1990, ApJ, 349, 274
Scharmer G.B. 1981, ApJ, 249, 720
Schmidt H. & Zirker J. 1963, ApJ, 138, 1310
Schulz N.S., Canizares C.R., Huenemoerder D., & Lee J.C. 2000, ApJ, 545, L135
Schulz W.D. 1964, J. Math. Phys., 5, 133
Sellmaier F., Yamamoto T., Pauldrach A., & Rubin R.H. 1996, A&A, 305, L37
Seward F.D., Forman W.R., Giacconi R., et al. 1979, ApJ, 234, L55
Shakura N.I. & Sunyaev R.A. 1973, A&A, 24, 337
Shlosman I., Vitello P., & Shaviv G. 1985, ApJ, 294, 96
Shlosman I. & Vitello P. 1993, ApJ, 409, 372
Simon M. & Axford W.I. 1966, Planet. Space Science, 14, 901
Springmann U. 1994, A&A, 289, 505
Springmann U. & Pauldrach A. 1992, A&A, 262, 515
Steidel C.C., Giavalisco M., Pettini M., Dickinson M., & Adelberger K.L. 1996, ApJ, 462, L17
Stein R.F. & Leibacher J. 1974, ARA&A, 12, 407
Stone J.M. & Norman M.L. 1992a, ApJS, 80, 753
Stone J.M. & Norman M.L. 1992b, ApJS, 80, 791
Stone J.M. & Norman M.L. 1994, ApJ, 433, 746
Thompson K.W. 1987, J. Comp. Phys., 68, 1
Thompson K.W. 1990, J. Comp. Phys., 89, 439
Turnshek D.A. 1984, ApJ, 280, 51
Uchida Y. & Shibata K. 1985, Publ. Astron. Soc. Japan, 37, 515

Ulrich R. 1970, ApJ, 162, 993

Ustyugova G.V., Koldoba A.V., Romanova M.M., Chechetkin V.M., & Lovelace R.V. 1999, ApJ, 516, 221

Van Leer B. 1977, J. Comp. Phys. 23, 267

Vitello P. & Shlosman I. 1988, ApJ, 327, 680

Vitello P. & Shlosman I. 1993, ApJ, 410, 815

Waldron W.L. & Cassinelli J.P. 2001, ApJ, 548, L45

Wax N. 1954, Selected Papers on Noise & Stochastic Processes, Dover, New York

Wegner M. 1999, Diploma thesis, Univ. Munich

Wessolowski U. 1996, in: Röntgenstrahlung from the Universe, eds: Zimmermann H., Trümper J., & Yorke H., MPE Report 263, Garching, p. 75

Weymann R.J., Turnshek D.A., & Christiansen W.A. 1985, in: Astrophysics of Active Galaxies and QSOs, ed: Miller J., OUP, Oxford, p. 333

Wolf B., Stahl O., & Fullerton A.W. (eds) 1999, Variable and Non-spherical Stellar Winds in Luminous Hot Stars, Springer, Berlin

Wu K., Chanmugam G., & Shaviv G. 1992, ApJ, 397, 232

Appended Papers

[1] Feldmeier A. 1995, A&A, 299, 523
[2] Feldmeier A., Anzer U., Börner G., Nagase F. 1996, A&A, 311, 793
[3] Feldmeier A., Kudritzki R., Palsa R., Pauldrach A., Puls J. 1997, A&A, 320, 899
[4] Feldmeier A., Puls J., Pauldrach A. 1997, A&A, 322, 878
[5] Feldmeier A. 1998, A&A, 332, 245
[6] Feldmeier A., Shlosman I. 1999, ApJ, 526, 344
[7] Feldmeier A., Shlosman I., Vitello P. 1999, ApJ, 526, 357
[8] Feldmeier A., Shlosman I. 2000, ApJ, 532, L125
[9] Feldmeier A., Shlosman I. 2002, ApJ, 564, 385
[10] Feldmeier A., Shlosman I., Hamann W-R. 2002, ApJ, 566, 392

1995A&A...299..523F

Astron. Astrophys. 299, 523–544 (1995)

ASTRONOMY
AND
ASTROPHYSICS

Time-dependent structure and energy transfer in hot star winds

A. Feldmeier

Institut für Astronomie und Astrophysik der Universität, Scheinerstr. 1, D-81679 München, Germany

Received 9 November 1994 / Accepted 3 January 1995

Abstract. We present time-dependent hydrodynamical models of radiation driven hot star winds, which are subject to a strong instability intrinsic to the radiative line force. The calculations are done using a newly developed radiation hydrodynamics code applying the Smooth Source Function method (Owocki 1991) to calculate the radiative acceleration. Assuming spherical symmetry, the wind consists of a sequence of narrow, dense shells, where each shell is bounded by a pair of reverse and forward shocks, in good agreement with comparable models by Owocki (1992). We find frequent encounters of two shells with subsequent merging of the shells into one. For *small* periodic base perturbations, the wind structure is also periodic, without a stochastic component. For *large* base perturbations, on the other hand, a continuous spectrum of wave frequencies is excited in the wind. Furthermore, our models show the shock decay to set in from about 5 stellar radii on.

The major theme of this paper is the *energy transfer* in the wind. Time-dependent supergiant wind models up to now simply assume radiative cooling to be efficient, and hence the shocks to be isothermal. To test this assumption and to calculate the X-ray emission, the energy equation is included in the simulations. A severe numerical shortcoming is then encountered, whereby all radiative cooling zones collapse and the shocks become isothermal again. We propose a new method to hinder this defect. Simulations of dense winds then prove radiative cooling to indeed be efficient *up to* 5 to 7 R_*. Shock temperatures are between 10^6 to 10^7 K, depending on the base perturbation. Beyond these radii, however, the cooling zones of strong shocks become broad and thereby alter the wind structure drastically: all reverse shocks disappear, leaving regions of previously heated gas. This gas cools as it advects to larger radii. Since, moreover, shell-shell collisions only occur up to 6 to 7 R_*, the wind can be divided into two regions: an *inner, active* one with frequent shocks and shell-shell collisions; and an *outer, quiescent* region with "old" hot material, and with no further shell collisions.

Key words: stars: early type – stars: mass-loss – hydrodynamics – instabilities

1. Introduction

The winds of hot, luminous OB stars are driven by the momentum transfer from the star's UV continuum radiation field to metal ions, which is accomplished in numerous line transitions of these ions. Building upon the work by Lucy & Solomon (1970), Castor et al. (1975), and Abbott (1980, 1982), the subsequent inclusion of the finite cone angle effect (Pauldrach et al. 1986; Friend & Abbott 1986), a detailed NLTE treatment of the wind (Pauldrach 1987), radiative transfer allowing for multiple scattering (Puls 1987), and the empirical inclusion of line blocking and shock emission (Pauldrach et al. 1994a) results in stellar wind models which are able to predict the correct mass loss rates and terminal velocities, and to reproduce the complete UV line spectrum (Pauldrach et al. 1994a,b).

The most severe restriction underlying these models is their intrinsic assumption of stationarity. However, a wealth of observational evidence exists for a distinct time-dependency of the winds: 1. In the absorption troughs of ultraviolet P Cygni profiles of strong but unsaturated metal lines one observes the appearance of so-called discrete absorption components (DACs) at 0.3 to 0.5 of the wind's terminal velocity, v_∞. The DACs propagate to near v_∞ on timescales of one to a few days (Prinja & Howarth 1986, 1988; Henrichs 1988; Kaper 1993, and ref. therein). DACs have also been found in the P Cygni profile of the subordinate optical line He I $\lambda5876$ of the O supergiants HD 151804 (Fullerton et al. 1992) and HD 152408 (Prinja & Fullerton 1994a,b), starting already at $0.1\,v_\infty$. Because the recurrence time-scale of the DACs seems to be correlated with the projected rotational velocity of the star (Prinja 1988), a presently favored model of DAC creation is by corotating interaction regions (CIRs; Mullan 1984, 1986). 2. Saturated UV P Cygni profiles often show variability of the blue absorption edge (Henrichs 1991; Kaper 1993), and the appearance of broad and black absorption troughs (Prinja & Howarth 1986; Kaper 1993). The blue edge variability is believed to be caused by (rarefied) high speed material in the wind. The black troughs are thought to be due to a multiple non-monotonic velocity field of the wind (because of, e.g., the occurence of shocks), which in consequence induces a very effective back-scattering of the photopheric radiation (Lucy 1982a, 1983; Puls 1993; Puls et al. 1993b). 3. The X-ray emission from OB stars (EINSTEIN: Harnden et al. 1979;

Seward et al. 1979; Cassinelli & Swank 1983; Chlebowski et al. 1989; ROSAT: Hillier et al. 1993; Cassinelli et al. 1994; Drew et al. 1994) was first proposed to stem from coronal emission regions just above the stellar photosphere (Hearn 1972, 1975; Cassinelli & Olson 1979). These coronal models were subsequently ruled out for mainly two reasons: (i) The deep-seated origin of the X-rays would lead to strong K-shell absorption in the overlying wind material, which is not observed (Cassinelli & Swank 1983; Hillier et al. 1993; Cassinelli et al. 1994). (ii) The green coronal emission line [Fe XIV]5303 Å is not found in high S/N spectra of ζ Pup (Baade & Lucy 1987). The presently favoured model of X-ray emission is therefore by strong shocks in the wind; this is discussed below. 4. A non-thermal component in the radio emission of many OB stars (Abbott et al. 1981, 1984b; Bieging et al. 1989) is interpreted to be synchrotron radiation by shock-accelerated particles (White 1985). This interpretation is supported by the correlation found between X-ray emission and non-thermal radio emission (Chlebowski 1989). 5. With mass loss rates inferred from radio data, the observed thermal IR emission of winds is often too large when a smooth, stationary wind model with a $\beta < 1$ velocity law is applied (Abbott et al. 1984a). Because the free-free IR emission is a density-squared process, this enhanced flux can be explained by clumpiness of the winds in the region of the IR formation (Abbott el al. 1984a; Lamers & Waters 1984; Puls et al. 1993a). Clumpiness close to the stellar photosphere may also influence the formation of optical transitions such as Hα (Ebbets 1982; Wolf et al. 1994; Kaufer et al. 1994; Puls et al. 1995) or He I λ5876 (Prinja & Fullerton 1994a,b). 6. Finally, recent observations by the Gamma Ray Observatory of a WR star (White 1994) suggest that the postulated γ-ray emission from hot star winds (White & Chen 1992a,b) has readily been detected. The γ-rays should stem from pion decays, where the pions in turn are produced by collisions of thermal ions with protons Fermi-accelerated in shocks. The energies of these γ-rays are ≈ 5 decades higher than observed X-ray energies.

The major cause of wind structure is thought to be the strong hydrodynamical instability intrinsic to the line driving of the wind. (Possible exceptions to this are the DACs, the appearance of which might be connected to photospheric perturbations, where the latter induce *stable*, large scale structures propagating through the wind.) Milne (1926) proposed in essence this instability (or runaway) mechanism for the first time, for single ions in a static atmosphere. However, these runaway ions would lose their excess energy by Coulomb collisions with surrounding ions. Contrary to this, the wind instability proposed by Lucy & Solomon (1970) does not apply to single ions, but instead to hydrodynamical fluid particles. The mechanism of this instability is discussed extensively by Owocki & Rybicki (1984; hereafter OR) and by Rybicki (1987). OR succeeded in the unification (the so-called "bridging law") of the disparate results of MacGregor et al. (1979) and Carlberg (1980), who proposed a strong wind instability, and Abbott (1980), who proposed stability instead. Following OR, unstable growth should only occur for optically thin perturbations of optically thick lines, whereas optically thick perturbations should be stable. A further twist came into the stability vs. instability discussion by Lucy's (1984) discovery of the *line drag effect*. This effect stabilizes the flow due to the enhanced back*scattered* flux from larger radii which is experienced by a particle with outward directed velocity perturbation. This leads to zero growth rates very close to the star; but already within one stellar radius (Owocki & Rybicki 1985) the growth rate has reached again half the value of the pure absorption case considered by Carlberg (1980) and OR.

Since the typical growth rate within a characteristic wind flow time is of the order of 100 e-folds, the growth of perturbations will quickly reach the non-linear regime. Phenomenological models of the fully developed wind structure were proposed by Lucy & White (1980), Lucy (1982b), and MacFarlane & Cassinelli (1989), and are discussed below. The first consistent numerical simulations of the unstable growth were presented by Owocki et al. (1988; hereafter OCR). The three central assumptions underlying their work are: (i) one-dimensional spherical symmetry of the flow; (ii) isothermality; and (iii) pure photon absorption in spectral lines (no re-emission). The latter assumption has been dropped in subsequent work (Owocki 1991, 1995) by the approximate inclusion of line scattering using the so-called smooth source function method (SSF). The principal wind structures of pure absorption models and SSF models (but not the location of onset of the structure) are identical: the stationary wind at time $t = 0$ is transformed into an outward migrating sequence of very narrow and dense shells, which are enclosed by a strong reverse shock on the starward side and a weaker forward shock on the outer side.

The central part of the present paper deals with relaxing the above assumption of isothermality, (ii). There are mainly three reasons for doing so: 1. To calculate the X-ray emission from a time-dependent wind model one needs to know the temperature distribution of the wind material. 2. Isothermality should be a good approximation only for *dense* winds with efficient radiative cooling, where cooling zones are short enough to have no influence on the wind dynamics. On the other hand, radiative energy losses are small in the thin winds of B near main sequence stars (Lucy & White 1980), and also in rarefied regions of OB supergiant winds. Besides at large distances from the star, such regions possibly also exist at small radii due to the extreme dilution of the intershell medium in time-dependent wind models. 3. The EUV radiation of shock heated matter has an important influence on the ionization balance in the wind (Pauldrach et al. 1994a,b).

The energy transfer and X-ray emission is also the concern of most phenomenological models of the wind structure so far: Lucy & White (1980) proposed the X-rays to originate from bow shocks surrounding radiatively driven blobs ploughing through rarefied, shadowed, and therefore not radiatively driven wind material. The energy dissipation due to the friction between these two components is accomplished in the shock fronts. In this model, X-rays from blobs lying close to the star should experience strong K-shell absorption in the overlying wind material, which is not observed (Cassinelli & Swank 1983). Lucy (1982b) simplified the 2-D blob model to a 1-D model of a sawtooth like sequence of forward shocks. Within this model, the mutual shadowing of shocks ("blobs") is included. Because of this shadowing, the distance between shocks is larger; therefore shocks can exist up to larger radii and K-shell absorption has almost no significance, in accord with observations. The shortcoming of this model is that the resulting X-ray spectrum is too soft and too weak (Lucy 1982b; Cassinelli & Swank 1983). Finally, MacFarlane & Cassinelli (1989) proposed a model for the X-ray emission from the main-sequence B0 star τ Sco, which is able to reproduce the observed EINSTEIN data well. In this model, the propagation of a *single* shell through the wind is followed. The radiative line force is assumed to be stable, and consequently the shell does not evolve from an initially small perturbation, but instead is created by a strong, arbitrary perturbation of the boundary (MacFarlane & Cassinelli 1989) or the initial (Cooper & Owocki 1992) conditions of the wind. The importance of single, strong shocks for the X-ray emission from winds has already been noted by Lucy (1982b) (cf. also Cassinelli et al. 1994).

The first hydrodynamical wind models including the *energy* transfer of the unstable growth of initially small perturbations were presented by Cooper & Owocki (1992). These authors encounter a numerical shortcoming due to the radiative cooling of the gas: cooling zones behind strong shocks are not resolved, instead the shocks become isothermal again. This is the case even on a very fine spatial grid. Because of this problem, Cooper & Owocki (1992) neglected completely the radiative cooling in *thin* winds. The X-ray flux from these models was found to be typically a factor of 10 smaller than the observed flux. Cooper & Owocki (1994) therefore concluded that a large fraction of the (thin) wind material above a certain radius is heated to X-ray temperatures, which was also suggested by Cassinelli et al. (1994). For dense winds with their efficient cooling, on the other hand, Cooper (1994) and Cooper & Owocki (1994) suppose the cooling zones behind shocks to be steady (i.e., the cooling time is much shorter than the time-scale for changes in shock parameters). The X-ray spectrum from the shocks of an *isothermal* wind model is then found by using a tabulation of the emission as function of post-shock temperature. Contrary to the case of thin winds, the calculated X-ray flux from dense winds is found to be typically a factor of 10 *larger* than the observed flux.

In the present paper, we concentrate on the *consistent* inclusion of the energy transfer in time-dependent hydrodynamical wind simulations. To this aim, the origin of the above collapse of the radiative cooling zones is revealed and a method proposed to hinder it. Besides the assumption of 1-D spherical symmetry still remaining, the further main restrictions of our calculations are: 1. Only dense winds of O supergiants are considered, leaving the study of thin winds of B main sequence stars to future work. 2. Only the wind *dynamics* is considered. The calculation of X-ray emission from the models and comparison with ROSAT observations will be given in a follow-up paper.

The rest of this paper is organized as follows: Sect. 2 describes the numerical technique applied in calculating time-dependent wind models. In Sect. 3, an *isothermal* model for a supergiant wind is presented and compared with results by Owocki (1992, 1994). Section 4 discusses the numerical problem of the collapse of the radiative cooling zones behind strong shocks by means of a simple test flow problem and proposes a method to hinder this collapse. In Sect. 5, wind models including the energy transfer are examined. Section 6 gives a summary of results.

2. Technique

2.1. The hydrodynamical equations

The radiation hydrodynamical wind equations are, assuming an inviscid, one-component flow,

$$\frac{\partial \rho}{\partial t} + \mathrm{div}(\rho\, \mathbf{v}) = 0, \tag{1}$$

$$\frac{\partial (\rho \mathbf{v})}{\partial t} + \mathrm{div}(\rho \mathbf{v} \otimes \mathbf{v}) = -\mathrm{grad}\, p - \rho\, \mathbf{g}_{\mathrm{grav}} + \rho\, \mathbf{g}_{\mathrm{line}}, \tag{2}$$

$$\frac{\partial e}{\partial t} + \mathrm{div}(e\, \mathbf{v}) = -p\, \mathrm{div}\, \mathbf{v} - \Lambda. \tag{3}$$

The thermal energy density, e, of an ideal gas is $e = p/(\gamma - 1)$, where $\gamma = 5/3$ is assumed in the following.

The expressions for the radiative line acceleration $\mathbf{g}_{\mathrm{line}}$ and for the radiative cooling function Λ ($\sim \rho^2$) are given below. The temperature dependence of both the line force and the radiative cooling rate should in principle be found from a time-dependent, non-LTE treatment of the wind plasma. At least the first of these will likely remain beyond the capacity of computers for the foreseeable future. Here we simply parameterize the temperature dependence as found from stationary equilibrium calculations by Raymond et al. (1976) [cooling function] and MacGregor et al. (1979) [radiative force].

In the following, we will restrict ourselves to 1-D spherical symmetry: the calculation of the radiative line force in 2 or more dimensions is beyond current computer capabilities. Physical justification for assuming a spherically symmetric flow comes from the fact that the unstable growth of waves with "lateral velocity polarization" is damped because of Lucy's (1984) line drag effect (Rybicki et al. 1990). As long as the amplitude of photospheric perturbations, which are *assumed* in the present paper to seed the wind structure, has no strong dependence on latitude or azimuth, one then would expect the appearance of shell-like structures in the wind. In more realistic 2-D and 3-D models, however, even weak azimuthal perturbations could grow nonlinearly and break the shells into clumps due to instabilities of the Rayleigh-Taylor or the Kelvin-Helmholtz type (cf. Chandrasekhar 1961).

2.2. The hydrodynamical scheme

Equations (1) to (3) are discretized using an operator-splitting time-explicit, finite differences Eulerian scheme on staggered grids (cf. Reile & Gehren 1991a,b). The advection terms in integral form are solved on the control volumes of these grids (see, e.g., Roache 1982). This automatically ensures the correct jump conditions at shocks (and the correct shock positions), *if* the hydrodynamical equations are in conservative form. However, Eq. (3) is the thermal (not the total) energy equation, which is not conservative. We will return to this point in the next section. The advection fluxes are calculated using van Leer's (1977) monotonic interpolation. For the calculations in the present paper we applied the *consistent advection* scheme of Norman et al. (1980), since otherwise spurious spikes would show up in the velocity field (Owocki 1991).

The consistent advection scheme after Norman et al. (1980; see also Norman & Winkler 1986, and Stone & Norman 1992) may be described as follows. Let $\mathbb{F}$ be a conserved quantity like mass, momentum (in the absence of forces), or total energy; let $f = \mathrm{d}\mathbb{F}/\mathrm{d}V$ (with volume V) be the $\mathbb{F}$-density, and let $\mathbf{F}(f) = \hat{f}\,\mathbf{v}$ be the corresponding flux vector. The circumflex in the last expression indicates that the f value is *interpolated*, e.g., using either the donor cell scheme, the van Leer scheme, or the piecewise parabolic scheme (Colella & Woodward 1984). This is necessary since f and $\mathbf{F}$ are defined at different locations on the staggered grids, i.e., f at volume centers and $\mathbf{F}$ on volume boundaries. Consistent advection now means the replacement of the above ("standard") flux expression by

$$\mathbf{F}(f) = \hat{f}\,\mathbf{v} \rightarrow \widehat{f/\rho}\;\mathbf{F}(\rho), \tag{4}$$

with mass flux $\mathbf{F}(\rho) = \hat{\rho}\,\mathbf{v}$.

Finally, the *pressure terms* in the momentum and the energy equation, as well as g_{grav} and g_{line} in the momentum equation, are discretized in a straightforward manner. – The *boundary conditions* at R_{min} and R_{max} are fixed via Riemann invariants. R_{min} is the stellar photosphere. Here, an isothermal exponential density stratification through which a sound wave propagates into the wind is assumed as boundary condition. At R_{max}, Hedstrom's (1979) nonreflecting boundary conditions are applied using the formalism described by Thompson (1987, 1990).

2.3. The energy equation

In supergiant winds with flow speeds of a few thousand km/s and thermal speeds of about 3 km/s for ions like Fe and Ni, the ratio of the thermal energy of these ions to their macroscopic flow energy is of the order of 10^{-6}. However, behind strong shock fronts this ratio can approach unity. Hence, the thermal energy is an ill-conditioned part of the total kinetic energy of the wind plasma. For this reason we solve the *thermal* energy equation instead of the conservative *total* energy equation.

To ensure correct shock jumps, *artificial viscosity* is used in the tensor formulation of Schulz (1964) and Winkler & Norman (1986). In this formulation, only the viscosity *coefficient* is "artificial", in that it depends on the velocity gradient.

To solve for the adiabatic part of the energy equation plus the contribution from artificial viscosity (but without the radiative cooling), the operator splitting scheme of Norman & Winkler (1986) is used. The central part of this scheme is an implicit expression for the pressure, which should "optimize" energy conservation. In contrast to this, the scheme proposed by Hawley et al. (1984) only ensures positivity of the thermal energy. After this adiabatic + viscous step, all variables are updated and the radiative cooling rate is calculated. Other possible operator splitting schemes include: (i) the one after Różyczka (1985), where adiabatic terms and radiative cooling terms are mixed; and (ii) the scheme after Mair et al. (1988), where the radiative cooling is calculated in two half-steps, i.e., before and after the solution of the adiabatic part of the energy equation. We use the simple scheme described above because it makes a clear distinction between adiabatic and non-adiabatic terms, and thereby allows a simple analysis of the numerical behaviour of the radiative cooling. Assuming the cooling function to be of power law form, $\Lambda = A\rho^2 T^\alpha$, the equation for radiative cooling in this scheme is (cf. Eq. (3)),

$$\frac{\mathrm{d}T}{\mathrm{d}t} = -BT^\alpha, \tag{5}$$

with constant B,

$$B = \frac{\mu(\gamma-1)}{k} A\rho. \tag{6}$$

μ and k are the mean molecular weight and the Boltzmann constant, respectively. Note that ρ in Eq. (6) is a constant, since the density is updated only once during the numerical time step, in solving the continuity equation. The solution of the differential equation (5), for $\alpha \neq 1$, is

$$T_{n+1} = T_n \left[1 - (1-\alpha)\frac{\Delta t}{\tau_{\mathrm{c},n}}\right]^{\frac{1}{1-\alpha}}, \tag{7}$$

with the *cooling time* (at time step n)

$$\tau_{\mathrm{c},n} = \frac{T_n^{1-\alpha}}{B}. \tag{8}$$

From the requirement that the term in square brackets in (7) is *positive*, one finds the time step limitation

$$\Delta t \leq \frac{\tau_{\mathrm{c},n}}{1-\alpha} \qquad \text{for} \qquad \alpha < 1. \tag{9}$$

For $\alpha \geq 1$, on the other hand, there is no limitation on the time step.

For time-explicit differencing of (5) (instead of solving the differential equation directly), one finds the time step limitation, again requiring positive temperatures, $\Delta t \leq \tau_{\mathrm{c},n}$. For the semi-implicit and fully implicit differencing of (5) (see Roache 1982) the time step limitation has to be calculated separately for each value of α. For the case $\alpha = -1/2$, which is of interest here (see below), one finds $\Delta t \leq \frac{4}{3\sqrt{3}}\tau_{\mathrm{c},n}$ (semi-implicit), and $\Delta t \leq \frac{2}{3\sqrt{3}}\tau_{\mathrm{c},n}$ (fully implicit).

These time step limitations from the demand for positive temperatures are to be distinguished from time step limitations from numerical stability. A linear stability analysis of the exact solution (7) of (5), as well as of the time explicit and time implicit versions of (5) all lead to the following result: For $\alpha < 0$, temperature perturbations always *grow* in course of time, $|\Delta T_{n+1}/\Delta T_n| > 1$, even for an arbitrary short time step

Δt . However, this does not indicate numerical instability, but instead is a simple manifestation of Field's (1965) cooling runaway: material which becomes cooler than its surroundings will usually enlarge this temperature difference in time, since radiative cooling proceeds more efficiently for cooler material. Field's isochoric instability criterion (the density is constant in (5)) is precisely $\alpha < 0$, see his Eq. (4a). It therefore appears to us that for $\alpha < 0$, no time step limitation can be drawn from a linear stability analysis of the radiative cooling equation.

For the calculations in this paper, we have chosen a time step

$$\Delta t = \min\,(\Delta t_{\mathrm{CFL}},\ \Delta t_{\mathrm{vis}},\ \Delta t_{\mathrm{cool}}), \tag{10}$$

where

$$\begin{aligned}
\Delta t_{\mathrm{CFL}} &= \sigma \min_{\mathrm{(grid)}} \frac{\Delta r}{a + |v|}, \qquad \sigma = 0.5, \\
\Delta t_{\mathrm{vis}} &= \min_{\mathrm{(grid)}} \frac{(\Delta r)^2}{2\nu}, \quad \nu = -(b\Delta r)^2 \min(0, \operatorname{div} v), \quad b = 1, \\
\Delta t_{\mathrm{cool}} &= \max\,(\frac{1}{3} \min_{\mathrm{(grid)}} \tau_{\mathrm{c}},\ \ \tau_{\mathrm{z}}).
\end{aligned} \tag{11}$$

Here, Δt_{CFL} is the Courant et al. (1928) time step, with a the sound speed. Δt_{vis} is the time step limitation from linear viscosity (cf. Roache 1982), which is also applied to (nonlinear) artificial viscosity (Stone & Norman 1992). $\tau_{\mathrm{c}}/3$ in the radiative cooling time step Δt_{cool} corresponds to half the maximum allowed time step (9) for $\alpha = -1/2$. τ_{z} is a lower cutoff time to prevent the resolution of prohibitively short cooling intervals. Under very general assumptions one can easily show that for a post-shock cooling time $\tau_{\mathrm{c}} < \Delta t_{\mathrm{CFL}}$ the corresponding cooling zone behind the shock front cannot be resolved since it is shorter than the grid distance. Therefore, it should be safe to assume $\tau_{\mathrm{z}} \equiv \Delta t_{\mathrm{CFL}}$, i.e., to neglect the limitation on the time step from radiative cooling altogether. Proceeding in this way, negative temperatures occur frequently; however, they can simply be replaced by some arbitrary *floor value* for the temperature. Test calculations we have performed for the extreme cases $\tau_{\mathrm{z}} = 0$ and $\tau_{\mathrm{z}} = \Delta t_{\mathrm{CFL}}$ indeed gave essentially the same results.

2.4. The radiative line force

The radiative acceleration in the radial direction (spherical symmetry is assumed) in an isolated spectral line of frequency ν_{L} and constant mass absorption coefficient κ_{L} is,

$$\begin{aligned}
g_{\kappa_{\mathrm{L}},\nu_{\mathrm{L}}}(r) = \frac{4\pi}{c^2} \kappa_{\mathrm{L}} \nu_{\mathrm{L}} v_{\mathrm{th}} \Bigg\{ \frac{1}{2} I_{\nu_{\mathrm{L}}}(R_*) \int_0^1 \mathrm{d}\mu\, \mu\, D(\mu) \quad \times \\
\int_{-\infty}^{\infty} \mathrm{d}x\, \phi\left(x - \frac{\mu v(r)}{v_{\mathrm{th}}}\right) P(x) e^{-(\tau_{\mathrm{L}}(r,\mu,x) - \tau_0)} \\
+ \frac{1}{2} \int_{-1}^{1} \mathrm{d}\mu\, \mu \int_{-\infty}^{\infty} \mathrm{d}x\, \phi\left(x - \frac{\mu v(r)}{v_{\mathrm{th}}}\right) \quad \times
\end{aligned}$$

$$\int_{\tau_0}^{\tau_{\mathrm{L}}(r,\mu,x)} d\tau'\, S_{\nu_{\mathrm{L}}}(r'(\tau'))\, e^{-|\tau_{\mathrm{L}}(r,\mu,x) - \tau'|} \Bigg\}. \tag{12}$$

Here, x is the normalized frequency variable of the line (assuming pure Doppler broadening with normalized profile function ϕ), $x_{\nu_{\mathrm{L}}} = \nu - \nu_{\mathrm{L}}/\Delta\nu_D$, where $\Delta\nu_D = \nu_{\mathrm{L}} v_{\mathrm{th}}/c$. The mass absorption coefficient κ_{L} (in cm^2/g) is taken to be constant, which is a good approximation for resonance lines. A core-halo approximation (optically thin continuum) has been applied in the above expression, where the function $D(\mu)$ describes the angle dependence of the photospheric intensity, and $P(x)$ is the photospheric profile of the line (the transmission of a Schuster-Schwarzschild layer is proposed by OCR). τ_0 is the optical depth at $r = R_*$ or $r \equiv \infty$, depending on whether the ray hits the stellar core or not.

For simplicity, it is assumed that the line corresponds to a *singlet* transition, and that the line is *isolated*, i.e., no line overlap effects are considered. For a discussion of the latter, see Owocki & Rybicki (1985), Puls (1987), and Puls et al. (1993b).

The total radiative force from a large number of wind driving lines is found by integration of the single-line force over the truncated CAK line distribution function (cf. OCR),

$$\begin{aligned}
g_{\mathrm{line}}(r) &= \int_0^{\infty} \mathrm{d}\kappa \int_0^{\infty} \mathrm{d}\nu\ N(\kappa, \nu)\ g_{\kappa,\nu}(r), \\
N(\kappa, \nu) &= \frac{1}{\nu} \frac{1}{\kappa_0} \left(\frac{\kappa_0}{\kappa}\right)^{2-\alpha} e^{-\kappa/\kappa_{\max}},
\end{aligned} \tag{13}$$

where $\alpha < 1$. The cutoff $\kappa_{\max} < \kappa_0$ is introduced to suppress unstable growth on length scales shorter than the grid resolution, which is due to (very) strong lines.

The idea of the *Smooth Source Function* method (Owocki 1991, 1995) is to assume that the line source function $S_{\nu_{\mathrm{L}}}(r)$ is "insensitive to the details of dynamical variations" (Owocki 1991), so that one may adopt the source function for a *stationary* flow. However, for a non-monotonic velocity field (due to, e.g., shocks), radiative couplings occur between different locations in the wind. In case of spatially *separated*, coupled resonance zones (i.e., if there exists a location r in between two coupled regions R_1 and R_2, such that $|(\mu v)_r - (\mu v)_{R_{1,2}}| > n v_{\mathrm{th}}$, with $n = O(1)$), an iteration procedure within the generalized Sobolev approximation of Rybicki & Hummer (1978) could be used to calculate the source function. This is done in Puls et al. (1993b) for *line formation* calculations in structured winds, and could be applied in future hydrodynamical simulations. In the present paper, only a *local* source function is used.

In both cases of optically thin and thick lines, simple analytical expressions can be given for the source function in local Sobolev approximation. For reasons of computing time, the calculations in the present paper are done using an opacity independent source function, which is taken here to be the source function for an optically thin line only, corresponding to pure geometric dilution of the radiation field. Calculations using the source function for an optically thick line can be found in Puls et al. (1994). Wind models using a source function which fixes the growth rate to the value predicted from the *linear* stability analysis of Owocki & Rybicki (1985) are discussed by Owocki (1994).

Again for reasons of computing time, the angle integration in (12) is replaced by a one-ray quadrature (Owocki 1991). The different domains of integration over solid angle in the direct and diffuse terms are accounted for by a scaling factor $(r/R_*)^2$. Using the Stefan-Boltzmann law, neglecting limb-darkening, and integrating over the truncated line distribution function one finds (see Owocki 1991 or Feldmeier 1993 for some missing steps),

$$\begin{aligned} g_{\text{line}}(r) \; = \; & \frac{\sigma T_{\text{eff}}^4}{c}\Gamma(\alpha)\left(\frac{\kappa_0 v_{\text{th}}}{c}\right)^{1-\alpha}\left(\frac{v_{\text{th}}}{c}\right)^{\alpha}\frac{R_*^2}{r^2} \quad \times \\ & \qquad \left\{ \int_{-\infty}^{\infty} \mathrm{d}x\,\phi\left(x - \frac{\mu v(r)}{v_{\text{th}}}\right)\eta_+^{-\alpha}(r,\mu,x) \right. \\ & + \frac{S(r) r^2}{I_* R_*^2} \int_{-\infty}^{\infty} \mathrm{d}x\,\phi\left(x - \frac{\mu v(r)}{v_{\text{th}}}\right) \quad \times \\ & \qquad \left. \left[\eta_-^{-\alpha}(r,\mu,x) - \eta_+^{-\alpha}(r,\mu,x)\right] \right\}. \end{aligned} \tag{14}$$

Here, Γ is the Gamma function, and $S \equiv \int \mathrm{d}\nu S_\nu$, $I_* \equiv \int \mathrm{d}\nu I_{*,\nu}$. In addition, $S_{\text{thin}}(r)/I_* = W$, with $W = \frac{1}{2}(1-\mu_*)$ the dilution factor, and $\mu_* = \sqrt{1-(R_*/r)^2}$. The functions $\eta_\pm$ are given by:

$$\begin{aligned} \eta_+(r,\mu,x) \; &= \; {\kappa_{\text{L}}}^{-1}\tau_{\text{L}}(r,\mu,x) - \eta_0(x) + \kappa_{\max}^{-1} + \sigma_e^{-1}\phi(x), \\ \eta_-(r,\mu,x) \; &= \; \eta_R(x) - {\kappa_{\text{L}}}^{-1}\tau_{\text{L}}(r,\mu,x) + \kappa_{\max}^{-1}. \end{aligned} \tag{15}$$

The term $\phi(x)/\sigma_e$ (with σ_e the Thomson scattering coefficient) in the expression for η_+ arises from the Schuster-Schwarzschild photospheric layer (cf. OCR). The boundary conditions used are $\eta_0 \equiv 0$ at the stellar core and $\eta_R(x) = R\,\rho(R)\,\phi(x-\mu_R v_R)$ at the maximum radius R, see Owocki (1991).

In the expressions for the line force up to now the wind was assumed to be isothermal. The *temperature dependence* of the force from an optically thin line can be written in the form $g_{\text{thin}}(r, T(r)) = F(T) g_{\text{thin}}(r, T_{\text{eff}})$. The function F then enters the total force from *all* contributing lines (optically thin and thick) in two ways: (i) as a multiplicative factor, as just defined; and (ii) in the expression for the optical depth, since hot material is more transparent ($F < 1$) than cold material. Finally, one has to account for the temperature dependence of v_{th} in the profile function. This latter step is accomplished in (12) by noting that both the products κv_{th} and $x v_{\text{th}}$ are independent of temperature, and therefore can be replaced by the corresponding products at T_{eff}.

For the function F we use the fit by MacFarlane & Cassinelli (1989) to the numerical results of MacGregor et al. (1979). We then have $F = 1$ below a certain cutoff temperature T_{cut}. Above T_{cut}, F drops exponentially.

2.5. The radiative cooling function

The radiative cooling function from Raymond et al. (1976) for an optically thin gas can be approximated in the temperature range $10^5\,\text{K} < T < 10^7\,\text{K}$ by a power law (N_{e} and N_{H} being the electron and hydrogen particle densities, respectively),

$$\Lambda = N_{\text{e}} N_{\text{H}} A_{\text{R}} T^{\alpha}, \tag{16}$$

where

$$\alpha = -\frac{1}{2}, \qquad \text{and} \qquad A_{\text{R}} = 1.64\;10^{-19}\;\text{erg}\,\text{cm}^3\,\text{K}^{\frac{1}{2}}\,\text{s}^{-1}. \tag{17}$$

A better fit to the Raymond et al. cooling function is achieved by assuming distinct power laws in 5 temperature sub-intervals (Rosner et al. 1978). However, in the present framework we use the simple fit (16), (17) only. The reason is that, depending on the value of α, two different *thermal instabilities* possibly complicate the wind dynamics: (i) Field's (1965) local runaway instability; and (ii) the global oscillatory instability of Langer et al. (1981, 1982). Therefore, using only one value for α certainly helps to keep the calculations more lucid, and at the same time should be a sufficiently good approximation for our present purpose, namely to investigate the principles of the energy transfer in the winds.

2.6. The wind model

Since ζ Puppies is a well-studied O supergiant, stellar parameters close to the ones of ζ Pup are used in the following calculations. Table 1 lists the stellar and wind parameters.

The line force instability has a significant growth rate only for velocity perturbations with a wavelength shorter than $\frac{1}{3}$ to $\frac{1}{2}$ the Sobolev length $L_{\text{Sob}} = v_{\text{th}}/(\mathrm{d}v_{\text{stat}}/\mathrm{d}r)$ of the stationary wind (OR). The numerical grid therefore has to be fine enough to resolve these very short length scales. We use 3 000 logarithmically spaced grid points out to $10\,R_*$, i.e., $\Delta r/r = 7.68\;10^{-4}$. The worst resolution of the Sobolev zones occurs in the region of maximum velocity gradients, i.e., close to the sonic point, and is $\min(L_{\text{Sob,stat.}}/\Delta r) \lesssim 3$.

The formation of structure in the wind is triggered by a photospheric sound wave which propagates out into the wind, acting as a seed perturbation there. Other photospheric triggering mechanisms, especially non-radial pulsations (see Baade 1991; Gies 1991) and strange mode oscillations (see Gautschy & Glatzel 1990; Kiriakidis et al. 1993), will be studied in future work. The dispersion relation for isothermal sound waves of period P in an isothermal atmosphere of scale height H is (Lamb 1932),

$$\lambda = \frac{\lambda_0}{\sqrt{1-(\lambda_0/4\pi H)^2}}, \qquad \text{with} \qquad \lambda_0 = aP. \tag{18}$$

a is the isothermal sound speed in the limit of $\Lambda \ll H$. Even for sound waves with a wavelength somewhat larger than H, the *linear* dispersion relation $\lambda = aP$ still holds approximately: In our model, $\lambda/H = 5.2$, but still $\lambda/\lambda_0 = 1.1$. The *acoustic cutoff*

Table 1. Stellar and wind parameters. The stellar parameters are taken from Kudritzki et al. (1983).

Parameter	Symbol	Value
Mass	M	$42\,M_\odot$
Temperature	$T_{\rm eff}$	42 000 K
Radius	R_*	$19\,R_\odot$
Luminosity	L	$1.0\,10^6 L_\odot$
Helium fraction	$Y = N_{\rm He}/N_{\rm H}$	0.16
Ionization degree	$I_{\rm H}$; $I_{\rm He}$	1; 2
Thomson coefficient	σ_e	$0.32\,{\rm cm}^2\,{\rm g}^{-1}$
Eddington factor	Γ	0.59
Scale height (isoth.)	H	$3.1\,10^{-3}\,R_*$
CAK exponent	α	0.72
Line force constant	$\kappa_0\, v_{\rm th}/c$	$1800\,{\rm cm}^2\,{\rm g}^{-1}$
Line strength cutoff	$\kappa_{\rm max}/\kappa_0$	10^{-3}
Mass loss rate	$\dot M$	$3\,10^{-6}\,M_\odot\,{\rm yr}^{-1}$
Escape velocity	$v_{\rm esc}$	$580\,{\rm km\,s}^{-1}$
Terminal speed	v_∞	$2\,000\,{\rm km\,s}^{-1}$
Sound speed (isoth.)	$a_{\rm iso}$	$23\,{\rm km\,s}^{-1}$
Thermal speed	$v_{\rm th}$	$0.3\,a_{\rm iso}$
Sound wave: Period	P	5 000 s
——Amplitude at R_*	$A = \delta\rho/\rho$	0.01
——Wavelength	λ	$8.7\,10^{-3}\,R_*$

period, on the other hand, at which the wavelength of a sound wave becomes infinite (i.e., the denominator in (18) becomes zero), is $P_{\rm cut} = 6.2$ h for the stellar parameters of Table 1.

3. Isothermal wind models

In this section, the energy equation is trivially solved by setting $p = a^2\rho$. This corresponds to the calculations by OCR and Owocki (1992, 1994). The reason to assume supergiant winds to be dynamically isothermal is their high density, which implies that radiative cooling should be efficient enough to keep cooling lengths short compared with dynamical length scales.

Figs. 1 shows the wind structure 10 days after model start. We have followed the calculation for this long time interval for two reasons: (i) To make sure that the wind has completely settled in its response to the photospheric sound wave. As will be seen below, this may sometimes take ≈ 1 week. (ii) To permit us to perform a Fourier transformation of the wind velocity (at fixed locations r) as a function of time.

As in the models by OCR and Owocki (1992, 1994), the wind in Fig. 1 consists of a sequence of very narrow, very dense shells. The shells are enclosed by a reverse shock on the starward facing side. On the outward side, it can actually not be decided from the rather poor resolution whether the shells are bounded by a forward shock or by a continuous, forward-facing compression wave (as opposed to a rarefaction wave; see Courant & Friedrichs 1948, Chap. III). Density contrasts of a few thousand occur at the reverse shocks, corresponding to Mach numbers of 30 and more. Because of these large compression ratios, the dense shells in Fig. 1 are very narrow and the reverse and forward shocks that enclose a shell propagate at about the same speed (cf. Sturrock & Spreiter 1965). The forward (reverse) shocks are faster (slower) in any reference frame than both the in- and outflowing material. Because of this, every wind particle passes at most through one shock; or, stated differently, a particle cannot leave a shell once it is in it.

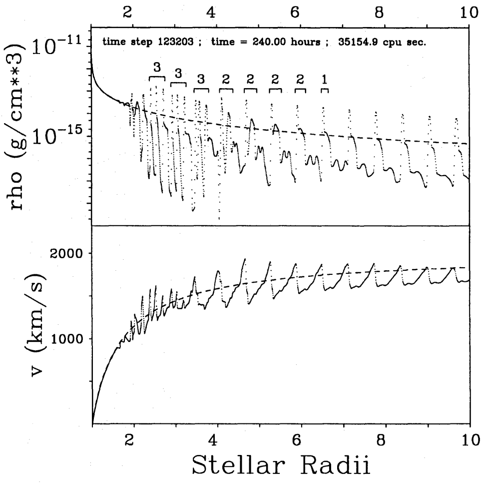

Fig. 1. Isothermal wind 10 days after model start. The values of ρ and v at each grid point are plotted. Dashed line: Stationary start model

It is interesting that the wind structure in Fig. 1, which results from the unstable amplification of the periodic base perturbations, appears itself to be quite stable. This is despite the fact that the material in front of the reverse shocks (i.e., on their left side) shows large velocity gradients, and thus might be expected to be subject to further, smaller scale instability. However, this material is strongly rarefied, so that no optically thick lines are present, which is the other prerequisite for unstable growth to occur. Inside the shells, on the other hand, the material is extremely dense, but here the velocity gradients are negative, which means these regions are stable as well. The regions in front of the forward shocks (i.e., on the right) are stable because of a combination of small velocity gradients (due to shadowing by material at smaller radii) and the depletion of the pre-shock gas. – In effect, the unstable amplification of the driving perturbations suppresses the formation of structure on other scales.

A striking fact about the wind model of Fig. 1 is its strong periodicity at radii larger than 4 R_*. The cause for the *seemingly* chaotic structure in Fig. 1 up to about 4 R_* is the creation of the shells in triples per period of the photospheric sound wave, with subsequent collisions among their members. n-tuples are indicated in the density run of Fig. 1 by $\overset{n}{\sqcap}$. The triple-wise creation of shells and their collisions thereafter are also clearly seen in

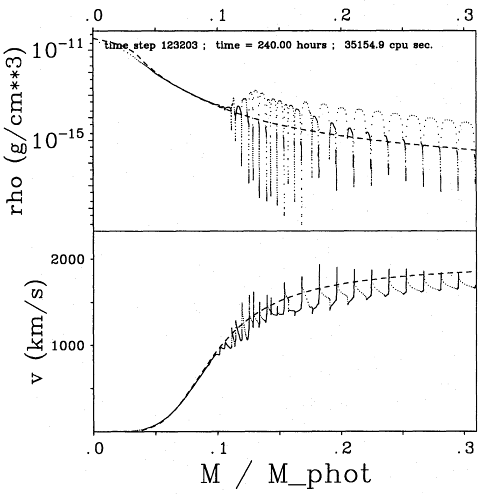

Fig. 2. Wind structure from Figs. 1, plotted against mass coordinate

Fig. 9 for a wind model including the energy transfer, and will be discussed further in Sect. 5.

From about 5 R_* on, the shocks which enclose the shells become weaker with increasing distance from the star. The reason for this is twofold: (i) The instability is strong only close to the star, where the velocity gradient is large. (ii) Shocks far out in the wind are shadowed by material close to the star. This shock decay is not present in models by Owocki and Cooper, where instead the shock amplitude stays almost constant as function of radius. The observable X-ray emission should depend sensitively on the maximum radius for formation of strong shocks. As found by Hillier et al. (1993) for ζ Pup, X-rays with energies below 1 keV originate from radii (much) larger than $10\,R_*$. Detailed modeling of the X-ray emission from time-dependent winds has to clarify the extent to which weak shocks (still present at large radii) are able to produce the observed soft X-ray component.

Following OCR, we introduce the mass coordinate

$$M(r,t) = 4\pi \int_{R_*}^{r} \mathrm{d}r'\, r'^2 \rho(r',t). \tag{19}$$

Figure 2 shows density and velocity of the wind model of Fig. 1, now plotted against M. The mass is given here in units of the "photospheric mass",

$$M_{\rm phot} = 4\pi R_*^2/\sigma_e, \tag{20}$$

which is derived by assuming an isothermal, plane-parallel exponential density stratification, with the location of the photosphere at optical depth unity for Thomson scattering.

Figure 2 shows that only a tiny fraction of the wind mass is actually accelerated to high velocities in front of the reverse shocks. Furthermore, almost the whole wind mass is localized within the dense shells. In the velocity run of Fig. 2, the reverse and forward shocks enclosing a shell are clearly separated.

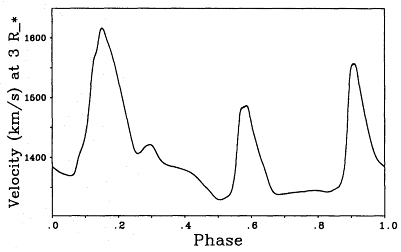

Fig. 3. Time series of the velocity at the fixed location $r = 3\,R_*$ in the wind, plotted against the phase of a wave with period $P = 5\,000$ s. 48.3 wave cycles are shown

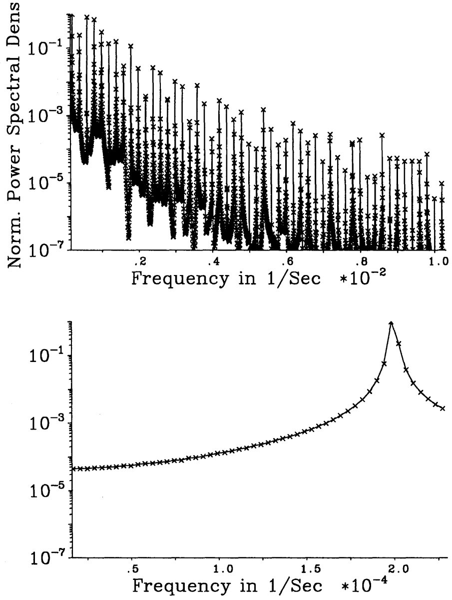

Fig. 4. Power spectrum of the time series of Fig. 3. *Upper panel*: Harmonic domain of the frequency $f = 1/5\,000\,\mathrm{s}^{-1}$ (leftmost peak). The first 50 overtones of this frequency are clearly seen. *Lower panel*: Subharmonic domain of $f = 1/5\,000\,\mathrm{s}^{-1}$ (right peak)

A powerful method to test for the periodic vs. chaotic nature of the wind structure is to analyze time series of hydrodynamical quantities at fixed locations in the wind. Figure 3 shows a time series of the velocity at $r = 3\,R_*$, plotted against the phase of a wave with period $P = 5\,000$ s. The time series starts at $t = 7.20$ days and ends at $t = 10.00$ days, i.e., shows 48.3 wave cycles. It is striking that even within this spatial region,

1995A&A...299..523F

which in the snapshot of Fig. 1 appears to be rather chaotic, the temporal signal is very nearly periodic. As in Fig. 1, one sees 3 shells passing by per 5000 s period. Figure 4 shows the power spectrum of this time series. In the power spectrum, besides the frequency of the photospheric sound wave the first 50 harmonic overtones, $\nu^{(n)} = (n+1)\nu_0$, of this frequency are seen. The reason for the excitation of these overtones is the (nonlinear) wave steepening due to the instability (Landau & Lifschitz 1991, p. 494): though the sound wave is deformed, it keeps its period, so that the Fourier spectrum consists of (all) the harmonic overtones of the wave's frequency. In the subharmonic domain of this frequency no signal is found, see the lower panel of Fig. 4. In particular, no period doubling occurs, which would be a very first hint of a realization of the Feigenbaum route to deterministic chaos (see, e.g., Schuster 1989) in the wind. Furthermore, the acoustic cutoff frequency of $1/6.2\,\mathrm{h}^{-1}$ does not show up. While a corresponding wave *is* present in early times of the simulation, it is damped within a couple of days. This is one reason for the rather long time it takes the wind to settle to a periodic response driven by the *explicit* base perturbation.

4. Collapse of the radiative cooling zone

Trying to repeat the above wind calculations including the energy equation results in the shortcoming that no radiative cooling zones are resolved. The shocks enclosing the shells appear to be isothermal again, whereas simple estimates show that the cooling zones behind strong reverse shocks should be resolved quite well by the numerical grid. In this section, we discuss the two major causes of this behaviour for a simple test flow, and present a method to hinder these defects.

4.1. The thermal instability oscillation

Consider the highly supersonic, plane-parallel flow of an ideal gas against a wall. A shock wave forms which propagates into the gas. Due to radiative cooling of the shock-heated gas the shock comes to a stop and the flow becomes stationary (where $\alpha < 3$ in Eq. (16) is necessary for this). The gas accretes onto the wall in an infinitely thin, infinitely dense layer. The analytical solutions for the stationary cooling zones, for different values of α, are listed in the fundamental paper by Chevalier & Imamura (1982; CI in the following).

A new kind of thermal instability due to radiative cooling was discovered by Langer et al. (1981) in numerical simulations of white dwarf accretion columns (AM Her systems). The linear analysis of this instability was performed by CI. The origin of the instability is the nonlinear dependence of the total cooling length on the immediate post-shock temperature. Detailed descriptions of the mechanism are given in Langer et al. (1982), Gaetz et al. (1988), and Wu et al. (1992). This instability is termed "*global* thermal instability" since it concerns the cooling zone as a whole, in contrast to the "local" thermal instability of Field (1965), which leads to a runaway cooling of single fluid particles. The instability is an oscillatory one (cf. Chandrasekhar 1961), with the cooling zone contracting and expanding periodically, and with the shock front at the very beginning of the cooling zone oscillating around its stationary rest position. The period of this oscillation can be estimated to be (Langer et al. 1982)

$$t_{\mathrm{osc}} \approx 6\,t_{\mathrm{c}}, \tag{21}$$

where t_{c} is again the cooling time. This estimate for the oscillation period is in very good agreement with results from the exact linear stability analysis, which typically gives $t_{\mathrm{osc}} \approx 5\,t_{\mathrm{c}}$, with a slight dependence on α. It is more difficult to derive the maximum value of α for which the oscillatory thermal instability still occurs, since this value depends on the detailed dynamics of the expanding and contracting cooling zone. CI as well as Imamura et al. (1984) find instability for $\alpha \lesssim 0.4$ in the fundamental mode, and for $\alpha \lesssim 0.8$ in the higher modes (see CI for the definition of the different modes). Bertschinger (1986) finds instability for $\alpha \lesssim 1$.

We suggest (cf. Feldmeier 1993, 1994) that the global thermal instability is the major cause for the numerical isothermality of strong shocks in wind simulations including energy transfer. Even if the numerical grid is fine enough to resolve the *stationary* radiative cooling zone, the cooling zone of minimum extent during the contraction phase can fall below the grid resolution. The numerical scheme "forgets" about the existence of the cooling zone then, and the shock becomes numerically isothermal. The reversible oscillation has thereby turned into an irreversible collapse.

To test this hypothesis, we consider the above plane-parallel, radiatively cooling gas flow. The pre-shock density and velocity are fixed to be 1 and -1, respectively. The cooling constant A is chosen so that the *stationary* cooling zone has an extent of $L_{\mathrm{c}} = 1$. The adiabatic exponent is $\gamma = 5/3$, and the Boltzmann constant as well as the atomic weight are both taken to be $k = \mu = 1$. The wall is located at $x = 0$.

Numerical results for the *stationary* cooling zones in case that there is *no* instability ($\alpha \geq 1$) are found to be in good agreement with the analytical solution given by CI. Figure 5 shows a calculation for $\alpha = 1$, and for a Mach number at the shock front of 10^{10} (which is meant to simulate an arbitrarily strong shock; the Mach number of the shock is controlled by the temperature assumed for the pre-shock gas). The position of the shock at $x = 1$ in Fig. 5 is wrong by 1 grid point. This is due to solving the non-conservative thermal energy equation including artificial viscosity.

We define the number "Res" to be the ratio of the length of the stationary cooling zone to the length of a grid interval,

$$\mathrm{Res} = L_{\mathrm{c}}/\Delta x \tag{22}$$

For the *unstable* case $\alpha = -1/2$ now, Fig. 6 shows the run of density, velocity, and temperature at subsequent moments of the oscillation cycle. The left column is for a calculation with Res = 30, the middle column for one with Res = 8; the rightmost column will be discussed below. The snapshots are separated by time intervals $\Delta t = 4$, which is the approximate cooling time, $t_{\mathrm{c}} \approx L_{\mathrm{c}}/v_{\mathrm{post}}$, where $L_{\mathrm{c}} = 1$ and $|v_{\mathrm{post}}| = 1/4$. (Note that the

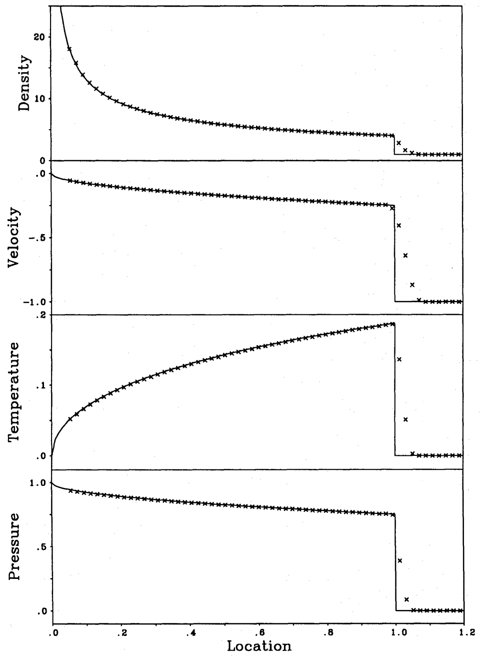

Fig. 5. Normalized (according to Appendix A) stationary radiative cooling zone for the test flow problem described in the text, with a cooling exponent $\alpha = 1$. *Full line*: Analytical solution after Chevalier & Imamura (1982). *Crosses*: Numerical solution

time axis in Fig. 6 is in units of $t_c = 4$.) The last snapshot is for $t = 60$, corresponding to 2 oscillation cycles.

Immediately after $t = 0$, a shock front is created which propagates away from the wall. The density on the first two or three grid points is much too low, whereas the temperature is too high. This is Noh's (1987) artificial *wall heating*, caused by the use of artificial viscosity. During the first 3 cooling times, the run of velocity, density, and temperature within the cooling zone approaches the analytical solutions for a *stationary* cooling zone. Yet, after about 4 to 5 cooling times both the velocity and density become nonmonotonic, and *secondary shocks* (cf. Falle 1975, 1981; Gaetz et al. 1988) form close to the wall. The cooling zones of these secondary shocks are not resolved in the present calculation, so they appear to be isothermal shocks; however, their resolution could easily be achieved by using a finer grid, (see Feldmeier 1993). After 5 cooling times, the primary shock at the very beginning of the cooling zone starts to propagate in direction of the wall. The maximum possible shock speed is the speed of the inflowing material, since otherwise the pre- and post-shock domain would interchange. The shock in fact almost reaches this maximum speed, at which moment hardly any temperature jump is seen ($t = 7\,t_c$). At $t = 8\,t_c$, the cooling zone has its minimum extent. Since the shock speed is zero then, the temperature jump is the same as for a stationary shock, $T_{\rm post} = 3/16$. On a sufficiently fine grid, the shock starts propagating away from the wall again (left column of Fig. 6), whereas on a coarse grid the shock collapses at the wall (mid column). In the latter case, the temperature jump of 3/16 is still found, but over the next 2 (or 3) grid intervals the material cools again to $T = 0$. Since already the (artificial) viscous shock layer is ≈ 3 grid intervals broad, this cooling zone is *not* resolved, hence the shock must be considered as a numerical isothermal shock.

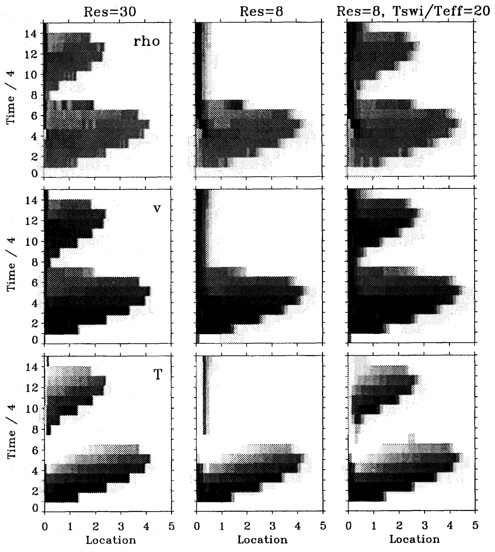

Fig. 6. Global thermal instability oscillations for $\alpha = -1/2$ at grid resolutions Res = 30 (resolved; left panel) and Res = 8 (collapsed; mid panel). The snapshots are separated by the cooling time $t_c = 4$. The right panel is for the same resolution as the mid panel, but now using $T_{\rm swi}/T_{\rm eff} = 20$, resp. $T_{\rm post}/T_{\rm swi} = 5$. This hinders the collapse of the cooling zone

4.2. Shock front cooling and advective diffusion

There is another numerical defect which might be responsible for the collapse of the cooling zones. The material of intermediate temperatures within the *artificially broadened* viscous shock layer cools more efficiently than the hot post-shock material. This could lead to an "eating" of the shock front into the cooling zone, and therefore a collapse of the latter. However, in appendix 6 it is shown that for a cooling exponent $\alpha = -1/2$, strong cooling within the viscous layer only takes place if the *post-shock* temperature implies that the cooling zone is narrower than the viscous layer. In this case, the cooling zone cannot be resolved on the grid anyway, since even the viscous layer is unresolved. Consequently, no enhanced cooling problem should exist in shock fronts followed by a cooling layer broader than a few grid distances.

Yet another mechanism which *is* possibly related to the cooling zones' collapse is *advective diffusion* (Owocki, priv. comm.). This defect would explain the observed influence of *advection* on the collapse (Feldmeier 1993, p. 185). We suggest that advective diffusion occurs at the *cold end* of the cooling zone, instead of occuring at the shock front as proposed by Owocki. Our reasoning has two parts: (i) Due to Field's (1965) cooling runaway, the temperature (and density) gradient is *infinite* at the cold edge. Therefore, a positive feedback between the diffusive errors of the numerical advection scheme and enhanced radiative cooling occurs. Interpolation errors of the advection scheme smear out the edge; since for small α the cooling rate is larger at smaller temperatures, the smeared out edge becomes steep again, thereby "eating" a certain distance into the cooling zone. At the sharp edge, then, new diffusive errors build up, etc. (ii) The speed is *continuous* at the cold edge, i.e., the same material always lies there (with new material being added constantly), and so the errors are *additive*. This is in contrast to shock fronts, where new particles always pass through, and errors *converge* to a certain value.

Loosely speaking, the cooling zone is destroyed from both ends: (i) from the oscillating shock side, due to the collapse during the contractional phase of the global thermal instability; and (ii) from the cold edge, due to the interplay between numerical diffusion and radiative cooling.

4.3. Modification of the cooling function

To hinder the collapse of the cooling zone caused by the oscillatory thermal instability, we propose the following procedure. The radiative cooling function is modified in the way shown in Fig. 7, namely: (i) Below a certain temperature $T_{\rm swi}$ the cooling function is assumed to have a *stable* slope $\alpha = +2$. (ii) At $T_{\rm swi}$ itself, the cooling function must be continuous, and this defines the cooling constant $\tilde{A}$ below $T_{\rm swi}$,

$$\tilde{A} = A\,T_{\rm swi}^{-5/2}. \tag{23}$$

The most critical time interval during the contraction of the cooling zone is defined by the following two instants: It *starts* at about the moment when the shock has almost disappeared because of propagation in the direction of the cold edge with the same speed as the incoming material; and it *ends* with the ultimate collapse of the cooling zone due to the shock approaching the cold edge. During the first moments of this time interval the material within the *whole* cooling layer radiates energy according to the *stable* cooling function with $\alpha = 2$ slope; at later times, it is still the material sufficiently close to the cold edge radiating according to an $\alpha = 2$ power law. Therefore, the shock's propagation in the direction of the cold edge is decelerated by the build up of excess pressure, so that the shock cannot approach the edge too closely. In addition to the stability of the $\alpha = 2$ slope, a further deceleration of the shock is caused by the lower cooling rate at $T < T_{\rm swi}$ of the modified as compared to the original cooling function – necessitating broader cooling zones.

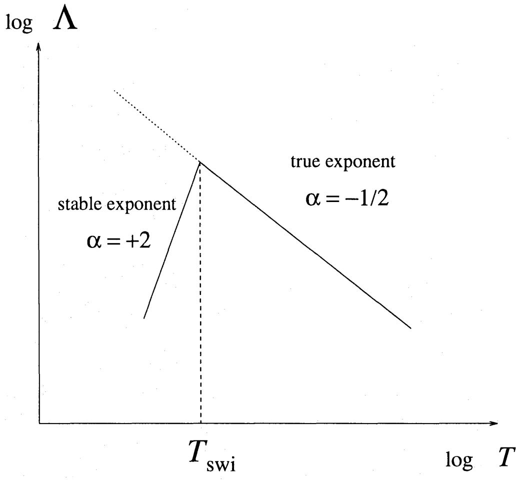

Fig. 7. Modification of the radiative cooling function at low temperatures, to hinder the collapse of the cooling zone

The right column of Fig. 6 shows a calculation with $T_{\rm swi}/T_{\rm eff} = 20$. The collapse is hindered, and the cooling length as well as the structure of the cooling zone agree well with those in the left column of Fig. 6, where the original cooling function with $\alpha = -1/2$ slope has been used on a finer grid.

Since *hot* gas radiates energy according to the original cooling function, the influence of the modified cooling function on the observed X-ray emission from the gas behind strong shocks in time-dependent stellar wind simulations should be small. More critical is the influence of the modification on the total cooling length. Since the material cools inefficiently at low temperatures, the cooling zones might be broadened artificially. We will now show that the influence of the low-temperature $\alpha = 2$ slope on the total cooling length is small.

The time needed for hot, shocked material to cool down again to wind temperature $T_{\rm eff}$ is,

$$t_{\rm c} = \int_{T_{\rm post}}^{T_{\rm eff}} {\rm d}t_{\rm c}. \tag{24}$$

The thermal energy equation for a fluid particle is (with ${\rm d}/{\rm d}t$ the Lagrangian derivative, and $\epsilon = e/\rho$ the specific thermal energy),

$$\rho\frac{{\rm d}\epsilon}{{\rm d}t} = -p\,{\rm div}\,\mathbf{v} - A\rho^2T^\alpha. \tag{25}$$

It is well known (e.g., Langer et al. 1981; CI) that the divergence term in (25) leads to near *pressure constancy* within the cooling zone. We therefore drop this term and instead assume the pressure to be constant,

$$\rho\frac{{\rm d}\epsilon}{{\rm d}t} = -A\rho^2T^\alpha, \qquad \text{with} \qquad p = {\rm const} = p_{\rm post}. \tag{26}$$

This leads to

$$\mathrm{d}t_\mathrm{c} = -\frac{k^2}{\mu^2(\gamma-1)}\, p_\mathrm{post}^{-1}\, \frac{\mathrm{d}T\, T^{1-\alpha}}{A}, \tag{27}$$

where the kinetic equation, $\epsilon = kT/\mu(\gamma-1)$, and the ideal gas equation have been used. The cooling length is

$$L_\mathrm{c} = \int\limits_{T_\mathrm{post}}^{T_\mathrm{eff}} \mathrm{d}t_\mathrm{c}\ \mid v_\mathrm{rel} \mid, \tag{28}$$

where the relative velocity between shock front and material behind the shock, v_rel, can be approximated by v_post, so that

$$L_\mathrm{c} = v_\mathrm{post}\, t_\mathrm{c}. \tag{29}$$

Let R be the ratio of the total cooling length using the modified cooling function to the cooling length using the original cooling function, i.e., without the modification below T_swi. The velocity v_post then cancels in R. Using (23) for the constant $\tilde{A}$, one has

$$R = \frac{\int_{T_\mathrm{post}}^{T_\mathrm{swi}} \mathrm{d}T\, T^{3/2} + \int_{T_\mathrm{swi}}^{T_\mathrm{eff}} \mathrm{d}T\, T^{-1}\, T_\mathrm{swi}^{5/2}}{\int_{T_\mathrm{post}}^{T_\mathrm{eff}} \mathrm{d}T\, T^{3/2}}. \tag{30}$$

Introducing dimensionless quantities,

$$t = T/T_\mathrm{eff}, \qquad t_\mathrm{s} = T_\mathrm{swi}/T_\mathrm{eff}, \qquad t_\mathrm{p} = T_\mathrm{post}/T_\mathrm{eff}, \tag{31}$$

this becomes finally

$$R \; = \; \frac{{t_\mathrm{p}}^{5/2} - {t_\mathrm{s}}^{5/2} + \frac{5}{2}\, {t_\mathrm{s}}^{5/2} \ln t_\mathrm{s}}{{t_\mathrm{p}}^{5/2} - 1}. \tag{32}$$

$$\approx \; 1 + \left(\frac{t_\mathrm{s}}{t_\mathrm{p}}\right)^{5/2} \left[\frac{5}{2}\, \ln t_\mathrm{s} - 1\right], \tag{33}$$

where in the last equation the strong shock approximation, $t_\mathrm{p} \gg 1$, has been used. Table 2 lists R as function of t_p and t_s.

The physical reason for the weak dependence of the total cooling length on T_swi found in Table 2 is that the extent of the cooling zone is fixed mainly by the material immediately behind the shock, which cools according to the original $\alpha = -1/2$ slope: since this material is thin (cooling rate $\sim \rho^2$) and hot (cooling rate $\sim T^{-1/2}$) it cools very inefficiently. Altogether, because of the dominance of the hot post-shock material (i) on the X-ray emission from stellar winds, and (ii) on the total cooling length, the modification of the cooling function below T_swi has actually only little influence on the model results.

Finally, we note that the $\alpha = 2$ slope below T_swi also hinders the collapse of the cooling zone due to the positive feedback between diffusive errors and enhanced radiative cooling at the *cold edge* of the cooling zone: As was shown by Field (1965), runaway cooling only occurs for $\alpha < 2$ if the gas cools isobarically. By this, using $\alpha = 2$, cooler material no longer cools more efficiently. Therefore, the cold edge remains smeared out, instead of being steepened again (which would cause new advective errors, and the edge to "eat" into the cooling zone).

Table 2. Dependence of the total cooling length on the temperature T_swi. R is the ratio of the cooling length using a modified cooling function below T_swi to the true cooling length.

$T_\mathrm{post}/T_\mathrm{eff}$	$T_\mathrm{swi}/T_\mathrm{eff}$	$R = \frac{L_{c,\mathrm{swi}}}{L_{c,\mathrm{true}}}$
300	10	1
	20	1
	30	1
200	10	1
	20	1
	30	1.1
100	10	1
	20	1.1
	30	1.4
50	10	1.1
	20	1.7
	30	3.1
40	10	1.1
	20	2.1
	30	4.7
30	10	1.3
	20	3.4
	30	8.5

5. Wind models including energy transfer

In this section, we use the same stellar, wind, and numerical parameters as in Sect. 3, and discuss three different wind models:

1. A model using the radiative cooling function (16) with an overall $\alpha = -1/2$ slope.
2. A model where this slope is changed to be $\alpha = +2$ below $T_\mathrm{swi}/T_\mathrm{eff} = 10$.
3. The same model as in 2, but with an amplitude of the photospheric sound wave of 25% instead of 1%.

5.1. *Estimate of cooling lengths*

We use Eq. (A9) from appendix A to estimate whether the spatial grid in wind simulations is fine enough to resolve typical stationary cooling zones. With the parameters from Table 1 we find

$$\frac{L_\mathrm{c}}{R_*} = 1.47\, 10^{-7}\, \frac{r^2}{R_*^2} \left(1 - \frac{R_*}{r}\right)^{\beta} \frac{(T_\mathrm{post}/T_\mathrm{eff})^2}{\rho_\mathrm{pre}/\rho_\mathrm{stat}}. \tag{34}$$

We use $\beta = 0.8$ (Pauldrach et al. 1986) for the underlying mean wind velocity law. Actually, the stationary velocity run in the snapshots of the wind structure in Figs. 1, 2, 8, etc. is, beyond the sonic point, the one of a $\beta = 0.8$ law. Table 3 lists the total cooling length (34) as function of the post-shock temperature and the depletion of the wind material relative to a stationary wind model, at the location $r = 4\, R_*$. The number of grid points per cooling zone is given in brackets. According to this table, *all* stationary cooling zones behind *strong* shocks should be resolved on the grid.

Table 3. Total cooling length (in units of R_*) as function of the post-shock temperature and the depletion of the wind material relative to a stationary wind model, at the location $r = 4\,R_*$. The number of grid points per cooling zone is given in brackets.

	$\frac{T_{\rm post}}{T_{\rm eff}}$=25	50	100	200
$\frac{\rho_{\rm pre}}{\rho_{\rm stat}}$=1	0.0012 (0.4)	0.0047 (1.5)	0.019 (6)	0.075 (24)
1/10	0.012 (4)	0.047 (15)	0.19 (62)	0.75 (240)
1/100	0.12 (39)	0.47 (150)	1.9 (620)	7.5 (2400)

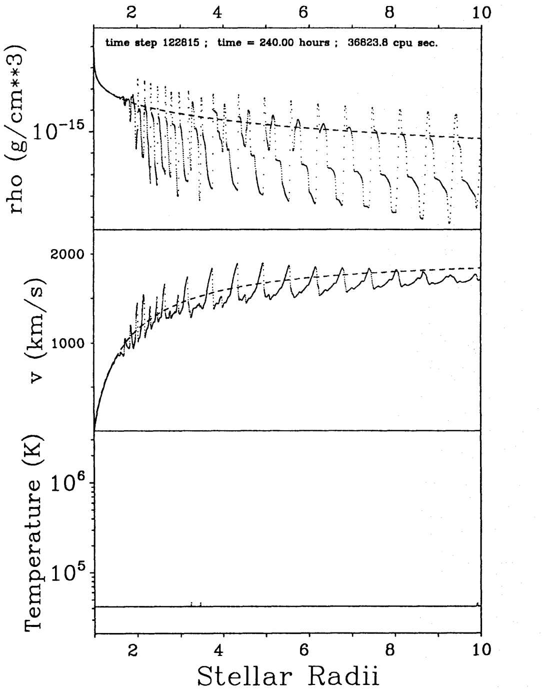

Fig. 8. Snapshot of the wind structure with energy equation included, but without modifying the cooling function at low temperatures. All cooling zones behind shocks are collapsed

5.2. The wind models

Figure 8 shows a snapshot of the wind 10 days after model start. The cooling function used is the one of Eqs. (16) and (17). Figure 9 shows the subsequent evolution of the density in the course of 20 000 s, i.e., four cycles of the photospheric sound wave.

No cooling layers behind shock fronts are resolved in Fig. 8. (Since already in this snapshot no hot gas is present, we do not show the run of temperature during the wind evolution in Fig. 9.) This is in accord with our expectation of the cooling zones' collapse. In Figs. 10 and 11 then, where a modified cooling function is used below $T_{\rm swi}/T_{\rm eff} = 10$, i.e., 420,000 K, this collapse is hindered and the cooling zones are well resolved. Figure 1 and Fig. 8 show almost identical wind structures; this is clear from the fact that both models are *isothermal* calculations in the end. (Small differences occur in extremely rarefied intershell regions, which contain hardly any material.)

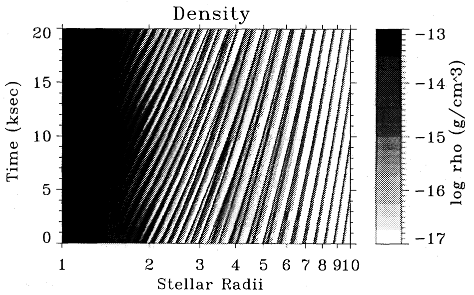

Fig. 9. Evolution of the wind structure from Fig. 8 (using an unmodified cooling function with slope $\alpha = -1/2$) during the next 20 000 s, i.e., 4 cycles of the photospheric sound wave

Up to about 4.5 to 5 R_*, the isothermal wind model(s) and the model with resolved cooling zones are also very similar. The reason is that the cooling zones are short compared with dynamical length scales, which supports the assumption of dynamical isothermality for dense supergiant winds in this spatial domain.

However, the cooling layers in this model are (much) shorter than what would be expected from Table 3. This is (mainly) due to the fact that the *dynamical* time required to deplete the intershell regions by adding the material located there to the narrow shells (which is accomplished by the radiative shocks) is shorter than the *cooling* time. The analytical solution for a *stationary* cooling zone from Appendix A therefore does not apply. Due to this intershell depletion, the pre-shock density becomes smaller with time, so that a broader cooling zone has to be established. The time necessary for this is of the order of the period of the thermal instability oscillation – which in turn is a few cooling times –, i.e., (much) larger than the dynamical time. Therefore, the cooling zones lag behind the actual dynamical situation, and one should observe them to be *shorter* than stationary cooling zones – as is actually the case.

Beyond about 5 R_*, the model with energy transfer differs drastically from the isothermal model. Consider the four rarefied intershell regions marked (a) to (d) in Fig. 10. It is within this sequence that *all* shocks in the wind are destroyed, leaving behind only *previously* heated material: At (a), a pronounced radiative shock is present; the material is heated in a front, and afterwards cools by radiative energy losses. Since the cooling zone is approximately isobaric, the density rises with falling temperature, which leads to the final compression of the material into a narrow, dense shell. From (a) to (b), the pre-shock density drops by about a factor of 6 due to the intershell depletion. This causes a broadening of the cooling layer, whereby

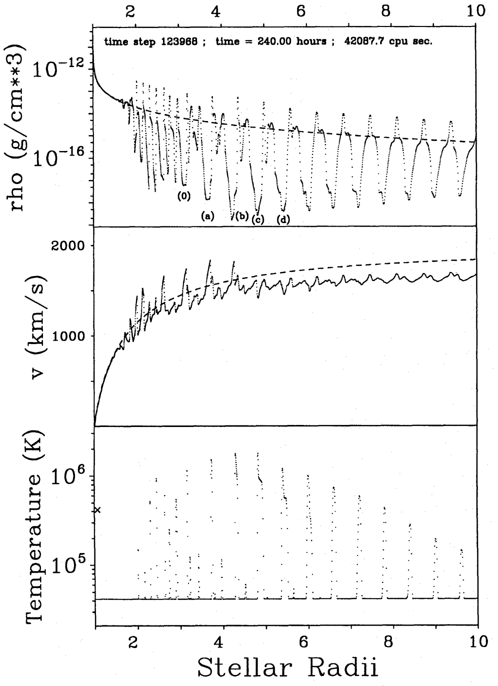

Fig. 10. Snapshot of the wind structure, where the cooling function is modified below $T_{\rm swi}/T_{\rm eff} = 10$ to have a slope $\alpha = 2$. The cross near the temperature axis indicates $T_{\rm swi}$

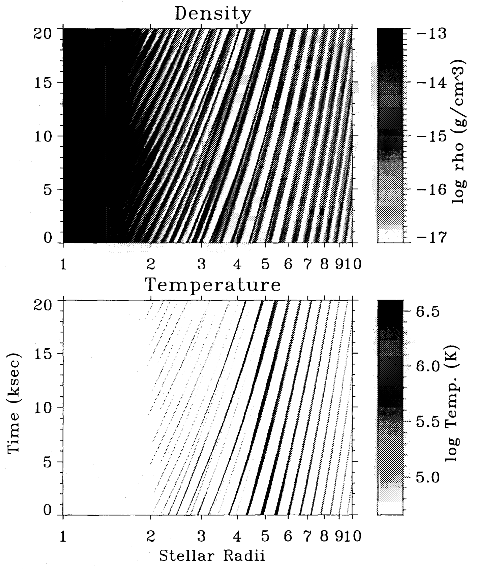

Fig. 11. Evolution during the next 20 000 seconds (after t = 10 days) of the model with $T_{\rm swi}/T_{\rm eff} = 10$ and amplitude $A = 1\%$

the shock front is driven in the direction of smaller radii, into the unshocked material. The pre-shock velocity and post-shock temperature therefore get slightly larger from (a) to (b). However, for later times the inward moving front passes regions of always slower material, until finally the front speed equals the speed of the inflowing material and the shock vanishes at (d): the temperature "jump" at (d) is about 10 grid intervals broad, instead of 3 intervals at a shock front; furthermore, no velocity jump is found at (d). The propagation of the front to smaller radii is directly seen in the sequence from (b) to (d), where the shock passes from the right side of the density minimum of the intershell region to its left side. The hot material at (d) (and at all larger radii) is the *remnant* of *previously* shock-heated material. This interpretation is supported by the fact that the density and temperature at (d) and at all larger radii are anti-correlated, as is the case in the isobaric radiative cooling zone behind a shock. The hot material then cools steadily by radiative energy losses and spherical expansion work during its further advection to larger radii. (We finally note that due to intershell depletion, the cooling zone at (a) is already broader than the corresponding one at (0); but not yet broad enough to destroy the shock front.)

The observational consequences of this shock destruction for the X-ray emission properties can only be tested by quantitative modeling of the X-ray spectra from structured wind models – this work is in progress now. We recall that already in the isothermal wind model shock *decay* (as opposed to shock destruction) sets in at about 5 R_*. In all models up to now therefore the bulk of X-ray emitting material is at small radii. This is in contrast to what is derived from ROSAT X-ray observations: Hillier et al. (1993) find that in the wind of ζ Pup, material with temperatures $T = 3\,10^6$ K has to be present up to radii of 20 to 50 R_*. One reason for the failure of our models to produce hot material beyond a few R_* is the small amplitude of only 1% of the photospheric sound wave. This will be seen below from a model with an amplitude of 25%. Besides that, the period of the sound wave also has an influence on the maximum temperatures that occur (Owocki 1992; Feldmeier 1993): for large periods, the shell distances are larger, and the material in between the shells can be accelerated to higher velocities before it finally encounters a reverse shock. So, at present we do not expect a real conflict between X-ray observations and the time-dependent wind models.

The mean velocity of the model with resolved cooling zones is somewhat smaller than the stationary wind velocity. This is mainly due to the fact that radiative driving is shut off for hot material. Furthermore, shadowing by material close to the star might be slightly more efficient in this model.

Up to about 4 R_* the wind structure in the model with resolved cooling zones seems to be as chaotic as in both isothermal models. However, from Figs. 9 and 11 it is evident that the cause of this are *shell-shell collisions*. The shells are created at $\approx 1.5\,R_*$ in *triples*, where the members of these triples collide

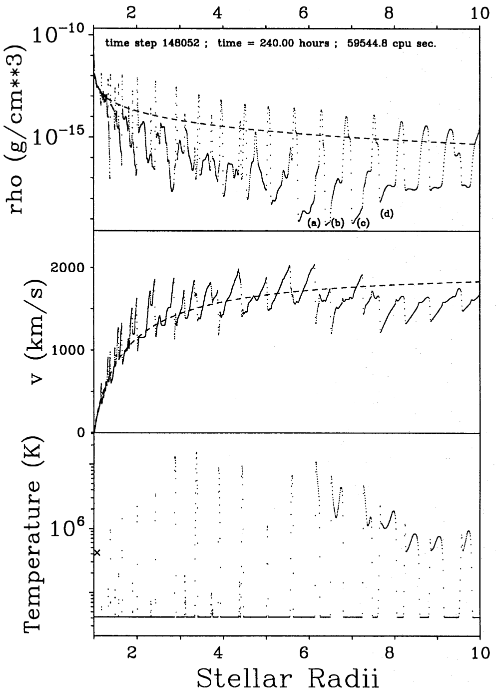

Fig. 12. Wind snapshot using a modified cooling function below $T_{\mathrm{swi}}/T_{\mathrm{eff}} = 10$. The amplitude of the photospheric sound wave is 25% now instead of 1% in the foregoing model

with each other, leaving only one shell per cycle of the photospheric sound wave beyond $\approx 6\,R_*$. There are no collisions between shells steming from subsequent cycles of the sound wave. We note that the shells would not collide if they simply "ride" the wind (Waldron et al. 1992, 1994). For shell collisions to occur, two requirements have to be met: (i) The shells influence each other ("non-local coupling"). This is actually the case in the time-dependent models since shells lying close to the star shadow, and therefore decelerate, shells at larger radii. (ii) The shells do *not* follow each other at constant time intervals. This is realized in the wind because of the triple-wise creation of shells; which, in turn, is connected to the excitation of harmonics of the photospheric sound wave that triggers structure formation. – It is easily seen that if either of these prerequisites is not fulfilled, shell collisions cannot occur; instead, all shells would follow (almost) the same path $r_{\mathrm{shell}}(t)$.

To test the influence of the amplitude A of the photospheric sound wave on the shock strength, Figs. 12 and 13 show a snapshot at t = 10 days and the subsequent evolution over 20 000 s of a model with $A = 25\%$. Maximum temperatures are now a factor of 10 higher than for $A = 1\%$, and reach $2\;10^7$ K between 3 and 6 R_*.

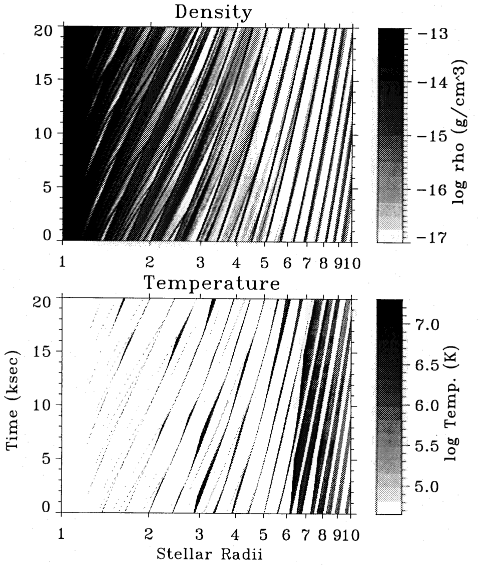

Fig. 13. Evolution during the next 20 000 seconds (after t = 10 days) of the model with amplitude $A = 25\%$

Up to about $6\,R_*$ dynamical isothermality should be a good approximation for this model. However, shock destruction due to the broadening of cooling zones occurs around $\approx 7\,R_*$, see the sequence from (a) to (d) in Fig. 12. At (a) and (b) radiative shocks are found, where the pre-shock density falls by a factor of 16 from (a) to (b). The corresponding broadening of the cooling zone is obvious from the temperature run of Figs. 12 and 13. The shock is driven to smaller radii, until it finally disappears at (d). The velocity jumps separating cold, dense gas from hot, thin gas (formerly heated in shocks) are due to the fact that the hot gas is no longer radiatively driven, wherefore the cold, fast gas rams into it supersonically. (Since post-shock temperatures are much lower in the previous $A = 1\%$ model, the corresponding drop in the radiative acceleration is not so significant there.) These *forward* shocks heat the already hot material to even higher temperatures; thereafter, the gas is cooled and compressed by radiative energy losses. The forward shock transition + radiative cooling zone is best seen in the temperature spike at the left verge of the hot, thin regions at $r > 7.5\,R_*$. (These points were brought to our attention by S. Owocki.) – Note that the hot gas left over at $10\,R_*$ still has a temperature of $\approx 10^6$ K. This is not too different from what is needed to model the ROSAT X-ray observations of ζ Pup (Hillier et al. 1993).

The structure formation in this model sets in closer to the star, at about $1.2\,R_*$ instead of $1.5\,R_*$ in the previous model. The shells are created in *quadruples* close to the star, where the members of these quadruples collide up to $3\,R_*$. There is some dynamical coupling between shells corresponding to *subsequent cycles* of the sound wave now: Relatively dense material in front of the forward shock side of one shell can be accelerated, after which it moves through the strongly rarefied intershell medium and finally collides with the reverse shock side of the next-outer shell. The last shell collisions occur between 6.5 to 7 R_*.

There is a definite temporal *non*-periodicity in Fig. 13. Figures 14 and 15 show the time series of wind velocity at 3 R_* (plotted against the phase of a wave with period $P = 5\,000$ s) and its power spectrum. The time series starts at 7.82 days and ends at 10.00 days, i.e., shows 37.7 wave cycles. The contrast to Figs. 3 and 4 for the time series and spectrum of the model with a base perturbation amplitude of $A = 1\%$ is striking. A major effect in Fig. 14 seems to be a *drift* of the wave. Since in the power spectrum of the $A = 1\%$ model signals (i.e., the harmonics of the sound wave) and noise (if there is any) are separated by 4 orders of magnitude, we must conclude that the "noise" in Fig. 15 has physical meaning and is not caused numerically. The source of this non-periodicity is not exactly clear at the moment, but seems to be connected with the coupling of shells from subsequent wave cycles. It is found (Owocki & Feldmeier, in prep.; Owocki 1995) that *without* any explicit perturbation at the base, *small-scale* structure develops in the wind from about 2 R_* on. This structure also shows a *continuous* spread of wave frequencies. In the cases of no perturbation, a broad-band perturbation, or a large-amplitude periodic perturbation, frequencies over a broad interval may principally grow on equal footing, since: (i) The instability growth rate is constant for all wavelengths shorter than a certain fraction ($\approx \frac{1}{3} \dots \frac{1}{2}$) of the Sobolev length (Owocki & Rybicki 1984, 1985). (ii) For zero perturbation amplitude it seems natural to assume that *numerical noise* (showing a continuous spread of frequencies) is created and amplified. On the other hand, for large base perturbation amplitudes, we speculate that some kind of *overmodulated* amplification occurs, again creating noise.

Whether a periodic or a stochastic ("turbulent") wind structure is realized depends fundamentally on the value of the non-dimensional "Reynolds" number connected with the wind instability. While the radiation field is the central quantity entering this number, to our knowledge no precise definition of the latter has been given up to now. However, the strong periodicity of the wind structure induced by *small* (here: $A = 1\%$) perturbations – as they are considered in *linear* stability analysis – gives a hint that the radiation Reynolds number of our models is still below the threshold(s) required for multi-mode excitation or stochastic behavior.

The question remains whether the contraction and expansion of the cooling zones due to the oscillatory thermal instability can be seen directly in the wind models. The period of this oscillation is $t_{\rm osc} \approx 20\, L_{\rm c}/v_{\rm jump}$, where $L_{\rm c}$ is the cooling length, and $v_{\rm jump}$ is the velocity jump at the shock front. For the model with $A = 1\%$, the oscillation periods should be about 10 to 30 hours, and for the $A = 25\%$ model $\approx$ 3 to 10 h. Each shock in Fig. 11 ($A = 1\%$) could be followed over $\approx$ 7 h, which is *less* than $t_{\rm osc}$. Furthermore, the dynamical time scale for shell-shell collisions, $t_{\rm coll} \approx 5 \dots 6$ h, is shorter than $t_{\rm osc}$. Hence, the thermal oscillation is also unobservable since changes in the shock properties due to shell-shell collisions take place in shorter times than $t_{\rm osc}$. In Fig. 13 for the $A = 25\%$ model, each shock could be followed over almost 15 hours before it is finally destroyed at $\gtrsim 7\, R_*$. During that time, 1 to 2 thermal oscillations should occur. However, $t_{\rm coll}$ is even shorter in this model (shell quadruples instead of triples; interaction between shells from different cycles of the sound wave), and ranges from $\approx$ 1 h close to the star to 4 h at larger distances. The thermal oscillation is therefore interrupted again. – To be more precise, $t_{\rm osc}$ and $t_{\rm coll}$ of the very narrow cooling zones, $L_{\rm c} \approx 0.02\, R_*$, at $\approx 4\, R_*$ are about

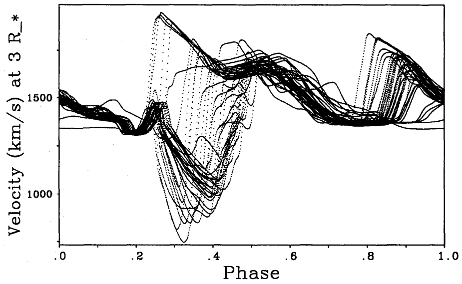

Fig. 14. Time series of the velocity at $r = 3\, R_*$ of the model with base perturbation amplitude $A = 25\%$, plotted against the phase of a wave with period $P = 5\,000$ s. 37.7 wave cycles are shown

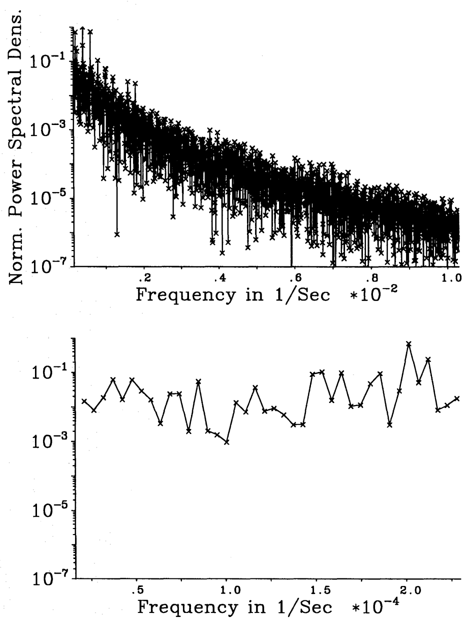

Fig. 15. Power spectrum of the time series of Fig. 14. *Upper panel*: Harmonic domain of the frequency $f = 1/5\,000\,{\rm s}^{-1}$. *Lower panel*: Subharmonic domain

equal (few hours). But these cooling zones are only resolved by ≈ 10 grid points, and numerical insufficiency becomes probable: as is found in simulations of the test flow problem from the previous section, modifying the cooling function below $T_{\rm swi}$ hinders the collapse of the cooling zone during the *first* oscillation cycle. Thereafter, a more or less *stationary* cooling zone often remains. Furthermore, we observed a strong damping of the thermal oscillation due to the *advection* of the shock across the numerical grid.

In summary, we believe that a mixture of physical and numerical effects causes the thermal oscillation to be unobservable in our calculations.

6. Summary

In this paper we have discussed time-dependent radiation driven winds of hot, luminous stars, where flow structures are due to the nonlinear, unstable growth of initially small, periodic base perturbations. We have found the following results for the fully developed wind structure:

1. Our models are in good general agreement with the ones by OCR and Owocki (1992, 1994): The wind consists of a sequence of dense, narrow shells which are enclosed by a reverse shock at the starward-facing side and by a forward shock at the outer side. The reverse shocks can have Mach numbers from 30 to 100, implying density contrasts of up to 10^3 to 10^4. The latter value is close to the principal upper limit for a wind with Mach number ≈ 100. The jump velocities of about 500 km/s at the reverse shocks agree well with the shock temperatures of some million degrees K as deduced from X-ray data (Cassinelli & Swank 1983; Hillier et al. 1993).

2. Shell-shell collisions are frequent up to $6 \dots 7\,R_*$. For these collisions to occur, it is necessary: (i) that the shells influence each other, e.g., by shadowing of the radiation field; and (ii) that the shells do not follow each other at constant time intervals.

3. The wind structure induced by a periodic base perturbation of *small amplitude* is also periodic. The power spectra of long time series of hydrodynamical quantities at fixed locations in the wind indicate the existence of only *discrete* harmonics (up to 50 and more) in this case. In contrast, for a *large amplitude* base perturbation, and also for the case of *no* explicit perturbation at all, the power spectra of the wind structure show a continuous spread of excited frequencies. The hierarchy of shock-shock mergers (or, stated differently: shell-shell collisions) occuring then resembles the picture of *compressible turbulence* as discussed by Burgers (1950) and Tatsumi & Tokunaga (1974). Empirical evidence for turbulence in dense Wolf-Rayet star winds in the form of a mass hierarchy of clumps is described by Moffat (1994a,b).

4. Inclusion of *energy transfer* in the hydrodynamical simulations results in the numerical shortcoming that no radiative cooling zones are resolved. The main cause of this collapse is the oscillatory thermal instability of Langer et al. (1981, 1982). During the *contraction* phase of this oscillation, the extent of the cooling zone may fall below the grid resolution. Consequently, the numerics "forgets" about the existence of the cooling zone, and the shock becomes a numerical isothermal shock. The reversible oscillation has turned into an irreversible collapse. – Furthermore, at the cold, dense end of the cooling zone, a positive feedback between advective diffusion errors and radiative cooling might occur. This leads to an "eating" of the cold edge into the cooling layer, accelerating the destruction of the latter.

5. Both the collapse caused by the oscillatory thermal instability and by the advective diffusion can be hindered by modifying the cooling function at low temperatures. Because the extent of the cooling zone is predominantly fixed by the hot and thin post-shock material – which is also responsible for the X-ray emission –, this modification at low temperatures has minor influence on the derived model results.

6. Up to about 5 to $7\,R_*$ (where the exact value depends on the base perturbation), the assumption of dynamical isothermality is found to be valid in our models of an O supergiant wind: radiative cooling zones behind strong shocks are short compared with dynamical length scales, and therefore have little influence on the wind dynamics. However, beyond these radii dynamical isothermality breaks down completely: all reverse shocks are quickly destroyed due to a broadening of the cooling zone, leaving behind previously heated hot, thin material. This material cools on its further advection through the wind. The question arises whether there is enough hot gas left at large radii to account for the observed soft X-ray component.

7. Quite independent of the amplitude of the base perturbation, the final shell-shell collisions occur between 6 to $7\,R_*$. Together with the results from the item (6) above, the wind can therefore be divided roughly into two distinct regions: an inner, active one with frequent radiative shocks, where shell-shell collisions occur; and an outer, quiescent region with "old" hot material left over from former shock heating, and where the shells follow each other without further collisions. Since the wind dynamics is rather predictable at large radii, the results computed explicitly here up to $10\,R_*$ could be extrapolated to larger distances from the star (e.g., to permit the calculation of X-ray spectra from a very large volume of the wind).

Our two main directions for *future work* on the radiation hydrodynamics of hot star winds are the following:

(I) While the modification of the cooling function below $T_{\rm swi}$ can hinder the collapse of cooling zones, we also plan to incorporate a *local mesh refinement* method (Berger & Oliger 1984; Berger & Colella 1989) in our code as an independent way to avoid the collapse. Applying the latter method, two other resolution problems occuring in time-dependent wind calculations could possibly be solved too: (i) The dense shells, in which most of the wind mass is localized, are poorly resolved in present calculations. (ii) The arbitrary exponential truncation of the line distribution function at $\kappa_{\rm max}$ is needed to artificially suppress unstable growth on very short length scales. The correct treatment of the latter small-scale structure might influence the large-scale dynamics of the wind, as is well known from turbulent flows.

(II) At present, using the SSF method, the source function is not calculated consistently from the actual wind dynamics. In particular, the perturbation of the diffuse radiation field is not accounted for. As found by Owocki & Rybicki (1985), this perturbation has a large influence on the phase relationship between perturbations in velocity, density, and the radiative force, i.e., on the propagation and growth characteristics of waves in the wind (a fact recently emphasised by Puls 1993). For wavelengths on the order of the Sobolev length, *correlated* density and velocity perturbations may thereby grow at an enhanced rate. These *outward* propagating sound waves ultimately steepen into *forward* shocks. It is not quite clear at the moment whether the nonlinear growth of these waves saturates more quickly than the growth of inward propagating waves – so that reverse shocks still would dominate the wind structure –, or whether forward and reverse shocks possibly are of about equal strength in the fully developed wind structure.

Finally, *diagnostic tools* to analyze the degree to which these hydrodynamical models can reproduce the observed variability features of hot star winds are currently being developed in the X-ray domain (Hillier et al. 1993; Pauldrach et al. 1994a,b; Cooper & Owocki 1994; Feldmeier et al., in prep.) and for UV and optical spectral lines (Puls et al. 1993b, 1994). Only by detailed comparison between observed and computed diagnostics can we learn which dynamical structures out of a variety of theoretically possible ones are actually realized in these winds.

Acknowledgements. I wish to thank Drs. S. Owocki, J. Puls, A. Pauldrach, R.-P. Kudritzki, A. Fullerton, L. Lucy, and G. Cooper for many interesting discussions. Special thanks go to C. Reile for many stimulating and helpful discussions on (numerical) hydrodynamics. J. Puls, A. Fullerton, and R.-P. Kudritzki are thanked for carefully reading the manuscript. This work was supported by the DFG in the "Gerhard-Hess-Programm" under contract Pa 477/1-1. The calculations were performed on a Cray Y-MP at the Leibniz-Rechenzentrum in München.

Appendix A: estimate of the cooling length

The radiative cooling function in the form defined by Chevalier & Imamura (1982; CI) is,

$$\Lambda = \rho^2 A_{\rm CI} \left(\frac{p}{\rho}\right)^{\alpha} . \tag{A1}$$

Consider the flow problem of Sect. 4.1, where an ideal gas streams highly supersonically against a wall. The analytical solution for the stationary, plane-parallel cooling zone, assuming a cooling exponent $\alpha = -1/2$, is

$$\begin{aligned} \xi = \left(\frac{93\sqrt{3}}{320} - \frac{\pi}{8}\right)^{-1} \Bigg\{ & \frac{\sqrt{-w - w^2}}{20} \times \\ & (15 - 10w + 8w^2 - 464w^3 - 512w^4) \\ & - \frac{3}{8} \arccos(1 + 2w) \Bigg\}, \end{aligned} \tag{A2}$$

with the total cooling length,

$$L_{\rm c} = \frac{1}{32} \left(\frac{93\sqrt{3}}{320} - \frac{\pi}{8}\right) \frac{v_{\rm pre}^4}{A_{\rm CI}\, \rho_{\rm pre}}, \tag{A3}$$

and the total cooling time,

$$t_{\rm c} = \frac{5}{224} \frac{v_{\rm pre}^3}{A_{\rm CI}\, \rho_{\rm pre}}. \tag{A4}$$

Here, $\xi = x/L_{\rm c}$ is the normalized spatial variable, and $w = v/v_{\rm pre}$ is the normalized velocity. $\xi = 1$ is the position of the shock front, with $\xi = 0$ the location of the wall, where the cooled gas accretes in an infinitely thin, infinitely dense layer. $\rho_{\rm pre}$ and $v_{\rm pre}$ are the pre-shock density and velocity, respectively. We follow the convention of CI to take $v_{\rm pre}$ as a *positive* quantity, whereas the velocity v itself is a negative quantity; therefore, w is always negative.

To estimate the extent of the stationary cooling layer behind a stellar wind shock, we change from the above CI definition of the cooling function to the standard definition (cf. Raymond et al. 1976),

$$\Lambda = N_{\rm e} N_{\rm H} A_{\rm R}\, T^{\alpha}, \tag{A5}$$

so that

$$A_{\rm CI} = \frac{N_{\rm e} N_{\rm H}}{\rho^2} \left(\frac{\mu}{k}\right)^{\alpha} A_{\rm R}. \tag{A6}$$

Let $I_{\rm H}$ and $I_{\rm He}$ be the hydrogen and helium ionization degrees, and $Y = N_{\rm He}/N_{\rm H}$ be the helium fraction by number. Using (i) the strong shock jump conditions, (ii) the continuity equation for a stationary wind, (iii) a β-velocity law $v_{\rm stat} = v_\infty\, [1-(R_*/r)]^{\beta}$, and (iv) the fit (16), (17) to the cooling function, one finds from (A3) that

$$\begin{aligned} \frac{L_{\rm c}}{R_*} = {} & 1.58\, 10^{-17}\, C\, \frac{T_{\rm eff}^2 v_\infty R_*}{\dot{M}} \times \\ & \frac{r^2}{R_*^2} \left(1 - \frac{R_*}{r}\right)^{\beta} \frac{(T_{\rm post}/T_{\rm eff})^2}{\rho_{\rm pre}/\rho_{\rm stat}}, \end{aligned} \tag{A7}$$

where a constant C of order unity has been introduced,

$$C = \frac{(1 + I_{\rm H} + Y(1 + I_{\rm He}))^{3/2}(1 + 4Y)^{1/2}}{I_{\rm H} + I_{\rm He} Y}. \tag{A8}$$

This can also be expressed in typical units for an O supergiant wind,

$$\begin{aligned} \frac{L_{\rm c}}{R_*} = {} & 1.74\, 10^{-10}\, C \left(\frac{T_{\rm eff}}{10\,000\,{\rm K}}\right)^2 \times \\ & \frac{v_\infty}{1\,000\,{\rm km\,s^{-1}}} \left(\frac{\dot{M}}{10^{-6} M_\odot {\rm yr}^{-1}}\right)^{-1} \frac{R_*}{R_\odot} \times \\ & \frac{r^2}{R_*^2} \left(1 - \frac{R_*}{r}\right)^{\beta} \frac{(T_{\rm post}/T_{\rm eff})^2}{\rho_{\rm pre}/\rho_{\rm stat}}. \end{aligned} \tag{A9}$$

The *total* cooling length (A3) is now compared with the common estimate

$$L_{\rm c}^{1/{\rm e}} \approx -\frac{e}{\dot{e}}\, v_{\rm post}, \tag{A10}$$

where $\dot{e}$ is the energy loss due to radiative cooling. Using the strong shock conditions again, this leads to

$$L_{\rm c}^{1/e} = \frac{9\sqrt{3}}{2048}\,\frac{v_{\rm pre}^4}{A_{\rm CI}\,\rho_{\rm pre}}. \tag{A11}$$

This is a factor of 2.2 *larger* than the *total* cooling length (A3). The reason is that Field's (1965) thermal runaway is not included in the estimate (A10): the latter assumes "only" an exponentially growing cooling rate, whereas due to the runaway the slope in density and temperature at the end of the cooling zone is infinite.

Appendix B: radiative cooling within the viscous shock layer

The viscous layer of a strong shock has a thickness on the order of a particle mean free path. Competing with this is the length scale, over which radiative energy exchange plays a role, which is given by the usually much larger mean free path of a photon (cf. Zel'dovich & Raizer 1967, Sect. 14). Therefore, the viscous layer of a radiative shock (= shock front + cooling zone) is usually much narrower than the radiative cooling zone, over which the shock heated gas loses its thermal energy again. In contrast, for a *numerical* shock the viscous layer is smeared out over a few grid points by artificial viscosity, or by the numerical diffusivity of the scheme. It is therefore possible that the cooling layer becomes shorter than the viscous layer.

For a sufficiently small cooling exponent α (for the exact value see below) the material within this viscous layer, where $T < T_{\rm post}$, cools more efficiently than the post-shock material. If the cooling time within the shock front is shorter than the time it takes the particle to pass the front, severe numerical errors in the structure of the radiative shock will occur. Enhanced cooling within the viscous layer may therefore be the reason for the collapsed cooling zones in stellar wind simulations.

However, we show in this appendix: For a cooling exponent $\alpha = -1/2$, and for a post-shock cooling layer which is broader than the shock front, radiative cooling within the latter is of minor importance. Therefore, cooling zones which are principally resolved on the grid, i.e., are at least of the thickness of the viscous layer, are free of the numerical defect of enhanced cooling.

Let $\tau_{\rm c,vis}$ be the local cooling time for a fluid particle at a certain location within the viscous layer. (We use the abbreviation "vis" for quantities within this layer.) Let $\langle\tau_{\rm c,vis}\rangle$ be the cooling time of this particle, averaged over its trajectory through the front, and let $\tau_{\rm c,post}$ be the cooling time corresponding to the post-shock temperature. Finally, let $t_{\rm cross}$ be the time it takes the particle to cross the viscous layer. Then, if

$$\frac{\langle\tau_{\rm c,vis}\rangle}{t_{\rm cross}} = \kappa_{\rm c}\,\frac{\tau_{\rm c,post}}{t_{\rm cross}} \le F, \tag{B1}$$

where $\kappa_{\rm c} = \langle\tau_{\rm c,vis}\rangle/\tau_{\rm c,post}$, and F is a number of order unity, cooling within the shock front will influence the appearance of the radiative shock.

Mihalas & Mihalas (1984, p. 243), give the temperature stratification within the viscous layer,

$$\frac{T(v)}{T_{\rm pre}} = 1 + (\gamma - 1)\frac{v_{\rm h} - v}{v_{\rm h}} + \frac{1}{2}\gamma(\gamma - 1)\left(\frac{v_{\rm h} - v}{a_{\rm pre}}\right)^2, \tag{B2}$$

where $v_{\rm h}$ is the *upstream* velocity (i.e., the high velocity at the shock), and $a_{\rm pre}$ is the sound speed at the pre-shock side. For a strong shock and $\gamma = 5/3$, we have then (with $v_{\rm vis}$ the velocity *relative* to the shock front),

$$T = \frac{1}{3}\frac{\mu}{k}(v_{\rm h} - v)^2 = \frac{1}{3}\frac{\mu}{k}(v_{\rm pre} - v_{\rm vis})^2. \tag{B3}$$

Behind the shock, we have the well-known relation,

$$T_{\rm post} = \frac{1}{3}\frac{\mu}{k}v_{\rm jump}^2. \tag{B4}$$

Since we allow for radiative cooling within the viscous layer, Eq. (B3), which was derived for a purely viscous layer, is only approximately valid.

The velocity run within the front is approximately linear. Therefore, the flow time for a particle through this layer (of thickness δ) is,

$$t_{\rm cross} = \int_0^\delta \frac{{\rm d}x}{v_{\rm vis}} = \int_0^\delta \frac{{\rm d}x}{v_{\rm pre}(1 - \frac{3}{4}\frac{x}{\delta})} = \frac{\delta}{v_{\rm jump}}\ln 4. \tag{B5}$$

Here, $v_{\rm post} = \frac{1}{4}v_{\rm pre} = \frac{1}{3}v_{\rm jump}$ was used for a strong $\gamma = 5/3$ shock. $t_{\rm cross}$ is short compared with dynamical times, i.e., stationarity and plane-parallel geometry can be assumed,

$$\frac{\rho_{\rm vis}}{\rho_{\rm post}} = \frac{v_{\rm post}}{v_{\rm vis}}. \tag{B6}$$

The cooling time is of the order

$$\tau_{\rm c} \equiv -\frac{e}{\dot{e}} = \frac{3}{2}\frac{k}{\mu}\frac{T^{1-\alpha}}{A\rho}, \tag{B7}$$

hence the ratio of the local cooling time inside the front to the post-shock cooling time is given by

$$\frac{\tau_{\rm c,vis}}{\tau_{\rm c,post}} = \left(\frac{T_{\rm vis}}{T_{\rm post}}\right)^{1-\alpha}\frac{\rho_{\rm post}}{\rho_{\rm vis}}. \tag{B8}$$

Collecting these results together, one has

$$\begin{aligned}\kappa_{\rm c} &= \frac{1}{t_{\rm cross}}\int_0^{t_{\rm cross}} \frac{\tau_{\rm c,vis}(t)}{\tau_{\rm c,post}}\,{\rm d}t \\ &= \frac{1}{t_{\rm cross}}\int_0^{\delta}\left(\frac{v_{\rm pre} - v_{\rm vis}}{v_{\rm jump}}\right)^{2-2\alpha}\frac{v_{\rm vis}}{v_{\rm post}}\,\frac{{\rm d}x}{v_{\rm vis}} \\ &= \frac{3}{\ln 4}\,\frac{1}{3 - 2\alpha}.\end{aligned} \tag{B9}$$

Here, it has been assumed that $\alpha < 3/2$: for larger values of α the integral diverges since the average cooling time inside the shock goes to ∞. From (B9) it follows that only for $\alpha < \frac{3}{2}(1 - \frac{1}{\ln 4}) \approx 0.418$ is $\kappa_c < 1$: Only for these values of α the averaged cooling time within the front is shorter than the post-shock cooling time.

For a cooling exponent $\alpha = -1/2$ one has from (B9),

$$\kappa_c \approx 0.541, \tag{B10}$$

i.e., $\alpha = -1/2$ is still not critical for enhanced cooling within the shock front, since the cooling time is on average only a factor of ≈ 0.541 shorter than the post-shock cooling time.

From (B1) one has, again using $\alpha = -1/2$, that cooling inside the viscous layer may modify the structure of the whole radiative shock only for

$$\tau_{c,\mathrm{post}} \le 2.56\, F \frac{\delta}{v_{\mathrm{jump}}} \tag{B11}$$

The post-shock cooling length is of the order

$$L_{c,\mathrm{post}} = \tau_{c,\mathrm{post}} \cdot v_{\mathrm{post}}, \tag{B12}$$

therefore only shocks with a radiative cooling zone of extent

$$\frac{L_{c,\mathrm{post}}}{\delta} \le 0.86\, F \tag{B13}$$

can be influenced by this defect. Since $F \approx 1$, this is no limitation at all. Radiative cooling within the viscous layer is therefore of no importance for those cooling zones which are principally resolved on the numerical grid.

Appendix C: resolution of the dense, cold domain of a radiative shock

Within a radiative cooling zone, Field's (1965) local thermal instability will generally occur: The subsonic post-shock domain is nearly isobaric (pressure differences will be compensated by sound waves), so that *cooling* leads to a *compression* of the gas. For isobaric cooling and a cooling exponent $\alpha < 2$ (Field 1965), material cools more efficiently at lower temperatures. This implies a *cooling runaway*, which shows up in the stationary CI-solutions for the radiative cooling zones in the infinite density and temperature gradients at the very end of the cooling zone (termed "ce", *cold edge*, in the following). This appendix deals with the numerical resolution of the infinite gradients at the "cold edge". For this, we demand the density to change from one grid point to the next by at most a factor of $F = O(1 \ldots 10)$. If i denotes the grid index, this implies

$$\frac{\rho_{i+1} - \rho_i}{\rho_i}\Big|_{\mathrm{ce}} \approx \frac{\rho_i' \cdot (x_{i+1} - x_i)}{\rho_i}\Big|_{\mathrm{ce}} \le F, \tag{C1}$$

The flow within the cooling zone is assumed to be stationary and plane-parallel, $\mathrm{d}_x(\rho v) = 0$, hence $(\rho'/\rho)|_{\mathrm{ce}} = (v'/v)|_{\mathrm{ce}}$ (a minus sign has been dropped which is of no significance in the following). With the normalized variables w and ξ from appendix A, the velocity gradient is given by

$$\frac{\mathrm{d}v}{\mathrm{d}x} = \frac{\mathrm{d}(w v_{\mathrm{pre}})}{\mathrm{d}(\xi L_c)} = \frac{v_{\mathrm{pre}}}{L_c} \left(\frac{\mathrm{d}\xi}{\mathrm{d}w}\right)^{-1}, \tag{C2}$$

The differential $\mathrm{d}\xi/\mathrm{d}w$ can be calculated from Eq. (A2). Since, for strong shocks, $w_{\mathrm{ce}} \to 0$, only the lowest order in w is kept. From (A2) it is

$$\frac{\mathrm{d}\xi}{\mathrm{d}w}\Big|_{w\to 0} = 722.82\, w^{2-\alpha}. \tag{C3}$$

Furthermore,

$$\Delta x_{\mathrm{ce}} \le \frac{F\rho_{\mathrm{ce}}}{\rho'_{\mathrm{ce}}} = \frac{F v_{\mathrm{ce}}}{v'_{\mathrm{ce}}} = \frac{F v_{\mathrm{ce}} L_c}{v_{\mathrm{pre}}} \frac{\mathrm{d}\xi}{\mathrm{d}w}\Big|_{\mathrm{ce}}. \tag{C4}$$

The radiative shock can be considered as an *isothermal* jump. Using the corresponding jump conditions ($\mathrm{Ma}_{\mathrm{iso}}$ being the isothermal Mach number), we have

$$\frac{\rho_{\mathrm{ce}}}{\rho_{\mathrm{pre}}} = \mathrm{Ma}_{\mathrm{iso}}^2 = \frac{v_{\mathrm{pre}}}{v_{\mathrm{ce}}} = w_{\mathrm{ce}}^{-1}, \tag{C5}$$

and therefore

$$\Delta x_{\mathrm{ce}} \le \frac{F L_c C}{\mathrm{Ma}_{\mathrm{iso}}^{6-2\alpha}}. \tag{C6}$$

This is the expression for the grid resolution necessary to resolve the cold edge of the radiative shock.

Assuming $F = 10$, $\alpha = -1/2$, an equidistant spatial grid from 1 to 10 stellar radii, and a shock with cooling length $L_c = 0.1\, R_*$ and Mach number $\mathrm{Ma}_{\mathrm{iso}} = 10$ (resp. 30), a total of $1.2\,10^5$ (resp. $2.7\,10^8$) grid points would then be needed to resolve the cold edge. These numbers are far beyond present computational capabilities. – In contrast, Fig. 5 shows a stationary cooling zone for $\alpha = 1$, $L_c = 1$, $\mathrm{Ma}_{\mathrm{iso}} = \sqrt{20}$, where only 1 point per L_c should guarantee resolution. Instead, 50 grid points per L_c were used in this calculation.

We conclude that in wind calculations it is not possible to resolve the domain of steep gradients that define the end of the radiative cooling zones. This is a further justification for modifying the cooling function at low temperatures to hinder the collapse of the cooling layer, since this low temperature domain cannot be handled correctly anyway. On the other hand, a *conservative* numerical scheme always guarantees the correct total *jumps* in the hydrodynamical quantities across a radiative shock.

References

Abbott D.C., 1980, ApJ 242, 1183

Abbott D.C., 1982, ApJ 259, 282

Abbott D.C., Bieging J.H., Churchwell E., 1981, ApJ 250, 645

Abbott D.C., Telesco C.M., Wolff S.C., 1984a, ApJ 279, 225

Abbott D.C., Bieging J.H., Churchwell E., 1984b, ApJ 280, 671

Baade D., 1991, in: Baade D. (ed.) ESO Conference Proc. 36, Rapid Variability of OB-Stars. ESO, Garching, p. 217

Baade D., Lucy L.B., 1987, A&A 178, 213

Berger M.J., Colella P., 1989, J. Comp. Phys. 82, 64

Berger M.J., Oliger J., 1984, J. Comp. Phys. 53, 484

Bertschinger E., 1986, ApJ 304, 154

Bieging J.H., Abbott D.C., Churchwell E.B., 1989, ApJ 340, 518

Burgers J.M., 1950, Proc. Acad. Sci. Amst. 53, 732

Carlberg R.G., 1980, ApJ 241, 1131

Cassinelli J.P., Olson G.L., 1979, ApJ 229, 304

Cassinelli J.P., Swank J.H., 1983, ApJ 271, 681

Cassinelli J.P., Cohen D.H., MacFarlane J.J., Sanders W.T., Welsh B.Y., 1994, ApJ 421, 705

Castor J.I., Abbott D.C., Klein R.I., 1975, ApJ 195, 157

Chandrasekhar S., 1961, Hydrodynamic and Hydromagnetic Stability. Oxford Univ. Press, Oxford

Chevalier R.A., Imamura J.N., 1982, ApJ 261, 543 (CI)

Chlebowski T., 1989, ApJ 342, 1091

Chlebowski T., Harnden F.R., Sciortino S., 1989, ApJ 341, 427

Colella P., Woodward P.R., 1984, J. Comp. Phys. 54, 174

Cooper R.G., 1994, PhD thesis, University of Delaware

Cooper R.G., Owocki S.P., 1992, in: Drissen L., Leitherer C., Nota A. (eds.) ASP Conference Series 22, Nonisotropic and Variable Outflows from Stars. ASP, San Francisco, p. 281

Cooper R.G., Owocki S.P., 1994, in: Moffat A.F.J., Fullerton A.W., Owocki S.P., St-Louis N. (eds.) Instability and Variability of Hot Star Winds. Kluwer, Dordrecht (in press)

Courant R., Friedrichs K.O., 1948, Supersonic Flow and Shock Waves. Interscience Publishers, New York

Courant R., Friedrichs K.O., Lewy H., 1928, Math. Annalen 100, 32

Drew J.E., Denby M., Hoare M.G., 1994, MNRAS 266, 917

Ebbets D., 1982, ApJS 48, 399

Falle S.A.E.G., 1975, MNRAS 172, 55

Falle S.A.E.G., 1981, MNRAS 195, 1011

Feldmeier A., 1993, PhD thesis, Universität München

Feldmeier A., 1994, in: Moffat A.F.J., Fullerton A.W., Owocki S.P., St-Louis N. (eds.) Instability and Variability of Hot Star Winds. Kluwer, Dordrecht (in press)

Field G.B., 1965, ApJ 142, 531

Friend D.B., Abbott D.C., 1986, ApJ 311, 701

Fullerton A.W., Gies D.R., Bolton C.T., 1992, ApJ 390, 650

Gaetz T.J., Edgar R.J., Chevalier R.A., 1988, ApJ 329, 927

Gautschy A., Glatzel W., 1990, MNRAS 245, 597

Gies D.R., 1991, in: Baade D. (ed.) ESO Conference Proc. 36, Rapid Variability of OB-Stars. ESO, Garching, p. 229

Harnden F.R., Branduardi G., Elvis M., et al., 1979, ApJ 234, L51

Hawley J.F., Smarr L.L., Wilson J.R., 1984, ApJS 55, 211

Hearn A.G., 1972, A&A 19, 417

Hearn A.G., 1975, A&A 40, 277

Hedstrom G.W., 1979, J. Comp. Phys. 30, 222

Henrichs H.F., 1988, in: Conti P.S., Underhill A.B. (eds.) O Stars and Wolf-Rayet Stars. NASA, Washington, p. 199

Henrichs H.F., 1991, in: Baade D. (ed.) ESO Conference Proc. 36, Rapid Variability of OB-Stars. ESO, Garching, p. 199

Hillier D.J., Kudritzki R.P., Pauldrach A.W., et al., 1993, A&A 276, 117

Imamura J.N., Wolff M.T., Durisen R.H., 1984, ApJ 276, 667

Kaper L., 1993, PhD thesis, Sterrenkundig Instituut Amsterdam

Kaufer A., Stahl O., Wolf B., 1994, AG Abstract Series 10, 41

Kiriakidis M., Fricke K.J., Glatzel W., 1993, MNRAS 264, 50

Kudritzki R.P., Simon K.P., Hamann W.R., 1983, A&A 118, 245

Lamb H., 1945, Hydrodynamics. Dover reprint, New York

Lamers H.J.G.L.M., Waters L.B.F.M., 1984, A&A 138, 25

Landau L.D., Lifschitz E.M., 1991, Hydrodynamik. Akademie-Verlag, Berlin

Langer S.H., Chanmugam G., Shaviv G., 1981, ApJ 245, L23

Langer S.H., Chanmugam G., Shaviv G., 1982, ApJ 258, 289

Lucy L.B., 1982a, ApJ 255, 278

Lucy L.B., 1982b, ApJ 255, 286

Lucy L.B., 1983, ApJ 274, 372

Lucy L.B., 1984, ApJ 284, 351

Lucy L.B., Solomon P.M., 1970, ApJ 159, 879

Lucy L.B., White R.L., 1980, ApJ 241, 300

MacFarlane J.J., Cassinelli J.P., 1989, ApJ 347, 1090

MacGregor K.B., Hartmann L., Raymond J.C., 1979, ApJ 231, 514

Mair G., Müller E., Hillebrandt W., Arnold C.N., 1988, A&A 199, 114

Mihalas D., Mihalas B.W., 1984, Foundations of Radiation Hydrodynamics. Freeman, San Francisco

Milne E.A., 1926, MNRAS 86, 459

Moffat A.F.J., 1994a, in: Klare G. (ed.) Reviews in Modern Astronomy 7. Astronomische Gesellschaft, Hamburg, p. 51

Moffat A.F.J., 1994b, in: Moffat A.F.J., Fullerton A.W., Owocki S.P., St-Louis N. (eds.) Instability and Variability of Hot Star Winds. Kluwer, Dordrecht (in press)

Mullan D.J., 1984, ApJ 283, 303

Mullan D.J., 1986, A&A 165, 157

Noh W.F., 1987, J. Comp. Phys. 72, 78

Norman M.L., Winkler K.-H.A., 1986, in: Winkler K.-H.A., Norman M.L. (eds.) Astrophysical Radiation Hydrodynamics. Reidel, Dordrecht, p. 187

Norman M.L., Wilson J.R., Barton R.T., 1980, ApJ 239, 968

Owocki S.P., 1991, in: Crivellari L., Hubeny I., Hummer D.G. (eds.) Stellar Atmospheres, Beyond Classical Models. Kluwer, Dordrecht, p. 235

Owocki S.P., 1992, in: Heber U., Jeffery S. (eds.) The Atmospheres of Early-Type Stars. Springer-Verlag, Heidelberg, p. 393

Owocki S.P., 1994, in: Moffat A.F.J., Fullerton A.W., Owocki S.P., St-Louis N. (eds.) Instability and Variability of Hot Star Winds. Kluwer, Dordrecht (in press)

Owocki S.P., 1995, ApJ (preprint)

Owocki S.P., Rybicki G.B., 1984, ApJ 284, 337 (OR)

Owocki S.P., Rybicki G.B., 1985, ApJ 299, 265

Owocki S.P., Castor J.I., Rybicki G.B., 1988, ApJ 335, 914 (OCR)

Pauldrach A., 1987, A&A 183, 295

Pauldrach A., Puls J., Kudritzki R.P., 1986, A&A 164, 86

Pauldrach A.W.A., Kudritzki R.P., Puls J., Butler K., Hunsinger J., 1994a, A&A 283, 525

Pauldrach A.W.A., Feldmeier A., Puls J., Kudritzki R.P., 1994b, in: Vanbeveren D., van Rensbergen W., de Loore C. (eds.) Evolution of Massive Stars. Kluwer, Dordrecht, p. 105

Prinja R.K., 1988, MNRAS 231, 21p

Prinja R.K., Fullerton A.W., 1994a, ApJ 426, 345

Prinja R.K., Fullerton A.W., 1994b, in: Moffat A.F.J., Fullerton A.W., Owocki S.P., St-Louis N. (eds.) Instability and Variability of Hot Star Winds. Kluwer, Dordrecht (in press)

Prinja R.K., Howarth I.D., 1986, ApJS 61, 357

Prinja R.K., Howarth I.D., 1988, MNRAS 233, 123

Puls J., 1987, A&A 184, 227

Puls J., 1993, Habilitation, Universität München

Puls J., Pauldrach A.W.A., Kudritzki R.P., Owocki S.P., Najarro F., 1993a, in: Klare G. (ed.) Reviews in Modern Astronomy 6. Astronomische Gesellschaft, Hamburg, p. 271

Puls J., Owocki S.P., Fullerton A.W., 1993b, A&A 279, 457

Puls J., Feldmeier A., Springmann U., Owocki S.P., Fullerton A.W., 1994, in: Moffat A.F.J., Fullerton A.W., Owocki S.P., St-Louis N. (eds.) Instability and Variability of Hot Star Winds. Kluwer, Dordrecht (in press)

Puls J., Kudritzki R.P., Pauldrach A.W.A., et al., 1995, A&A (preprint)

Raymond J.C., Cox D.P., Smith B.W., 1976, ApJ 204, 290

Reile C., Gehren T., 1991a, A&A 242, 142

Reile C., Gehren T., 1991b, in: Crivellari L., Hubeny I., Hummer D.G. (eds.) Stellar Atmospheres, Beyond Classical Models. Kluwer, Dordrecht, p. 303

Roache P.J., 1982, Computational Fluid Dynamics. Hermosa Publishers, New Mexico

Rosner R., Tucker W.H., Vaiana G.S., 1978, ApJ 220, 643

Różyczka M., 1985, A&A 143, 59

Rybicki G.B., 1987, in: Lamers H.J.G.L.M., de Loore C.W.H. (eds.) Instabilities in Luminous Early Type Stars. Reidel, Dordrecht, p. 175

Rybicki G.B., Hummer D.G., 1978, ApJ 219, 654

Rybicki G.B., Owocki S.P., Castor J.I., 1990, ApJ 349, 274

Schulz W.D., 1964, J. Math. Phys. 5, 133

Schuster H.G., 1989, Deterministic Chaos. VCH Verlagsgesellschaft, Weinheim

Seward F.D., Forman W.R., Giacconi R., et al., 1979, ApJ 234, L55

Stone J.M., Norman M.L., 1992, ApJS 80, 753

Sturrock P.A., Spreiter J.R., 1965, J. Geophys. Res. 70, 5345

Tatsumi T., Tokunaga H., 1974, J. Fluid Mech. 65, 581

Thompson K.W., 1987, J. Comp. Phys. 68, 1

Thompson K.W., 1990, J. Comp. Phys. 89, 439

Van Leer B., 1977, J. Comp. Phys. 23, 276

Waldron W.L., Klein L., Altner B., 1992, in: Drissen L., Leitherer C., Nota A. (eds.) ASP Conference Series 22, Nonisotropic and Variable Outflows from Stars. ASP, San Francisco, p. 181

Waldron W.L., Klein L., Altner B., 1994, ApJ 426, 725

White R.L., 1985, ApJ 289, 698

White R.L., 1994, in: Moffat A.F.J., Fullerton A.W., Owocki S.P., St-Louis N. (eds.) Instability and Variability of Hot Star Winds. Kluwer, Dordrecht (in press)

White R.L., Chen W., 1992a, ApJ 387, L81

White R.L., Chen W., 1992b, in: Drissen L., Leitherer C., Nota A. (eds.) ASP Conference Series 22, Nonisotropic and Variable Outflows from Stars. ASP, San Francisco, p. 274

Winkler K.-H.A., Norman M.L., 1986, in: Winkler K.-H.A., Norman M.L. (eds.) Astrophysical Radiation Hydrodynamics. Reidel, Dordrecht, p. 71

Wolf B., Kaufer A., Rivinius T., Stahl O., 1994, AG Abstract Series 10, 40

Wu K., Chanmugam G., Shaviv G., 1992, ApJ 397, 232

Zel'dovich Ya.B., Raizer Yu.P., 1967, Physics of Shock Waves and High-Temperature Hydrodynamic Phenomena, Vol. II. Academic Press, New York

This article was processed by the author using Springer-Verlag LaTeX A&A style file *L-AA* version 3.

Astron. Astrophys. 311, 793–802 (1996)

ASTRONOMY
AND
ASTROPHYSICS

Vela X–1: how to produce asymmetric eclipses

A. Feldmeier[1], **U. Anzer**[2], **G. Börner**[2], **and F. Nagase**[3]

[1] Universitäts-Sternwarte, Scheinerstr. 1, D-81679 München, Germany
[2] Max-Planck-Institut für Astrophysik, Karl-Schwarzschild-Str. 1, D-85740 Garching, Germany
[3] The Institute of Space and Astronautical Science, 3-1-1, Yoshinodai, Sagamihara, Kanagawa, 229 Japan

Received 19 October 1995 / Accepted 9 December 1995

Abstract. Light curves of the X-ray pulsar Vela X–1 obtained with the ASCA satellite show a strong asymmetry in the hard energy band during the eclipse of the X-ray source: a steep drop at ingress is followed by a gradual decline, whereas only a steep increase is observed at egress. X-ray scattering off the dense accretion wake trailing the neutron star cannot explain the gradual decline because of the long persistence of the latter ($\Delta\phi = 0.11$). Instead we propose that scattering in an extended photoionization wake is responsible. This wake is caused by the switch-off of the radiative force that drives the B supergiant wind during the passage through the highly ionized Strömgren region surrounding the X-ray source. The stalled gas then trails the neutron star, which moves relative to the B star surface (no corotation). A model for the Vela X–1 system which assumes that the B star does not rotate gives too large a phase extent for the dense wake and can be ruled out. Including the B star rotation in an approximate way, the relative azimuthal motion of the neutron star is slower and the wake covers a smaller phase interval. Finally, we assume that the Strömgren sphere does not reach too deep into the wind accelerating region. The wind can then reach a certain fraction of the terminal velocity before the radiative force is switched off. This elongates the photoionization wake further and both its phase extent and its scattering efficiency match the observations.

Key words: hydrodynamics – binaries: eclipsing – stars: mass-loss – stars: neutron – X-rays: stars – stars: Vela X–1

1. Introduction

1.1. The observations

Vela X–1 is an X-ray pulsar in a binary system which consists of the B 0.5 Ib supergiant HD 77581 and an accreting neutron star orbiting with a period of 8.96 d. The physical parameters for this system were summarized by Nagase (1989) as $R_c = 34.0\,R_\odot$, $a = 52.9 R_\odot$, $M_c = 23.0\,M_\odot$ and $M_x = 1.77 M_\odot$. The X-ray pulsar is eclipsed for a phase interval of approximately 0.22 of its orbit. Recently these eclipses were studied in great detail by Nagase et al. (1994). They analyzed observations obtained on June 25–26 and July 5–6, 1993 with the ASCA GIS2 detector. The light curves obtained for the energy bands between 1 keV – 3 keV and 3 keV – 10 keV are shown in Fig. 1. The observations in the 3 keV – 10 keV band show a very pronounced eclipse. The intensity outside the eclipse, I_0, can be estimated to be approximately 10 counts/s. The light curve drops very steeply at the phases $\phi = -0.11$ and $\phi = 0.11$. In addition, there is a gradual decline from $I = 0.7$ counts/s at $\phi = -0.11$ to $I = 0.1$ counts/s at $\phi = 0$ and a plateau of $I = 0.1$ counts/s from $\phi = 0$ to $\phi = 0.11$. The observations in the 1 keV – 3 keV band show only very small variations. One can ascribe the intensity outside of the eclipse, I_0, to the direct emission from the neutron star, whereas the lower intensity during the eclipse phase represents scattered light that originates from an extended region around the neutron star.

1.2. The models

Vela X–1 is powered by the accretion of material from the wind that the supergiant HD 77581 propels. This then leads to the typical Bondi-Hoyle accretion flow and since the wind is highly supersonic, strong shocks will develop. The details of such flows have been calculated numerically in two-dimensional and three-dimensional configurations by many groups (e.g., Livio et al. 1986; Anzer et al. 1987; Fryxell & Taam 1989; Taam & Fryxell 1989; Matsuda et al. 1991; Ruffert & Arnett 1994). The typical length scale of these flows is the accretion radius r_a given by

$$r_a = \frac{2GM_x}{v^2}, \tag{1}$$

with $v^2 = v_{\rm wind}^2 + v_{\rm orbit}^2$. Since $v_{\rm orbit} = 280$ km/s, one obtains $r_a = 10^{11}$ cm for $v_{\rm wind} = 600$ km/s and $r_a = 6 \times 10^{10}$ cm for $v_{\rm wind} = 800$ km/s. The numerical simulations show that the high density region of the accretion cone extends over several accretion radii, therefore the typical dimensions will range between

---

Send offprint requests to: A. Feldmeier. feld@usm.uni-muenchen.de

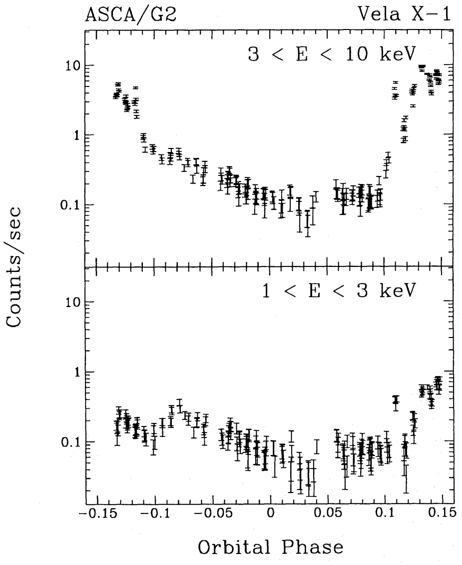

Fig. 1. X-ray light curve of Vela X–1, obtained with the ASCA GIS2 detector on June 25–26 and July 5–6, 1993.

10^{11} cm and a few times 10^{11} cm. This then implies that the partial eclipsing of this cone, which is at a distance of 3.7×10^{12} cm from the primary, will only cover a phase $\Delta\phi < 0.01$. Therefore it cannot explain the gradual decline in scattered X-rays observed between $\phi = -0.11$ and $\phi = 0$. One has to look for another mechanism that can produce asymmetric density enhancements over larger spatial dimensions.

Such a mechanism is the switch-off of the radiative driving force due to the ionization by X-rays in combination with the relative azimuthal motion of the wind gas with respect to the neutron star (Fransson & Fabian 1980; Ho & Arons 1987). The wind of B supergiants is accelerated by the UV radiation emitted by the star. But in the neighborhood of the X-ray source the wind is highly ionized and therefore the driving force is strongly reduced. This effect can be characterized by the ionization parameter ξ, which is defined as

$$\xi = \frac{L_{\rm x}}{nr^2} \tag{2}$$

(Hatchett & McCray 1977). For $\xi > \xi_{\rm cr}$ the radiative driving force is basically switched off. If the X-ray luminosity is high enough, or the density sufficiently low, then the switching off of the driving force occurs close to the surface of the giant. The wind velocities will then be strongly reduced and this in turn leads to a large density enhancement relative to the undisturbed wind. This effect has been studied by Fransson & Fabian (1980) and Blondin et al. (1990). The dense gas in the trailing photoionization wake should lead to enhanced photoelectric absorption of X-rays at late orbital phases prior to eclipse; and possibly also to X-ray scattering into the observer's line of sight after eclipse ingress. Blondin et al. (1990) calculated this wake structure, including all relevant heating and cooling processes, in a 2-D simulation of the flow in the orbital plane, under the further restriction that the primary and the X-ray source *corotate*. However, their focus is on dense filaments due to nonsteady accretion onto the compact object. These simulations, and the ones by Blondin (1994), were recently extended by Blondin & Woo (1995) to account for the full 3-D geometry of the disrupted wind in the *high X-ray luminosity* system SMC X–1. Here, the X-ray source ionizes and heats the gas down to the photosphere of the primary, which therefore does not propel a radiatively driven wind, but instead a thermal wind on its X-ray irradiated side. The primary is again assumed to corotate with the X-ray source. The most prominent latitudinal flows are found to be: (1) a focusing of the radiatively driven shadow wind into the equatorial plane due to rotation of the primary star, which leads to the formation of a wind-compressed disk (Bjorkman & Cassinelli 1993; Owocki et al. 1994); and (2) an expulsion of the radiatively driven wind from the equatorial plane by a strong thermal pressure gradient. The latter is built up by X-ray heating of stalled wind gas which left the X-ray shadow, and is deflected by the Coriolis force towards the X-ray source. Woo et al. (1995) find that this gas of highly varying column density is responsible for the irregular light curve observed soon after egress with the *Ginga* satellite. On the other hand, the gradual decline observed in the X-ray count rate prior to ingress of the X-ray source is caused by absorption in the thermal wind. We want to emphasize that the interesting results of Blondin and Woo (1995) will not be applicable to Vela X–1 because (i) in Vela X–1 the X-ray luminosity is a factor 1/60 lower; and (ii) the rotational velocity of the companion is a factor 1/4 below the breakup value. Therefore one expects that the winds in Vela X–1 and SMC X–1 should be substantially different from each other.

In the present paper we construct a simple model specifically designed for the intermediate luminosity system Vela X–1 ÷ HD 77581 in order to determine if scattering in a dense photoionization wake (which is caused by the reduced radiative driving force within the Strömgren zone) can explain the extended decline of the X-ray light curve observed after ingress (as opposed to pre-ingress absorption discussed by Woo et al. 1995). These model calculations are presented in Sect. 2 and their application to Vela X–1 discussed in Sect. 3. In Sect. 4 we give our conclusions.

2. Models of stellar winds with local ionization

2.1. Non-rotating B star

The winds of hot, luminous stars are driven by momentum transfer from the stellar UV radiation field to metal ions, which is accomplished in numerous line transitions. Coulomb collisions then spread this momentum over the whole wind plasma, which consists mainly of hydrogen and helium. The full theory of these winds includes a detailed treatment of their (i) hydrodynamics

(Castor, Abbott & Klein 1975, CAK in the following; Abbott 1980); (ii) NLTE (Pauldrach 1987; Pauldrach et al. 1994); (iii) radiative transfer (Puls 1987; Pauldrach et al. 1994); (iv) hydrodynamic stability (Owocki, Castor & Rybicki 1988); (v) and, for thin winds, plasma effects (Springmann & Pauldrach 1992). In the present paper, however, we follow a simplified approach in which we use the parameterized expression for the line force driving a spherical symmetric flow (cf. below) after CAK,

$$\tilde{g}_{\rm rad} = \frac{K}{r^2}\, f(v, v'; r; \alpha) \left(\frac{|v'|}{\rho}\right)^{\alpha} . \qquad (3)$$

Here, $v' = \partial v / \partial r$. The finite disk correction factor, f, is given in Eq. (50) of CAK. The CAK exponent α (which describes the relative contribution of optically thin, $\alpha = 0$, and thick lines, $\alpha = 1$, to the force) is assumed to be $\alpha = 0.7$. The constant K, which is proportional to the CAK constant k, is chosen so that the wind has the mass loss rate given by observations of HD 77581. Finally, for a discussion of the underlying assumption in (3) that material always experiences the full stellar continuum radiation field, independent of the sign of v', we refer to Cranmer & Owocki (1996).

The force expression (3) has to be modified because the pulsar represents a strong source of X-rays orbiting the supergiant. The dominating effect of this X-ray source is the ionization of the wind. The strength of the ionization can be characterized by the ionization parameter ξ. In the immediate neighborhood of the neutron star the gas will be completely ionized whereas at larger distances the ionization will be only partial. Since the radiative acceleration requires the presence of elements in a low state of ionization, high values of ξ imply a small radiative acceleration, while for sufficiently small ξ the full radiative force operates. This transition of the acceleration will be gradual, but based on the results obtained by MacGregor et al. (1979), one would expect that it occurs over a fairly narrow range of ξ values. Therefore, we shall take a step function in ξ with $g_{\rm rad} = 0$ for $\xi > \xi_{\rm cr}$ and $g_{\rm rad} = \tilde{g}_{\rm rad}$ for $\xi < \xi_{\rm cr}$. Fransson & Fabian (1980) and Blondin et al. (1990) have argued that $\xi_{\rm cr} = 300$ erg cm s^{-1} is a reasonable value for this transition and we shall follow this suggestion here. The condition $\xi = \xi_{\rm cr}$ now defines the extent of the Strömgren region and this region moves together with the X-ray pulsar through the stellar wind. In this paper (for simplicity) we shall limit our investigation to the orbital plane since this is the region where the effects of interest are the most pronounced. This is further justified by the fact that for Vela X–1 the ratio of the equatorial rotation speed of the primary ($\approx (80/\sin i)$ km/s; cf. Sect. 2.2) to the critical, breakup speed (350 km/s; Dupree et al. 1980) is ≤ 0.25, which is far below the minimum ratio of $\geq 0.7 \ldots 0.8$ at which the formation of a wind-compressed disk should set in (see Fig. 11 of Bjorkman & Cassinelli 1993). Blondin & Woo (1995) find furthermore that only in the presence of a wind-compressed disk is a significant outflow of gas driven away from the equator by the expulsion of gas from the equatorial plane.

We restrict the geometry of our model even further by performing only *one-dimensional*, time-dependent calculations for a strictly radially directed wind flow. More specifically, in applying the hydrodynamical equations in *spherical* symmetry, the flow geometry is thought of as a *cone* of infinitesimal opening angle. The orbiting Strömgren region then passes through this wind ray periodically, and the stalled gas moves outwards at approximately constant speed, i.e., at only slowly dropping density ($\approx r^{-2}$), so that this gas shows up as a trailing, dense wake. Our simulations are therefore similar to those of Fransson & Fabian (1980). However, the radiation force used by the latter authors is not the CAK force (3), but instead is fixed to give a pre-specified stationary velocity field for the wind; during the passage of the Strömgren region the line driving is then again (essentially) switched off.

Since we consider only radial wind rays (in the corotating frame, i.e., the Coriolis force is not treated), the stalled gas in our simulations does not undergo a large *compression* as in the simulations by Blondin et al. (1990): these authors calculate the full 2-D wind structure in the orbital plane. However, they assume corotation of the B star and the neutron star, so that a stationary flow (in the corotating frame) can build up. The trajectories of stalled gas passing through the Strömgren zone are strongly bent by the Coriolis force, so that on the trailing side of the zone they approach (i.e., the gas is compressed) the trajectories of small curvature of accelerated particles which pass sideways by the Strömgren zone.

Since optical observations show that Vela X–1 is far from corotation (see next section), we feel justified to supplement the calculations by Blondin et al. by time-dependent 1-D simulations. We have to keep in mind however, that the full photoionization wake from a 2-D calculation which includes the Coriolis force should be more trailing, and will have a larger integrated column density than the wake computed here. – Another justification for assuming 1-D spherical symmetry is that we are mainly interested in the eclipse behavior of the column density and therefore can neglect contributions from accretion filaments for which a 2-D simulation would be mandatory. – A final motive for performing 1-D calculations is that in deep wind layers flow phenomena occur which necessitate a very fine grid resolution; the latter may not be achievable in present 2-D or 3-D calculations.

Since in 1-D simulations we cannot determine the geometrical shape of the highly ionized region consistently from the actual density stratification (as done by Blondin et al. 1990), we take the following simplified approach: (i) The orbit of the neutron star around the B star is assumed to be circular. (ii) We assume the region of turned-off radiative force to be a strict sphere (cf. Hatchett & McCray 1977). The location and extent of this Strömgren sphere are taken from the approximate values for the Vela X–1 system (cf. Dupree et al. 1980), with $r_{\rm min} = 1.1\,R_{\rm c}$ for the inner radius in our first two models (#1 and 2), and $= 1.2\,R_{\rm c}$ in the final model (#3); the outer radius is always assumed to be $r_{\rm max} = 3.7\,R_{\rm c}$. The X-ray source is located at a distance $a = 1.5\,R_{\rm c}$. We assume that the wind is *isothermal*, i.e., the energy equation is trivially solved by setting the pressure $p = {c_{\rm s}}^2 \rho$, with $c_{\rm s}$ the isothermal sound speed. The errors that result from not resolving cooling zones behind regularly appearing shocks (cf. below) should be minor, since the wind is dense enough to ensure efficient radiative cooling. We have to solve then the continuity equation,

$$\frac{\partial \varrho}{\partial t} + \frac{1}{r^2}\frac{\partial}{\partial r}\left(r^2 \varrho v_{\mathrm{r}}\right) = 0, \tag{4}$$

and the momentum equation,

$$\frac{\partial(\varrho v_{\mathrm{r}})}{\partial t} + \frac{1}{r^2}\frac{\partial}{\partial r}\left(r^2 \varrho v_{\mathrm{r}} v_{\mathrm{r}}\right) = -\frac{\partial p}{\partial r} - \varrho g_{\mathrm{grav}}(r) + \varrho g_{\mathrm{rad}}(r,t). \tag{5}$$

From (5) we obtain the radial velocity $v_{\mathrm{r}}(r,t)$ for a chosen azimuthal angle φ_0. The velocity field $\hat{v}_{\mathrm{r}}(r,\varphi)$ for any given time t_0 is obtained by the transformation (with Ω_{orb} the orbital angular velocity)

$$\hat{v}_{\mathrm{r}}(r,\varphi) = v_{\mathrm{r}}(r, t_0 - \varphi/\Omega_{\mathrm{orb}}). \tag{6}$$

We use a standard time-explicit Eulerian code (for details, see Feldmeier 1995; Reile & Gehren 1991) to solve Eqs. (4) and (5) in integral = conservation form on a staggered grid, where the advection fluxes are calculated by using van Leer's (1977) monotonic interpolation. We also experimented with piecewise parabolic advection, PPA, after Colella & Woodward (1984). However, since our main interest here is in rather smooth flow regions and not in strong shock dynamics, PPA does not show much benefit over van Leer's method. We use Hedstrom's (1979) non-reflecting boundary conditions by applying the formalism of Thompson (1987, 1990) at both the inner and outer boundary. This should minimize reflections from waves leaving the calculational domain, which are notorious for the difficulties they cause at the inner boundary of calculations like ours. This will be discussed in the following paragraphs. The model parameters relevant for our calculations are chosen to match the system of Vela X–1 ÷ HD 77581 (cf. the Introduction). Fig. 2 shows a simulation (Model 0) of the wind where the (unperturbed = stationary) mass loss rate is taken to be $\dot{M} = 10^{-6}\,M_\odot/\mathrm{yr}$. The B star is assumed in this model *not* to rotate, and the orbital period of the neutron star is $P_{\mathrm{orb}} = 2\pi/\Omega_{\mathrm{orb}} = 8.96$ d.

Fig. 2 shows the 23rd and 24th crossing of the Strömgren sphere through the wind ray after the start of the model. Therefore, initial transients should have mostly died out. However, differences between successive cycles still exist; as is discussed in the following, they possibly never vanish. Starting from the inner edge of the Strömgren sphere at $r = 1.1\,R_{\mathrm{c}}$, a perturbation propagates in the direction of the B star photosphere, which it reaches after 1.5 days. This perturbation is a direct consequence of the line-force cutoff together with the gravitational pull of the primary, by which material is *decelerated*, $\delta v < 0$, and *compressed*, $\delta\varrho > 0$. Each of these *anti*-correlated changes in density and velocity corresponds to an *inward* propagating wave. Or, more specifically for the situation at hand: the accumulation of material at the lower edge of the Strömgren sphere acts as an inward-moving piston, which drives a wave ahead of it. The total velocity jump over this decelerating region is always (much) smaller than the sound speed, so that this wave is not a shock, but a radiative-acoustic wave (Abbott 1980), i.e., a sound wave modified by the radiation line force. As shown by Abbott, such waves can propagate downwards only from below the *critical point* of the stationary wind solution, which in our model is located slightly above the deepest point of the Strömgren sphere.

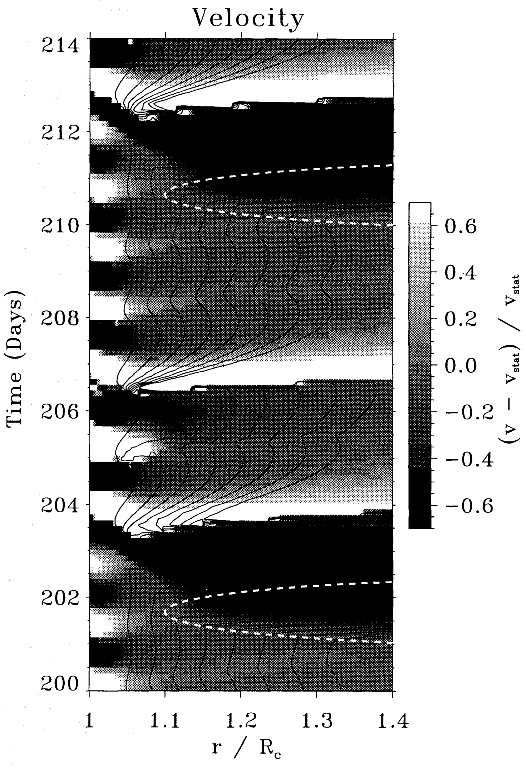

Fig. 2. *Model 0*: Grey-scale rendition of the deviation of the wind speed from the stationary speed in the inner wind region, over about 2 orbits of the Strömgren sphere (the latter is indicated by dashed lines). The overlaid contour lines are at absolute velocities between 20 and 300 km/s, in steps of 40 km/s. The model parameters are: $P_{\mathrm{orb}} = 8.96$ d; $\dot{M} = 10^{-6}\,M_\odot/\mathrm{yr}$; and the Strömgren sphere extends from 1.1 to 3.7 R_{c}. The inner boundary, $r = R_{\mathrm{c}}$, is located in the B star photosphere where $\tau_{\mathrm{c}} = 1$ and $c_{\mathrm{s}}/v_{\mathrm{stat}} \approx 350$. For further explanations, see text.

When the downward traveling perturbation reaches subsonic wind layers with an almost barometric density stratification, it excites a distinctive wave motion (cf. Owocki 1991 for a detailed description of the mechanism), which is seen in Fig. 2 as broad black/white bands, and also in the contour lines. We term this motion a *Lamb wave*, since its period is very close to the acoustic cutoff period of an isothermal barometric atmosphere, $T_{\mathrm{acc}} = 4\pi H/c_{\mathrm{s}} = 1.38$ d (where $H = 0.00733\,R_{\mathrm{c}}$ is the scale height, and $c_{\mathrm{s}} = 18.77\,\mathrm{km/s}$ for our model), which was introduced by Lamb (1906, §303). The central property of these waves is their effectively infinite wavelength ($\lambda \gg H$), so that "the whole atmosphere lifts (or drops) coherently" (Mihalas & Mihalas 1984, p. 192)[1]. Lamb waves have a phase lag of 90 degree between density and velocity fluctuations, and consequently they do not transport energy.

The material which piled up at the lower rim of the Strömgren sphere propagates outward in the form of a dense, narrow clump, which can be seen in Fig. 2 as a white band reaching up to (and beyond) $1.4\,R_\mathrm{c}$. This clump is followed by a second one, which is formed two cycles of the Lamb wave after the first. We find that the *physical* properties of both these clumps, especially their density contrast over the surroundings (as function of radius), depend strongly on the amplitude of the Lamb wave in the *inner subsonic region*. However, this wave amplitude in turn depends strongly on at least the following *numerical* aspects: (i) the location of the inner boundary with respect to the sonic point; (ii) the boundary conditions applied on this innermost point (e.g., non-reflecting, fixed inflow, etc.); (iii) the spatial grid resolution. To study the influence of item (i) (cf. Owocki et al. 1994; Owocki & Feldmeier, in preparation), we have performed two simulations, where the only difference between them is that the inner boundary is located in one at a velocity $c_\mathrm{s}/v_\mathrm{stat} \approx 350$ (Model 0, which is shown in Fig. 2), corresponding to the B star photosphere (where the Thomson electron scattering optical depth equals unity); and in the other case the inner boundary is located much closer to the sonic point, at $c_\mathrm{s}/v_\mathrm{stat} \approx 10$ (Model 1; and all following models). For the latter model, we find that the Lamb wave on the innermost grid point has a density amplitude of a few millipercent. The density at $r \gtrsim 1.1\,R_\mathrm{c}$, i.e., slightly above the deepest point of the Strömgren sphere, varies by a few times 10%. In this case there is almost no indication of isolated, dense clumps at these radii. However, dense clumps exist in this model at somewhat larger radii, as is clearly seen in Fig. 4. On the other hand, for Model 0 which has a deep inner boundary at $c_\mathrm{s}/v_\mathrm{stat} \approx 350$, much larger density fluctuations at the inner boundary ($\gtrsim 5\%$, and still growing with radius), and at the location $r = 1.15\,R_\mathrm{c}$ (by factors of ≈ 35) are shown in Fig. 3; at the latter radius, pronounced clumps are now seen after the passage of the Strömgren sphere. We will return to a more detailed discussion of this figure after the next paragraph.

To minimize the influence of the inner *boundary conditions* on the outer wind (item (ii) above), we apply Thompson's (1987, 1990) non-reflecting boundary conditions, which allow waves to leave the grid with minimum reflection. Finally, as is the case with the location of the inner boundary, the density fluctuations and clump properties depend strongly on the *grid resolution* (item (iii) above). All models presented here use 3000 logarithmically spaced grid points between 1 and 7 R_c. Using 1000 points instead, the density fluctuations are again much larger. To conclude this discussion, we can assert that in our models (except #0) the influence of Lamb waves on the outer wind structure (dense clumps; density stratification) is at least minimized. Numerical artifacts should therefore not affect our conclusions concerning the properties of X-ray lightcurves.

To return to Fig. 3, it is found that two clumps are *always* released per orbit of the Strömgren sphere, and *either one or two* cycles of the Lamb wave lie between these clumps. However, *whether one or two Lamb cycles occur for a certain passage of the sphere does not seem to be predictable*: we use the designation "N", with $N = 1, 2, 3, \ldots$, for a sequence of $N + 1$ orbits of the Strömgren sphere where during the first orbit the clump #2 appears *two* Lamb cycles after clump #1, and over the next N orbits clump #2 appears already *one* Lamb cycle after clump #1. Following Model 0 (inner boundary = photosphere) over t = 500 days (where only the first 250 days are shown in the figure), we find the sequence of clump releases to be

$$N_1 N_2 N_3 \ldots = 22232123112324223. \tag{7}$$

There is no period in this sequence. We take this as an indication of *stochastic* or *chaotic* behavior of the model. The most probable root seems to be the approximate (2:13) resonance (and higher resonances) of the orbital period (8.96 d) and the acoustic cutoff period (1.38 d).

This assumption is supported by Model 2, which will be discussed in the next section, where the B star is assumed to *rotate*. There, approximately 11 Lamb cycles occur between two passages of the Strömgren sphere, instead of 6.5 cycles in Models 0 and 1. The Lamb wave is therefore more strongly damped between two passages. Since already the lowest resonance is of type (6:67), this resonance should not then become apparent, and the sequence of clump releases should be strictly periodic – as is indeed found from Model 2. Still, our time series in Fig. 3 is not long enough to apply standard analysis techniques (return maps, attractor reconstruction, Poincare sections; cf. Lichtenberg & Lieberman 1983; Perdang 1991) to gain more insight into the physical causes underlying (7). On the other hand, more systematic studies of (i) longer time series that explore (ii) the full parameter space of periodic versus stochastic behavior are hard to perform on current work stations, where each of our models typically requires a few cpu-days to run.

The influence of this chaotic behavior on our model predictions is minor: As stated above, the resonance is (almost) absent in Model 2. Furthermore, in Model 3 (with the same rotation velocity of the B star as in Model 2) the deepest point of the Strömgren sphere at $1.2\,R_\mathrm{c}$ is located (far) above the critical point at $\gtrsim 1.1\,R_\mathrm{c}$. Therefore, no perturbation can propagate downwards into subsonic wind layers. The Lamb wave then decays in time, and the resonance with the orbital period becomes unimportant. For Model 1, on the other hand, it is seen from Fig. 4 that the dense wake which trails the Strömgren sphere is more or less enclosed by the two clumps discussed above. The stochastic release of the clumps during subsequent passages of the Strömgren sphere leads to a variation of the phase extent of this wake between $\Delta\phi \approx 0.27 \ldots 0.33$. However, even the minimum $\Delta\phi$ is much too large to explain the observed X-ray lightcurve, so that Model 1 has to be rejected on observational grounds.

---

[1] Lamb waves are excited in the earth atmosphere, e.g., by volcano eruptions and solar eclipses, see Beer (1974).

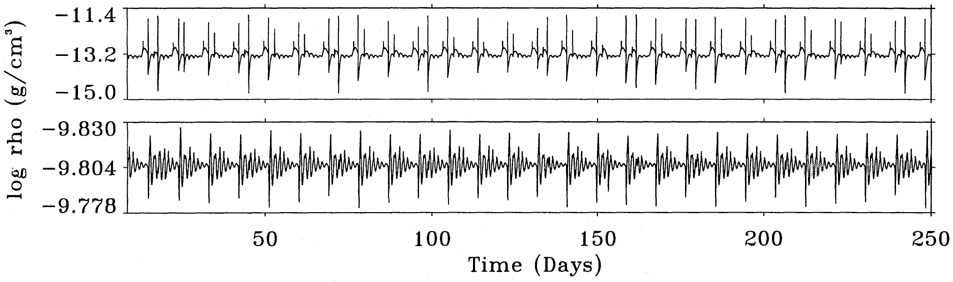

Fig. 3. *Model 0*: Time series of the wind density at the inner boundary $r = R_c$ (the B star photosphere; lower panel) and at $r = 1.15\,R_c$ (upper panel). For further discussion, see text.

2.2. *Effects of rotation*

Observations indicate that the star HD 77581 rotates with an equatorial velocity of about $(80/\sin i)$ km/s. This implies a rotational period of $P_{\rm rot} = 21.5$ d assuming $\sin i = 1$. Such a stellar rotation could have some effect on the density structure of the perturbed stellar wind because it leads to a non-vanishing φ-component of the velocity field. From the conservation of angular momentum one obtains

$$v_\varphi = (80/\sin i)\,(R_c/r)\,{\rm km/s}. \tag{8}$$

Because of this behavior the problem becomes intrinsically two-dimensional. But for our present study we want to keep the model as simple as possible. Therefore we replace the velocity law of (8) by rigid rotation with $\Omega_{\rm rot} = 2\pi/P_{\rm rot}$. Then, relative to this rotating gas, the X-ray source will orbit with a period $P^1_{\rm orb}$ given by

$$P^1_{\rm orb} = \left(\frac{1}{P_{\rm orb}} - \frac{1}{P_{\rm rot}}\right)^{-1} = 15.4\,{\rm d}. \tag{9}$$

This simplified configuration then allows the same type of one-dimensional analysis as in the non-rotating situation but now in a rotating frame of reference. The difference between the true azimuthal velocity and the velocity in our model is given by

$$\Delta v_\varphi = (80/\sin i)\left(\frac{r}{R_c} - \frac{R_c}{r}\right)\,{\rm km/s}, \tag{10}$$

which is about $\Delta v_\varphi \approx 70$ km/s at the position of the neutron star. Since Δv_φ is about $\frac{1}{4} v_{\rm orb}$ we expect the errors to be fairly small. Note that for the outer parts of the Strömgren sphere this velocity difference becomes much larger and therefore our model will not be very accurate there. But these regions have a low density and therefore do not contribute significantly to the scattering processes in which we are primarily interested. For comparison with the model of the non-rotating configuration we computed a model which also has $\dot M = 10^{-6} M_\odot$/yr (Model 2). The results are shown in Figs. 6 and 7.

A comparison of Models 1 and 2 shows that in the case of slow rotation (compared to orbital velocity) the density enhancement due to the ionization extends over a much larger orbital phase than in the case where the rotational velocity is comparable to the orbital velocity. This is of great importance for the modeling of the observed eclipse light curves, as will be discussed in the next section. One also sees that the shock spiral trails over a much wider range of azimuths in the non-rotating configuration. But this difference is probably a result of the assumption of $v_\varphi = \Omega_{\rm rot} r$ which becomes more and more unrealistic as r increases. We expect that for $r > 2\,R_c$ the true solution will be closer to Model 1.

We have also performed a model computation for $v_{\rm rot} = (80/\sin i)$ km/s and $\dot M = 2 \times 10^{-6} M_\odot$/yr (Model 3) and show the results in Figs. 8 and 9. The main effect in this model is that the Strömgren sphere becomes smaller (assumed now to extend from 1.2 to 3.7 R_c) and therefore the reduction of the radial velocity also becomes smaller, i.e., the radial velocity in the perturbed region stays larger. Therefore the high density region is more compressed in the azimuthal direction. Since the reduction of the radial velocity is smaller, there is a correspondingly smaller increase in relative density. But this effect is approximately compensated by the fact that in the new model the unperturbed density is everywhere larger by a factor 2. Consequently, the actual density enhancements are very nearly the same as those of the earlier models.

3. Application to Vela X–1

We shall now discuss how the results of the previous section can be used to model the X-ray luminosity of Vela X–1. The observations made in the 3 keV – 10 keV band show a strong modulation with orbital phase. The pre-eclipse intensity of $I_0 \approx 10$ counts/s exhibits a sharp drop to $I \approx 0.7$ counts/s, which is followed by a slow decline to 0.1 counts/s (see Fig. 1). If one interprets the latter as the background intensity then one finds $\Delta I = 0.6$ counts/s for the amplitude of the declining component. I_0 can be taken as the X-ray intensity of the unobscured pulsar. If we interpret ΔI as being due to X-ray scattering from an extended high density region trailing the neutron star then a scattering efficiency of the order of 6% would be sufficient to explain the observations. The observed gradual decline would then result from an increasing obscuration of the extended high

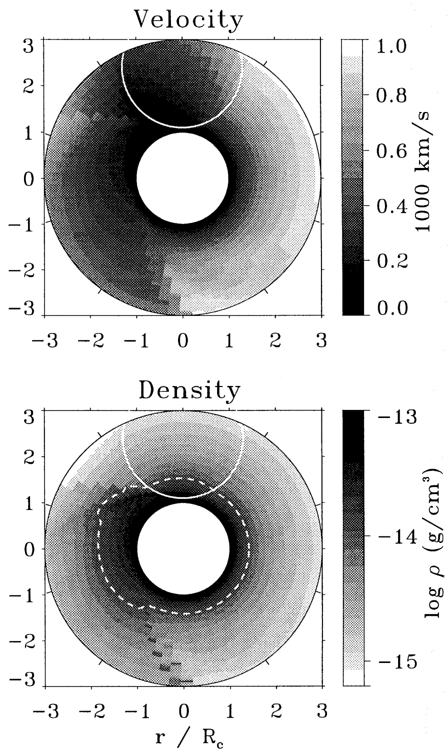

Fig. 4. *Model 1*: Velocity field and density stratification of the B supergiant wind in the presence of an orbiting Strömgren sphere (indicated by the off-center circle). The *time*-dependence of the wind (over an orbit of the Strömgren sphere) was translated into a *phase*-dependence in the orbital plane using (6). The dashes at the outer circle $r_{\max} = 3\ R_c$ indicate phase differences of 0.1. The dashed white line is at a density of 10^{-14} g/cm^3, and indicates the approximate boundary of the dense wind region. The B star is assumed *not* to rotate, i.e., $P_{\rm orb} = 8.96$ d. The mass loss rate is $\dot{M} = 10^{-6}\ M_\odot$/yr, and the Strömgren sphere reaches from 1.1 to 3.7 R_c.

density wake by the supergiant. The long duration of this eclipsing process, which is characterized by $\Delta\phi \approx 0.11$, constrains the spatial dimensions of the scattering region.

The model with a non-rotating giant is not applicable to the system Vela X–1 ÷ HD 77581 because optical observations show quite convincingly that HD 77581 rotates with a fairly large velocity. In addition our calculations show that for this configuration the high density region extends over much too large an angular range, which results in values for $\Delta\phi$ that are also much too large.

The other two models that we have calculated include this observed rotation in an approximate way, as described in the previous section. The first model is based upon a mass loss rate of $\dot{M} = 10^{-6} M_\odot$/yr. The high density region extends over a much smaller area. If we define this region by $\varrho \geq 10^{-14}$ g/cm^3 (regions with smaller densities give negligible contributions to the X-ray scattering) we see from Fig. 6 that this high density region becomes more and more eclipsed by the B star during a phase interval (starting from ingress of the X-ray point source) of $\Delta\phi \approx 0.17$. For the optically thin case we can also estimate the scattering ratio from the relation

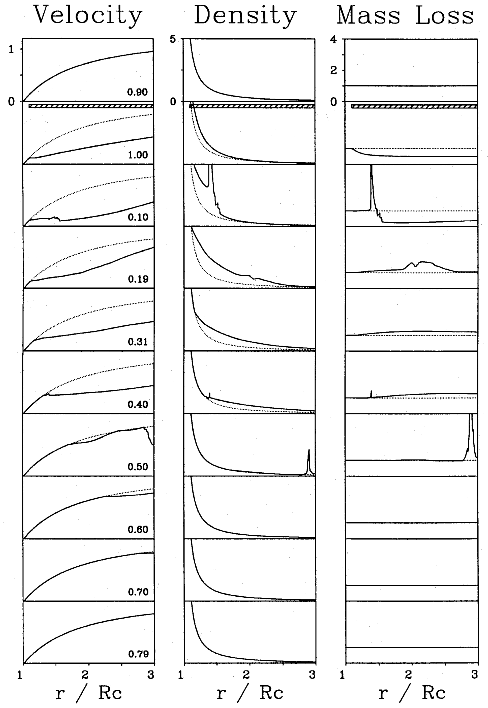

Fig. 5. *Model 1*: Snapshots of the wind structure over one orbit of the Strömgren sphere, at phase differences of ≈ 0.1. The velocity is in units of 1000 km/s, the density in units of 10^{-14} g/cm^3, and the mass loss rate in units of $10^{-6}\ M_\odot$/yr. (The range of all axes is the same as the range of the top panel axes.) The dotted curves are for the stationary wind, and the hatched rectangles around phase 1 indicate the Strömgren sphere. Notice the dense clumps at phases 0.1 and 0.5.

$$\frac{I_{\rm sc}}{I_0} = \frac{w}{4\pi}\, \ell \bar{n}\, \sigma_{\rm x}. \qquad (11)$$

Here w is the solid angle subtended by the high density region as seen from the neutron star, ℓ the length of a typical light path through this region and $\bar{n} = \bar{\varrho}/m_{\rm p}$ represents an appropriately averaged particle density. $\sigma_{\rm x}$ is the total cross section for X-rays in the range 3 keV – 10 keV. For the solid angle we take $w = \Delta\varphi \cdot \Delta\vartheta$ with $\Delta\varphi$ estimated from Fig. 6 to be approximately 0.25π. Our models do not constrain the value of $\Delta\vartheta$; but if we assume that the high density region also extends over a height

1996A&A...311..793F

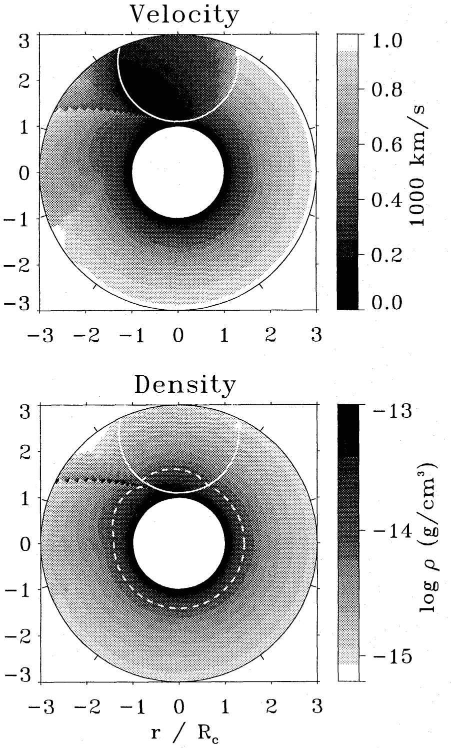

Fig. 6. *Model 2*: The B star is now assumed to rotate with period 21.5 d, i.e., the relative orbital period between the X-ray source and wind gas is $P^{1}_{\rm orb}$ = 15.4 d. The mass loss rate is $\dot{M} = 10^{-6}\ M_{\odot}$/yr, and the Strömgren sphere extends from 1.1 to 3.7 $R_{\rm c}$. The dashed white line is again at $\varrho = 10^{-14}$ g/cm^3.

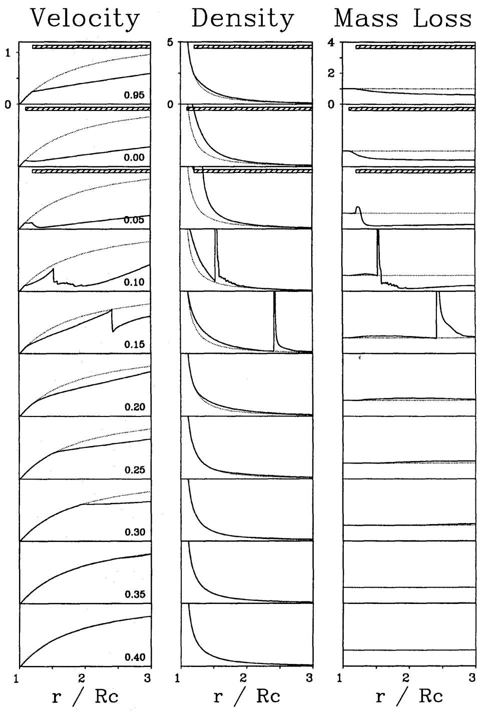

Fig. 7. *Model 2*: Snapshots of the wind structure over half an orbit of the Strömgren sphere. The units are the same as in Fig. 5.

comparable to the Strömgren sphere, one obtains as a rough estimate $\Delta\vartheta \approx \pi/2$. This leads to $w/4\pi \approx 0.1$. We also used Figs. 6 and 7 to obtain estimates of ℓ and $\bar{n}$. We find $\ell \approx 2\times10^{12}$ cm and $\bar{n} \approx 1.5\times10^{10}$ cm^{-3}. A value for $\sigma_{\rm x}$ can be obtained from the paper by Morrison & McCammon (1983). From their values of $\sigma_{\rm x} = 1.5\times10^{-23}$ cm^2 for E = 3 keV, 3.5×10^{-24} cm^2 for 5 keV and 1.7×10^{-24} cm^2 for 8 keV we estimate as an average over the observed X-ray spectrum a value of $\sigma_{\rm x} = 10^{-23}$ cm^2. With these values (11) gives $I_{\rm sc}/I_0 \approx 0.03$. This value is a factor 2 too small compared to the observations. We therefore conclude that this model has both too large a value for $\Delta\phi$ and too small a value for $I_{\rm sc}/I_0$.

The second model with rotation (Model 3) has twice as large a mass loss rate of $\dot{M} = 2\times10^{-6} M_{\odot}$/yr. From Figs. 8 and 9 one can again estimate the relevant physical parameters. We find: $\Delta\phi \approx 0.1$, $\Delta\varphi = 0.4\pi$, $\ell \approx 1.8\times10^{12}$ cm and $\bar{n} \approx 2\times10^{10}$ cm^{-3}. This leads to $w/4\pi \approx 0.15$ and $I_{\rm sc}/I_0 \approx 0.05$. We see that the effect of increasing $\dot{M}$ is twofold: it reduces $\Delta\phi$ and increases $I_{\rm sc}/I_0$. Both quantities are now much closer to the values derived from the X-ray observations. But this model also has the property that in the case of the stationary flow the high density region extends to fairly large radii. This means that for eclipse egress there is also an extended scattering region which could produce a gradual increase in X-ray intensity during the egress phase. But at present it is not clear whether the resulting X-ray light curve would be compatible with the observations. This question can only be answered on the basis of detailed scattering calculations. On the other hand, we want to stress that the column densities in our photoionization wake are *lower* limits due to the neglect of the Coriolis force. The high mass loss rate of Model 3 should therefore be an upper limit needed to match the observations.

The reduction of the wind velocity which we have introduced to explain the X-ray scattering also has consequences for the calculated mass accretion rates. We find for our Model 2 $v_{\rm wind}$ = 100 km/s and $\varrho = 1.5\times10^{-14}$ g/cm^3 at the location of the neutron star (i.e., at $r = a$, ϕ = 0). This gives $r_{\rm a} = 5\times10^{11}$ cm and $\dot{M}_{\rm acc} = 3.5\times10^{17}$ g/s. The corresponding values for Model 3 are $v_{\rm wind}$ = 250 km/s and $\varrho = 3\times10^{-14}$ g cm^{-3}, which leads to $r_{\rm a} = 3\times10^{11}$ cm and $\dot{M}_{\rm acc} = 3.2\times10^{17}$ g/s. This result can be compared to the accretion rate that is required to generate the observed mean X-ray luminosity of $L_{\rm x} = 5\times10^{36}$

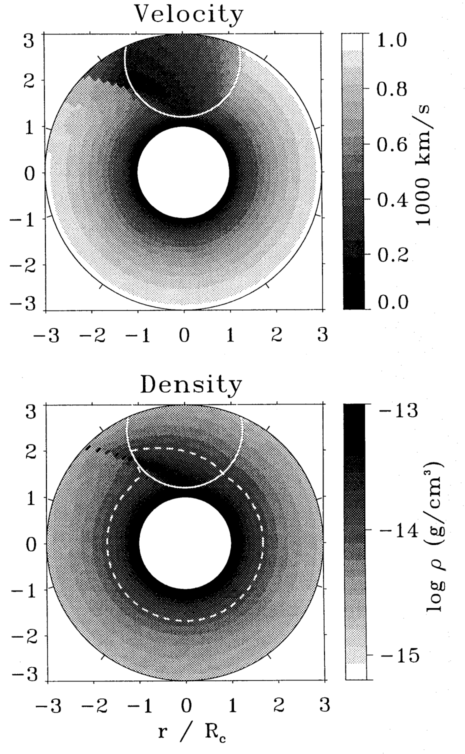

Fig. 8. *Model 3*: The orbital period is again (as in Model 2) assumed to be P^1_{orb} = 15.4 d; however, the mass loss rate is twice as large, $\dot{M} = 2 \times 10^{-6}\, M_\odot/\mathrm{yr}$, and the Strömgren sphere extends only from 1.2 to (again) 3.7 R_c. The dashed white line is at $\varrho = 10^{-14}$ g/cm^3.

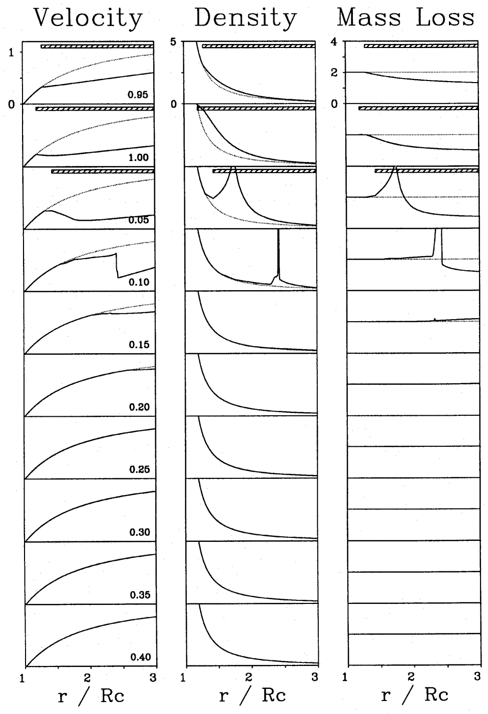

Fig. 9. *Model 3*: Snapshots of the wind structure.

erg/s. If one takes $L_\mathrm{x} = 0.1c^2\, \dot{M}_\mathrm{acc}$ then the observations require $\dot{M}_\mathrm{acc} = 5 \times 10^{16}$ g/s, which is much smaller than the values calculated above. A better agreement between the two could be reached if either the efficiency of producing X-rays were lower or if the system were located at a larger distance.

For example, if we arbitrarily decrease the X-ray production efficiency so that $L_\mathrm{x} = 0.02\, c^2\, \dot{M}_\mathrm{acc}$, we find that $\dot{M}_\mathrm{acc} = 2.5 \times 10^{17}$ g/s. Alternately, if we assume that the system is actually at twice its usual distance, $\dot{M}_\mathrm{acc} = 2 \times 10^{17}$ g/s. Both these values are much closer to our theoretical result. Thus, the correctness of either of these assumptions would evidently be sufficient to reconcile our models with the observations.

4. Conclusions

We have demonstrated that an extended region of enhanced X-ray scattering which trails the orbiting neutron star can explain the observed asymmetric X-ray light curve of Vela X–1. We argued that the typical accretion wake resulting from the gravitational attraction of the neutron star cannot produce the observed intensity variations and showed that the effects of X-ray ionization can lead to the required configuration. This ionization greatly reduces the radiative driving force of the stellar wind from the primary star, which causes the wind gas to stall and an extended region of high density to be formed. We have studied this effect in simple one-dimensional time-dependent models and found that for certain parameters of the system the observations could be matched. Such an analysis can give estimates for the parameters of the mass flow originating from the primary. Therefore the X-ray light curves can be used as a diagnostic tool which allows one to constrain the physics of this stellar wind flow. But in order to achieve this we need both more detailed models and better observations. For this reason we intend to calculate in the future 2-D wind models, determine the Strömgren region in a self-consistent way by including heating and cooling effects, and perform more detailed scattering calculations. On the observational side one would like to have several observing sequences each of which covers an entire eclipse period, and extends sufficiently into the pre-eclipse and the post-eclipse phase to determine the intensity I_0 accurately.

There is also the possibility that this high density wake could obscure the radiation from the optical star at phases close to 0.5. But simple estimates indicate that the column densities in this wake are much too small to produce observable effects; one would only get intensity variations of less than 0.1%. Therefore this effect can probably not be used to learn more about the system.

Another point which needs more detailed study is the fact that our models produce a very high mass accretion rate. The open question here is whether $\dot{M}_{\rm acc}$ can really be as high as 3×10^{17} g/s or whether one has to try to find other regimes of wind parameters which would produce the same X-ray scattering light curves but at the same time have a sufficiently low accretion rate.

Acknowledgements. We thank Drs. A. Pauldrach, J. Puls, S. Owocki, and C. Reile for interesting discussions, and A. Fullerton for carefully reading the manuscript. This work was supported by the DFG under contract Pa 477/1-2.

References

Abbott D.C., 1980, ApJ 242, 1183
Anzer U., Börner G., Monaghan J.J., 1987, A&A 176, 235
Beer T., 1974, Atmospheric waves. Wiley, New York
Bjorkman J.E., Cassinelli J.P., 1993, ApJ 409, 429
Blondin J.M., 1994, ApJ 435, 756
Blondin J.M., Woo J.W., 1995, ApJ 445, 889
Blondin J.M., Kallman T.R., Fryxell B.A., Taam R.E., 1990, ApJ 356, 591
Castor J.I., Abbott D.C., Klein R.I., 1975, ApJ 195, 157 (CAK)
Colella P., Woodward P.R., 1984, J. Comp. Phys. 54, 174
Cranmer S.R., Owocki S.P., 1996, ApJ, in print
Dupree A.K., et al. , 1980, ApJ 238, 969
Feldmeier A., 1995, A&A 299, 523
Fransson C., Fabian A.C., 1980, A&A 87, 102
Fryxell B.A., Taam R.E., 1988, ApJ 335, 862
Hatchett S., McCray R., 1977, ApJ 211, 552
Hedstrom G.W., 1979, J. Comp. Phys. 30, 222
Ho C., Arons J., 1987, ApJ 321, 404
Lamb H., 1906, Hydrodynamics. Dover reprint, New York
Lichtenberg A.J., Lieberman M.A., 1983, Regular and stochastic motion. Springer-Verlag, New York
Livio M., Soker N., de Kool M., Savonije G.J., 1986, MNRAS 218, 593
MacGregor K.B., Hartmann L., Raymond J.C., 1979, ApJ 231, 514
Matsuda T., Sekino N., Sawada K., Shima E., Livio M., Anzer U., Börner G., 1991, A&A 248, 301
Mihalas D., Mihalas B., 1984, Foundations of radiation hydrodynamics. Freeman, San Francisco
Morrison R., McCammon D., 1983, ApJ 270, 119
Nagase F., 1989, Publ. Astron. Soc. Japan 41, 1
Nagase F., Zylstra G., Sonobe T., Kotani T., Inoue H., Woo J., 1994, ApJ 436, L1
Owocki S.P., 1991, in: Hidayat B., van der Hucht K.A. (eds.) Wolf-Rayet stars and interrelations with other massive stars in galaxies. Kluwer, Dordrecht
Owocki S.P., Castor J.I., Rybicki G.B., 1988, ApJ 335, 914
Owocki S.P., Cranmer S.R., Blondin J.M., 1994, ApJ 424, 887
Pauldrach A., 1987, A&A 183, 295
Pauldrach A.W.A., Kudritzki R.P., Puls J., Butler K., Hunsinger J., 1994, A&A 283, 525
Perdang J., 1991, in: Baade D. (ed.) Rapid variability of OB stars: nature and diagnostic value. ESO, Garching, p. 349
Puls J., 1987, A&A 184, 227
Reile C., Gehren T., 1991, A&A 242, 142
Ruffert M., Arnett D., 1994, ApJ 427, 351
Springmann U., Pauldrach A.W.A., 1992, A&A 262, 515
Taam R.E., Fryxell B.A., 1989, ApJ 338, 297
Thompson K.W., 1987, J. Comp. Phys. 68, 1
Thompson K.W., 1990, J. Comp. Phys. 89, 439
Van Leer B., 1977, J. Comp. Phys. 23, 276
Woo J.W., Clark G.W., Blondin J.M., Kallman T.R., Nagase F., 1995, ApJ 445, 896

This article was processed by the author using Springer-Verlag LaTeX A&A style file version 3.

Astron. Astrophys. 320, 899–912 (1997)

ASTRONOMY
AND
ASTROPHYSICS

The X-ray emission from shock cooling zones in O star winds[*]

A. Feldmeier[1], **R.-P. Kudritzki**[1,2], **R. Palsa**[1], **A.W.A. Pauldrach**[1], **and J. Puls**[1]

[1] Institut für Astronomie und Astrophysik der Universität, Scheinerstr. 1, D-81679 München, Germany
[2] Max-Planck-Institut für Astrophysik, Karl-Schwarzschild-Str. 1, D-85740 Garching, Germany

Received 16 April 1996 / Accepted 17 September 1996

Abstract. A semi-empirical model is developed for the X-ray emission from O star winds, and used to analyze recent ROSAT PSPC spectra. The X-rays are assumed to originate from cooling zones behind shock fronts, where the cooling is primarily radiative at small radii in the wind, and due to expansion at large radii. The shocks are dispersed in a cold background wind whose X-ray opacity is provided by detailed NLTE calculations.

This model is a natural extension of the Hillier et al. (1993) model of isothermal wind shocks. By assuming spatially constant shock temperatures, these authors achieved good fits to the data only by postulating two intermixed shock families of independent temperature and filling factor – i.e., by adjusting in parallel four parameters. By applying the present model to the analysis of high S/N PSPC spectra of three O-stars (ζ Pup, ι Ori, ζ Ori), we achieve fits of almost the same quality with only two parameters. This supports the idea that the two- or multi-component X-ray spectra are indeed due to stratified cooling layers.

Key words: hydrodynamics – radiative transfer – shock waves – stars: early-type – X-rays: stars

1. Introduction

The X-ray satellite ROSAT, with its high energy resolution and sensitivity, in particular at soft photon energies, is an ideal tool to investigate the nature of the X-ray emission of hot, luminous stars. Hillier et al. (1993) presented a high quality ROSAT PSPC spectrum of the O4 I(f) star ζ Pup over the energy range from 0.1 to 2.5 keV. They were able to interpret this spectrum by a simple model in which the X-rays arise from shocks distributed with a constant filling factor throughout the wind. A large fraction of the emission from these shocks is absorbed by the ambient cool wind material, for which the wavelength dependent opacity is calculated from detailed non-LTE stellar wind models. As it turns out, this cool wind opacity is crucial for the emergent X-ray spectrum which shows a maximum at 0.85 keV and a significant drop towards lower energies (cf. Fig. 10).

Hillier et al. achieved a reasonable fit to the observations with the assumption that all shocks were characterized by a single temperature of $\log T$ [K] ≈ 6.60 (see their Fig. 2). But the flux deficiency in the calculated spectrum for energies below 0.45 keV indicated that a cooler shock component of $\log T \approx 6.30$ and of roughly equal filling factor as the hotter component should be present (Fig. 4 of Hillier et al., and Fig. 10 of the present paper). For the B bright giant ϵ CMa (B2 II), on the other hand, Drew et al. (1994) and Cohen et al. (1996) claim that a one-temperature model is incapable of explaining the ROSAT spectrum, while good fits can be achieved with a two-temperature model.

Generally, the wind shocks should have a cooling zone of decreasing temperature and increasing density that contributes significantly to the X-ray spectrum (cf. Krolik & Raymond 1985). Therefore, the use of a one- or two-temperature hot plasma emission coefficient, while valuable for the ad hoc characterization of shock properties for individual hot stars, is of course questionable. Consequently, it is important to investigate how the structure of a cooling zone behind the shock modifies the emission coefficient and the theoretical emergent X-ray spectrum.

Such an investigation is the purpose of the present paper. We extend the concept of randomly distributed shocks embedded in the absorbing cool wind, as used by Hillier et al., and replace their mono-temperature integral over the emitting region to account for cooling gas behind the shock front. We adopt simple approximations (§2) for the shock structure in the inner region of a stellar wind, where the cooling time is shorter than the flow time and the shocks are radiative; and for the outer regions, where the shocks are non-radiative, i.e., they only cool by adiabatic expansion. In §3, we apply this model to three O stars with high signal-to-noise ROSAT PSPC spectra to test how the theoretical X-ray spectrum is modified by the introduction of structured shocks. A summary of the results is given in §4.

2. Simple post-shock models

Since radiation driven winds are inherently unstable (Lucy & Solomon 1970; Carlberg 1980; Owocki & Rybicki 1984, 1985;

Send offprint requests to: A. Feldmeier: feld@usm.uni-muenchen.de

[*] Based on observations obtained with the ROSAT X-ray satellite.

Lucy 1984), it is reasonable to attribute the X-ray emission of hot stars to shocks in their stellar winds. Hillier et al. (1993) considered non-stratified, isothermal shocks, where the density and temperature of the hot gas behind the front are constant with radius. The energy emitted by hot gas from a volume $\mathrm{d}V$ into the full solid angle 4π is

$$\epsilon_\nu(r) = e_\mathrm{s}(r)\, n_\mathrm{p}(r)\, n_\mathrm{e}(r)\, \Lambda_\nu(n_\mathrm{e}(r), T_\mathrm{s}(r))\, \mathrm{d}V \quad [\mathrm{erg/s}]. \tag{1}$$

Here, $n_\mathrm{p}(r)$ is the proton density, $n_\mathrm{e}(r)$ the electron density, $T_\mathrm{s}(r)$ the temperature, and $e_\mathrm{s}(r)$ the volume filling factor of hot gas behind a shock front located at radius r. The frequency dependent cooling function of a hot plasma, Λ_ν, is calculated using the most recent version of the Raymond-Smith code (Raymond & Smith 1977). Hillier et al. neglected the density dependence in the argument of Λ_ν and adopted $\Lambda_\nu = \Lambda_\nu(10^{10}\ \mathrm{cm}^{-3}, T_\mathrm{s})$ throughout the wind, which is a good approximation that we also used in the following. To avoid any further explicit reference to the density of the hot post-shock gas, we redefine the filling factor so that n_p and n_e in (1) (and in subsequent equations) are the *stationary*, 'cool' wind densities. Notice that we do not introduce a factor of 16 here as did Hillier et al. (1993) to account for the density jump at a strong shock. The present definition is more convenient to compare the filling factors from different models of the X-ray emission from hot star winds with differing densities of hot gas.

To account for the temperature and density stratification in the shock cooling layer, ϵ_ν is replaced by an integral over this zone,

$$\begin{aligned}
\hat{\epsilon}_\nu(r) &= e_\mathrm{s}(r)\, n_\mathrm{p}(r)\, n_\mathrm{e}(r)\, \hat{\Lambda}_\nu(T_\mathrm{s}(r))\, \mathrm{d}V, \\
\hat{\Lambda}_\nu(T_\mathrm{s}(r)) &= \pm \frac{1}{L_\mathrm{c}} \int\limits_{r}^{r\pm L_\mathrm{c}} f^2(r')\, \Lambda_\nu(T_\mathrm{s}(r)\, g(r'))\, \mathrm{d}r',
\end{aligned} \tag{2}$$

where r is again the location of the shock front, and r' is the coordinate in the cooling layer of extent L_c. The '+' sign corresponds to a reverse shock, the '$-$' sign to a forward shock. The functions f and g describe the normalized density and temperature stratification in the post-shock region, respectively. $f = g = 1$ returns the non-stratified, isothermal shocks. With the introduction of the dimensionless coordinate

$$\xi = 1 - \frac{|r - r'|}{L_\mathrm{c}}, \tag{3}$$

$\hat{\Lambda}_\nu$ can be written as (using the same symbols f and g again)

$$\hat{\Lambda}_\nu(T_\mathrm{s}) = \int_0^1 f^2(\xi)\, \Lambda_\nu(T_\mathrm{s}\, g(\xi))\, \mathrm{d}\xi. \tag{4}$$

In principle, the functions $f(\xi)$ and $g(\xi)$ have to be calculated from time-dependent hydrodynamic simulations of radiation driven winds. This is the topic of a forthcoming paper. In the present paper we take a first step by using simplified analytical models for the radiative and adiabatic shocks typically found in such numerical calculations.

2.1. Stationary radiative shocks

The decisive quantity to distinguish between alternative post-shock models is the cooling time, t_c, required by the shocked matter to return to the ambient wind temperature again,

$$t_\mathrm{c} = \frac{L_\mathrm{c}}{v_\mathrm{po}} \int_0^1 \frac{\mathrm{d}\xi}{h(\xi)}. \tag{5}$$

Here, $h = |v - v_\mathrm{s}|/v_\mathrm{po}$, where v and v_s are the wind speed and the shock speed, respectively, in the stellar frame; v_po is the absolute value of the speed of post-shock gas (i.e., gas immediately behind the front) relative to the front. Therefore, $v_\mathrm{po} h(\xi)$ is the speed of gas in the cooling zone relative to the shock front. If t_c is small compared with the dynamical flow time t_f,

$$t_\mathrm{f} = \frac{r}{v(r)}, \tag{6}$$

the shock can be regarded as stationary.

Because of the very high temperature in the post-shock region, the radiative acceleration of matter can be neglected. The same is true for gravitational acceleration, since for strong shocks the gravity scale height is large compared with the cooling length L_c. In such a case then, the post-shock structure is given by the stationary, 1-D plane-parallel gasdynamic equations, which include radiative cooling in the energy equation. This problem has been discussed by Chevalier & Imamura (1982; CI in the following) for special cases, where the frequency integrated cooling function follows a power law in temperature,

$$\Lambda(T) = \int_0^\infty \Lambda_\nu(T)\, \mathrm{d}\nu = A_\mathrm{R}\, T^\alpha. \tag{7}$$

In the following we shall use $A_\mathrm{R} = 1.64 \times 10^{-19}\, \mathrm{erg\, cm^3\, s^{-1}\, K^{1/2}}$ and $\alpha = -1/2$ as a reasonable approximation to the cooling function of a hot plasma for temperatures in the range $10^{4.8} \le T \le 10^{7.3}$ K (Cox & Tucker 1969; Raymond et al. 1976). Extending the analysis of CI to the cooling exponent $\alpha = -1/2$, we obtain the solution

$$\begin{aligned}
f(\xi) &= \frac{1}{h(\xi)}, \\
g(\xi) &= \tfrac{1}{3}\, h(\xi)(4 - h(\xi)), \\
\xi(h) &= \frac{1}{93\sqrt{3} - 40\pi} \Big\{ -120 \arccos\left(1 - \tfrac{1}{2}h\right) \\
&\quad + \sqrt{4h - h^2}\, \left(60 + 10h + 2h^2 + 29h^3 - 8h^4\right) \Big\},
\end{aligned} \tag{8}$$

where $0 \le h \le 1$. The total cooling time and cooling length are

$$\begin{aligned}
t_\mathrm{c} &= \frac{40}{7} \frac{C}{A_\mathrm{R}} \frac{v_\mathrm{po}^3}{\rho_\mathrm{po}}, \\
L_\mathrm{c} &= \frac{93\sqrt{3} - 40\pi}{10} \frac{C}{A_\mathrm{R}} \frac{v_\mathrm{po}^4}{\rho_\mathrm{po}},
\end{aligned} \tag{9}$$

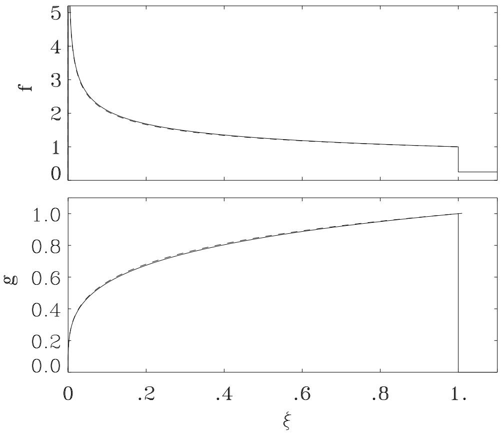

Fig. 1. Post-shock structure for a steady radiative shock after Eq. (8). The density function f and temperature function g defined in (2) are shown. Dashed line: approximation for f and g after (11).

where for a hydrogen/helium gas the constant C is given by (with m_p the proton mass, k the Boltzmann constant)

$$C = \frac{m_\mathrm{p}^{5/2}}{k^{1/2}} \frac{(1+4Y)^{5/2}}{(1+IY)(2+[1+I]Y)^{1/2}}. \tag{10}$$

The helium fraction by number is $Y = n_\mathrm{He}/n_\mathrm{H}$, and I is the number of free electrons provided per helium nucleus; hydrogen is assumed to be fully ionized. Fig. 1 shows the density function f and the temperature function g.

To the best of our knowledge, the function $\xi(h)$ in (8) cannot be inverted analytically to give $h(\xi)$. From a Taylor expansion at $h = 0$ and the requirement that $h(1) = 1$ at the beginning of the cooling zone, we find

$$h(\xi) = a\,\xi^{2/7}\left[1 + \left(\frac{1}{a} - 1\right)\xi^{2/7}\right], \tag{11}$$

where $a = \left[\frac{7}{10}\left(\frac{93\sqrt{3}}{40} - \pi\right)\right]^{2/7} \approx 0.87225$. This is accurate to better than 1.4% over the *whole* cooling zone, see Fig. 1, and is therefore used in the following.

With (8) and (11), the post-shock structure is well defined and the cooling function of the stratified shock can be calculated according to (4). The result is shown in Fig. 2 for $\log T_\mathrm{s} = 6.6$ (for gas of solar composition). The stratified shock emits significantly more radiation at soft energies, and less above 1.3 keV than an isothermal shock. This can be understood from Fig. 3. In the temperature-energy plane the Raymond-Smith function $\Lambda_\nu(T_\mathrm{s})$ has a maximum at ($\log T = 6.25; E = 0.5$ keV). According to (4), all layers with $T \leq T_\mathrm{s}$ contribute with increasing weight factor f^2 to the cooling function $\hat{\Lambda}_\nu(T_\mathrm{s})$ for structured shocks. For $\log T_\mathrm{s} = 6.6$ and $E \leq 0.5$ keV, $\Lambda_\nu(T_\mathrm{s}\,g)$ passes the maximum and, thus, $\hat{\Lambda}_\nu(T_\mathrm{s})$ becomes larger than $\Lambda_\nu(T_\mathrm{s})$. For $\log T_\mathrm{s} = 6.6$ and $E > 1$ keV, $\Lambda_\nu(T_\mathrm{s})$ decreases so rapidly that the weighting factor f^2 is not able to compensate and $\hat{\Lambda}_\nu(T_\mathrm{s}) < \Lambda_\nu(T_\mathrm{s})$ results. Fig. 4 shows the ratio $\hat{\Lambda}_\nu/\Lambda_\nu$ in the temperature-energy plane.

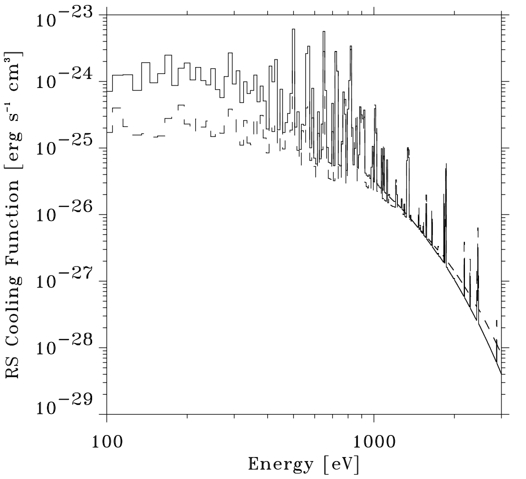

Fig. 2. Cooling function versus energy for $\log T = 6.6$. Solid: stratified radiative shock emission $\hat{\Lambda}_\nu(T)$; dashed: Raymond-Smith function $\Lambda_\nu(T)$.

To calculate the X-ray emission from an *ensemble* of embedded wind shocks, we need to know the shock temperature T_s and the filling factor e_s as functions of radius. Notice that while the density and temperature stratification, f and g, within the cooling zone are 'microscopic' functions, i.e., they depend on short-scale radiative cooling only, T_s and e_s are 'macroscopic' quantities which depend on the actual wind dynamics. One might try however to derive some ad hoc conclusions about them. Concerning the filling factor, a simple argument may proceed as follows: assume for the moment that the shock temperature is independent of radius in regions where the wind has reached a substantial fraction of its terminal velocity. From (9), the cooling length then grows as $L_\mathrm{c} \propto 1/\rho \propto r^2$. If we assume furthermore that no shocks are created beyond a certain location in the wind, and that the shocks are also not destroyed on their further propagation, the filling factor grows as $e_\mathrm{s} \propto r^2$.

However, time-dependent hydrodynamic simulations (Owocki et al. 1988; Owocki 1992; Feldmeier 1995) of initially small perturbations which grow in an unstable wind confirm these conclusions only partially[1]: here, the shock temperatures and shock spacing result from complex wind dynamics, which

---

[1] In these simulations, the smooth, stationary wind is usually transformed into a sequence of narrow, dense shells, which are separated by almost void regions. On their starward side, the shells are bound by a strong reverse shock, which decelerates a fast, inner wind stream. On their outer side, they are bound by a weak forward shock which overtakes the slower gas ahead of it (at larger radii), and compresses it into the shell.

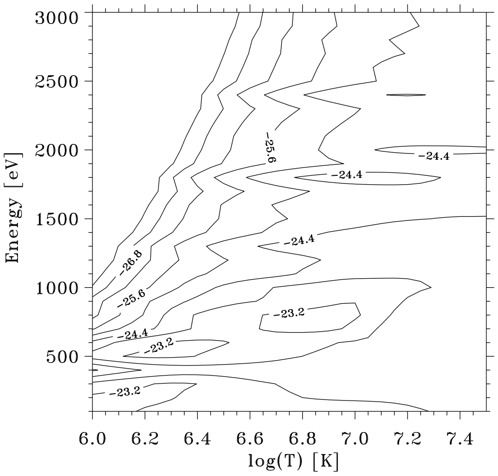

Fig. 3. Isocontours of log Λ_ν in the log T–energy plane.

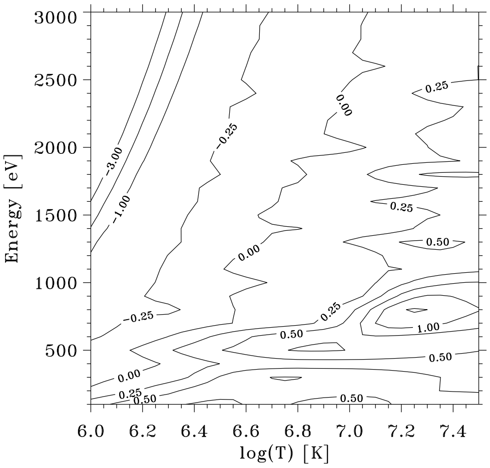

Fig. 4. Isocontours of log $(\hat\Lambda_\nu/\Lambda_\nu)$ in the log T–energy plane.

lead to frequent mergers of shocks. Notice that the latter falsify the above assertion that shocks should keep their identity. The results from these calculations are broadly consistent with constant or slowly decreasing temperatures *and* filling factors of hot gas as a function of radius. However, the details of the wind dynamics are still largely unknown, (i) due to approximations in the treatment of the radiative transfer, the small-scale structure in the wind, and thermal instabilities (see below); and (ii) since neither the location (photosphere vs. wind), the nature (pulsations, waves, noise, etc.), nor the temporal coherence (periodic vs. stochastic) of the seeding perturbations are known at present from variability observations of hot stars (cf. the volume edited by Moffat et al. 1994). Thus, for simplicity, we shall suppose in the following constant T_s and e_s throughout the wind.

Two further important restrictions have to be made. The first one concerns the thermal instability of radiative shocks. Langer et al. (1981, 1982) and CI have pointed out that for temperature exponents $\alpha \lesssim 1$ in the cooling function power law (7), a global thermal instability exists that leads to a periodic contraction and expansion of the cooling zone, i.e., to an oscillation in the position of the shock. The typical timescale of this oscillation is of the order of a few cooling times. Since the density and temperature stratification of the post-shock region change during the course of this contraction and expansion, and since these quantities enter non-linearly into the shock emission coefficient, the thermal instability will certainly affect the emitted spectrum. In the model presented here, we have simply neglected these effects to keep them analytically tractable.

The second restriction is given by the assumption that the cooling time t_c is small compared with the dynamical flow time t_f. We expect that far out in the wind at low densities, t_c will become larger than t_f and the assumption will fail. Using the stationary wind velocity law (where $\hat r \equiv r/R_*$, v_∞ is the terminal velocity, and with assumed value of β = 1),

$$v(r) = v_\infty\left(1 - \frac{b}{\hat r}\right), \qquad b = 0.99, \tag{12}$$

and the equation of continuity together with (6) and (9), we obtain for the ratio of cooling to flow time (where $\dot M$ is the mass loss rate; and T_6 is the temperature in units of 10^6 K),

$$\frac{t_\mathrm{c}}{t_\mathrm{f}} = 5.37\times10^{-4}\left(\frac{v_\infty}{10^3\,\mathrm{km/s}}\right)^2\left(\frac{\dot M}{10^{-6}\,\mathrm{M}_\odot/\mathrm{yr}}\right)^{-1}\frac{R_*}{10\,R_\odot}\times \frac{(1+4Y)(2+[1+I]Y)}{1+IY}\,T_{\mathrm{s},6}^{3/2}\,\hat r\left(1-\frac{b}{\hat r}\right)^2, \tag{13}$$

and for the ratio of the cooling length to the position of a shock, r_s,

$$\frac{L_\mathrm{c}}{r_\mathrm{s}} = 1.75\times10^{-5}\,\frac{v_\infty}{10^3\,\mathrm{km/s}}\left(\frac{\dot M}{10^{-6}\,\mathrm{M}_\odot/\mathrm{yr}}\right)^{-1}\frac{R_*}{10\,R_\odot}\times \frac{(1+4Y)^{1/2}(2+[1+I]Y)^{3/2}}{1+IY}\,T_{\mathrm{s},6}^{2}\left(\hat r - b\right). \tag{14}$$

For the O star ζ Pup, e.g., we find from Table 1 (using I = 1, cf. Sect. 3),

$$\begin{aligned}\frac{t_\mathrm{c}}{t_\mathrm{f}} &= 2.59\times10^{-3}\,T_{\mathrm{s},6}^{3/2}\,\hat r\left(1-\frac{b}{\hat r}\right)^2,\\ \frac{L_\mathrm{c}}{r_\mathrm{s}} &= 4.62\times10^{-5}\,T_{\mathrm{s},6}^{2}\left(\hat r - b\right).\end{aligned} \tag{15}$$

For T_s = 5 × 10^6 K, e.g., we obtain for ζ Pup $r_0 = 36\,R_*$ for the radius at which $t_\mathrm{c}/t_\mathrm{f}$ is unity. At this radius, $L_\mathrm{c}/r_\mathrm{s}$ = 0.04 is still small.

However, as discussed before, the actual wind dynamics may be far from stationary, and due to the progressive accumulation of the wind gas into dense shells, these values for r_0 may be (much) too large. This is discussed further in the next section.

For X-ray photons which stem from radii larger than r_0, the approximations made in this section will be invalid. Consequently, we next study an alternative approximation that will hold for locations beyond r_0.

2.2. Constant velocity adiabatic shocks

Far out in the wind, where $r \gg r_0$, the radiative cooling of the shocks can be neglected. We thus expect spherical segments of shocks that started at much smaller radii will expand undergoing adiabatic cooling only. In addition, the unperturbed wind has achieved its terminal velocity and radiative acceleration is small. Simon & Axford (1966; SA in the following) have treated such a problem for a pair of reverse-forward shock waves which propagate at constant velocity through the outer solar wind and/or interplanetary medium. As mentioned before, such pairs of shocks which enclose a shell of dense material are also expected from time-dependent hydrodynamic simulations of hot star winds.

SA solve the spherical problem of a driven shell (see below for the precise meaning) in terms of the similarity variable

$$\eta = \frac{r}{v_\mathrm{f}\, t}, \tag{16}$$

where v_f is the velocity of the forward shock front, which is therefore located at $\eta_\mathrm{f} = 1$. (At $t = 0$, the whole shell is at $r = 0$.)

This similarity variable is appropriate only for the case that all flow features (shocks and contact discontinuities) move at constant speeds. As discussed by SA, this corresponds to a temporally constant mass loss rate of the source after the shell release, where the latter is caused by a sudden jump of the density and velocity (and therefore, usually, of the mass loss rate; cf. Appendix A). The general case of a similarity variable $\eta = r/At^\delta$ corresponds to a time dependence $v_f \propto t^{\delta-1}$ of the speed of all flow features, and a change in mass loss rate $\dot{M} \propto t^{\delta-1}$ of the source after throwing off the shell. This temporal behaviour of source conditions is meant to mimic a solar flare and the subsequent return to the quiescent wind. – However, for the *radiation* driven winds of hot stars it is at present not clear how the non-similarity dynamics at small radii serves as an inner boundary condition for the similarity solution (possibly) achieved at large distances. As discussed in the foregoing section, this is both due to the unknown nature of the wind perturbations, and to the intricate shock dynamics with frequent merging, etc. (in Appendix B we shall demonstrate for a simple example how shock collisions can influence the propagation characteristics of the shocks, i.e., the parameter δ). In particular, it seems possible that the outer, adiabatic flow belongs to the class of similarity problems for which, according to Zel'dovich & Raizer (1967, Chap. XII, p. 794), the "self-similar motion originates as a result of some non-selfsimilar flow that approaches a self-similar regime asymptotically", and where the similarity exponent δ cannot be determined in advance by dimensional considerations or from the conservation laws, but has to be found from the actual solution of the problem. In light of these uncertainties, our assumption of constant shock speeds and therefore constant shock temperatures in the outer similarity regime appears to be a reasonable 'minimum hypothesis'.

One may then try to derive the radial dependence of the filling factor e_s of the completely macroscopic (T_s, e_s and f, g) adiabatic shocks: since all shells move at the same speed, and since the forward shocks propagate faster than the reverse shocks, every forward shock should eventually overtake the reverse shock of the neighboring shell ahead of it. As long as all shock speeds remain constant, and the distance between successive shells is small compared with the radii the shells are located at, $e_\mathrm{s} \propto r$. However, as shown in Appendix B, this does not imply the existence of an outer, hot corona. Instead, the filling factor of hot gas always remains < 1 (or even $\ll 1$), while it is the fraction of gas which passed through a shock transition which approaches unity.

Furthermore, time-dependent wind simulations of unstable growth show that many (if not most) radiative reverse shocks, instead of being progressively transformed into adiabatic reverse shocks at large radii $r_0 \gg 10\,R_*$, are suddenly destroyed at intermediate radii $\lesssim 10\,R_*$, and leave behind hot, adiabatic cooling gas which was heated in the front at previous times (Feldmeier 1995). – Due to these two processes of shock merging and shock destruction, a monotonically decreasing or roughly constant filling factor is more appropriate than the increasing filling factor asserted above. In the following, a constant e_s will be supposed.

Finally, in the comparison with observations it is important to realize that exposure times of ROSAT are of the order of some 1000 seconds, whereas for $r \gtrsim 100\,R_*$ the flow time is some 10^5 seconds. Therefore, every exposure reflects the momentary position and stratification of shocks in the outer wind. As a consequence, the post-shock solutions $\rho(\eta)$ and $T(\eta)$ obtained by SA describe purely spatial structures in our case, since the time t in the definition of η can be regarded as constant for every exposure.

In terms of the similarity variable from (16), the hydrodynamic quantities are written as

$$v(r,t) = \frac{rV(\eta)}{t}, \quad \rho(r,t) = \frac{\rho_0\sigma(\eta)}{r^2}, \quad p(r,t) = \frac{\rho_0\pi(\eta)}{t^2}. \tag{17}$$

Note that the velocity of *every* flow feature f, i.e., shocks and contact discontinuities, is then $V_f \equiv 1$, since $v_f = r_f\, V_f/t$ and also $v_f = r_f/t$.

The positions of the reverse shock, η_r, and the contact discontinuity inside the shell, η_c, are found from numerical integration of the ordinary differential equation (10) of SA. The two integration constants which determine a special solution are chosen to be

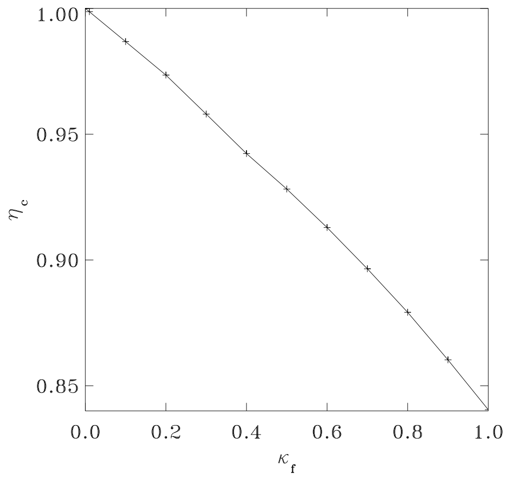

Fig. 5. Dependence of the position η_c of the contact discontinuity on the inflow parameter $\kappa_f = v_{f,pr}/v_f$.

$$\begin{aligned} \kappa_f &= v_{f,pr}/v_f, \\ \Theta &= T_{r,po}/T_{f,po}. \end{aligned} \tag{18}$$

Here and in the following, indices ‘r’ and ‘f’ refer to the reverse and forward shock, respectively. SA fixed $\kappa_f = 1$ for the solar wind by neglecting the ambient wind speed as compared with the forward shock speed. In general, for a non-negligible speed v_∞ ahead of the forward shock, one finds (with μ the mean atomic weight)

$$\kappa_f = \left(1 + \frac{3}{4}\frac{v_\infty}{v_{f,ju}}\right)^{-1} = \left(1 + \sqrt{\frac{3\mu m_p}{16k}}\,\frac{v_\infty}{\sqrt{T_{f,po}}}\right)^{-1}, \tag{19}$$

where v_{ju} is the velocity jump across the shock, and in the first equality $v_{pr} = \frac{4}{3}v_{ju}$ and $v_f = v_{hi} + \frac{1}{3}v_{ju}$ (with v_{hi} the velocity immediately behind the shock front) have been used for a strong shock in a gas with $\gamma = 5/3$. For typical O star wind speeds, and temperatures of the forward shock up to 10^7 K, $0 \leq \kappa_f \leq 0.3$.

The position of the contact discontinuity and of the reverse shock are then functions of κ_f and Θ,

$$\begin{aligned} \eta_c &= \eta_c(\kappa_f), \\ \eta_r &= \eta_r(\kappa_f, \Theta). \end{aligned} \tag{20}$$

The (numerically derived) function $\eta_c(\kappa_f)$ is shown in Fig. 5. A good fit to this is

$$\eta_c = 1 - 0.1314\kappa_f - 0.02857{\kappa_f}^2. \tag{21}$$

The function $\eta_r(\kappa_f, \Theta)$ is determined by Fig. 6. For different values of κ_f, Fig. 6 shows the dependence of the ratio of the cooling lengths of the reverse and forward shock, $(\eta_c - \eta_r)/(1 - \eta_c)$, on Θ. In the range $0 \leq \kappa_f \leq 0.3$, this can be approximated by

$$\frac{\eta_c - \eta_r}{1 - \eta_c} = (1 - \kappa_f + {\kappa_f}^2)\,\Theta^{\frac{1}{2} - 0.31\kappa_f + 0.55{\kappa_f}^2}. \tag{22}$$

From Fig. 6 (and also from the foregoing equation),

$$\lim_{\kappa_f \to 0} \frac{\eta_c - \eta_r}{1 - \eta_c} = \sqrt{\Theta}, \tag{23}$$

or, stated differently: for every adiabatic shock with small cooling length (i.e., with sufficiently low post-shock temperature) the cooling length scales as the square root of the post-shock temperature,

$$\lim_{L_c/r \to 0} L_c \propto \sqrt{T_{po}}. \tag{24}$$

This can be understood as follows. The adiabatic energy equation for a fluid particle is (with $\mathrm{d}/\mathrm{d}t$ the Lagrangian derivative) $\mathrm{d}T/\mathrm{d}t = -(\gamma - 1)\,T\,\mathrm{div}\,v$. Therefore, the cooling length scales as $L_c \approx -T(\mathrm{d}T/\mathrm{d}t)^{-1}\,v_{po} \propto (\mathrm{div}\,v)^{-1}\,v_{po}$. Assuming pressure constancy in the cooling zone (see below) one finds from the Euler equation that the velocity gradient is $v' \approx 0$. Assuming spherical symmetry, it follows that $L_c \propto \frac{r}{2v}\,v_{po}$. For all shocks with a velocity jump which is small compared with the stationary wind flow speed one can identify $v \approx v_{stat}$. Furthermore, since for such weak shocks the cooling zone is short compared with dynamical length scales, $L_c \ll r$, the radius r in the foregoing expression for L_c is a well-defined, single location. Using finally $v_{po} \propto \sqrt{T_{po}}$, the above assertion $L_c \propto \sqrt{T_{po}}$ follows.

Within the cooling layers behind the forward and reverse shocks, the spatial post-shock coordinate ξ introduced in (3) can be related to η by

$$\begin{aligned} \eta &= \eta_c + \xi(1 - \eta_c) \quad \text{forward shock}, \\ \eta &= \eta_c - \xi(\eta_c - \eta_r) \quad \text{reverse shock}, \end{aligned} \tag{25}$$

where $0 \leq \xi \leq 1$.

SA give a power-law expansion (their Eq. 11) for the density and temperature in the neighborhood of the contact discontinuity, that leads to the following functions f and g in (2) (the first position in the braces corresponds to the forward shock, the second to the reverse shock),

$$\begin{aligned} f(\eta) &= \{1, \Theta^{-1}\}\left(\frac{\eta_{\{f,r\}}}{\eta}\right)^2 h(\eta)^{-4/9}, \\ g(\eta) &= \frac{1}{f(\eta)}, \\ h(\eta) &= \frac{(\eta_c/\eta)^3 - 1}{(\eta_c/\eta_{\{f,r\}})^3 - 1}. \end{aligned} \tag{26}$$

Again we defined $f_f = g_f = 1$ immediately behind the forward shock (notice that $\sigma(\eta) \equiv 4\eta^2 f(\eta)$, since SA use the convention $\sigma_{f,pr} = 1$). In taking $g = 1/f$, we assume the pressure to

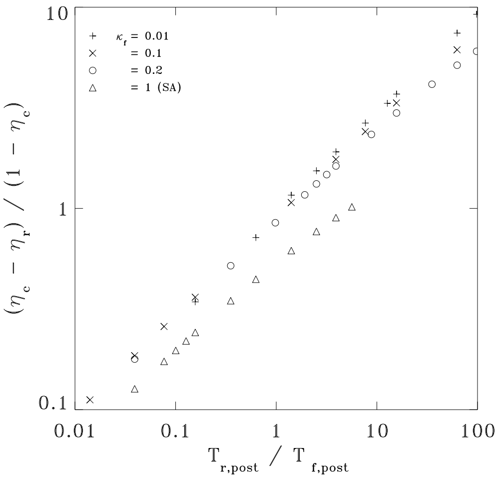

Fig. 6. Dependence of the ratio of the cooling lengths of the reverse and forward shock, $(\eta_c - \eta_r)/(1 - \eta_c)$, on the shock temperature ratio Θ, for different values of the inflow parameter κ_f.

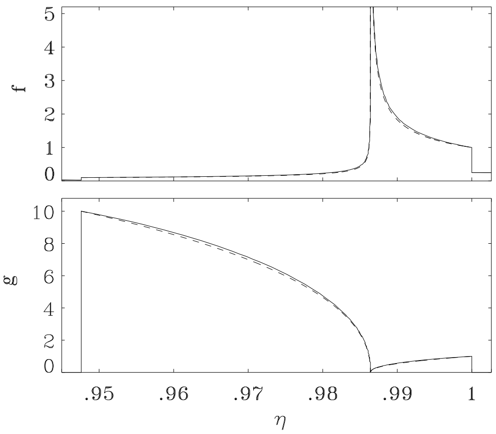

Fig. 7. Full line: exact numerical solution for the SA shell (κ_f = 0.1; Θ = 10). Dashed line: approximate analytical solution (26).

be constant through both cooling zones, $\pi_{po} = \frac{3}{4}{\kappa_f}^2$, which is actually a very good approximation (cf. SA). This pressure constancy also allowed us to fix the density at the reverse shock. As can be seen from Fig. 7, the expansion (26) also describes the overall run, found by numerical integration, of f and g within the cooling zones very well, and is therefore used to calculate the emission coefficient (2) analytically.

Comparing Figs. 1 and 7, one sees that the cooling in the adiabatic shock proceeds more uniformly (i.e., the change in slope over the cooling zone is smaller) than in the radiative shock. The reason is that the gas in the radiative shock undergoes runaway cooling (Field 1965), i.e., it cools the better the colder and therefore denser it already is. This is also reflected in Fig. 8 where the cooling functions of an adiabatic shock (Θ = 1 is used here) and a radiative shock of temperature $\log T$ = 6.6 are shown. The adiabatic shock has more emission at low energies, and less emission at high energies than the radiative shock; i.e., the adiabatic shock has the softer spectrum.

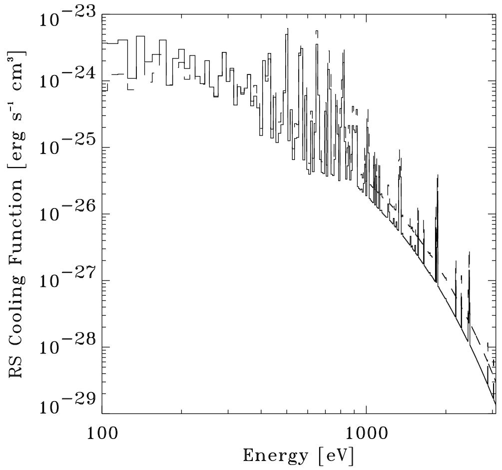

Fig. 8. Cooling function versus energy for $\log T$ = 6.6 of an adiabatic shock with Θ = 1 (full line) and of a radiative shock (dashed line).

3. Spectral fits for three selected O stars

We assume that the shock temperature, T_s, and the volume filling factor, e_s, have one single, unique value (i) for radiative and adiabatic shocks, and (ii) for reverse and forward shocks. T_s and e_s are then the only two parameters to fit the X-ray spectrum. These restrictions are again meant to make our model directly comparable to the Hillier et al. model, with the one central difference that we use structured cooling zones behind shocks instead of isothermal shocks. We solve the X-ray transfer via a formal integral, where the wind flow is assumed to be spherically symmetric. The X-ray emission is given by (2). (As in Hillier et al., we assume that no X-rays are emitted from below R_{min} = 1.5 R_*.) The bound-free and line opacities for the cold background wind are taken from full NLTE models, and the K-shell opacity is treated for the elements C, N, O, Ne, Mg, Si, S (Daltabuit & Cox 1972).

In the following we present results for the three O stars from Table 1. (The analysis of the full sample of 42 O stars observed with the ROSAT PSPC is topic of a forthcoming publication; preliminary results are given in Kudritzki et al. 1996). They should be ideal candidates to test our X-ray model since they have among the highest signal-to-noise ratio within our full sam-

Table 1. Parameters of the analyzed O stars.

star	classif.	$\frac{T_{\rm eff}}{10^3\,{\rm K}}$	$\log g$	$\frac{R_*}{R_\odot}$	Y	$\frac{v_\infty}{\rm km/s}$	$\frac{\dot M}{10^{-6}\,M_\odot/{\rm yr}}$	$\log\left(\frac{N_{\rm H}}{\rm cm^{-2}}\right)$
ζ Pup	O4 I(f)	42	3.6	19	0.12	2250	5.9	20.00
ι Ori	O9 III	34	3.5	18	0.18	2350	0.8	20.30
ζ Ori	O9.7 Ib	32	3.2	24	0.10	1850	2.4	20.48

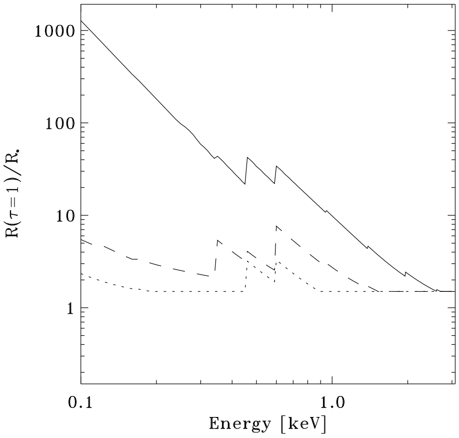

Fig. 9. Location of optical depth unity for X-rays in the ROSAT energy band for the three stars from Table 1: ζ Pup (full); ι Ori (dotted); ζ Ori (dashed).

ple. Furthermore, their stellar and wind parameters are known to a good accuracy: for ζ Pup, the photospheric parameters are taken from Kudritzki et al. (1983) with the log g correction for 'unified' effects and centrifugal forces from Puls et al. (1996). For ι Ori, photospheric parameters are from Lamers & Leitherer (1993) and references therein; and for ζ Ori from Voels et al. (1989). The terminal velocities for all three stars are from Haser (1995). The mass loss rates are from Puls et al. (1996), where for ι Ori and ζ Ori the measurements of Lamers & Leitherer have been reanalyzed. Additionally, the mass loss rate of ζ Ori has been recalibrated to the photospheric parameters from Voels et al. and the terminal velocity from Haser, following the procedure described in Puls et al. Metal abundances (which enter through the opacities) are derived for ζ Pup from an analysis of UV spectra (Pauldrach et al. 1994; Haser 1995). For ι Ori we assume CNO processed material, and for ζ Ori we presently assume solar abundances. Finally, the interstellar hydrogen column densities, $N_{\rm H}$, are from Shull & van Steenberg (1985) using interstellar Ly-α. This is certainly advantageous over deriving $N_{\rm H}$ from the X-ray fits themselves.

We notice that ζ Ori showed an *episodic* change in its X-ray emission during a period of 2 days from Sep 23 to 25 in 1992, when the count rate in the energy band from 0.6 to 2.4 keV increased by $\approx$ 30% (Berghöfer & Schmitt 1994). The latter authors proposed a single, strong reverse shock as the cause. This event is not included in our data set which reaches only to Sep 19, 1992. For ζ Pup, on the other hand, Berghöfer et al. (1996) found a *modulation* of period 16.7 hours and amplitude $\lesssim$ 10% of the count rate in the energy band from 0.9 to 2.0 keV. This was traced back to periodic density variations at the wind base. Since our data set for ζ Pup covers $\approx$ 16 cycles of this modulation, the data should define a proper average emission. – In total, we conclude that our present *stationary* model for the X-ray emission should be adequate to analyze the ROSAT observations of the above three program stars.

For the comparison of our model fits with the ROSAT observations we have also to consider sources of uncertainties of the data themselves, especially due to the calibration of the PSPC. As advised by the ROSAT User's Handbook (Oct 1994, draft version) we excluded energies above 2.2 keV when fitting the observed spectrum due to insufficient calibration of the effective area and energy response above 2 keV. The Handbook also recommends not using energies below 0.11 keV (detector channel 11) for observations taken after October 11th 1991. Half of the integration time for ζ Ori, and all the integration time for ζ Pup and ι Ori occurred after this date. Therefore we excluded the first data point in the observed spectrum. Finally, uncertainties in the calibration of the PSPC detector response can account for $\approx$ 20% of the deviations between model and observation at the prominent dip in the observed spectra near 0.4 keV. We therefore also ignored the 2 to 4 data points in the range from 0.38 keV to 0.48 keV in the fitting procedure.

Fig. 9 shows the location of optical depth unity (with optical depth zero at the observer) in the winds of the three stars from Table 1, for X-ray energies in the ROSAT band. From this figure it is clear that soft X-rays can escape the dense wind of ζ Pup only from large radii. Physically, this is due to the fact that helium starts to recombine to He$^+$ from $\approx 6\,R_*$, which increases the opacity enormously (cf. Hillier et al. 1993). In contrast, helium stays fully ionized in the winds of ι Ori and ζ Ori up to very large radii. Accordingly, the ROSAT spectrum of ζ Pup (cf. Fig. 10) is harder than that of ι Ori (Fig. 11). The spectrum of ζ Ori in Fig. 12 lies intermediate between the former two. This is mostly due to the larger $N_{\rm H}$ in direction of this star than of ι Ori.

Also shown in Figs. 10, 11, and 12 are our best fits to the ROSAT spectra of ζ Pup, ι Ori, and ζ Ori respectively, together with the fits from the Hillier et al. isothermal shock model assuming one or two hot components. Table 2 gives the post-shock

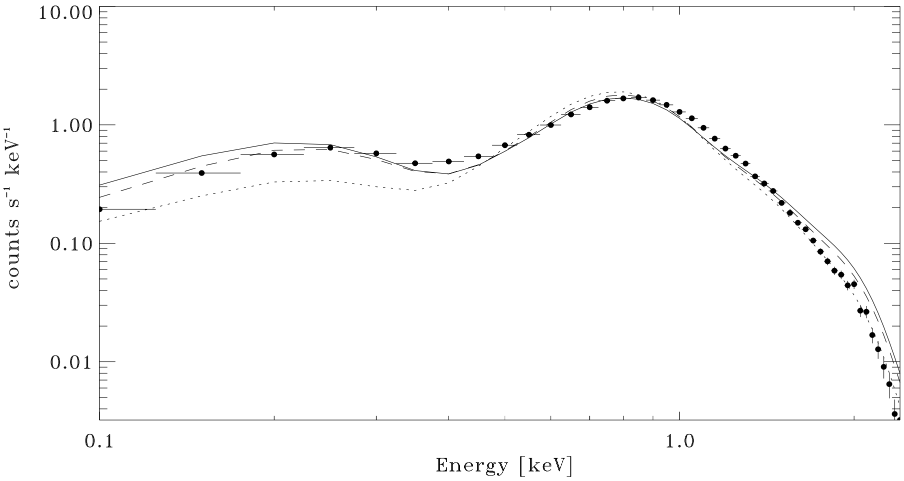

Fig. 10. ROSAT PSPC spectrum of ζ Pup (error bars) together with our best fit (full line) assuming inner radiative and outer adiabatic shocks. For comparison, the best fits from a one-component (dotted line) and two-component (dashed line) isothermal shock model after Hillier et al. (1993) are also shown.

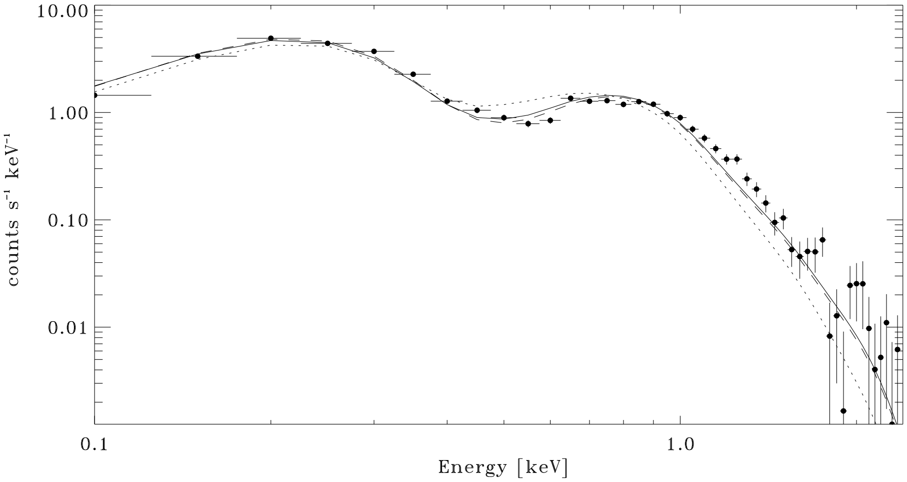

Fig. 11. Spectrum and fits of ι Ori. Labeling of the curves as in Fig. 10.

temperatures and the volume filling factors derived for the three stars. The following conclusions can be drawn from this.

(1) Temperatures: The post-shock temperatures of the present model with resolved cooling zones are, for all three stars, $\approx 30\%$ higher than the temperatures of the hotter shock family of the two-component model after Hillier et al.; they are 60% to 80% higher than the temperatures from their one-component model. The need for higher temperatures in the present approach is clear from the fact that the Hillier et al. temperatures correspond to averages over the cooling zones.

(2) Filling factors: (a) The sum of the two individual filling factors from the two-component model after Hillier et al. is about equal to the filling factor from their one-component model. (b) The latter is about 2.7 times the filling factor from our

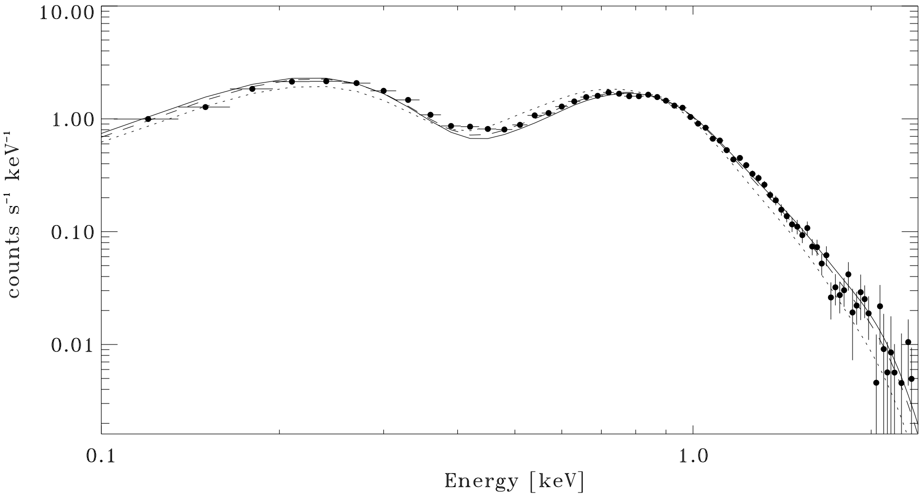

Fig. 12. Spectrum and fits of ζ Ori, cf. Fig. 10.

Table 2. Derived post-shock temperatures and volume filling factors for the O stars from Table 1; both for the present wind model which assumes radiative and adiabatic shock cooling zones, and for the one- and two-component isothermal shock models after Hillier et al. (1993).

		cooling zones	isothermal	
			2-comp.	1-comp.
ζ Pup	$\log T_s$ =	6.75	6.64 / 6.20	6.54
	e_s [10^{-3}] =	4.3	6.8 / 4.4	11
ι Ori		6.68	6.58 / 6.14	6.43
		35	53 / 31	96
ζ Ori		6.68	6.57 / 6.27	6.46
		5.0	7.9 / 4.3	14

model with resolved cooling zones. – The reason for (a) is that the Raymond-Smith function at energies $0.1 \lesssim E$ [keV] $\lesssim 0.5$ and temperatures $6.3 \lesssim \log T \lesssim 6.7$ can be very roughly approximated (cf. Fig. 3) by $\Lambda_\nu(T) \approx A_\nu T^\alpha$, with $\alpha \gtrsim -1/2$. This implies a comparable contribution from both the hotter and colder component to the soft X-ray flux, i.e., the total filling factor is the sum of the individual filling factors. – The main reason for (b) is the density stratification of the cooling zone: for simplicity we consider only radiative shocks, and use $h(\xi) = \xi^{2/7}$ as an approximation to (11). We suppose that the frequency *integrated* emission from a radiative shock and an isothermal shock should be equal. For the cooling function from (7), with exponent $\alpha = -1/2$, Eqs. (1) and (2) give then

$$(e/\sqrt{T})_{\rm iso} = 7\sqrt{3}\,(2-\sqrt{3})\,(e/\sqrt{T})_{\rm rad} \approx 3.2\,(e/\sqrt{T})_{\rm rad}. \quad (27)$$

Since the temperatures are fixed from the spectral fits, where typically $T_{\rm rad} \approx 1.7\,T_{\rm iso}$ results (cf. item 1), we are left with $e_{\rm iso} \approx 2.5\,e_{\rm rad}$, in good agreement with the above figure of 2.7.

(3) Fit quality: Our fits with 2 adjustable parameters are better than (or, in the case of ζ Ori, equally as good as) the one-component fits of Hillier et al. (also 2 parameters), and are almost as good as their two-component fits (4 parameters). This is one of the main results of the present paper. – Actually, we find that the two-component Hillier et al. model has too many free parameters, in that the temperature of the hotter component is often left unconstrained by the fit procedure by orders of magnitude. The fits are then to be considered somewhat fortuitous. Furthermore, we note that the one-component fit for ζ Ori is already very good, and only minor achievements can be won from the other two models. ζ Ori seems to be exceptional in this respect since no other star in our full sample can be fitted equally well with a one-temperature model.

As was discussed in the foregoing sections, time-dependent hydrodynamic simulations of hot star winds indicate (i) that reverse shocks are generally stronger than forward shocks; and (ii) that the reverse shocks are abruptly destroyed at relatively small radii, instead of being gradually transformed into adiabatic shocks at large radii. We simulate this shock destruction by applying $r_0 = 8\,R_*$ (cf. Section 2.2) in our fit procedure, since in a first, crude approximation the leftover, adiabatic cooling gas can again be viewed as an SA cooling layer. This gives almost identical results to the ones in Table 2: the derived temperatures and filling factors differ by ≈ 10% only, and the fit quality is about equal. To test the importance of item (i), we assume $\Theta = 10$ for adiabatic shells, instead of $\Theta = 1$ above. Using a large r_0 from stationary wind densities (cf. Eq. 13), the fit quality is again comparable to the one from Figs. 10 to 12 (however, usually not as good), and the derived temperatures and filling factors differ by $\approx$ 30%. Finally, applying both $r_0 = 8\,R_*$ and $\Theta = 10$ at once results in definitely poorer fits, and the derived parameters differ by $\approx$ 40% from the ones in Table 2. – However, we do not consider either Θ or r_0 to be adequate fit parameters; instead they should be fixed to plausible values. Valuable information in this respect may – hopefully – be gained from time-dependent hydrodynamic wind simulations.

The question remains as for the influence of the interstellar column density on our results. Varying $\log N_{\rm H}$ within the estimated error bounds of Shull & van Steenberg, $\Delta \log N_{\rm H}$ = (ζ Pup: ± 0.05; ι Ori: ± 0.15; ζ Ori: ± 0.1), alters the temperatures by $\Delta \log T_{\rm s}$ = (∓ 0.01; ∓ 0.08; ∓ 0.06), and the filling factors by $\Delta e_{\rm s} = (\pm 0.2; \pm 10; \pm 1) \times 10^{-3}$ for the model with cooling zones. Recently, Haser (1995) derived a column density to ζ Ori of $\log N_{\rm H}$ [cm^{-2}] = 20.34, which is slightly off the error interval of Shull & van Steenberg (1985). This low $N_{\rm H}$ results in a somewhat poorer fit: because the free-free opacity drops $\approx E^{-3}$, the hard part of the spectrum is practically left unaltered – and so should be the fit parameters. On the other hand, the soft X-ray flux is enhanced by lowering the column density, and deviates from the ROSAT data then. Assuming that the true $N_{\rm H}$ to ζ Ori lies at the lower edge of values allowed by Shull & van Steenberg (1985), our shock temperature for ζ Ori from Table 2 would be 15% too low, and the filling factor 25% too high.

Finally we add some comments about the fit quality near the dip at 0.4 keV. As mentioned above, we ignored the data points in this neighborhood due to calibration uncertainties in the detector response. If, on the other hand, these data points are included, the largest deviations between model and observation are found if helium is fully ionized throughout the wind. The reason is that in the latter case the K-shell opacity is the dominant opacity source at energies around 0.4 keV. Preliminary test calculations indicate that especially a change in carbon abundance can have a large effect on the dip due to its proximity to the C IV K-shell edge at 0.347 keV. But even the nitrogen and oxygen K-shell edges which are located at somewhat higher energies can affect the dip. The reason is that monochromatic photons are spread out over several detector channels. Future work will have to show to what degree this can remove deviations between model and observation at energies near 0.4 keV.

We close this section with a comparison of our method and results with those of Cohen et al. (1996). These authors used both ROSAT and EUVE data to constrain high-temperature emission models for the B giant ϵ CMa (B2 II). They arrived at the strong conclusion that the simplest model (from a hierarchy of increasing complexity) to fit both the X-ray spectrum and the five observed EUV iron emission lines between $\approx$ 40 and 70 eV simultaneously is one where: (i) the hot gas is distributed through a cold background wind, (ii) the opacity of this cold wind for EUV radiation and soft X-rays is included, and (iii) the emitting plasma has a continuous temperature distribution. Contrary, a two-temperature model is not sufficient. The total number of free parameters of this fit model is five, where $\dot{M}/v_\infty$ is taken as a free parameter which characterizes the wind attenuation. Notice that all three items (i) to (iii) are also specific to the model presented here.

Cohen et al. make a power-law Ansatz for the temperature dependence of the differential emission measure, $Q \propto T^a$, where Q is defined as $Q(T) \equiv n_{\rm p} n_{\rm e} {\rm d}V/{\rm d}T$, i.e.

$$\epsilon_\nu = \int n_{\rm p} n_{\rm e}\, \Lambda_\nu(T)\, {\rm d}V = \int Q(T)\, \Lambda_\nu(T)\, {\rm d}T. \qquad (28)$$

Translating this to our approach from Sec. 2 where temperature changes are due to (radial) cooling zones only, $T = T(\xi)$, but where the shock-temperature is *not* a function of radius, we have

$$Q \propto f^2 \frac{{\rm d}\xi}{{\rm d}g} \propto \frac{1}{g^2 g'}\ , \qquad (29)$$

with the functions f and g – where $T \propto g$ – defined in (2), and $g' \equiv {\rm d}g/{\rm d}\xi$. In the second proportionality of (29) we made use of the approximation that the pressure is almost constant in the cooling zone, $f \propto 1/g$, cf. (8) and (26). For radiative shocks then, from (11), $g \propto \xi^{2/7}$, i.e. $g' \propto g^{-5/2}$, or $a = 1/2$. In contrast, for adiabatic shocks, g is seen from (26) to vary between $g \propto \xi^2$ and $g \propto \xi^{2/3}$, which corresponds to $a = -5/2$ and $a = -3/2$, respectively. Cohen et al. (1996) found from their fits $a = -0.8 \pm 0.35$, which lies within this range of a-values for radiative vs. adiabatic shocks. We can even push this argument further. Our calculated X-ray spectra in the present paper are dominated by inner radiative shocks, with the outer adiabatic shocks serving more or less as a correction term to the soft X-ray flux. On the other hand Cohen et al. analyze a rather thin wind with $\dot{M} \approx 2 \ldots 6 \times 10^{-8}\ M_\odot$/yr, and correspondingly derive filling factors of $\lesssim 0.1$ which are larger than our values in Table 2. (Notice that the global filling factor of Cohen et al. 1996 is identical to our local filling factor since the latter is assumed to be radius independent.) Both the low $\dot{M}$ and the rather large filling factor are hints that cooling by adiabatic expansion may already be competitive to radiative cooling in this B star wind at low heights – which in turn could be a plausible explanation why the value for a of Cohen et al. lies between the above values for radiative vs. adiabatic shocks. However, this is speculation since in principle we believe that some kind of radial temperature stratification is realized in the wind; our claim is therefore only that our fit model is consistent with the findings of Cohen et al. (1996).

4. Summary

We have generalized the isothermal shock emission coefficient of the X-ray transfer model of Hillier et al. (1993) to include the effects of radiative and adiabatic cooling layers behind shock fronts. Under the assumption that all shocks in the wind have the same temperatures and filling factors, our fits to high-quality ROSAT PSPC spectra of three selected O stars are of about the same quality as the two-component fits of Hillier et al., where the latter authors however had to adjust twice as many parameters. Furthermore, the shock temperatures and filling factors derived from the two-component model are consistent with the temperature and density stratification of cooling zones. This supports the idea that the observed two- (or multi-) component X-ray spectra can be traced back to such stratified cooling zones. However, we cannot exclude an additional contribution from a radius-dependency of shock temperatures and filling factors.

Our model establishes a robust framework within which certain X-ray properties of hot stars – here: temperatures and filling factors – are defined, probably in an averaged sense. Therefore, it should be adequate to *analyze* the sample of ROSAT PSPC observations of 42 O stars. However, the model is meant as a first approximation only to the real structures which emit X-rays in hot star winds. A discussion of such possible flow phenomena, including shell collisions and 'old' hot gas leftover from shock destruction, is given in Feldmeier (1995).

The ROSAT data pose severe constraints on hydrodynamic models which try to *synthesize* the X-ray spectra from the emission of instability-generated shocks. The most serious concern is the rather small amount of hot gas usually predicted from these models, with filling factors being one or two orders of magnitude below those derived from spectral fits; but this could be the result of our present lack of knowledge of the trigger mechanism. The spectrum synthesis from time-dependent hydrodynamic wind models will be the subject of a forthcoming paper.

Acknowledgements. We thank Drs. A. Fullerton, S. Owocki, U. Springmann, J. Hillier, S. Haser, L. Lucy, W. Ockham, and H. Wendker for enlightening discussions, and J. Schmitt and T. Berghöfer for supplementary PSPC spectra of ζ Ori. This work was supported by the BMFT under contract 50 OR 9304, and by the DFG under contracts Pa 477/1-1 and 1-2.

Appendix A: inner and outer mass flow of the adiabatic shell

Here we derive an approximate expression which relates the properties of an adiabatic SA shell with the jump in the mass loss rate of the star at the time the shell is released.

Using (17), the mass flow $\dot{M} = 4\pi r^2 \rho v$ through a sphere of radius r can be written as

$$S \equiv \eta\sigma V = \frac{\dot{M}}{4\pi v_{\rm f}\rho_0}, \tag{A1}$$

where S is the dimensionless mass flux. Since S and $\dot{M}$ are constant outside the shell, we have (using $\rho_0 \equiv \rho_{\rm f,pr} r_{\rm f}^2$)

$$\dot{M}_{\rm source} = \dot{M}_{\rm in} = 4\pi\rho_{\rm f,pr} r_{\rm f}^2 v_\infty \frac{v_{\rm f}}{v_\infty} S_{\rm in} = \dot{M}_{\rm out}\frac{v_{\rm f}}{v_\infty} S_{\rm in}, \tag{A2}$$

where $\dot{M}_{\rm source}$ is the mass flux of the source at $r = 0$, and $\dot{M}_{\rm in}$ (resp. $\dot{M}_{\rm out}$) is the mass flow ahead of the reverse (resp. forward) shock. Using (18), we have

$$\frac{\dot{M}_{\rm in}}{\dot{M}_{\rm out}} = \frac{1}{1-\kappa_{\rm f}}\, S_{\rm in}. \tag{A3}$$

This ratio is infinite in SA since they used $v_\infty = 0 = \dot{M}_{\rm out}$. Applying the usual shock jump conditions, and assuming the analytical SA solution in the neighborhood of the contact discontinuity (their Eq. 11, our Eq. 26) to apply over the whole shell (see Fig. 7 for the accuracy of this approximation), we have finally

$$\frac{\dot{M}_{\rm in}}{\dot{M}_{\rm out}} = \frac{1}{1-\kappa_{\rm f}}\frac{\eta_{\rm r}^3}{\Theta}\left(1+\frac{12}{5}\left[\left(\frac{\eta_{\rm c}}{\eta_{\rm r}}\right)^3-1\right]\right). \tag{A4}$$

For sufficiently weak shocks $\kappa_{\rm f} \approx 0$ and $\eta_{\rm r} \approx \eta_{\rm c} \approx 1$, and the last equation reduces to a trivial consequence of the presumed pressure constancy inside the shell,

$$\frac{\dot{M}_{\rm in}}{\dot{M}_{\rm out}} \approx \frac{T_{\rm po,for}}{T_{\rm po,rev}} = \Theta^{-1}. \tag{A5}$$

Appendix B: shock collisions in the outer wind

A SA shell, which is enclosed by two adiabatic shocks, expands on its propagation through the wind: the front of the outer, forward shock propagates faster than the shell center (i.e., the contact discontinuity), whereas the front of the inner, reverse shock propagates slower than the shell center. Therefore, if similar SA shells follow upon each other, every forward shock should eventually overtake the reverse shock ahead of it. The question arises (cf. §2) whether this leads to an outer, hot corona surrounding the star. In this appendix we show that instead the shock collision causes a sawtooth-like sequence of forward shocks to occur. Its filling factor of hot gas is roughly comparable with that of the inner SA shells. However, the forward shocks decay with radius, even if the inner SA shocks have constant strength (at least long before any mutual interactions). Since both the SA shells and the forward shocks are similarity solutions asymptotically (i.e., for large distances between shells or shocks), this illustrates how a shock collision can change the similarity parameter δ. In the absence of detailed knowledge of the wind dynamics, we took this in §2 as a justification to fix the value of δ from the outset.

We set up the following hydrodynamic test of multiple adiabatic shells. The initial data are for a stationary, spherical symmetric wind of constant velocity, and density $\rho \propto 1/r^2$. In the SA solution, a single shell is created by a sudden jump in density and speed at the source location $r = 0$ at time $t = 0$. To create multiple shells instead, we use the step function

$$F(t) = H\left(t \bmod \tau - \tfrac{1}{2}\tau\right), \tag{B1}$$

where H is the Heavyside function, and τ is the time interval between the release of two shells. We apply as an inner boundary condition

$$\begin{aligned} v(r_{\rm min}, t) &= v_0[1-F(t)] + v_s F(t), \\ \rho(r_{\rm min}, t) &= \rho_0[1-F(t)] + \rho_s F(t). \end{aligned} \tag{B2}$$

The values for v_0, ρ_0 and v_s, ρ_s are chosen from the analytical approximation (26) to the single-shell SA solution for $\kappa_{\rm f} = 0.1$, and equal post-shock temperatures, $\Theta = 1$. We chose $v_{\rm f} = 1$ and $\rho_0 = 1/r_{\rm min}^2$. The temperature of the start

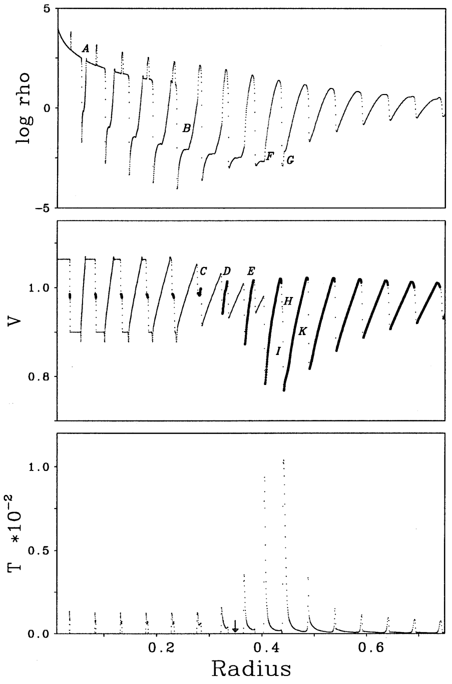

Fig. 13. Hydrodynamic test calculation of multiple SA shells, with a forward/reverse shock merger at $r \approx 0.45$ (normalized units). Dots indicate pre-shock gas, filled circles post-shock gas.

model, and also at the inner boundary over the course of time, is $T = 10^{-8}(1 - \kappa_{\rm f})^2/\gamma$ (we use units $k = m_{\rm p} = 1$ here, so that $T_{\rm po} = \frac{3}{16}\kappa_{\rm f}{}^2$), resulting in strong shocks of Mach number $\approx 10^3$. Finally, $\tau = 0.05$ is chosen, which results in a shock collision at $r \approx 0.45$. We use 5,000 logarithmically spaced grid points from $r_{\rm min} = 0.01$ to $r_{\rm max} = 1$. As long as the relative speed of forward and reverse shocks remains constant, the logarithmic grid ensures a shell to be equally well resolved at all radii, since both the grid distance and the shell extension grow $\propto r$. (In Fig. 13, already 1330 grid points lie in between $r_{\rm min}$ and the location of the first reverse shock.) The model is followed up to a time $t = 4$, corresponding to 4 flow times from the inner to the outer grid boundary. However, even at $t = 1$ the flow structure is almost identical to the one in Fig. 13. We used a time-explicit hydrodynamics code which solves the continuity, momentum, and energy equations in integrated form on a staggered grid by applying van Leer (1977) advection. For details we refer to Reile & Gehren (1991) and Feldmeier (1995).

We find from this simulation that the shock collision transforms the inner shell sequence into an outer forward shock sequence, where the latter decays with radius. We now look into this transformation in some more detail.

1. The use of a step function creates two forward facing rarefaction waves (cf. Courant & Friedrichs 1948; Zel'dovich & Raizer 1967) with a linear velocity law between subsequent shells, seen at A or B in Fig. 13. The waves are separated from each other by a region of $v(r,t) = r/t$, $\rho(r,t) = {\rm const}/t^3$ (the density plateau at B). A forward shock occurs both at the tail of the inner and at the head of the outer wave. (The shocks appear to be isothermal since their cooling zones are not resolved. We will not refer to these shocks any more in the following, but only to the shell enclosing shocks.) Fluid particles propagate through this whole domain from right to left. Notice that at A the rarefaction waves and the shell shocks are still separated by regions of stationary wind (v = const and $\rho \propto 1/r^2$), while at B and beyond they are in contact.

2. The velocity law of the rarefaction waves causes a decreasing pre-shock speed at both shocks from about C on. The shocks 'project' this velocity law into the post-shock domain, cf. D and beyond. In this way, the forward shock is accelerated, and the reverse shock is decelerated. At this stage, the shocks move away from the shell center in a symmetric fashion.

3. However, from E on an asymmetry shows up between forward shocks (getting weaker, and less accelerated) and reverse shocks (getting stronger, and more strongly decelerated). The reason is that the forward shock propagates into a strongly increasing density stratification, the reverse shock into a decreasing stratification.

4. From F to G, the reverse shock propagates through the broad density minimum, and sweeps up the gas located there. H and I show the forward and reverse shock just before merging.

5. Beyond K then, only forward shocks exist, which decay with radius. Finally, notice that for the inner shell sequence a gas element can undergo at most one shock transition by entering a shell, while for the outer forward shock sequence every gas element undergoes repeated shock transitions. This is indicated in the velocity diagram of Fig. 13 by marking pre-shock gas with dots, and post-shock gas with filled circles.

This sequence of events depends somewhat on the special boundary conditions (step function) chosen. However, by applying instead a power law decline in source conditions after shell throw-off, the shell sequence is again transformed into a forward shock sequence, so that this result should hold quite generally. Notice that the use of a power law leads to decelerated shells which can no longer be described by the SA similarity variable (16).

References

Berghöfer T.W., Schmitt J.H.M.M., 1994, ApSS 221, 309
Berghöfer T.W., Baade D., Schmitt J.H.M.M., et al., 1996, A&A 306, 899
Carlberg R.G., 1980, ApJ 241, 1131
Chevalier R.A., Imamura J.N., 1982, ApJ 261, 543 (CI)
Cohen D.H., Cooper R.G., MacFarlane J.J., et al., 1996, ApJ 460, 506
Courant R., Friedrichs K.O., 1948, Supersonic flow and shock waves. Interscience Publishers, New York
Cox D.P., Tucker W.H., 1969, ApJ 157, 1157
Daltabuit E., Cox D., 1972, ApJ 173, L13

Drew J.E., Denby M., Hoare M.G., 1994, MNRAS 266, 917
Feldmeier A., 1995, A&A 299, 523
Field G.B., 1965, ApJ 142, 531
Haser S., 1995, PhD thesis, Universität München
Hillier D.J., Kudritzki R.P., Pauldrach A.W., et al., 1993, A&A 276, 117
Krolik J.H., Raymond J.C., 1985, ApJ 298, 660
Kudritzki R.P., Simon K.P., Hamann W.R., 1983, A&A 118, 245
Kudritzki R.P., Palsa R., Feldmeier A., Puls J., Pauldrach A.W.A., 1996, in: Zimmermann H.U., Trümper J., Yorke H. (eds.) Röntgenstrahlung from the universe. MPE Report 263, Garching, p. 9
Lamers H.J.G.L.M., Leitherer C., 1993, ApJ 412, 771
Langer S.H., Chanmugam G., Shaviv G., 1981, ApJ 245, L23
Langer S.H., Chanmugam G., Shaviv G., 1982, ApJ 258, 289
Lucy L.B., 1984, ApJ 284, 351
Lucy L.B., Solomon P.M., 1970, ApJ 159, 879
Moffat A.F.J., Owocki S.P., Fullerton A.W., St-Louis N. (eds.), 1994, Instability and variability of hot star winds. Kluwer, Dordrecht
Owocki S.P., 1992, in: Heber U., Jeffery S. (eds.) The atmospheres of early-type stars. Springer, Heidelberg, p. 393
Owocki S.P., Rybicki G.B., 1984, ApJ 284, 337
Owocki S.P., Rybicki G.B., 1985, ApJ 299, 265
Owocki S.P., Castor J.I., Rybicki G.B., 1988, ApJ 335, 914
Pauldrach A.W.A., Kudritzki R.P., Puls J., Butler K., Hunsinger J., 1994, A&A 283, 525
Puls J., Kudritzki R.P., Herrero A., et al., 1996, A&A 305, 171
Raymond J.C., Smith B.W., 1977, ApJS 35, 419
Raymond J.C., Cox D.P., Smith B.W., 1976, ApJ 204, 290
Reile C., Gehren T., 1991, A&A 242, 142
Shull J.M., van Steenberg M.E., 1985, AJ 294, 599
Simon M., Axford W.I., 1966, Planet. Space Sci. 14, 901 (SA)
Van Leer B., 1977, J. Comp. Phys. 23, 276
Voels S.A., Bohannan B., Abbott D.C., Hummer D.G., 1989, ApJ 340, 1073
Zel'dovich Ya.B., Raizer Yu.P., 1967, Physics of shock waves and high-temperature hydrodynamic phenomena. Academic Press, New York

This article was processed by the author using Springer-Verlag LaTeX A&A style file *L-AA* version 3.

Astron. Astrophys. 322, 878–895 (1997)

ASTRONOMY
AND
ASTROPHYSICS

A possible origin for X-rays from O stars

A. Feldmeier, J. Puls, and A.W.A. Pauldrach

Universitäts-Sternwarte, Scheinerstr. 1, D-81679 München, Germany

Received 10 October 1996 / Accepted 16 November 1996

Abstract. X-ray spectra of hot, massive stars provide convincing evidence for thermal emission that extends far out into their stellar winds. Accordingly, strong shocks were proposed as sources of the X-ray emission, where the shocks result from the line-driven instability. We show from hydrodynamic simulations that the emission from individual shocks which grow out of initially small perturbations may fall one or two orders of magnitude below the observed flux. Instead, we find that mutual collisions of dense shells of gas formed in deep wind regions can lead to shocks with a much stronger emission which almost matches the observed flux.

This model predicts strong variability of the X-ray emission, which is not observed. We propose that – in contrast to the presently assumed spherical symmetry of the wind – the emission stems from a large number of independent, radial cones so that fluctuations average out over the whole emitting volume.

Key words: stars: early-type – X-rays: stars – hydrodynamics – instabilities – shock waves

1. Introduction

Over the past years, it has become possible to determine fundamental stellar parameters like radii and masses from quantitative spectroscopy of radiation driven winds of hot, luminous stars (Kudritzki & Hummer 1990; Pauldrach et al. 1994; and references therein). The recently proposed wind-momentum luminosity relation (Kudritzki et al. 1995) opens the prospect of using OBA supergiants as extragalactic distance indicators. A vexing problem, however, which affects the detailed analyses of the winds, is their non-stationarity. Observational evidence for this comes especially from (i) the so-called discrete absorption components, which propagate through the absorption troughs of unsaturated P Cygni profiles (Prinja & Howarth 1986; Henrichs 1988; Prinja & Fullerton 1994); and (ii) the strong X-ray fluxes from essentially all OB stars, which are nowadays interpreted to be indicative of vigorous flow disruptions. The X-ray emission, e.g., may have severe implications for the ionization balance in the wind (Pauldrach et al. 1994; MacFarlane et al. 1994). In the present paper we investigate certain wind features which result from the strong line-driven instability, and which may be the origin of the X-ray emission.

1.1. Observations

a) X-ray luminosity. The most distinctive property of the X-ray emission from O stars is the scaling of their X-ray luminosity with the bolometric luminosity, $L_x/L_{\rm bol} \approx 10^{-7}$ (Harnden et al. 1979; Seward et al. 1979; Long & White 1980; Pallavicini et al. 1981; Cassinelli et al. 1981). Sciortino et al. (1990) find from the EINSTEIN catalog of 289 Galactic O stars that $L_x \propto L_{\rm bol}^{\alpha}$, with α = 1.08 (-0.22, +0.06), and a mean value $\log(L_x/L_{\rm bol}) = -6.4$. However, the total range of values reaches from -5.4 to -7.4 (Chlebowski et al. 1989). From detailed spectral fits to ROSAT PSPC data for 42 O stars, Kudritzki et al. (1996) find $\log(L_x/L_{\rm bol}) = -6.7$ with somewhat tighter bounds of -6.0 and -7.2. The range of validity of the $L_x/L_{\rm bol}$ relation seems to be confined to the O stars: from ROSAT observations of near-main-sequence B stars, Cassinelli et al. (1994) find that $\log(L_x/L_{\rm bol}) \approx -7$ holds only up to spectral type B1. By B3, the X-ray luminosity has already dropped to $10^{-9}L_{\rm bol}$. Furthermore, Wessolowski (1996) finds *no* relationship between L_x and $L_{\rm bol}$ from ROSAT PSPC data for 61 WN-type Wolf-Rayet stars. With the availability of large stellar samples and/or high-quality spectral data it has recently become possible to search for weaker dependence of L_x on other stellar parameters than $L_{\rm bol}$: Sciortino et al. (1990) from the EINSTEIN catalog find no correlation of L_x with the wind terminal velocity, stellar rotation rate, and mass loss rate; but they do find strong correlations with the wind momentum flux, $\dot{M}v_\infty$ ($\dot{M}$ the mass loss rate; v_∞ the terminal velocity), and with the wind kinetic energy flux, $\frac{1}{2}\dot{M}v_\infty^2$. In contrast, Kudritzki et al. (1996) find a strong correlation of the temperature of X-ray emitting gas (which was not considered by Sciortino et al. 1990) with the ratio $\frac{1}{2}\dot{M}v_\infty^2/L_{\rm bol}$, and a strong correlation of L_x with $\dot{M}/v_\infty$, where the latter quantity is an (approximate) measure of the mean wind density. However, more systematic studies are still needed.

b) Spectrum. The X-ray spectra of OB stars are consistent with a thermal origin in a plasma of temperatures 10^6 to a few

---

Send offprint requests to: A. Feldmeier. feld@usm.uni-muenchen.de

10^7 K. To achieve good *fits* to the data using a thermal emission model, three prerequisites have been found to be necessary over the years (Cassinelli et al. 1981; Cassinelli & Swank 1983; Hillier et al. 1993; Corcoran et al. 1993, 1994; Cohen et al. 1996; Feldmeier et al. 1996): (i) wind absorption has to be included, especially for soft X-rays below 1 keV; (ii) the X-ray emission must extend far out into the wind; and (iii) a temperature stratification has to be assumed (or at least two independent hot components). *Direct* observational evidence for the thermal origin of the X-ray emission comes from the recent detection of line emission using the BBXRT and ASCA (Corcoran et al. 1993, 1994). (However, already Cassinelli & Swank 1983 found emission near 2 keV in the EINSTEIN SSS spectrum of ζ Ori, which they suggested could be *interpreted* as line emission.) Waldron (1991) finds direct evidence for wind absorption from a correlation between X-ray hardness ratio and 6 cm radio data. Finally, we mention that the derived filling factors of hot gas are on the order of 0.1 to 1% for O stars (Hillier et al. 1993) and may possibly approach unity for near-main-sequence B stars (Cassinelli et al. 1994).

c) Variability. Collura et al. (1989) analyzed EINSTEIN IPC data of 12 OB stars for variability. Three stars were found to be long-term variables above the 4σ significance level, e.g., ζ Puppis with an effective fractional amplitude of $\approx 40\%$ in the soft band on a time scale of $\gtrsim$ 1 day. Only τ Sco was found to show marginal short-time variability (above the 3σ significance level) during a time scale of $\approx$ 50 s and with fractional amplitude 30%. However, as reported in Berghöfer & Schmitt (1994a), a reanalysis of the data by the above authors provided no evidence for variability of ζ Pup. Cassinelli et al. (1994) did not find variability on time scales larger than 1 ks for any of the 12 near-main-sequence B stars they surveyed with the ROSAT PSPC. The short-time variability below 1 ks that was found for 3 stars – e.g. for τ Sco with period of 125 s – was attributed to spacecraft wobble. The study of Berghöfer & Schmitt (1994a) using ROSAT PSPC data gives no indication of variability for σ Ori and ζ Ori (the latter star will be the principal subject of the present paper) on time scales from hour(s) to 3 years – with the one notable exception (Berghöfer & Schmitt 1994b) of a 30% increase in the count rate of ζ Ori in the hard band (0.6 to 2.4 keV) from Sept 23 to Sept 25, 1992. The count rate then returned to its value before the increase over the next $\approx$ 0.5 to 1 year. In contrast, during Sept 19/20, 1991 the level of absolute variations in the X-ray count rate of this star was well below 10% for 20 observations taken with an average integration time of $\approx$ 1000 s. The analysis of 57 OB stars from the ROSAT all-sky survey also showed no significant variability on a time scale of $\approx$ 2 days (Berghöfer & Schmitt 1995). A recent, interesting detection of X-ray variability is reported in Berghöfer et al. (1996) for ζ Pup: they find a *periodic* modulation with $P = 16.7$ hours both in the equivalent width of the Hα line and in the count rate between 0.9 and 2.0 keV, the latter with an amplitude of 6%. This modulation is indicative of periodic variations in the density at the wind base.

1.2. Critical review of previous models

We review here the mechanisms proposed for the X-ray emission from single O stars. This rules out colliding winds as sites of X-ray emission. We also do not consider shocks close to wind compressed disks – the latter proposed by Bjorkman & Cassinelli (1993) to occur possibly for Be stars.

a) Base corona. Hearn (1972, 1973) suggested the dissipation of radiation driven sound waves as a mechanism of chromospheric or coronal heating in hot stars, and estimated the thickness of a base corona (Hearn 1975) from the equivalent width of Hα to be $\approx 1\ R_*$ for ζ Ori. The latter number was revised downwards to be smaller than $0.1\ R_*$ by Cassinelli et al. (1978). Cassinelli & Olson (1979) studied a coronal model to explain the observed superionization in OB star winds by Auger ionization. However, soon after the launch of the EINSTEIN satellite, this base corona model was found to be inconsistent with the X-ray data from O stars (Long & White 1980; Cassinelli et al. 1981; Cassinelli & Swank 1983), since the soft X-rays below 1 keV were not so strongly attenuated by wind absorption as the slab model would suggest. Especially, the K-shell edge of oxygen at $\approx$ 0.6 keV was not detected. A corona as dominant X-ray source was also ruled out for the O4 If star ζ Puppis from the non-detection of the coronal [Fe XIV] 5303 Å line (Baade & Lucy 1987). – Waldron (1984) proposed a recombination stellar wind model for early-type stars where the wind is thermally initiated by a corona, and at some distance from the star the gas cools and recombines to make radiative driving efficient. Due to the large emission measure of the corona, helium is mostly doubly ionized, thereby reducing the wind opacity for X-rays. Still, this model is subject to the same principal criticisms as the static corona and can also be ruled out (Cassinelli & Swank 1983; Baade & Lucy 1987).

b) Blob model. Lucy & White (1980) proposed a phenomenological model for the structure of unstable line-driven winds (where the instability mechanism was suggested by Lucy & Solomon 1970). Here, radiatively driven clumps plough through ambient wind gas, where the latter is shadowed by the blobs and is therefore not radiatively driven; X-rays should then originate from the shocks preceding the blobs. While free parameters of the model can be adjusted to give the observed X-ray luminosity of, e.g., ζ Pup, the spectrum is inconsistent with the observations: since the bow shocks should have maximum strength close to the star, soft X-ray attenuation is again far too strong in this model (Lucy 1982; Cassinelli & Swank 1983).

c) Forward shocks. The blob model was revised by Lucy (1982) to include the effect of blob-blob shadowing. The gas dynamical description was modified from a sequence of blobs to a sawtooth-like sequence of radiatively driven forward shocks. Here, inner shocks shadow outer shocks and cause them to decay. As a consequence of this shock destruction mechanism, X-ray emission can continue far out into the terminal flow. Although, for the first time, a strong flux of soft X-rays is predicted in accordance with the observations, the model suffers from the shortcoming (Lucy 1982; Cassinelli & Swank 1983) that the predicted X-ray luminosity is a factor of $\approx$ 20 too small. However, by the ad hoc assumption that a small number of shocks is exceptionally strong, the model can be brought into agreement with the data (Cassinelli & Swank 1983).

d) Inverse Compton scattering. (This model only attempts to explain an eventual extra component of hard X-ray emission.) White (1985) identified the nonthermal radio emission from some of the most luminous hot stars (Abbott et al. 1984; Bieging et al. 1989) with synchrotron radiation from electrons which are accelerated to relativistic speeds by the first-order Fermi mechanism in wind shocks of the type proposed by Lucy (1982). Pollock (1987) and Chen & White (1991) proposed that inverse Compton scattering of stellar UV photons by this relativistic electrons can generate hard X-ray emission at energies larger than 2 keV (and γ-ray emission up to 50 MeV). (However, due to this Compton cooling these relativistic electrons close to the star cannot survive to large radii to produce the above mentioned synchrotron radiation: therefore, as proposed by White & Chen 1992 and Chen & White 1994, the accelerating shocks have to propagate beyond the radio photosphere at > 100 stellar radii to supply fresh relativistic electrons.) The emerging spectra should follow a power law, $F_\nu \propto E^{-1/2}$, which could explain the shallow decline of the SSS data for three Orion belt stars (Cassinelli & Swank 1983): the measured decline is indeed much flatter than the exponential tail of a thermal component with temperature of a few million degrees as derived from the spectrum below 2 keV.

e) Reverse shocks. After the fundamental finding of Owocki et al. (1988) that the line-driven instability of early-star winds leads to the formation of strong *reverse* shocks instead of strong forward shocks, MacFarlane & Cassinelli (1989) set up a phenomenological model for the thin wind of τ Scorpii (B0 V). Here, a large base perturbation leads to the formation of a double shock – a pair of strong reverse and forward shocks enclosing a dense shell – which propagates out through the wind. By adjusting the strength of the shock (via the base perturbation), this double shock can reproduce the EINSTEIN spectra of τ Sco within an order of magnitude. – First results on X-ray synthesis from full hydrodynamic simulations, where hot gas evolves from the growth of initially small perturbations due to the line-driven instability, are due to Cooper & Owocki (1992, 1994) and Cooper (1994; cf. also Cohen et al. 1996). They use a different approach for the thin winds of early B stars near the main sequence, and for thick winds of O supergiants: for thin winds, radiative cooling is assumed to be unimportant, and only adiabatic cooling is included in the energy equation. This leads to large amounts of hot gas in the wind – however, still not enough to explain the observed X-ray luminosity. This is another hint that in thin winds large fractions of the gas must be X-ray emitting (Cassinelli et al. 1994). For thick winds, on the other hand, Cooper & Owocki (1992) report severe numerical problems with including radiative cooling. They therefore calculate an *isothermal* wind structure, which should be a fairly good approximation to the actual wind dynamics because of short radiative cooling zones. From the properties of the calculated shocks (their mass inflow and velocity jump, i.e., their temperature), Cooper & Owocki calculate the corresponding X-ray spectra by assuming *steady-state* radiative cooling zones of known emission behind these shocks. Surprisingly, the calculated X-ray luminosity for their O supergiant model is a factor of 10 *larger* than the observed value (while the spectral shape is about the same). We shall return to this issue in Sect. 3.

In the following we present an extension to this last item, e). We find in our models that single reverse shocks give an X-ray emission which is typically one or two orders of magnitude below the observed flux. Yet, mutual collisions of dense shells of gas compressed in the shocks give rise to a much stronger emission which can almost reproduce the observations. The paper is organized as follows. After a discussion of our technique of hydrodynamic simulations and X-ray synthesis in Sect. 2, we examine in Sect. 3 the X-ray emission from the wind structure at selected instants. This will give the clue to the origin of strong emission in shell-shell collisions, which are the topic of Sect. 4. The dichotomy between the observed constancy of X-ray emission and the variability of synthesised spectra is discussed in Sect. 5. Finally, Sect. 6 gives a summary and prospects for future work.

2. Technique

2.1. Hydrodynamics

The continuity, radial momentum, and energy equation for a spherically symmetric flow (the latter approximation is discussed below) are,

$$\frac{\partial \rho}{\partial t} + \frac{1}{r^2}\frac{\partial}{\partial r}\left(r^2 \rho v\right) = 0 \tag{1}$$

$$\frac{\partial(\rho v)}{\partial t} + \frac{1}{r^2}\frac{\partial}{\partial r}\left(r^2 \rho v^2\right) = -\frac{\partial p}{\partial r} - \rho g + \rho g_l, \tag{2}$$

$$\frac{\partial e}{\partial t} + \frac{1}{r^2}\frac{\partial}{\partial r}\left(r^2 e v\right) = -\frac{p}{r^2}\frac{\partial}{\partial r}\left(r^2 v\right) - Q(\rho, T), \tag{3}$$

where the standard symbols are used, and where g_l is the radiative line acceleration; e is the thermal energy density, which for an ideal gas is $e = p/(\gamma - 1)$; in the following, $\gamma = 5/3$ is assumed. Q is the total power radiated per unit volume. (We neglect heating by re-absorption.)

The assumptions underlying our present approach are the same as in Feldmeier (1995), with the formulation of the line force as developed by Owocki et al. (1988) and Owocki (1991). We here only discuss some central concepts.

(1) We use a standard time-explicit, Eulerian finite difference scheme (cf. Reile & Gehren 1991) to solve the above equations on staggered grids. The advections terms are calculated using van Leer (1977) fluxes through the boundaries of adjacent control volumes, and we apply the so-called "consistent advection" after Norman et al. (1980). At the inner boundary – which is chosen to be the stellar photosphere of continuum optical depth unity – we use the method of Thompson (1987, 1990) to fix the Riemann invariants, here in an exponential density stratification through which a perturbation propagates. At the highly supersonic outer boundary, zeroth order extrapolation is

adequate. – For details on the operator splitting sequence, artificial viscosity to smear out shock fronts, and the calculation of pressure work and radiative cooling (including time step limitations), see Feldmeier (1995). We add here that heat conduction is not included in our present simulations. While heat conduction may be important at temperatures $\gtrsim 10^7$ K (e.g., MacFarlane & Cassinelli 1989), we accept the error introduced by neglecting it in favor of keeping the number of physical processes and interacting phenomena small.

(2) Spherical symmetry is a severe restriction of the present approach, and is only justified by computational demands. While in the final section of this paper we shall interpret the calculated hydrodynamical structures as corresponding approximately to independent radial wind cones of small opening angle, our procedure for X-ray synthesis (cf. below) assumes full 4π symmetry – so that fluctuations in the hydrodynamical structure lead to strong X-ray variability, cf. Sect. 5.

(3) The line force is calculated by using the so-called "smooth source function" method (Owocki 1991; Owocki & Puls 1996). The total force is the sum – weighted by the line-strength distribution function of Castor et al. (1975) – of the force on a singlet transition, for which a pure Doppler profile and a constant mass absorption coefficient κ is assumed. The latter should be a good approximation for strong resonance lines and lines with a lower metastable level, both of which dominate the line force. We assume further that no line-overlap occurs. The force on a single line is calculated via a formal integral with prespecified, local source function. In the present paper we use a source function which corresponds to purely geometric dilution of the radiation field, i.e., to optically thin lines. To calculate the flux, the Doppler width of a line is resolved by three frequency points, where the frequency integral extends over ± 3 Doppler widths. The angle integral is approximated by a one-ray quadrature, and, finally, the temperature dependence of the line force is taken into account using the results of MacGregor et al. (1979)

(4) In the expression for the total power radiated, $Q = n_{\rm e} n_{\rm H} \Lambda(T)$, we use a power law fit to the Raymond et al. (1976) cooling function for an optically thin plasma, $\Lambda(T) = A\,(T/T_0)^\delta$, with $\delta = -1/2$, $T_0 = 10^6$ K, and $A = 1.6 \times 10^{-22}$ erg cm^3 s^{-1}. While an interval-wise power-law fit would be more accurate, we use the above global approximation in order to keep the temporal evolution of the cooling layer due to the oscillatory thermal instability (Langer et al. 1981, 1982) as simple as possible – since, as discussed by Walder & Folini (1996), this evolution shows a complex dependence on the value of δ. The significance of this oscillation for stellar wind simulations is that the cooling zone of minimum extent during each cycle is shorter than any achievable grid resolution. This results in a "loss" of the cooling layer, i.e., the shock collapses to an *isothermal* shock. To prevent this, we alter the cooling function to have a *stable* exponent $\delta = 2$ below some temperature $T_{\rm swi}$ (Feldmeier 1995). We use here $T_{\rm swi} = 15\,T_{\rm eff}$ ($= 4.7 \times 10^5$ K; see below): smaller $T_{\rm swi}$ can essentially not prevent the collapse of cooling zones, while larger $T_{\rm swi}$ would influence the soft X-ray spectrum emitted.

In the present paper we study an O supergiant wind model with stellar parameters (listed in Table 1) close to that of ζ Ori. This star should be an ideal candidate to test X-ray emission models since: (i) it has among the highest signal-to-noise ratio within our full sample of 42 O stars observed with the ROSAT PSPC (Kudritzki et al. 1996); and (ii) its stellar and wind parameters are known to a good accuracy. Additionally, there are no indications that helium recombines in the wind of ζ Ori. In contrast, for the dense wind of the O supergiant ζ Puppis, Hillier et al. (1993) found evidence that helium recombines to He$^+$ from about 6 R_* on. This enhances the background opacity enormously, and consequently these authors concluded that the observed X-rays at ≈ 0.5 keV must be emitted from radii larger than 30 R_*, and X-rays below 0.2 keV from $r > 100\ R_*$. With our present hydrodynamic models we see no possibility to generate or maintain the corresponding amounts of hot gas at these large distances (cf. Sect. 3). However, since ζ Pup is possibly the only, at most one of a very few stars in our sample which shows helium recombination, we feel justified to analyse the X-ray emission properties of the more standard candidate ζ Ori instead, and leave the re/investigation of the peculiar wind of ζ Pup (especially the location of He recombination) to a future study.

Photospheric parameters for ζ Ori are taken from Voels et al. (1989), while the wind terminal velocity and interstellar hydrogen column density are from Haser (1995). For the mass loss rate we assume an average of the results obtained by Lamers & Leitherer (1993) from Hα, $\dot{M} = 3.9 \times 10^{-6}\ {\rm M}_\odot/{\rm yr}$, the reanalysis of these data by Puls et al. (1996), $\dot{M} = 3.6 \times 10^{-6}\ {\rm M}_\odot/{\rm yr}$ for $\beta = 1$, and the value from radio measurements, again from Lamers & Leitherer (1993), $\dot{M} = 2.5 \times 10^{-6}\ {\rm M}_\odot/{\rm yr}$. As a typical value for O star winds, we set the CAK exponent to $\alpha = 0.7$ (cf. Pauldrach et al. 1986), and the line force constant is fixed at a value which results in the average above mass loss rate, $\dot{M} = 3 \times 10^{-6}\ {\rm M}_\odot/{\rm yr}$. The line strength cutoff $\kappa_{\rm m}$ of Owocki et al. (1988) terminates the line list at the strongest lines, in order to prevent the development of subgrid structure. The thermal speed is representative for driving ions like C, N, and O. Finally, the photospheric barometric scale height and the acoustic cutoff period (above which sound waves cannot propagate vertically through the atmosphere) are listed in Table 1.

2.2. Photospheric perturbation

In time-dependent wind simulations so far (Owocki et al. 1988; Owocki 1992), a photospheric sound wave is assumed to trigger perturbations that grow in the presence of the line-driven instability. However, the coherence of the wave leads to a periodic wind structure, at least for small wave amplitudes. As will become clearer in later sections, the amount of hot gas in this regular structure is too small to explain the observed X-ray flux. Therefore, to generate more hot gas in the wind, we propose two different types of irregular perturbations which should lead to enhanced dynamical interactions in the wind, e.g. shell collisions, and therefore possibly to enhanced heating.

Table 1. Stellar parameters for ζ Ori.

Spectral type		O9.7 Ib
Temperature	$T_{\rm eff}$	31 500 K
Mass	M	$34\,M_\odot$
Gravity	$\log g$	3.2
Radius	R_*	$24\,R_\odot$
Luminosity	L	$5.1 \times 10^5 L_\odot$
Terminal speed	v_∞	1 850 km/s
Mass loss rate	$\dot{M}$	$3 \times 10^{-6}\,M_\odot/{\rm yr}$
Helium fraction	$n_{\rm He}/n_{\rm H}$	0.1
Distance	d	450 pc
ISM column density	$\log(N_{\rm H}\,{\rm cm}^2)$	20.34
Thomson coefficient	σ_e	$0.34\,{\rm cm}^2/{\rm g}$
Eddington factor	Γ	0.39
CAK exponent	α	0.7
Line force constant	$\kappa_0\, v_{\rm th}/c$	$5950\,{\rm cm}^2/{\rm g}$
Line strength cutoff	$\kappa_{\rm m}/\kappa_0$	10^{-3}
Sound speed (isoth.)	a	20.7 km/s
Thermal speed	$v_{\rm th}$	$0.3\,a$
Scale height	H	$2.6 \times 10^{-3}\,R_*$
Acoustic cutoff period	$T_{\rm cut}$	7.34 h

The first is a kind of "tunable" sound wave, where at certain instants the amplitude and period of the wave changes abruptly. More specifically, after a certain coherence time T has elapsed, over which the wave has an amplitude A and period P, we choose three random numbers $0 < \xi_T, \xi_A, \xi_P < 1$ to define a new coherence time, wave amplitude, and wave period by

$$X = X_{\rm m}^{(1-\xi_X)}\, X_{\rm M}^{\xi_X} . \tag{4}$$

Here, X stands for any of T, A, or P, and subscripts 'm' or 'M' refer respectively to the prespecified minimum or maximum of the corresponding quantity. To avoid discontinuities in the amplitude, we furthermore apply these changes only after a full wave cycle is finished. Finally, $T_{\rm m} = P_{\rm m} = 10^3$ s and $T_{\rm M} = P_{\rm M} = 10^4$ s is chosen, and we consider the two cases $A_{\rm M} = 0.3$ resp. 0.5, where $A_{\rm M}/A_{\rm m} = 10$ is assumed. The time series of the photospheric velocity for $A_{\rm M} = 0.3$ is shown in Fig. 1, its power spectrum in Fig. 2.

While our perturbation amplitudes are chosen to be as large as possible (to generate strong wind structure) – yet still be subsonic in the photosphere (see below) – the perturbation *periods* are determined from the following considerations. The radiative force which acts on the extremely rarefied, optically thin gas between strong wind shocks (for a discussion of the typical wind structure see Sect. 3) causes unresolvably steep velocity fields. This led Owocki et al. (1988) to introduce the cutoff parameter $\kappa_{\rm m}$, by which much shallower, numerically manageable velocity gradients are achieved. To still be able to reach shock velocity jumps which are large enough to heat gas to X-ray temperatures, Owocki et al. (1988) induced large *distances* between subsequent wind shocks by applying photospheric perturbations with long wavelengths, i.e., with periods as those above. However, one has to keep in mind that maximally unstable (harmonic) perturbations have a much shorter wavelength (typically by a factor of 100) which is on order of the Sobolev length and below (Owocki & Rybicki 1984; where the stationary wind speed grows by an ion thermal speed over a Sobolev length). Therefore, it seems possible that – opposite to the wind models to be discussed in the following – strong structure may (more naturally?) also develop on much shorter lengthscales. However, such structure is not easily anticipated, and clarification has to come from future numerical simulations.

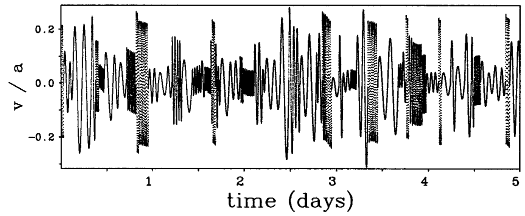

Fig. 1. Time series of the radial photospheric velocity (in units of the isothermal sound speed) due to a "tunable" sound wave.

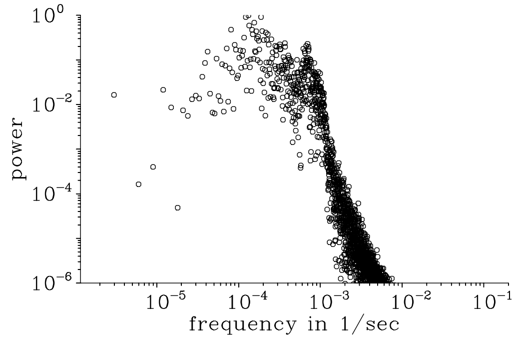

Fig. 2. Power spectrum of the sound wave from Fig. 1.

To ensure that waves with periods as short as 1000 seconds (actually even 500 s) can propagate on the numerical grid, we use 250 equidistant grid points from $1\ R_*$ to $1.05\ R_*$. At the latter radius the wind is already highly supersonic ($6.5\ a$), and the Doppler effect has stretched the wavelength so that a coarser grid is appropriate. Over the next 3750 points, a logarithmic grid with ${\rm d}r/r = const$ is laid out to $30\ R_*$. Finally, a short grid with 20 points establishes a smooth link of differentials ${\rm d}r$ between the above two grids.

As a second type of photospheric perturbation we consider the physically somewhat more meaningful Ornstein-Uhlenbeck (1930) stochastic process (where the latter are generalizations of discrete Markovian chains to a continuous time variable). This process is set up here for the stochastic variable u (the velocity perturbation), and mimics photospheric turbulence via a solution of the Langevin equation (cf. Wax 1954 for a collection of classical papers on the subject, and Risken 1989 for a textbook),

$$\frac{\mathrm{d}u}{\mathrm{d}t} + \frac{u}{t_\mathrm{c}} = \Gamma(t), \tag{5}$$

where t_c is the relaxation time. The fluctuating or stochastic force, $\Gamma(t)$, has zero mean (ensemble averages understood) and a correlation function which corresponds to white noise (the meaning of the constant q becomes clearer from the next equation),

$$\begin{aligned} \langle \Gamma(t) \rangle &= 0, \\ \langle \Gamma(t_1)\Gamma(t_2) \rangle &= q\delta(t_1 - t_2). \end{aligned} \tag{6}$$

The velocity correlation function is then, for times $t_1, t_2 \gg t_\mathrm{c}$ found to be (cf. Risken 1989, p. 34),

$$\langle u(t_1)u(t_2) \rangle = \tfrac{1}{2} q t_\mathrm{c}\, e^{-|t_1 - t_2|/t_\mathrm{c}}, \tag{7}$$

which gives for time intervals $|t_1 - t_2| \ll t_\mathrm{c}$,

$$D(\tau) \equiv \langle (u(t+\tau) - u(t))^2 \rangle \propto \tau, \tag{8}$$

where D is the so-called structure function. The relation $D \propto \tau$ is also found for the *Lagrangian* structure function for fluid turbulence in the Kolmogorov inertial range (cf. Landau & Lifshitz 1989, p. 132; Monin & Yaglom 1987, Sects. 21.2 to 21.4). The use of the Langevin equation to describe Lagrangian fluid turbulence is reviewed by Pope (1994); cf. also Gail et al. (1974). – In contrast, however, the inertial range structure function in the *Eulerian* frame is found to be $D(\tau) \propto \tau^{2/3}$ (Landau & Lifshitz), so that our use of the Langevin equation to generate a stochastic process with spectrum $E \propto \omega^{-2}$ (white noise) at a fixed *location* – i.e., the photosphere – can only be a very approximate description for inertial range turbulence, which has a spectrum $E \propto \omega^{-5/3}$ instead.

For the two models presented in Sect. 3 we have chosen (via the above variable q) a velocity dispersion $\sigma_u/a = 0.1$ and 0.25. Due to the Gaussian distribution of $u(t)$, this corresponds roughly to $A_\mathrm{M} = 0.2$ and 0.5, cf. Fig. 3. As relaxation time we assume, in accordance with the periods from the foregoing sound wave model, $t_\mathrm{c} = 5000$ s. The time series of the Langevin process is shown in Fig. 3, and its power spectrum in Fig. 4. Notice the white noise form of the spectrum, $E(\omega) \sim \omega^{-2}$, for frequencies larger than ${t_\mathrm{c}}^{-1}$.

Finally, we turn to a brief discussion of the physical significance of these photospheric perturbations. Using Fourier techniques to separate turbulent ("Gaussian") from rotational velocity fields in observed helium profiles, Conti & Ebbets (1977) and Ebbets (1979) find a turbulent velocity dispersion of ≈ 30 km/s, i.e. $\approx 1.5\, a$ for hot supergiants. Even with the principal criticism that it is not quite clear as to which degree these analyses apply to *expanding* atmospheres (Mihalas 1979 and references therein; Kudritzki 1992; Haser 1995), our turbulent photospheric velocity fields of maximum amplitude $\delta v/a = 0.2 \ldots 0.5$ used in the present paper should lie within the margins allowed by observations.

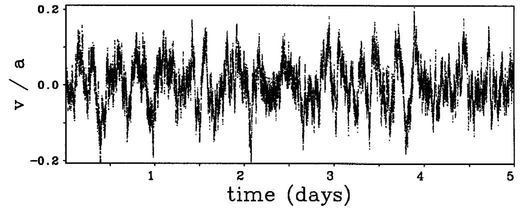

Fig. 3. Time series of the photospheric velocity due to Langevin turbulence.

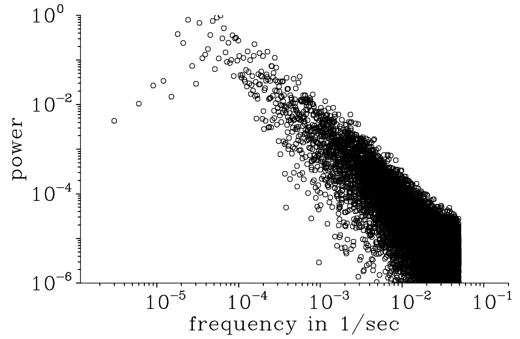

Fig. 4. Power spectrum of the signal in Fig. 3.

At least two other types of photospheric perturbations which may trigger structure formation in the wind are discussed in the literature: pulsations (for non-radial pulsations in general: Baade 1991; Fullerton et al. 1996; Gies 1996); for strange mode pulsations: Gautschy & Glatzel 1990; Glatzel 1994) and macroscopic magnetic fields (with emphasis on dipoles: Underhill & Fahey 1984; Stahl et al. 1993; Bohlender 1994; Henrichs et al. 1994). However, since the azimuthal coherence scales of both pulsations and macroscopic magnetic fields are large, they should be connected (if there is such a connection at all) with "large-scale" phenomena in the wind, especially with the so-called discrete absorption components (Cranmer & Owocki 1996) and/or the so-called "bananas" (Owocki et al. 1995) observed in non-saturated P Cygni profiles. – In contrast, the observed constancy of the X-ray fluxes from OB stars gives strong evidence for the stochastic nature of the emission process. We return to this issue in Sect. 5.

2.3. Synthesis of X-ray spectra

To calculate the X-ray spectrum emitted from a structured, spherically symmetric wind we use a formal integral approach (cf. Hillier et al. 1993; Feldmeier et al. 1996). The absorption coefficient is given as the sum of bound-free and line opacities for the cold wind taken from a stationary NLTE model for ζ Ori, and the K-shell opacity for the elements C, N, O, Ne, Mg, Si, S (Daltabuit & Cox 1972). The X-ray emission of hot gas is

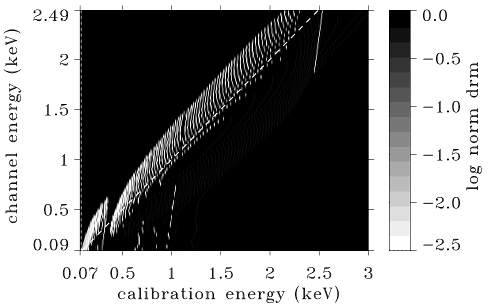

Fig. 5. Greyscale rendition of the ROSAT detector response matrix (drm; including effective detector area) appropriate for observations of ζ Ori. The dashed white line indicates a detector with infinite resolution. The null-response at 0.28 keV is due to the Carbon edge of the entrance window material.

calculated using the recent version of the Raymond & Smith (1977) code. Finally, ISM opacities are calculated after Morrison & MacCammon (1983), and the ROSAT detector response matrix used to convert incident photon fluxes to count rates is shown in Fig. 5.

The spectrum shown in Fig. 8 (identical to the one in Feldmeier et al. 1996) consists of 53 single observations taken over 1.5 years, with integration times typically from 500 to 1500 seconds. The *episodic* event from Sept 23 to 25 in 1992, when the count rate increased by $\approx$ 30% (Berghöfer & Schmitt 1994b) is *not* included in our data set, which reaches only to Sept 19, 1992. The dashed line in the figure is a best *fit* to the data using the empirical X-ray emission model of Hillier et al. (1993) where isothermal hot regions of radius-independent temperature and filling factor are assumed to be distributed through the whole wind. This fit serves here to find the approximate spectrum incident on the detector (before being convolved with the drm), which is shown as dashed line in the lower panel of Fig. 8. The corresponding "stellar" emergent spectrum gives an X-ray luminosity in the ROSAT energy band of $L_x = 4.9 \times 10^{32}$ erg/s.

3. The X-ray emission at selected instants

In this section we discuss the X-ray emission from the wind at certain instants when the calculated and observed spectra agree well. This serves mainly to identify the hot gas responsible for the emission and to discuss its properties, which suggests that this gas originates in radial shell-shell collisions. These are the topic of the next section.

3.1. A wind model out to 100 R_*

As a preparatory consideration we have to determine the spatial extent of the wind relevant for X-ray emission. To this end we ran a simulation out to 100 R_*. This model uses 7000 grid points, with 1000 points spaced equidistantly up to 1.1 R_*, and 6000 points spaced according to $\mathrm{d}r/r = const$ out to 100 R_*; the tunable sound wave was used as the triggering perturbation. The simulation took somewhat more than one cpu month on a $\approx$ 20 Mflop workstation, until a model time of 10 days. At this time, the gas initially located at the inner boundary had reached the outer boundary, and the whole computational domain was influenced by (previous) photospheric perturbations which triggered the formation of wind structure, and possibly of hot regions.

Fig. 6 shows a snapshot of the density, velocity, and temperature of the wind at t = 10 d. The dashed line corresponds to a stationary wind with a β = 0.8 velocity law (Pauldrach et al. 1986), which serves as an initial condition. The structure caused by unstable growth at radii below 10 R_* has been described by Owocki et al. (1988) and Owocki (1991, 1992) so that we limit ourselves here to some additional remarks, especially on the outer wind structure. – Primary radiative reverse shocks are destroyed around 5 R_* (Feldmeier 1995). A strong shock which is seen in the velocity field of Fig. 6 at $\approx$ 5.5 R_* is a forward shock (preshock side at large radii, postshock side at small radii), and can be termed a "secondary" shock in that it is not directly caused by the radiative instability, but is due to fast, cold, inner gas ramming into slow, hot, outer gas. This latter, very rarefied intershell gas – which is spread over almost 2 R_*! – was at former times heated in a reverse shock which was meanwhile destroyed. Since all driving ions are stripped, the radiative force on this hot gas is negligible and the gas stalls. Furthermore, because of its low density, radiative cooling is very inefficient, and the gas can only cool via adiabatic expansion on its advection to outer wind regions. No essentially new ingredients to the wind dynamics occur in the outer regions $> 20 \ldots 30$ R_*. Occasionally (e.g., at $\approx$ 65 R_* in Fig. 6), relatively strong forward shocks similar to the one just described form at the inner edge of an old, hot region. We furthermore find a few, rather strong reverse shocks in the outer wind, e.g., at 20 and 24 R_* in Fig. 6. They show the same characteristics as inner reverse shocks, i.e., very rarefied gas is accelerated to high velocities by the large radiative force on optically thin lines, until this fast gas undergoes a decelerating shock transition. However, we never find more than three or four of these shocks over the full range from 10 to 100 R_*. The gross appearence of the outer structure is that of a return to a smooth wind: remaining hot gas cools, velocity gradients smooth out, and the dense shells expand, which leads to a homogenization of the mass distribution. Since typical velocity differences inside the shell are of the order of the sound speed, both the inertia and pressure forces are of the same magnitude and the shell expansion is due to their combined action.

We mention here as a side remark that one has to be cautious about estimating the extent of cooling zones behind wind shocks from *stationary* wind conditions. Such estimates may differ significantly from the cooling lengths found in dynamical simulations, especially since in the latter case the gas in front of reverse shocks is extremely rarefied, and since furthermore a hierarchy of mutual shock collisions causes abrupt changes in the cooling zones.

We find that for the above model, at all times, the total spatial domain from 30 to 100 R_* contributes *less than a few permille* to

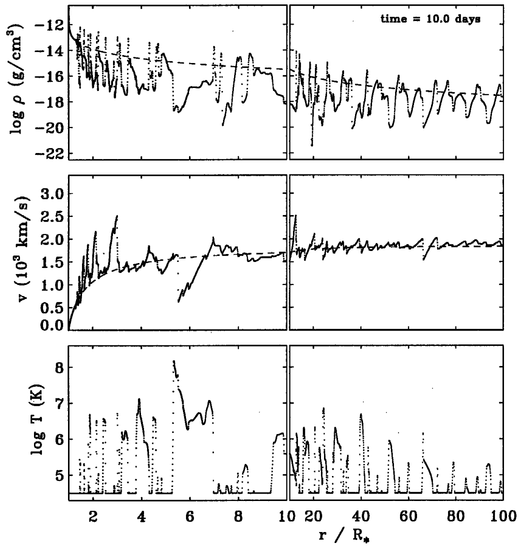

Fig. 6. Snapshot out to 100 stellar radii of the wind perturbed by a tunable photospheric sound wave. The density, velocity, and temperature are marked at each numerical grid point. The dashed line corresponds to a stationary wind with β = 0.8 velocity law.

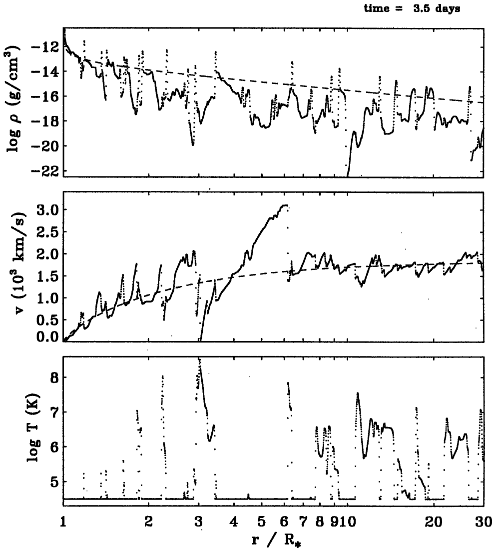

Fig. 7. Snapshot of the wind structure 3.5 d after model start. The photospheric disturbance is a tunable sound wave.

the total X-ray emission from the structured wind. This justifies our consideration of only the restricted range from 1 to 30 R_* in the following models. (The wind attenuation of X-rays from 30 R_* to infinity is calculated assuming a stationary wind with $v = v_\infty$ and $\rho \propto r^{-2}$.)

3.2. Photospheric sound wave as wind perturbation

Fig. 7 shows a snapshot of the wind perturbed by the tunable photospheric sound wave of maximum amplitude A_M = 0.5, at 3.5 days after model start. A strong *forward* shock occurs slightly above 3 R_*, and terminates only at *negative* gas velocities. (In the vicinity of this forward shock, at $r \lesssim 3\ R_*$, a strong reverse shock is found.) Such negative velocities appear regularly in the present models with large perturbation at the wind base. However, this gas is extremely rarefied and does not contribute in any observable manner to the X-ray emission; consequently we forgo here a discussion of the reality of this inflow. The second, very pronounced shock in Fig. 7 is located slightly above 6 R_*. The significance of this reverse shock will be seen below.

Farther out from this very strong shock (with a velocity jump of 1700 km/s!), only a few more, much weaker reverse shocks occur (at $\approx 8, 10, 21, 28\ R_*$), which heat gas to soft X-ray temperatures of $\approx 1 \times 10^6$ K. Yet, the bulk of the outer hot gas is just leftover from former shock destruction.

The top panel of Fig. 8 shows the observed ROSAT spectrum of ζ Ori together with the spectrum synthesised from the wind structure of Fig. 7. *Both at soft and hard energies, the calculated flux matches the observed flux well*; the maximum deviation, at $\approx$ 0.6 keV, is a factor of 3. The bottom panel of the figure shows the number of photons incident on the detector, both for the time-dependent wind model and for the best fit to the data. From the model spectrum we find L_x = 5.4 × 10^{32} erg/s, in good agreement with L_x = 4.9 × 10^{32} erg/s from the data fit. It therefore appears that the line-driven instability is able to generate sufficient amounts of hot gas in the time-dependent wind model to match the ROSAT spectra from these stars.

This comes quite as a surprise for the following reason: the best fit to the ROSAT data of ζ Ori, assuming isothermal hot gas of radius-independent temperature T and volume filling factor f as the thermal X-ray source gives $T \approx 10^{6.5}$ K and $f \approx 0.01$ (Feldmeier et al. 1996), where the filling factor refers to hot gas at the density of the *stationary* wind. While most hot gas in Fig. 7 has indeed temperatures between 10^6 and 10^7 K, the gross density of this gas is (at least) a factor of 30 to 50 below that of the stationary wind, and its filling factor is smaller than 0.5. Since the emission scales $\propto f\rho^2$, this implies that the X-ray flux from the time-dependent structure should be a factor (at least) 20 to 50 below the ROSAT data.

Cooper 1994 from a rather similar wind structure claims instead $\langle L_\mathrm{cal} \rangle \approx 10 L_\mathrm{obs}$! However, this result seems to be due to the inadequate assumption that *stationary, radiative* cooling zones should build up behind the strong shocks found in an *isothermal* wind simulation, where the X-ray emission is then calculated from the known properties of such radiative shocks. Especially, since their cooling length scales inversely with the

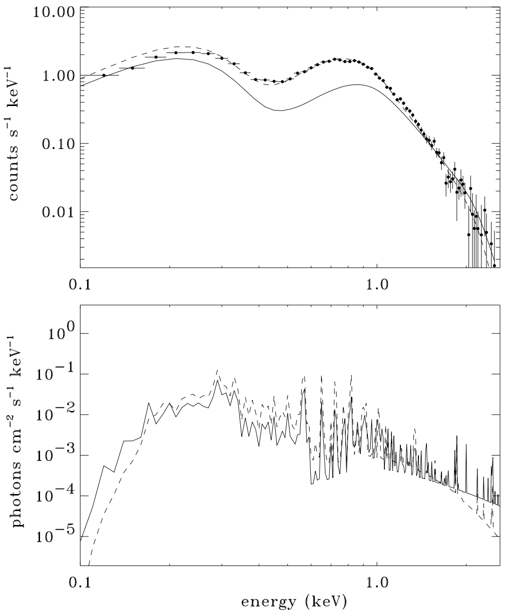

Fig. 8. Upper panel, error bars: ROSAT PSPC spectrum of ζ Ori. Full line: calculated X-ray spectrum from the wind structure of Fig. 7; dashed line: best isothermal fit to the data. Lower panel: number of photons incident on the detector for the wind structure from Fig. 7 (full line) and the best fit to the data (dashed line). The two panels differ by the detector response matrix.

preshock density, the low X-ray emissivity ($\sim \rho^2$) of a tenuous gas is partially compensated by the corresponding cooling zone being very extended. However, the rarefied gas in front of reverse shocks from hydrodynamic simulations implies cooling lengths of order (10 to) 100 R_*, i.e., meaningless volume filling factors $\gg 1$ for the typical shock separations of order 1 R_*.

The solution to the above paradoxical situation (i.e., *sufficient* instead of too few X-ray emission from a wind structure with mostly thin, hot gas) comes from Fig. 9, which shows the same snapshot as Fig. 7 but now with the X-ray emission $n_{\rm e} n_{\rm H} \Lambda_\nu(T)\, {\rm d}V$ (units erg/s) from the indicated numerical grid cells of volume ${\rm d}V$. (For our low densities of X-ray emitting gas, the function Λ_ν is practically independent of density). We see that *most X-rays stem from the single shock located slightly above* 6 R_* ("overlooked" in the above estimate) with gas-densities in the hot post-shock region *close to and even exceeding stationary wind densities*. We shall see in the next section that this shock is the site of a shell collision – in which a fast shell is added to the cold, very dense edge of the shock cooling layer – and therefore has rather different properties from the majority of hot gas.

For the moment we notice that only a few shocks (never more than 5; and usually only 1 or 2 dominating ones) emit almost all the observable X-rays in our simulations. This bears some resemblance to the work of MacFarlane & Cassinelli (1989), where a single pair of strong reverse and forward shocks was also found to be able to account for the total X-ray emission from the B0 V star τ Sco.

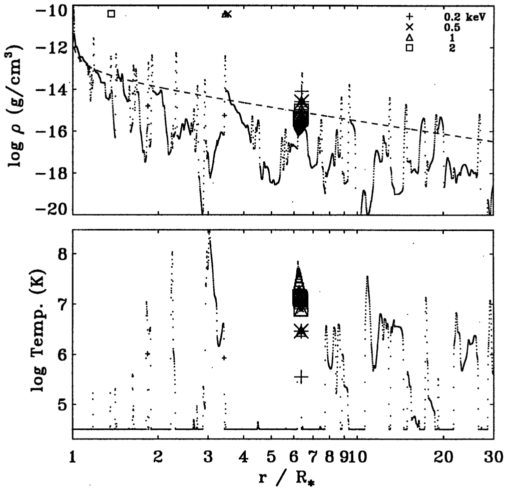

Fig. 9. The wind structure of Fig. 7 again, with the X-ray emitting gas marked: from maximum to minimum size of a symbol (+, x, etc.), the emission $n_{\rm e} n_{\rm H} \Lambda_\nu(T)\, {\rm d}V$ (in erg/s) drops by a factor of 100. The energies corresponding to the different symbols are given at the upper right corner, and the location of wind optical depth unity (where $\tau = 0$ at infinity) at these energies is shown at the upper margin.

While the observed and calculated spectra in Fig. 8 agree very well at low energies, there are (at least) two reasons that this coincidence might be fortuitous, and therefore not very significant. (i) In this snapshot, as in most others, the soft component is emitted from a few spatial grid cells only, i.e., the hydrodynamic structure is certainly underresolved for this spectral domain. (ii) The temperature of the gas which emits the soft component is typically in the range from 5×10^5 to 10^6 K – and is therefore certainly affected by our artifical change of the cooling function below $T_{\rm swi} = 4.7 \times 10^5$ K.

We notice that the hard energy tail of the spectrum from the time-dependent simulation in the bottom panel of Fig. 8 shows a shallower decline than the best fit achieved by assuming an isothermal gas at $10^{6.5}$ K. The reason is simply the presence of much hotter gas in the hydrodynamic simulation, and this fact provides an alternative explanation for the possible presence of hard X-ray components in measured spectra instead of the inverse Compton scattering at relativistic electrons (Chen & White 1991), cf. the Introduction.

Fig. 10 shows a greyscale rendition of the contribution function, where the latter gives the *exact* contribution to the total emergent X-ray emission at energy E from gas located within a certain radial range. We find that the emergent spectrum over

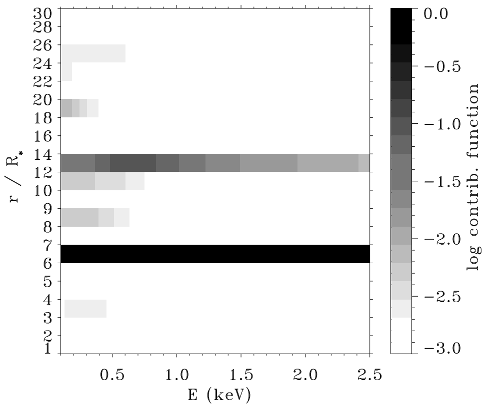

Fig. 10. Greyscale rendition of the contribution function, which is the ratio of emergent X-ray luminosity at energy E (abscissa), from gas located between radii r_i and r_{i+1} (ordinate), to the total emergent luminosity at E.

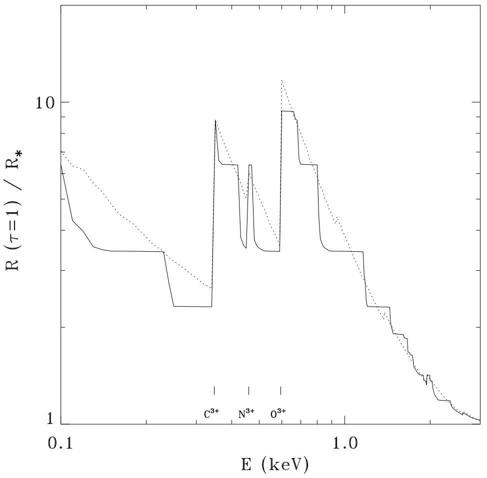

Fig. 11. Location of optical depth unity in the wind, for X-rays in the ROSAT energy range. Full line: time-dependent wind model of Fig. 7. Dashed line: stationary wind model. Three dominant K-shell edges are marked at the bottom margin.

the full ROSAT bandpass is indeed emitted almost single by the shock discussed above. At energies around 0.7 keV, however, a minor contribution of $\approx$ 10% stems from the gas between 12 and 14 R_*. Furthermore, we conclude from this and many other snapshots that more than 90% of the observed X-rays in our models are emitted from below 10 R_*, i.e., from wind regions where acceleration is important.

Fig. 11 shows the location of optical depth unity in the wind (with $\tau = 0$ at infinity) for energies in the ROSAT spectral range. Astonishingly, the $r(\tau = 1)$ curves are rather similar for the time-dependent and the stationary wind model. The reason is that the wind gas can only be compressed once into a shell and then remains there for all subsequent times. Any wind particle can therefore be displaced from its location in the stationary wind by at most the intershell distance, which for radii $r < 10\ R_*$ in Fig. 7 is typically 1 R_* (at most 2 or 3 R_*). The same conclusion holds then for the location of optical depth unity.

Finally, Fig. 12 shows a two-dimensional cut through the emitting and absorbing wind gas. The emitting volumes, as seen by an observer at $r = \infty$, are concentric cylindrical tubes (spherical symmetry is assumed), the terminating surfaces of which (at $\tau \approx 1$) are sections through spheres (at least if the $\tau = 1$ surface lies within a dense shell, which is mostly the case). The reason for the discontinuous jumps of the $\tau = 1$ surfaces at certain values of p is that the optical depth of a shell grows with increasing line of sight angle between z and r, and thus with p.

3.3. Photospheric turbulence as wind perturbation

We repeat in short the discussion from the last section for the model assuming photospheric Langevin turbulence with maximum amplitude $A_{\rm M} = 0.2$ as the triggering perturbation. Fig. 13 shows a snapshot of the wind at 3 d after model start. The most dominant – reverse – shock occurs slightly above 4 R_* here. Shock destruction sets in at $\approx 5\ R_*$ again, and beyond this radius most hot gas is leftover from former shocks only. However, exceptional reverse shocks are also found at very large distances 20 and 27 R_*. Forward shocks with temperatures of order 10^6 K occur at the edges of cold and hot gas at 12 and 15 R_*.

The X-ray emission from the wind structure in Fig. 14 shows again good agreement with the soft and hard regions of the ROSAT spectrum. The maximum deficiency, around 0.7 keV, is by a factor of 4. As before, the hard energy tail of the incident detector spectrum has a shallower decline than the empirical fit using an isothermal emission model with $T_{\rm shock} = 10^{6.5}$ K.

Fig. 15 leads to the same conclusion as was reached in the last section: almost all the emergent X-rays originate from a single, strong reverse shock (of velocity jump 2200 km/s here, and located at $\lesssim 4.5\ R_*$), where the density of the hot, emitting gas is close to and even larger than in a stationary wind. A further contribution at the 10% level (cf. Fig. 16) stems from the outer rim (at $\gtrsim 7\ R_*$) of a broad region of hot intershell gas. As will become clearer in the next section, a shell collision with subsequent shock destruction has just occured at this latter site. Finally, we note that the hot gas seen in the figure below 3 R_* does not contribute significantly to the emergent X-ray radiation, since it is located below the radius where $\tau = 1$ for the corresponding energies.

4. Shell collisions as origin of X-ray emission

To understand the origin of gas heating which leads to X-ray emission, we show in Fig. 17 a greyscale rendition of the wind

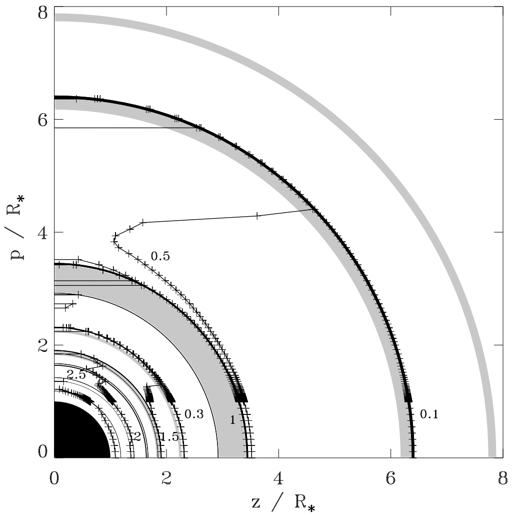

Fig. 12. The (p, z)-geometry of X-ray radiative transfer for the wind structure from Fig. 7. The observer is located at $(z = \infty, p = 0)$. The plus signs, connected by full lines, show the surfaces of optical depth unity at the energies indicated (in keV). The shaded regions show gas hotter than 10^6 K. The narrow, black regions are dense shells where the density is higher than three times the local density of the stationary wind.

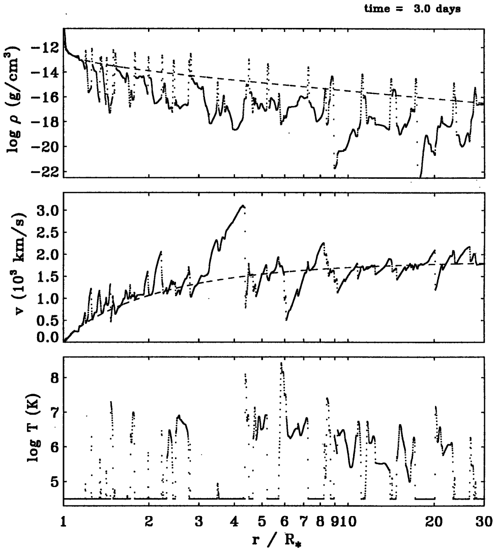

Fig. 13. Snapshot of the wind structure triggered by photospheric Langevin turbulence at three days after model start.

evolution from 3.2 to 4.6 days after model start, with the tunable sound wave as the triggering perturbation. The strong emission at $t = 3.5$ days and $r \gtrsim 6\ R_*$ in Fig. 9 *is now seen to be due to a shell collision*. Even more than that, from the density diagram of Fig. 17 it is clear that significant X-ray emission stems *only* from sites of shell collisions. (The conclusion in the other direction, however, is not true: not every shell collision is the origin of significant X-ray emission.)

We notice from this figure that the snapshot at $t = 3.5$ days appears to be exceptional. While other shell collisions lead to short flashes of X-ray emission (of duration ≈ 500 s; see below), X-rays are generated here over almost 2.5 hours. The reason is that several tiny shells are fed into an outer, pronounced shell, which is then the site of strong emission. Furthermore, we notice that the strongest shell collisions in the figure lead to X-ray flashes still a factor of 10 more intense.

The temperature diagram in Fig. 17 shows a sudden expansion of the cooling zone after each strong shell collision. This is the process of shock destruction (Feldmeier 1995). However, in the latter paper we claimed somewhat misleadingly that the *progressive* rarefication of the intershell gas being fed into the shells causes the broadening of the cooling zones. We now see that the process is instead initiated by an *abrupt* change in preshock conditions after a shell collision: immediately after the merger, extremely rarefied intershell gas is being fed through the shock. This causes radiative cooling to cease and the shock to be pushed into the preshock gas.

The large number of shell collisions in our simulations can be traced back to the existence of two rather different shell populations: (1) very dense shells which move almost according to a stationary wind velocity law. (The fact that most of the gas mass in a time-dependent wind still follows a stationary velocity law was noticed by Owocki et al. 1988, cf. their Fig. 10; see also Puls et al. 1993, Fig. 2); and (2) fast "mini"shells with a density close to stationary values. As is obvious from Fig. 17, in almost all cases the X-ray flash occurs when a fast minishell rams into an outer, pronounced shell. – The formation of pronounced shells can be followed back almost into the photosphere, and corresponds to the largest perturbations which occur there. The momentum the shells gain from faster, inner gas which runs into them (through a reverse shock) is used up again by the shells overtaking and sweeping up dense gas ahead of them (eventually through a forward shock): the shells become fat, not fast. However, with the intershell gas being gradually swept up, ultimately (from about $1.2\ R_*$ on) the remaining gas ahead of the forward shock of a shell can be accelerated (the line-driven instability at work!) all the way through the *broad* and *empty* intershell region, i.e., the momentum is now in a small-mass, high-velocity blob.

Fig. 18 shows a time sequence of the shell collision around $r = 4.2\ R_*$ and $t = 3.64$ d from Fig. 17. We have chosen this instant since it gives a somewhat clearer picture than the multiple collision with very tiny shells at 3.5 days. (We note in passing that two interesting snapshots of a shell collision, however

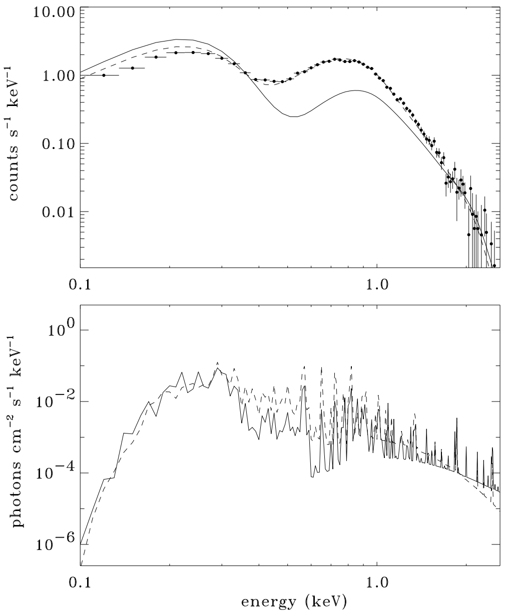

Fig. 14. Upper panel: ROSAT observed spectrum and spectrum for the Langevin model from Fig. 13. Lower panel: number of photons incident on the detector.

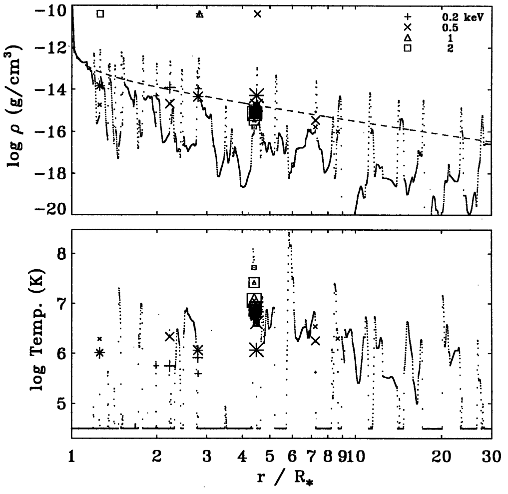

Fig. 15. The Langevin model from Fig. 13, with X-ray emitting gas marked. The symbols are as in Fig. 9.

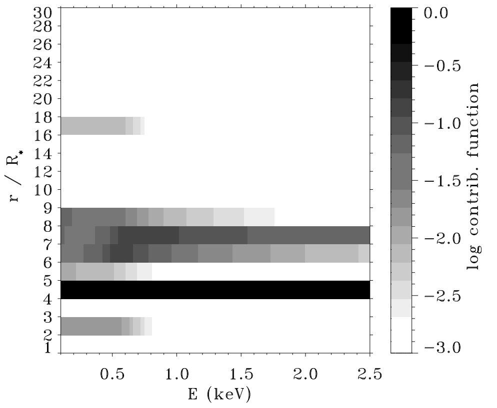

Fig. 16. Contribution function for the Langevin model, cf. Fig. 10.

discussed in the framework of X-ray variability due to shock merging, can be found in Cooper 1994, Fig. 6.9). – The sequence is shown in the frame of a particle which moves through a stationary wind with a $\beta = 0.8$ velocity law, where this particle is initially located at the position of the shell marked *A*. Since the comoving frame coordinate of this shell remains close to 0 during the time series, we see that this shell *is* actually moving roughly according to a $\beta = 0.8$ law. During the first five snapshots of Fig. 18, the fast shell *A'* drives the shock front *B* ahead of it, thereby compressing the cooling zone spanned by *A* and *B*. At 3.62 days, *A'* has merged with *A*. The kinetic energy of relative motion is thermalized during this inelastic collision, and for a short moment both prerequisites necessary for significant X-ray emission are met: the gas has a high density *and* a high temperature. From the figure one finds a relative motion of *A* and *A'* of $\approx$ 700 km/s, which corresponds to a temperature of $\approx 10^7$ K when thermalized. The length scale of this hot and dense region is that of the radiative shock through which the shell *A'* is added to *A*. Due to the high density, radiative cooling is efficient and the cooling zone behind the shock is very thin. Shortly after *A'*, a similar shell *A"* (of relative velocity $\approx$ 800 km/s) merges with *A*, which leads to a stronger X-ray emission at t = 3.64 d than the previous merger at t = 3.62 d. However, this difference is simply due to the coarse temporal resolution of the sequence. Finally, the last three snapshots of Fig. 18 show that extremely rarefied intershell gas is passing through the shock front; radiative cooling ceases therefore and the shock is pushed into the preshock gas, which ultimately leads to the destruction of the shock.

The duration of such a strong shell collision can be estimated as follows. The thickness of a minishell is the radial extent of swept-up gas – which is a substantial fraction of the intershell distance, i.e., a few times 0.1 R_* – divided by the compression factor, i.e., the Mach number squared at the reverse shock, where Ma = 20 is a typical value in our models. For a relative velocity of 800 km/s between minishell and pronounced shell, the collision time is then of order 10 seconds. Yet, the collision time in our simulations is much longer since we cannot resolve

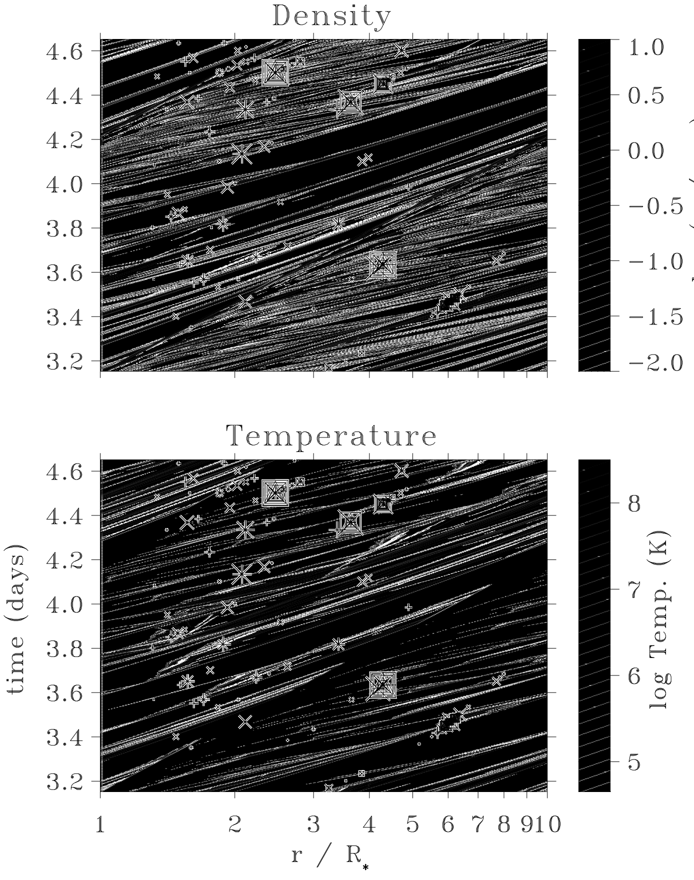

Fig. 17. Greyscale rendition of the evolution of wind density and temperature, with structure formation triggered by a tunable photospheric sound wave. The snapshot of Fig. 7 is taken from this sequence at time 3.5 d. The density is in units of its stationary value, and the coding of the symbols (crosses, squares, etc.) which indicate X-ray emission, $n_e n_H \Lambda_\nu(T)\,\mathrm{d}V$, is identical to that in Fig. 9.

the minishells on such tiny length scales, but instead they are smeared out over $\approx$ 5 grid zones, which gives a collision time of $\approx$ 500 seconds. However, the amount of heat generated, and therefore of X-rays emitted in the collision depends only on the total mass that is stopped, and should therefore be correctly estimated in our simulations.

We notice that, if the mechanism proposed here is indeed dominant, then the X-ray emission from hot star winds is a true multiscale problem: the total dynamical range of the wind is resolved numerically by $\lesssim 10^4$ grid points; individual wind structures (rarefaction regions between subsequent shells, which possibly collide at later times) by $\lesssim 10^3$ grid points; radiative cooling zones behind strong shocks – which in Feldmeier et al. (1996) were already defined as being of "microscopic" length scale – by $\lesssim 10^2$ points; and the sites of heating during a shell collision – which in the present paper are identified as origin of strong X-ray emission – by $\lesssim$ 10 points.

We close this section by considering the energy cascade in the wind from working rate of radiative forces to shock dissipation rate to X-ray emission rate. The first column in Table 2 specifies these numbers for the Lucy & White (1980) blob model, and the second column is an update (White & Chen 1994) for the Lucy (1982) forward shock model. The remaining columns are for the present time-dependent model, i.e., for the snapshots at 3.5 and 3 days of the wind perturbed by sound waves and by Langevin turbulence, respectively.

Here, the individual shocks in the models were examined to find the ratio of wind kinetic energy dissipated in the fronts. The 'efficiency' ratio, η, of heat radiated into X-rays in the ROSAT energy range, $\eta = L_{\mathrm{X,emit}}/L_{\mathrm{shock}}$, is determined from the constraint that the product of the first four rows in the table gives the ratio $L_{\mathrm{X,emerg}}/L_{\mathrm{bol}}$ in the fifth row. For temperatures in the range $10^{6.7}$ to 10^8 Kelvin, $\eta > 0.5$ should hold if most of the dissipated energy is radiated away – i.e., if wind heating plays no major role, as is the case in our models.

To gain a clearer view of the energetics of shell collisions, in addition to the snapshots from the last section (column 'total' in the table) we also examined the case when X-ray emission

Table 2. The energy cascade in the wind.

	Lucy & White	White & Chen	sound wave		Langevin turb.	
	(1980)	(1994)	total	no coll.	total	no coll.
$\frac{L_{\rm wind}}{L_{\rm bol}}$	$3.5 \cdot 10^{-3}$	10^{-2}	$1.7 \cdot 10^{-3}$	...	...	...
$\frac{L_{\rm shock}}{L_{\rm wind}}$	0.1	10^{-2}	$2 \cdot 10^{-2}$	10^{-4}	$2 \cdot 10^{-2}$	10^{-4}
$\frac{L_{\rm X,emit}}{L_{\rm shock}}$	0.1	1	$5 \cdot 10^{-2}$	0.4	$3 \cdot 10^{-2}$	1
$\frac{L_{\rm X,emerg}}{L_{\rm X,emit}}$	$2 \cdot 10^{-3}$	10^{-3}	0.16	0.31	0.15	0.19
$\frac{L_{\rm X,emerg}}{L_{\rm bol}}$	$7 \cdot 10^{-8}$	10^{-7}	$2.8 \cdot 10^{-7}$	$2.3 \cdot 10^{-8}$	$1.7 \cdot 10^{-7}$	$3.3 \cdot 10^{-8}$
$\frac{L^{\rm model}_{\rm X,emerg}}{L^{\rm obs}_{\rm X,emerg}}$	1.3	1	1.1	0.09	0.7	0.13

from collisions is artificially suppressed by setting the gas temperature at these sites to $T_{\rm eff}$ (column 'no coll.' in the table). For the latter case, the steady shocks indeed emit almost all the dissipated energy (which is a fraction 10^{-4} of $L_{\rm wind} = \frac{1}{2}\dot{M}v_\infty^2$) into X-rays, $\eta \lesssim 1$. ($\eta = 0.4$ for the sound wave model indicates that we did not succeed in flagging all collision sites, cf. below.) Yet, the emergent X-ray flux lies a factor of 10 below the observed flux. Including the shell collisions then gives an enhancement of the ratio of wind kinetic energy transformed into heat by a factor of 200. However, the efficiency η drops by a factor of roughly 10, so that now the emitted X-ray flux matches the observed one.

The reason for the reduced efficiency is the following. The dense, narrow shells of gas which pass through some of the fronts at these selected instants are rare events, and lead to a *momentary* dissipation rate (and X-ray emissivity) which is much larger than the true, long-time average. In contrast to a steady shock, the gas conditions in the vicinity of a collision site already imply a much lower dissipation rate and X-ray emission. On the other hand, the X-ray emission as calculated from the snapshot reflects the history of gas heating. The reduction in efficiency reflects then the ratio of the duration of shell collisions (roughly 500 s) to the time interval between them (a few hours).

Our *overall* efficiency of transfering wind kinetic energy into X-rays is more than one decade smaller than in the models of Lucy & White (1980) and Lucy (1982). This is compensated by the lower X-ray absorption in our model. However, this may point to possible difficulties of the present approach to generate sufficient X-ray flux when (much) denser winds are considered.

5. X-ray variability

Since the shell collisions in Fig. 17 occur on a short timescale, and since only a few collisions occur at a given time, the X-ray emission from the wind is highly variable. Fig. 19 shows the X-ray luminosity in the ROSAT band for our four models (two different base amplitudes for each the photospheric sound wave and Langevin turbulence model) together with a fifth model which serves as a numerical test case. The latter has a refined grid in deep wind layers so that filtering of short-scale photospheric waves is reduced. Except for this difference, it is identical to the Langevin model with small base perturbation amplitude. No systematic offset is seen from the figure to occur between these two models, which implies that those photospheric pertubations that are important for the X-ray emission can indeed propagate out into the wind. – Two facts are apparent from the figure (and will be quantified below in Fig. 21):

(1) *The average X-ray luminosity from the models is only a factor of two to three below the observed value.* We feel this to be strong evidence that shell collisions may indeed be efficient enough to generate the X-ray emission from hot star winds. This especially in light of two numerical uncertainties, which both should lead to an *under*estimate of the X-ray flux: first, the resolution problem of radiative cooling zones (cf. Sect. 2.1) leads to a direct loss of hot gas; and second, the cutoff parameter $\kappa_{\rm m}$ (Owocki et al. 1988), which is introduced to make the radiative instability numerically manageable, causes artificial radial stretching of the wind structure, and thereby probably leads to a reduced collision rate along a wind ray.

(2) The $L_x(t)$ distributions of all five models appear to be quite similar. Due to the different perturbation mechanisms applied (sound wave vs. turbulence) this means that our results for the X-ray emission should be robust – even with individual shell collisions being rather delicate processes.

The *minimum* L_x in the figure corresponds to the emission from individual radiative shocks and leftover hot gas, but with no shell-collisions taking place: notice that this minimum lies a factor of ≈ 30 below the observed L_x, as was also estimated in Sect. 3.2 to be the contribution from shocks and old hot gas to the emission. This shows that *shell collisions can lead to an X-ray emission which is on average one order of magnitude larger than the emission from individual shocks and leftover hot gas.*

The question arises whether the L_x at successive instants in Fig. 19 are statistically dependent or independent. The sampling

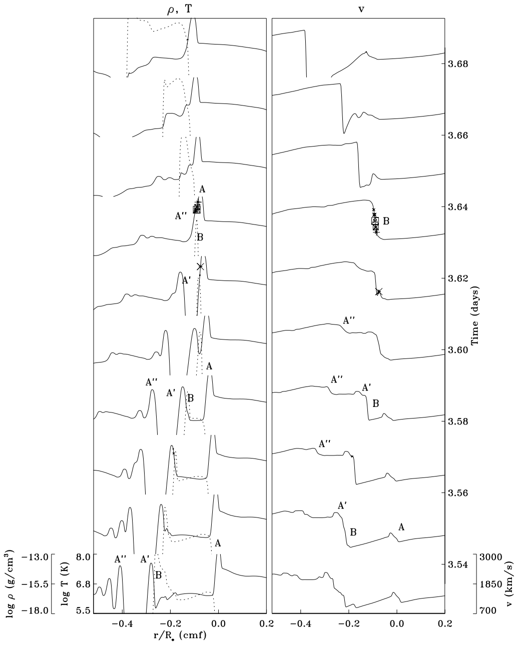

Fig. 18. Time sequence of the shell collision at $r = 4.2\ R_*$ and $t = 3.64$ days from Fig. 17. The left panel shows the density (full line) and temperature (dashed line), the right panel the velocity; axes are indicated for the panel bottom. An outer, pronounced shell, *A*, and two small, inner shells, *A'* and *A"*, are marked. *B* is the reverse shock of shell *A*. The spatial coordinate is in the frame of a particle which moves according to a $\beta = 0.8$ velocity law, and which is initially located at the position of shell *A*.

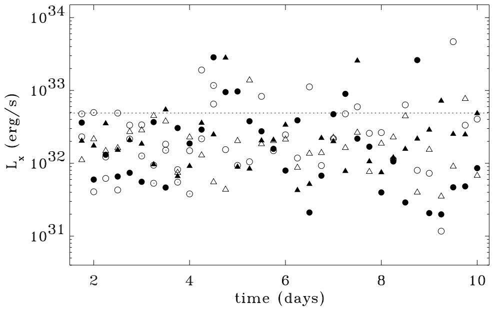

Fig. 19. X-ray luminosity in the ROSAT energy band vs. time, for five numerical wind simulations with different types of base perturbation (triangles: sound wave – circles: Langevin turbulence), and different perturbation amplitudes (open symbols: small – filled symbols: large amplitude). Circles with a dot in the center are for a Langevin test model with very fine grid resolution (this model only up to 4.5 days). The dotted line at $L_x = 4.9 \times 10^{32}$ erg/s is the emergent X-ray luminosity deduced for ζ Ori from a one-temperature fit to the ROSAT data.

time is 6 hours in this plot, i.e., much longer than the interval over which an individual shell collision takes place (about 500 seconds), and also longer than the correlation time of photospheric perturbations, which is between 10^3 and 10^4 seconds. Indeed, at a few instants changes in L_x as large as a factor of 100 are found in Fig. 19 within one sampling time. Therefore, subsequent L_x are – to a large degree – independent. However, there are one, possibly two long-time trends seen in this diagram: (i) up to 4 days, the L_x distribution is narrower than at later times. This is interpreted to be due to the presence of initial transients, i.e., the wind has not yet settled to its limit cycle. (ii) After 4 days, it seems that the width of the L_x distribution grows monotonically with time. However, this is possibly an effect of small sample size in that rare events – i.e., very high or low luminosities – only show up after long time intervals.

One may ask whether it would not be more appropriate to compare time-averaged, synthesised X-ray spectra instead of snapshots with the ROSAT data. While the computational effort in doing so would be high, our results should be rather insensitive to such averaging – at least for the most interesting time intervals of 1000 s, which correspond to typical single ROSAT observations – for essentially two reasons. (1) From a few tests we find that L_x values close to the center of the distributions in Fig. 19 vary only by ±20% over 1000 seconds. (2) The total width of the L_x distributions should also be almost invariant, since: (i) the minimum L_x is due to *frequent* radiative shocks and leftover hot gas; and (ii) the maximum L_x is due to strong shell collisions of duration ≈ 500 seconds and ≈ 5 hours apart, i.e., this maximum should already be sampled in Fig. 19, and should remain approximately the same under 1000 s averaging.

The temporal average (from 4 to 10 days after model start) of the calculated X-ray spectra is shown in the upper panel of Fig. 20. All four models give, on average, about the correct flux of soft X-rays from 0.1 to 0.4 keV. The largest deviations, by an average factor of ≈ 5, occur for all models between 0.6 and 1 keV. For hard X-rays above 1 keV then, the models predict a flux roughly a factor of 2 or 3 below the observed flux. Furthermore, while the average count rate for the sound wave model with strong base perturbation amplitude (0.5) is, over the whole energy range, almost twice as large as for the small amplitude (0.3) model, the count rate for the turbulence model with small amplitude (0.2) is approximately equal to that with large amplitude (0.5) – actually even somewhat *larger*! Only for the latter Langevin models we can therefore conclude that unstable growth has saturated at a level independent of the base perturbation amplitude before the X-ray emitting region is reached, whereas for the sound wave model the emission (still) scales with the amplitude. The lower panel of the figure shows the ranges spanned by the X-ray spectra during these 6 days. No major systematic offsets between the models are found except for the above mentioned factor of two, and except for an enhanced flux at hard X-rays of the sound wave model with large

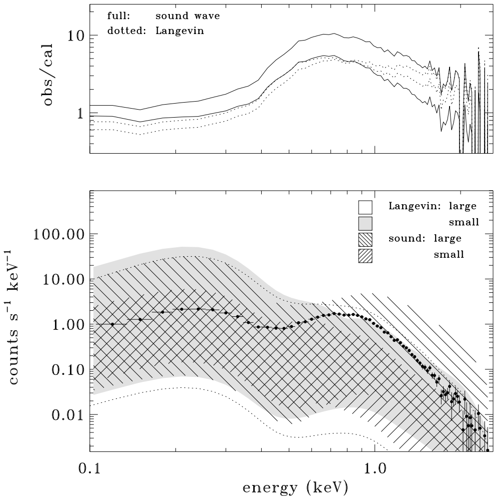

Fig. 20. Temporal variability of the calculated spectra from 4 to 10 days. Upper panel: temporal averages of the observed to calculated count rates. Lower panel: total range of count rates spanned by the different models.

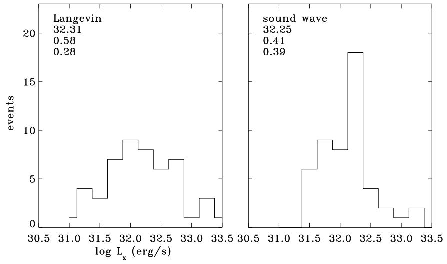

Fig. 21. Distribution function for the Langevin and sound wave model between 4 and 10 days, where "events" refer to Fig. 19. The numbers at top of the panels are the mean value, the standard deviation, and the skewness of the distributions, respectively.

perturbation amplitude. However, the latter hump is spanned up by two snapshots only, i.e., by very sparse events.

We reach the critical test of the present model of X-ray emission. Except for the episodic rise in September 1992, Berghöfer & Schmitt (1994a) found the absolute variations in the X-ray count rate of ζ Ori to be well below 10%. In stark contrast, we find a variability over 2.5 decades in the X-ray luminosity. – We propose, as an outlook to future calculations, that the observed stationarity of the X-ray emission is achieved via a *lateral fragmentation of the emitting and absorbing shells into clouds or clumps*, so that fluctuations along individual wind rays average out over the whole emitting volume. This assumption is consistent with our use of *stochastic* photospheric base perturbations, for which horizontal coherence lengths should be small. (For a typical coherence time t_c = 5000 s in our models, the stellar surface could consist of $\gtrsim 10^5$ patches.) Furthermore, as shown by Rybicki et al. (1990), horizontal velocity fluctuations will be strongly damped due to the line-drag effect (Lucy 1984), hence the line-driven instability should not mix gas from wind rays originating in different photospheric conditions. If, finally, horizontal mixing due to the Rayleigh-Taylor and Kelvin-Helmholtz instabilities (cf. Chandrasekhar 1961) is negligible, and if also the stellar rotation speed is low, we can roughly interpret the temporal snapshots of Fig. 19 as corresponding to the emission from different *radial* cones of small opening angle at one *single* time. To get a quantitative estimate for the required fragmentation then, we argue as follows. We neglect X-ray absorption in the wind (which is not too bad an approximation for ζ Ori); this reduces the radiative "transfer" to a linear problem, one of adding up the emission from individual cones. We assume further that each emitting cone has the same opening angle (i.e., base area), and that the temporal mean and standard deviation of L_x is the same for all cones. From Fig. 21 we find that the mean of the calculated log L_x distribution is 32.3, with standard deviations $\sigma(\log L_{x,\rm cal})$ = 0.4 and 0.6 for the sound wave and Langevin models, respectively. Identifying the maximum *absolute* changes of $\leq$ 7% found by Berghöfer & Schmitt (1994a) with a three sigma interval, we have $\sigma(\log L_{x,\rm obs})$ = 0.01. Since σ drops with the square root of the number of emitting cones, a few thousand independent radial cones would ensure the observed flux constancy.

6. Summary and future work

Our one-dimensional, hydrodynamic model of an O supergiant wind which is subject to the line-driven instability showed that the crash of small, fast blobs into massive, slow blobs can release an X-ray flux which almost matches the observed one. (On the other hand, the X-ray spectral *shape* gives only minor constraints on any model building attempt at this more principal stage – as was also noticed by Cassinelli & Swank 1983, MacFarlane & Cassinelli 1989, and Cooper & Owocki 1994.)

A number of questions were raised during this study, which give the directions for future, more quantitative work.

1. A 3-D Monte Carlo approach is needed for the X-ray transfer which allows patching of the full solid angle into emitting and absorbing wind cones – to study how X-ray flux constancy is achieved via volume averaging. On the other hand a larger number of *radial* shell collisions, and a corresponding reduction in the flux variability could also be achieved by using larger, i.e., more natural values of the cutoff parameter $\kappa_{\rm m}$ together with shorter perturbation periods. However, methods have to be developed first to handle the steep intershell velocity field that results from increasing $\kappa_{\rm m}$.

2. A systematic study is needed over the full range of spectral types O3 to O9 and luminosity classes I to V to find which relation(s) our models predict between L_x and $L_{\rm bol}$ – and other stellar parameters, possibly. The fundamental relation $L_x \approx$

$10^{-7} L_{\rm bol}$ – with no wind quantity entering – remains astonishing for wind-embedded X-ray sources.

3. A detailed investigation of the dynamics of blob-blob collisions is needed, together with a method to achieve better spatial resolution of the blobs and therefore of the collision process in a full hydrodynamic simulation. An interesting question in this context is raised by the finding (Feldmeier et al. 1996) that fits to ROSAT spectra which assume radiative shocks as fundamental emitting entities are superior to fits which assume isothermal hot gas. How does this translate to the present finding that blob-blob collisions are the strongest sites of X-ray emission? Can we identify the radiative shocks from the above fits with the radiative shocks through which small, fast blobs coalesce with pronounced, slow blobs?

Acknowledgements. We thank Drs. S. Owocki, L. Lucy, R.P. Kudritzki, U. Springmann, A. Fullerton, W. Lingl, R. Palsa, and H. Lesch for interesting discussions, and A. Fullerton for carefully reading the manuscript. Most of the ROSAT data for ζ Ori were made available by Drs. J. Schmitt and T. Berghöfer. This work was supported by the DFG under contract Pa 477/1-2, and by the BMBF under contract 50 OR 9304.

References

Abbott D.C., Bieging J.H., Churchwell E., 1984, ApJ 280, 671
Baade D., 1991, in: Baade D. (ed.) Rapid variability of OB stars: nature and diagnostic value. ESO Proc. 36, Garching, p. 217
Baade D., Lucy L.B., 1987, A&A 178, 213
Berghöfer T.W., Schmitt J.H.M.M., 1994a, A&A 290, 435
Berghöfer T.W., Schmitt J.H.M.M., 1994b, Sci 265, 1689
Berghöfer T.W., Schmitt J.H.M.M., 1995, Adv. Space Res. 16, 163
Berghöfer T.W., Baade D., Schmitt J.H.M.M., et al., 1996, A&A 306, 899
Bieging J.H., Abbott D.C., Churchwell E.B., 1989, ApJ 340, 518
Bjorkman J.E., Cassinelli J.P., 1993, ApJ 409, 429
Bohlender D.A., 1994, in: Balona L.A., Henrichs H.F., Le Contel J.M. (eds.) Pulsation, rotation and mass loss in early-type stars. Proc. IAU Symp. 162. Kluwer, Dordrecht, p. 155
Cassinelli J.P., Olson G.L., 1979, ApJ 229, 304
Cassinelli J.P., Swank J.H., 1983, ApJ 271, 681
Cassinelli J.P., Olson G.L., Stalio R., 1978, ApJ 220, 573
Cassinelli J.P., Waldron W.L., Sanders W.T., et al., 1981, ApJ 250, 677
Cassinelli J.P., Cohen D.H., MacFarlane J.J., Sanders W.T., Welsh B.Y., 1994, ApJ 421, 705
Castor J.I., Abbott D.C., Klein R.I., 1975, ApJ 195, 157
Chandrasekhar S., 1961, Hydrodynamic and hydromagnetic stability. Oxford
Chen W., White R.L., 1991, ApJ 366, 512
Chen W., White R.L., 1994, Ap&SS 221, 259
Chlebowski T., Harnden F.R., Sciortino S., 1989, ApJ 341, 427
Cohen D.H., Cooper R.G., MacFarlane J.J., et al., 1996, ApJ 460, 506
Collura A., Sciortino S., Serio S., et al., 1989, ApJ 338, 296
Conti P.S., Ebbets D., 1977, ApJ 213, 438
Cooper R.G., 1994, PhD thesis, Univ. Delaware
Cooper R.G., Owocki S.P., 1992, PASPC 22, 281
Cooper R.G., Owocki S.P., 1994, Ap&SS 221, 427
Corcoran M.F., Swank J.H., Serlemitsos P.J., et al., 1993, ApJ 412, 792
Corcoran M.F., Waldron W.L., MacFarlane J.J., et al., 1994, ApJ 436, L95
Cranmer S.R., Owocki S.P., 1996, ApJ 462, 469
Daltabuit E., Cox D., 1972, ApJ 173, L13
Ebbets D., 1979, ApJ 227, 510
Feldmeier A., 1995, A&A 299, 523
Feldmeier A., Kudritzki R.P., Palsa R., Pauldrach A.W.A., Puls J., 1996, A&A, in press
Fullerton A.W., Gies D.R., Bolton C.T., 1996, ApJS 103, 475
Gail H.P., Hundt E., Kegel W.H., Schmid-Burgk J., Traving G., 1974, A&A 32, 65
Gautschy A., Glatzel W., 1990, MNRAS 245, 597
Gies D.R., 1996, in: Strassmeier K.G., Linsky J.L. (eds.) Stellar surface structure. Proc. IAU Symp. 176. Kluwer, Dordrecht, p. 121
Glatzel W., 1994, MNRAS 271, 66
Harnden F.R., Branduardi G., Elvis M., et al., 1979, ApJ 234, L51
Haser S., 1995, PhD thesis, Univ. München
Hearn A.G., 1972, A&A 19, 417
Hearn A.G., 1973, A&A 23, 97
Hearn A.G., 1975, A&A 40, 277
Henrichs H.F., 1988, in: Conti P.S., Underhill A.B. (eds.) O stars and Wolf-Rayet stars. NASA SP-497, Washington, D.C., p. 199
Henrichs H.F., Kaper L., Nichols J.S., 1994, in: Balona L.A., Henrichs H.F., Le Contel J.M. (eds.) Pulsation, rotation and mass loss in early-type stars. Proc. IAU Symp. 162. Kluwer, Dordrecht, p. 517
Hillier D.J., Kudritzki R.P., Pauldrach A.W., et al., 1993, A&A 276, 117
Kudritzki R.P., 1992, A&A 266, 395
Kudritzki R.P., Hummer D.G., 1990, ARA&A 28, 303
Kudritzki R.P., Lennon D.J., Puls J., 1995, in: Walsh J.R., Danziger I.J. (eds.) Science with the VLT. Springer, Heidelberg, p. 246
Kudritzki R.P., Palsa R., Feldmeier A., Puls J., Pauldrach A.W.A., 1996 in: Zimmermann H.U., Trümper J.E., Yorke H. (eds.) Röntgenstrahlung from the Universe. MPE Report 263, Garching, p. 9
Lamers H.J.G.L.M., Leitherer C., 1993, ApJ 412, 771
Landau L.D., Lifshitz E.M., 1989, Hydrodynamics. Academic Press
Langer S.H., Chanmugam G., Shaviv G., 1981, ApJ 245, L23
Langer S.H., Chanmugam G., Shaviv G., 1982, ApJ 258, 289
Long K.S., White R.L., 1980, ApJ 239, L65
Lucy L.B., 1982, ApJ 255, 286
Lucy L.B., 1984, ApJ 284, 351
Lucy L.B., Solomon P.M., 1970, ApJ 159, 879
Lucy L.B., White R.L., 1980, ApJ 241, 300
MacFarlane J.J., Cassinelli J.P., 1989, ApJ 347, 1090
MacFarlane J.J., Cohen D.H., Wang P., 1994, ApJ 437, 351
MacGregor K.B., Hartmann L., Raymond J.C., 1979, ApJ 231, 514
Mihalas D., 1979, MNRAS 189, 671
Monin A.S., Yaglom A.M., 1987, Statistical fluid mechanics, Vol. 2. MIT Press, Cambridge
Morrison R., McCammon D., 1983, ApJ 270, 119
Norman M.L., Wilson J.R., Barton R.T., 1980, ApJ 239, 968
Owocki S.P., 1991, in: Crivellari L., Hubeny I., Hummer D.G. (eds.) Stellar atmospheres: beyond classical models. Kluwer, Dordrecht, p. 235
Owocki S.P., 1992, in: Heber U., Jeffery S. (eds.) Atmospheres of early-type stars. Springer, Heidelberg, p. 393
Owocki S.P., Puls J., 1996, ApJ 462, 894
Owocki S.P., Rybicki G.B., 1984, ApJ 284, 337
Owocki S.P., Castor J.I., Rybicki G.B., 1988, ApJ 335, 914
Owocki S.P., Cranmer S.R., Fullerton A.W., 1995, ApJ 453, L37
Pallavicini R., Golub L., Rosner R., et al., 1981, ApJ 248, 279
Pauldrach A., Puls J., Kudritzki R.P., 1986, A&A 164, 86

Pauldrach A.W.A., Kudritzki R.P., Puls J., Butler K., Hunsinger J., 1994, A&A 283, 525
Pollock A.M.T., 1987, A&A 171, 135
Pope S.B., 1994, Ann. Rev. Fluid Mech. 26, 23
Prinja R.K., Fullerton A.W., 1994, ApJ 426, 345
Prinja R.K., Howarth I.D., 1986, ApJS 61, 357
Puls J., Owocki S.P., Fullerton A.W., 1993, A&A 279, 457
Puls J., Kudritzki R.P., Herrero A., et al., 1996, A&A 305, 171
Raymond J.C., Smith B.W., 1977, ApJS 35, 419
Raymond J.C., Cox D.P., Smith B.W., 1976, ApJ 204, 290
Reile C., Gehren T., 1991, A&A 242, 142
Risken H., 1989, The Fokker-Planck equation. Springer, Berlin
Rybicki G.B., Owocki S.P., Castor J.I., 1990, ApJ 349, 274
Sciortino S., Vaiana G.S., Harnden F.R., et al., 1990, ApJ 361, 621
Seward F.D., Forman W.R., Giacconi R., et al., 1979, ApJ 234, L55
Stahl O., Wolf B., Gäng T., et al., 1993, A&A 274, L29
Thompson K.W., 1987, J. Comp. Phys. 68, 1
Thompson K.W., 1990, J. Comp. Phys. 89, 439
Uhlenbeck G.E., Ornstein L.S., 1930, Phys. Rev. 36, 823
Underhill A.B., Fahey R.P., 1984, ApJ 280, 712
Van Leer B., 1977, J. Comp. Phys. 23, 276
Voels S.A., Bohannan B., Abbott D.C., Hummer D.G., 1989, ApJ 340, 1073
Walder R., Folini D., 1996, A&A, in press
Waldron W.L., 1984, ApJ 282, 256
Waldron W.L., 1991, ApJ 382, 603
Wax N., 1954, Selected papers on noise and stochastic processes. Dover, New York
Wessolowski U., 1996, in: Zimmermann H.U., Trümper J.E., Yorke H. (eds.) Röntgenstrahlung from the Universe. MPE Report 263, Garching, p. 75
White R.L., 1985, ApJ 289, 698
White R.L., Chen W., 1992, PASPC 22, 274
White R.L., Chen W., 1994, Ap&SS 221, 295

This article was processed by the author using Springer-Verlag LaTeX A&A style file *L-AA* version 3.

Astron. Astrophys. 332, 245–250 (1998)

ASTRONOMY
AND
ASTROPHYSICS

The line-driven instability in Sobolev approximation

A. Feldmeier

Universitäts-Sternwarte, Scheinerstr. 1, D-81679 München, Germany

Received 22 August 1997 / Accepted 1 December 1997

Abstract. Line-driven winds, e.g., of OB stars, are subject to a strong hydrodynamic instability. As a corollary to the comprehensive linear stability analysis performed by Owocki & Rybicki (1984), we present here a simplified derivation of the growth rates from applying a *second order* Sobolev approximation. This is applicable for perturbation wavelengths larger than the Sobolev length, and covers the physically most interesting regime of perturbations which can develop into strong reverse shocks, and heat the gas to X-ray temperatures. Since the usual WKB approximation is not applied, we furthermore find the existence of a limiting wavelength beyond which perturbances do not grow, but instead decay.

Key words: stars: early-type – hydrodynamics – instabilities – shock waves

1. Introduction

Lucy & Solomon (1970) noticed the existence of a new hydrodynamic instability for line-driven winds, which resembles the runaway mechanism described by Milne (1926) for static atmospheres.

MacGregor et al. (1979) and Carlberg (1980) derived the linear growth rates of this so-called line-driven instability by assuming flow perturbations are optically thin. Contrary to their results, Abbott (1980) found that growth rates of long-scale perturbations, for which the Sobolev approximation could be applied, are zero. Owocki & Rybicki (1984; OR in the following) 'bridged' these opposing results by showing that harmonic perturbations of wavelength λ shorter than one third to one half the Sobolev length, $L = v_{\rm th}/v'$ (primes indicate spatial differentiation), are highly unstable at the constant rate given by MacGregor et al. (1979) and Carlberg (1980); for $\lambda > L$, on the other hand, the growth rate drops as λ^{-2}, implying marginal stability for $\lambda \rightarrow \infty$.

Subsequent analytic work on the instability was concerned with: (1) the influence of scattering, e.g., flow stabilization due to line drag (Lucy 1984; Owocki & Rybicki 1985); (2) growth rates for non-radial velocity perturbations (Rybicki et al. 1990); and (3) growth rates for flows with optically thick continuum (Owocki & Rybicki 1991; Gayley & Owocki 1995).

Numerical wind simulations by Owocki et al. (1988) and Owocki (1991) showed the occurence of broad rarefaction regions over which the gas is highly accelerated, and is eventually decelerated again in a strong reverse shock, which heats the gas to X-ray temperatures. Subsequent radiative cooling compresses this gas into dense and narrow clouds. The idea that such clouds should correspond to the observed discrete absorption features in P Cygni profiles is meanwhile mostly ruled out (cf. Puls et al. 1993; Cranmer & Owocki 1996; and the volume edited by Moffat et al. 1994). On the other hand, after some initial difficulties (Cooper & Owocki 1992, 1994), it seems now plausible (Feldmeier et al. 1997) that the observed X-ray emission from O stars (cf. Hillier et al. 1993, and references therein) stems from instability-generated shocks.

The present paper returns to the issue of linear stability analysis, with a twofold aim: (1) to present an easy and straightforward derivation of growth rates, which, for the physically most interesting regime of moderate long-scale perturbations, complements the more elaborate analyses of OR and Lucy (1984); and (2) to show how the second order Sobolev approximation implies an *unstable growth* of inward propagating radiative-acoustic waves, where the latter were firstly described by Abbott (1980) and result already from a first order Sobolev treatment.

A related second order expansion was already performed earlier by Owocki (1991, priv. comm.) to show that the line force in (first order) Sobolev approximation is to one order in L more accurate for pure scattering lines than for pure absorption lines. The aim of this investigation was to explain certain difficulties which are encountered when one tries to reproduce the stationary wind solutions of Castor et al. (1975; CAK in the following) and Pauldrach et al. (1986) – which both apply first order Sobolev approximation – by using instead the exact line force for the case of pure line absorption (Owocki et al. 1988; Poe et al. 1990). In another context, the second order Sobolev approximation was also considered by Sellmaier et al. (1993).

Notice that the derivation given below is for pure absorption lines in a purely radial flow from a point source of radiation. According to Lucy (1984) and Rybicki et al. (1990), the growth rates are then *maximum* ones.

Send offprint requests to: feld@usm.uni-muenchen.de

2. Instability from second order Sobolev approximation

The reason that Abbott (1980) found no indication of wind instability is that he used the Sobolev approximation in lowest order, even for the flow perturbations. E.g., consider an optically thick line, with line force per unit mass $g_T \sim v'/\rho$ (Sobolev 1960; Castor 1974). By assuming harmonic perturbations, this implies a phase shift of 90° between velocity perturbations, δv, and the response of the line force, δg. Hence, the line force does no net work on the velocity perturbation over a full cycle, and the perturbation does not grow (OR).

To see how the instability arises, we consider at first the expression for the exact line force, before the Sobolev approximation is applied. Let $\tilde{x}$ be the frequency displacement from line center, ν_l, in Doppler units, $\Delta\nu_D = \nu_l v_{\rm th}/c$ ($v_{\rm th}$ the ionic thermal speed, c the speed of light), as measured in the observers frame. For radially directed photons, the force per unit mass due to photon absorption in a single line is,

$$g_l(r) = g_t(r) \int_{-\infty}^{\infty} d\tilde{x}\, \phi\left(\tilde{x} - \frac{v(r)}{v_{\rm th}}\right) e^{-\tau(\tilde{x},r)}. \qquad (1)$$

g_t is the force due to an optically thin line, with κ the mass absorption coefficient, and F_ν the stellar flux at the line frequency,

$$g_t = \frac{\kappa\, \Delta\nu_D\, F_\nu}{c}, \qquad (2)$$

and the radial optical depth is

$$\tau(\tilde{x}, r) = \int_{R_*}^{r} dr'\, \kappa(r')\rho(r')\phi\left(\tilde{x} - \frac{v(r')}{v_{\rm th}}\right), \qquad (3)$$

with R_* the stellar radius. In first order Sobolev approximation, κ, ρ, and dv/dr are assumed to be constant over the narrow region, i.e., the Sobolev zone, over which photons of given frequency can be absorbed in the line transition. This implies

$$g_l = g_t\, \frac{1 - e^{-\tau_1}}{\tau_1}, \qquad (4)$$

where

$$\tau_1(r) = \kappa(r)\, \rho(r)\, v_{\rm th}/v'(r). \qquad (5)$$

Introducing then a velocity perturbation, δv, into (1) and (3) leads to a rather complex expression. To allow a further progress, MacGregor et al. (1979) and Carlberg (1980) assumed that the exponential term is not affected by the perturbation, i.e., the perturbation is optically thin.

As will be discussed in Sect. 4, the velocity jumps which are caused by the corresponding short-scale perturbations are rather small, namely of order the thermal speed, and cannot explain, e.g., the observed X-ray emission from OB stars.

We are therefore primarily interested in long-scale perturbations, which, despite of their reduced growth rates (cf. below), can still grow into saturation and give rise to large velocity, temperature, and also density jumps. Notice that $\delta\tau \approx 0$ can then no longer be assumed. However, as will be shown in the following, the growth rates are then easily derived from applying a second order Sobolev approximation.

The *bridging length* where this long-scale limit breaks down, and the λ^{-2} increase of the growth rate bends over to the constant, maximum rate given by Carlberg (1980), is set by the Sobolev length. This can be seen from the fact that the first order Sobolev approximation does *not* lead to an instability (Abbott 1980), while the second order approach leads to the correct growth rates for long-scale perturbations. The second order approximation differs from the first order one by terms in L.

2.1. Optical depth in second order Sobolev approximation

Let x be the frequency displacement in the comoving frame,

$$x = \tilde{x} - \frac{v(r)}{v_{\rm th}}, \qquad (6)$$

and assume *small* perturbations, so that the wind velocity field remains monotonic. Then (3) can be transformed to a frequency integral,

$$\tau(x, r) = \kappa\, v_{\rm th} \int_x^{\infty} dy\, \frac{\rho}{v'}[s(y)]\, \phi(y), \qquad (7)$$

where the integration variable is defined as $y = \tilde{x} - v(s)/v_{\rm th}$. As before, κ is assumed to be constant over the Sobolev zone, which is a reasonable assumption for resonance lines and transitions from metastable levels, both dominating the line force. Performing a Taylor series expansion of ρ/v' to first order (and abbreviating $\rho_r \equiv \rho(r)$, etc.),

$$\frac{\rho_s}{v'_s} = \frac{\rho_r}{v'_r}\left[1 + \left(\frac{\rho'_r}{\rho_r} - \frac{v''_r}{v'_r}\right)(s - r)\right]. \qquad (8)$$

From (6), and again to first order,

$$s - r = -\frac{v_{\rm th}}{v'_r}\,(y - x). \qquad (9)$$

We consider now only the Doppler core of the line, where de-shadowing effects are most pronounced, and therefore the growth rates are largest (OR). With $\Phi(x) \equiv \int_x^\infty dy\, \phi(y)$, and since $x\phi(x) = -\frac{1}{2}\phi'(x)$ for a Doppler profile, the optical depth in second order Sobolev approximation is,

$$\tau_2(x, r) \;=\; \tau_1(r)\left[\Phi(x) - \frac{v_{\rm th}}{2v'_r}\left(\frac{\rho'_r}{\rho_r} - \frac{v''_r}{v'_r}\right)\big(\phi(x) - 2x\Phi(x)\big)\right]. \qquad (10)$$

Remember that $\tau_1(x, r) = \tau_1(r)\, \Phi(x)$ is the optical depth from a first order treatment.

The divergence of the expression $2x\Phi(x)$ in (10) for $x \to -\infty$ is an extrapolation artefact of the linear expansions performed in (8) and (9), and is compensated for by higher order terms in the Taylor series. In any case, this term enters the force response δg only via the combination $2x\Phi(x)\phi(x)$, which vanishes for $x \to -\infty$ (see below).

We separate v and ρ into their stationary components (subscript '0') plus a harmonic perturbation,

$$v(r,t) \;=\; v_0(r) + \delta v\, \exp\left[i\left(k_* \frac{v_*}{v_0(r)} r - \omega t\right)\right],$$
$$\rho(r,t) \;=\; \rho_0(r) + \delta\rho\, \exp\left[i\left(k_* \frac{v_*}{v_0(r)} r - \omega t\right)\right]. \tag{11}$$

Here, δv and k are assumed to be real, while $\delta\rho$ and ω are complex to allow for arbitrary phase shifts between velocity and density perturbations, and for unstable growth, respectively. The expression $k_* v_* r/v_0(r)$, where asterisks refer to an arbitrary, however *fixed* location in the stellar rest frame, accounts for the stretching of perturbations in the accelerating velocity field v_0 (i.e., λ/v_0 is independent of radius). For perturbations which originate in the photosphere, e.g., one could choose $v_* = v(R_*)$. Note that if the sound speed is small compared to *any* other speed (flow speed and wave speeds), pressure forces can be neglected, and the above expression for wave stretching is *exact*.

Inserting (11) into (10), and keeping only terms linear in δv and $\delta\rho$, gives

$$\frac{\delta\tau_2(x,r)}{\tau_1(r)} = \frac{\delta\rho}{\rho_0}\left[\Phi(x) - \frac{v_{\rm th}}{2v_0}\big(i\chi - q\big)\big(\phi(x) - 2x\Phi(x)\big)\right] - $$
$$-\frac{\delta v}{v_0}\left[\Phi(x) - \frac{v_{\rm th}}{2v_0}\big(i\chi - 4 - qt\big)\big(\phi(x) - 2x\Phi(x)\big)\right] i\chi. \tag{12}$$

Here, $\delta\tau_2$ is given modulo the exponential terms from (11), and the dimensionless wavenumber χ is defined as

$$\chi = k_* v_* \frac{v_0 - r v_0'}{v_0 v_0'}. \tag{13}$$

Since we will concentrate mostly on the case $r v_0' \ll v_0$, i.e., the outer wind, we can approximate

$$\chi \approx \frac{v_0}{v_0'}\, k = \frac{v_0}{v_{\rm th}}\, Lk. \tag{14}$$

Finally, we introduced in (12),

$$q \;=\; \frac{v_0 v_0''}{{v_0'}^2} \;=\; -(4\mathrm{r} - 3),$$
$$t \;=\; \frac{3v_0 - 2r v_0'}{v_0 - r v_0'} \;=\; \frac{3\mathrm{r} - 4}{\mathrm{r} - 3/2}, \tag{15}$$

where $\mathrm{r} = r/R_*$, and the second equalities hold for the CAK velocity law for a wind from a point source, $v_0(r) = v_\infty\sqrt{1 - \mathrm{r}^{-1}}$, with terminal wind speed v_∞.

2.2. The perturbed line force

Introducing the comoving frame frequency, x, in (1), and applying a small perturbation $\delta\tau(x,r)$, gives

$$\delta g_l(r) = -g_t(r) \int_{-\infty}^{\infty} dx\, \phi(x)\, e^{-\tau(x,r)}\, \delta\tau(x,r). \tag{16}$$

To avoid tedious expressions, we set $\tau = \tau_1$ in the exponential. Inserting also $\delta\tau = \delta\tau_2$ from (12) we find, for optically thick lines (subscript 'T'),

$$\frac{\delta g_T}{g_T} \;=\; -\big[1 - \epsilon(i\chi - q)\big]\, \frac{\delta\rho}{\rho_0} + i\chi\, \big[1 - \epsilon(i\chi - 4 - qt)\big]\, \frac{\delta v}{v_0}. \tag{17}$$

Note that actually we assumed $\tau \gg 1$ here; as above, δg_T is to be understood modulo the exponential terms. The (small) number ϵ is defined as

$$\epsilon = \frac{v_{\rm th}}{2v_0(r)} E(\tau), \tag{18}$$

where

$$E(\tau) = \tau^2 \int_{-\infty}^{\infty} dx\, \phi(x)\, [\phi(x) - 2x\Phi(x)]\, e^{-\tau\Phi(x)}. \tag{19}$$

The integral E, which is easily evaluated numerically, is of order unity for $\tau \gg 1$, and depends only weakly on τ, namely $E \sim \sqrt{\ln\tau}$ (Castor 1974).

The decisive fact in (17) is the occurence of a positive feedback between velocity and force perturbations, $\delta g_T/g_T = \epsilon\chi^2 \delta v/v_0$. First, note the dependence of growth rates $\delta g/\delta v \sim \lambda^{-2}$, in accordance with the results by OR. Moreover, also the quantitative values agree well with those from the long-wavelength limit of the bridging law by OR, cf. their Eq. (28). E.g., for a line of optical depth $\tau = 10$ we find a growth rate which is 20% smaller than that given by OR; in view of the different approximations performed by them and in our derivation, this is completely admissible.

From (18), the growth rate is almost constant for all moderately optically thick lines, except for a dependence on $v_{\rm th}$ (atomic species), and the above weak dependence on τ. This allows us to estimate the response of the *total* line force on perturbations, which is needed below for the derivation of dispersion relations. Following CAK, we assume that the total line force is the simple sum of individual contributions from all lines, i.e., line overlap is neglected; and furthermore that the ratio of the force due to all thin lines to the force from all thick lines is $(1-\alpha)/\alpha$, where $0 < \alpha < 1$, and typically $\alpha \approx 2/3$ for O supergiants. Since, by Eq. (2), the force per unit mass due to an optically thin line is not affected by perturbations, one obtains $\delta g_L/g_L = \alpha\, \delta g_T/g_T$. For the CAK wind in the limit of vanishing sound speed, the total line force can be written $g_L = -g/(1-\alpha)$, with g the gravitational acceleration. Hence, the Euler equation reads $v_0 v_0' = \alpha\, g_L$, and the response of the total line force to a perturbation is

$$\delta g_L = v_0 v_0'\, \frac{\delta g_T}{g_T}, \tag{20}$$

with $\delta g_T/g_T$ from (17).

2.3. Dispersion relation

By inserting (17) and (20) into the linearized continuity and Euler equations for the harmonic perturbations $\delta\rho$ and δv *in* *the stellar rest frame*, and neglecting sphericity terms and gas pressure, we obtain

$$\begin{aligned}
&(-i\omega/v_0' + i\chi + 1)\,\frac{\delta\rho}{\rho_0} \;+\; (i\chi - 1)\,\frac{\delta v}{v_0} = 0,\\
&(1 - i\epsilon\chi + aq)\,\frac{\delta\rho}{\rho_0} \;+ \\
&\qquad +\; (-i\omega/v_0' + 1 + i\epsilon\chi[i\chi - 4 - qt])\,\frac{\delta v}{v_0} = 0.
\end{aligned} \tag{21}$$

We introduce a dimensionless phase speed, ω_1, and growth rate, ω_2,

$$\omega_1 = \frac{\mathrm{Re}(\omega/v_0')}{\chi}, \qquad \omega_2 = \frac{\mathrm{Im}(\omega/v_0')}{\epsilon\chi^2}, \tag{22}$$

and set the determinant of (21) to zero, which gives

$$\begin{aligned}
&\omega_1^2 - \omega_1(1 - 4\epsilon) - 2\epsilon(1 + \omega_2) + \epsilon^2\chi^2\omega_2(1 - \omega_2) - 2\chi^{-2} \;+ \\
&\qquad + \epsilon q(\omega_1 t - t - \chi^{-2}) = 0,\\
&\omega_1(2 + 2\epsilon\chi^2\omega_2 - \epsilon\chi^2) + \epsilon\chi^2(1 - \omega_2 + 4\epsilon\omega_2) + 5\epsilon \;+ \\
&\qquad + \epsilon q\big(\omega_2\epsilon t\chi^2 + 1 + t\big) = 0.
\end{aligned} \tag{23}$$

The essential result from this equation system can be found analytically, by assuming that

$$\chi \gg 1, \qquad \epsilon \approx 0, \qquad \epsilon\chi \approx 0, \tag{24}$$

and keeping terms in $\epsilon\chi^2$ (see below for a justification). This reduces (23) to

$$\begin{aligned}
&\omega_1^2 - \omega_1 = 0,\\
&\omega_1\left(2\omega_2 - 1 + \frac{2}{\epsilon\chi^2}\right) + 1 - \omega_2 = 0.
\end{aligned} \tag{25}$$

The two solution branches correspond to fast growing waves which propagate inward, and slowly decaying waves which propagate outward,

$$\begin{aligned}
&\omega_1 = 0, \;\; \omega_2 = 1 && \text{(inward)},\\
&\omega_1 = 1, \;\; \omega_2 = -2/\epsilon\chi^2 && \text{(outward)}.
\end{aligned} \tag{26}$$

By inserting these results into (21), and by using again (24), the ratio of relative perturbation amplitudes is found to be

$$\begin{aligned}
\frac{\delta\rho/\rho_0}{\delta v/v_0} &= -1 && \text{(inward)},\\
&= i\chi && \text{(outward)}.
\end{aligned} \tag{27}$$

For an interpretation of this result, note that the continuity equation reads *in the comoving frame* and after applying the WKB approximation (i.e., mean flow gradients neglected), $d\delta\rho/dt + \rho_0\, d\delta v/dz = 0$, or, for harmonic perturbations, $\delta\rho/\rho_0 = \delta v/v_\phi$, with phase speed $v_\phi = \omega/k$.

From (26), the *unstable* waves propagate inward at a phase speed $v_\phi = 0$ in the observer's frame, or $v_\phi = -v_0$ in the comoving frame, i.e., they stand with respect to the star. Eventually, these waves should steepen into reverse shocks, as is indeed found from numerical simulations. The phase shift between density and velocity fluctuations is 180°, similar to the case of ordinary, inward propagating sound waves.

The *damped* waves, on the other hand, propagate outward at a phase speed $v_\phi = v_0$ in the stellar rest frame, or $v_\phi = 0$ in the comoving frame, i.e., they stand with respect to the wind. (In order to derive this from the amplitude relations (27), one has to set $\chi^{-1} = 0$.) By including pressure terms, Abbott (1980) found more exactly $v_\phi = a^2/v_0$ in the comoving frame. Also, the phase shift of these waves is 90°, instead of being 0° for ordinary, outward propagating sound waves.

Abbott (1980) termed both these long-scale modes *radiative-acoustic* waves.

Finally, (24) remains to be justified. By assuming $\epsilon \lesssim v_{\mathrm{th}}/v_0 \approx 0$, we are restricted to the highly supersonic, outer wind. Then, $\epsilon\chi \approx 0$, since rv_0' can be neglected in χ, so that $\chi \approx v_0 k/v_0'$, and $\epsilon\chi \approx Lk$. The latter quantity is small compared to unity in the considered long wavelength limit. Finally, with $\chi \gg 1$ we are restricted to perturbations for which the WKB approximation is valid, i.e., to wavelengths shorter than the wind scale height, v_0/v_0'.

2.4. Limiting wavelength for unstable growth

Yet, since we did not apply the WKB approximation to derive (21), this system contains more information regarding the long wavelength regime than does the analysis of OR. Especially, one can derive an upper limiting wavelength, λ_c, above which even inward propagating waves are no longer unstable, but decay instead.

Assume for the moment that curvature terms of the velocity field can be neglected, i.e., $q = 0$. For not too small χ, the numerical solution of (23) shows that $-\omega_1 \ll 1$ for the inward mode, and ω_1^2 can be neglected in (23). With $\epsilon \approx 0$, and setting the growth rate $\omega_2 = 0$, we find from (23),

$$\chi_c = \sqrt{2}\,\epsilon^{-1/4}. \tag{28}$$

Assuming again that $\chi \approx v_0 k/v_0'$, one finds that (as was to be expected) the critical wavelength λ_c is set by the scaleheight of the wind, v_0/v_0'. E.g., for the CAK velocity law,

$$\lambda_c = 2\sqrt{2}\,\pi\,\epsilon^{1/4}\,(r - R_*)\,\frac{r}{R_*}. \tag{29}$$

Except close to the star, λ_c is rather large. An easy calculation shows that, for $\lambda \lesssim \lambda_c$, even the growth rates from (17) are so small that such perturbances would not grow significantly over a wind flow time. Hence, λ_c from (29) is of not much practical interest. (Note also that for such large values of λ_c, one would have to include sphericity terms in the above derivation.)

Finally, the numerical solution of (23) shows that *curvature* terms, v_0'', are rather unimportant in the outer wind, and lead to a small downward revision of λ_c only. Interestingly, however, curvature terms imply that also outward propagating waves can become unstable within a certain wavelength regime. Yet, since the corresponding growth rates are very small, this issue is of academic interest only.

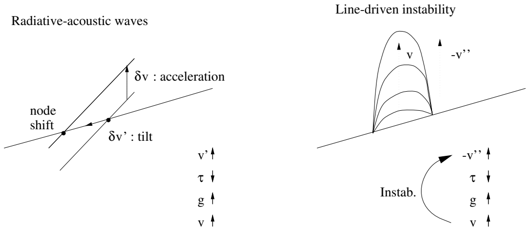

Fig. 1. *Left:* the occurence of long-scale, inward propagating waves in *first* order Sobolev approximation. *Right:* the line-driven instability in *second* order Sobolev approximation. Upward (downward) pointing arrows indicate that the corresponding quantity rises (drops) as consequence of a flow perturbation.

We close this section with a perspective. Present numerical simulations of winds subject to the line-driven instability are cpu-time expensive because the line force is integrated directly, without applying any Sobolev approximation. Our above results imply, however, that the quantitatively correct, linear growth rates can be alternatively obtained from a second order Sobolev treatment. It is furthermore known (Owocki et al. 1988) that these linear rates hold over almost the full growth regime, until they quickly drop to zero when saturation is reached, i.e., when the thermal band becomes optically thin. It seems therefore plausible to perform instability simulations using the cheap Sobolev line force in second order instead of a more elaborate line transfer.

One has to keep in mind, however, that such a method, based on higher-order extrapolation of local conditions, does not incorporate the inherently nonlocal physics that occurs within the nonlinear growth of the instability. Furthermore, in order that a meaningful comparison with non-local integral methods, especially the Smooth Source Function method of Owocki (1991), can be done, it may be necessary to first develop the second order Sobolev forms for the diffuse force terms.

3. Why are radiative-acoustic waves unstable?

We give here some simple, heuristic arguments for the occurence of unstable, radiative-acoustic waves in line-driven winds.

Assume that at some location, r, in the wind, the velocity field experiences an accidental perturbation, and becomes slightly steeper, as is the case, e.g., at the zero crossing of a harmonic perturbation. Since the first order Sobolev force per unit mass due to a thick line is $\sim v'/\rho$, the perturbed gas experiences a larger force, and is accelerated to higher velocities. From the left panel of Fig. 1, one sees that then the node around which the band is tilted is shifted inward. Correspondingly, if the velocity field becomes shallower at some node, the line force drops, the gas is decelerated, and the node is also shifted inward. Thus, long-scale harmonic perturbations of the velocity field, for which the Sobolev approximation can be applied, induce inward propagating waves.

The instability arises then from second order (curvature) terms. The optical depth τ_2 from (10) drops for a concave deformation ($v_0'' < 0$) of the thermal band, i.e., an elevation. (We have assumed here that the 'mean' v' over the perturbation remains constant). In consequence, the line force rises, and the perturbed gas is accelerated to higher speeds. This enhances the elevation, and the curvature increases *further*. The right panel of Fig. 1 displays this feedback between perturbations in v and v''. Similarly, for a convex deformation, i.e., a trough, the line force drops, and the trough becomes deeper.

In later stages, when fast gas starts to overtake slow gas, the original sine-wave perturbation is transformed into a sawtooth. Here, the gas is highly accelerated over a broad velocity elevation, and subsequently decelerated in a narrow, reverse shock front. The corresponding kind of behavior is found for the solutions of the inviscid Burgers equation, $\partial u/\partial t + u\,\partial u/\partial z = 0$.

4. Short-scale vs. long-scale perturbations

Carlberg (1980) pointed out that the growth of optically thin, short-scale perturbations (OR) should saturate at small velocity amplitudes of a few thermal speeds. By then, the perturbed gas is essentially shifted into the unshadowed continuum, and any further velocity shift does not provide more flux or force.

In contrast, the long-scale perturbations analysed in the previous section can grow to much larger amplitudes before they become optically thin.

This suggests that the fast-growing, short-scale perturbations can be considered as *noise* superimposed on the process of a *slow* and *coherent* tilt of the thermal band over large distances, as induced by perturbations with $\lambda \gg L$. This view is supported by numerical simulations of O supergiant winds where a spectrum of base frequencies is injected into the flow (Feldmeier et al. 1997). Here, the longest waves grow into saturation, giving rise to shocks with velocity jumps of up to v_∞.

Obviously, one has to ensure that the growth time of such long-scale perturbations is still short as compared to the flow time. For O star winds, the longest base perturbations which can still grow into saturation give typical distances between subsequent, strong reverse shocks of $\approx 1\,R_*$ at distances from the star where the wind has essentially reached its terminal speed (note: wavelength stretching). On the other hand, optically thin perturbations which grow at maximum rate give structural length scales in the outer wind of shorter than $10^{-2}\,R_*$.

Furthermore, it is presently not clear whether velocity amplitudes are the most relevant measure of importance of the wind structure, e.g., because only a very small amount of wind material is actually involved in such large velocity amplitudes (Owocki et al. 1988). Thus other measures, for example dissipation of wind kinetic energy, might be more strongly influenced by the structure at smaller scale.

5. Summary

While unstable growth rates for both the limiting regimes of short-scale perturbations, $\lambda < L$, and very long-scale perturbations, $\lambda \gg L$, were formerly discussed using simplifying assumptions (i.e.: optically thin perturbations, resp. lowest order Sobolev approximation), we have found that the physically most interesting regime of moderate long-scale perturbations, $\lambda > L$, which was hitherto only treated within the elaborate analyses of OR and Lucy (1984), is also accessible to a simplified approach using second order Sobolev approximation.

While the standard, first order approach demonstrates the existence of so-called radiative-acoustic waves, the second order treatment shows the inward branch of these waves to be unstable: accidental, positive perturbations in the velocity field of the wind imply larger absolute curvatures; this reduces the optical depth, raises the line force, and consequently leads to a *further* acceleration.

Somewhat astonishingly therefore, the radiative-acoustic waves according to Abbott (1980) and the line-driven instability seem to have a similar basis, stemming respectively from first and second-order Sobolev approximation. On the other hand, Owocki & Rybicki (1986) showed by using a Green's function analysis that the true signal propagation speed in an unstable wind which is driven by pure absorption lines is the ordinary *sound* speed. Future work has to clarify this dichotomy.

Our analysis allows one to abandon the usual WKB approximation, and to account for wave stretching. We hope that the simplicity of this approach also leads to an applicability in cases of, e.g., more complex flow geometries, as may occur in line-driven winds from accretion disks in quasars or cataclysmic variables.

Acknowledgements. Special thanks to the referee, Dr. S. Owocki, who at first pointed out to me some interesting results from expanding the line force into a power series of Sobolev length. Further thanks to Drs. J. Puls and C. Norman for many interesting discussions. This work was supported by DFG under contracts Pa 477/1-2 and 1-3.

References

Abbott D.C., 1980, ApJ 242, 1183
Carlberg R.G., 1980, ApJ 241, 1131
Castor J.I., 1974, MNRAS 169, 279
Castor J.I., Abbott D.C., Klein R.I., 1975, ApJ 195, 157 (CAK)
Cooper R.G., Owocki S.P., 1992, PASPC 22, 281
Cooper R.G., Owocki S.P., 1994, Ap&SS 221, 427
Cranmer S.R., Owocki S.P., 1996, ApJ 462, 469
Feldmeier A., Puls J., Pauldrach A.W., 1997, A&A 322, 878
Gayley K.G., Owocki S.P., 1995, ApJ 446, 801
Hillier D.J., Kudritzki R.P., Pauldrach A.W., et al., 1993, A&A 276, 117
Lucy L.B., 1984, ApJ 284, 351
Lucy L.B., Solomon P.M., 1970, ApJ 159, 879
MacGregor K.B., Hartmann L., Raymond J.C., 1979, ApJ 231, 514
Milne E.A., 1926, MNRAS 86, 459
Moffat A.F., Owocki S.P., Fullerton A.W., St-Louis N., 1994, Ap&SS 221
Owocki S.P., 1991, in: Crivellari L., Hubeny I., Hummer D.G. (eds.) Stellar atmospheres: beyond classical models. Kluwer, Dordrecht, 235
Owocki S.P., Rybicki G.B., 1984, ApJ 284, 337 (OR)
Owocki S.P., Rybicki G.B., 1985, ApJ 299, 265
Owocki S.P., Rybicki G.B., 1986, ApJ 309, 127
Owocki S.P., Rybicki G.B., 1991, ApJ 368, 261
Owocki S.P., Castor J.I., Rybicki G.B., 1988, ApJ 335, 914
Pauldrach A., Puls J., Kudritzki R.P., 1986, A&A 164, 86
Poe C.H., Owocki S.P., Castor J.I., 1990, ApJ 358, 199
Puls J., Owocki S.P., Fullerton A.W., 1993, A&A 279, 457
Rybicki G.B., Owocki S.P., Castor J.I., 1990, ApJ 349, 274
Sellmaier F., Puls J., Kudritzki R.P., et al., 1993, A&A 273, 533
Sobolev V.V., 1960, Moving envelopes of stars. Harvard University Press, Cambridge

This article was processed by the author using Springer-Verlag LaTeX A&A style file *L-AA* version 3.

The Astrophysical Journal, 526:344–356, 1999 November 20

DYNAMICS OF LINE-DRIVEN WINDS FROM DISKS IN CATACLYSMIC VARIABLES. I. SOLUTION TOPOLOGY AND WIND GEOMETRY

Achim Feldmeier and Isaac Shlosman
Department of Physics and Astronomy, University of Kentucky, Lexington, KY 40506-0055; achim@pa.uky.edu, shlosman@pa.uky.edu
Received 1999 February 9; accepted 1999 July 2

ABSTRACT

We analyze the dynamics of two-dimensional stationary, line-driven winds from accretion disks in cataclysmic variable stars. The driving force is that of line radiation pressure, in the formalism developed by Castor, Abbott, & Klein for O stars. Our main assumption is that wind helical streamlines lie on straight cones. We find that the Euler equation for the disk wind has two eigenvalues, the mass-loss rate and the flow-tilt angle with the disk. Both are calculated self-consistently. The wind is characterized by two distinct regions, an *outer* wind launched beyond four white dwarf radii from the rotation axis and an *inner* wind launched within this radius. The inner wind is very steep, up to 80° with the disk plane, while the outer wind has a typical tilt of 60°. In both cases, the wind cone dispersion is small because of a good alignment between the wind and the radiative flux vectors from the disk. We, therefore, provide an insight into the formation of the biconical geometry of disk winds as suggested by observations and kinematical modeling. The wind collimation angle appears to be robust and depends on the disk temperature stratification only. The flow critical points lie high above the disk for the inner wind but close to the disk photosphere for the outer wind. Comparison with existing kinematical and dynamical models is provided. Mass-loss rates from the disk as well as wind velocity laws are discussed in the second paper in this series.

Subject headings: accretion, accretion disks — novae, cataclysmic variables — stars: mass loss — stars: winds, outflows

1. INTRODUCTION

Accretion disks are ubiquitous in astrophysical systems ranging from newborn stars to compact objects, such as white dwarfs, neutron stars and black holes, both stellar and galactic. Because of their high temperatures and large surface areas, disks appear to be among the most luminous objects in the universe. Strong dissipative processes that accompany accretion around compact objects can release radiation energy in and above the disk, leading naturally to radiation-driven winds, similar to winds from hot stars. Observational signatures of such winds have been unambiguously detected in cataclysmic variables (CVs) (Heap et al. 1978; Krautter et al. 1981; Klare et al. 1982; Córdova & Mason 1982) and in active galactic nuclei (hereafter AGNs; Arav, Shlosman, & Weymann 1997, and references therein), but understanding them proved to be challenging. In this and the following paper (Feldmeier, Shlosman, & Vitello 1999, hereafter Paper II), we focus on different aspects of disk winds in CVs, such as their two-dimensional geometry, solution topology, mass-loss rates, and velocity profiles. AGN disk winds will be discussed elsewhere.

Theoretical understanding of winds from accretion disks is hampered by their intrinsically multidimensional character and by the richness of various physical processes supplementing the basic hydrodynamics of the flow. A number of different driving mechanisms for disk winds have been predicted and analyzed, from magnetic torques to X-ray disk irradiation (i.e., Compton-heated and thermally driven winds) to resonance line pressure (e.g., Blandford & Payne 1982; Begelman, McKee, & Shields 1983; Córdova & Mason 1985; Woods et al. 1996). Disks in nonmagnetic CVs with high accretion rates, $\gtrsim 10^{-9}\, M_\odot\ \mathrm{yr}^{-1}$, have an energy output that peaks in the (far-) ultraviolet, similarly to O, B, and WR stars. Their spectra exhibit features which bear similarity to those found in hot and massive stars and which are attributed to winds driven by radiation pressure in resonance and subordinate lines of abundant chemical elements, i.e., so-called line-driven winds (LDWs). Observational evidence in favor of LDWs from hot stars and disks includes but is not limited to the P Cygni line profiles of C IV, N V and Si IV, ionization levels, high terminal velocities and their correlation with the luminosity, and UV line behavior during continuum eclipse in CVs.

The pioneering work by Lucy & Solomon (1970), Castor (1974), and Castor, Abbott, & Klein (1975, hereafter CAK) showed that O star winds result from scattering of radiation in the resonance lines of abundant elements. The elegantly formulated theory of the LDWs from O stars by CAK, Cassinelli (1979), Abbott (1980, 1982), Pauldrach, Puls, & Kudritzki (1986), and others (for a textbook account, see Lamers & Cassinelli 1999) was successfully applied to individual objects. Further refinements of this theory by Owocki & Rybicki (1984, 1985) and Owocki, Castor, & Rybicki (1988) addressed the issue of stability of the flow.

First application of the LDWs to accretion disks emphasized the nonspherical ionizing continuum and driving force as well as a biconical geometry of the outflow (Shlosman, Vitello, & Shaviv 1985; Vitello & Shlosman 1988). Under a broad range of conditions, disk atmospheres in CVs and AGNs become dynamically unstable because the line opacity effectively brings them into a super-Eddington regime. Continuum photons absorbed by the UV resonance lines and reemitted isotropically contribute to the momentum transfer to the wind. This process can be described as a resonant scattering that conserves the number of photons throughout the wind and results in terminal wind velocities of the order of the escape speed at the base of the flow.

The dynamics and radiation field of disk LDWs employed by Shlosman et al. (1985) and by Vitello & Shlosman (1988) were oversimplified. Both were approximated by a one-dimensional planar model allowing for divergence of the flow streamlines and geometrical dilution of the radiation field. Nineteen resonance lines in the range of 500–1600 Å were included in the calculation of the radiation force. It was noted that disk LDWs are more restrictive than stellar winds and that their development is strongly governed by the ionization structure in the wind.

Subsequently, a variety of two-dimensional kinematical models for disk winds in CVs, supplemented by a three-dimensional radiation transfer in the Sobolev approximation, were explored (Shlosman & Vitello 1993; Vitello & Shlosman 1993). Calculations using an alternative Monte Carlo radiation transfer method, albeit with frozen-in ionization, gave similar results (Knigge, Woods, & Drew 1995). Constrained by synthetic line profiles and by calculated effects of varying basic physical parameters, such as accretion and mass-loss rates, temperature of the boundary layer, rotation, and inclination angle, the available phase space for wind solutions was sharply reduced. Wind-resonant scattering regions exhibiting a strongly biconical character regardless of the assumed velocity and radiation fields were identified and mapped. This allowed us to match the observed line shapes from a number of CVs and to put forward a number of predictions, which were verified in high-resolution *HST* observations (Shlosman, Vitello, & Mauche 1996; Mauche et al. 1999). Most important, rotation was positively identified as the dominant factor shaping the UV line profiles in CVs, thus confirming that the disk and not the white dwarf is the wind source.

The above one-dimensional dynamical and two-dimensional kinematical modelings suffered from uniqueness problems that can be removed only by invoking the two-dimensional wind dynamics. Recent successful attempts by Proga, Stone, & Drew (1998; hereafter PSD) to model the two-dimensional time-dependent radiation hydrodynamics of disk LDWs was a major breakthrough in our understanding of this phenomenon. PSD basically confirmed that kinematical models of disk winds had sampled the correct parameter range and provided the scaling laws between different wind characteristics, e.g., between mass-loss rate and accretion luminosity, and delineated the phase space for possible time-dependent solutions. A number of empirical relationships were put forward which require a physical explanation.

In this paper, we focus on the two-dimensional geometry of a disk LDW in the presence of a realistic radiation field in CVs. We analyze solutions of the wind Euler equation, emphasizing differences in the solution topology with that of CAK stellar winds. In Paper II, we address issues related to the mass-loss rates and velocity laws of CV winds. The possible contribution to wind driving by magnetic stresses is ignored (e.g., Blandford & Payne 1982; Pudritz & Norman 1986; Emmering, Blandford, & Shlosman 1992), as are jetlike outflows seen in other disk systems (Livio 1997).

This paper is organized as follows. Section 2 reviews the relevant aspects of CAK theory for LDWs from O stars. Section 3 addresses the two-dimensional geometry of disk LDWs, as well as the radiation field above the CV disk. Section 4 deals with an analytic solution for vertical winds above an isothermal disk, and § 5 analyzes the solution topology and flow geometry for tilted winds above a disk with a realistic temperature stratification. Section 6 compares our results with other models and observations, and § 7 summarizes our basic conclusions.

2. CAK THEORY FOR O STARS

2.1. *The Stellar Line Force*

The CAK theory for LDWs from O stars forms the basis for our model of CV winds and is therefore briefly summarized here. CAK assume a line-distribution function per unit ν and κ, from UV to IR,

$$N(\nu, \kappa) = \frac{1}{\nu}\frac{1}{\kappa_0}\left(\frac{\kappa_0}{\kappa}\right)^{2-\alpha} , \qquad (1)$$

where ν is the line frequency and κ (in cm^2 g^{-1}) is the mass absorption coefficient normalized to κ_0, which refers roughly to the strongest driving line in the flow (Owocki et al. 1988). For the power exponent, $0 < \alpha < 1$ holds, where the lower limit corresponds to purely optically thin lines and the (unrealistic) upper limit to purely optically thick lines. Puls, Springmann, & Lennon (1999) derive $\alpha = \frac{2}{3}$ from Kramers's formula applied to resonance lines of hydrogenic ions. Similar values of α are obtained from detailed non-LTE calculations for dense O-supergiant winds (Pauldrach 1987; Pauldrach et al. 1994). On the other hand, for low-density winds, e.g., from B stars near the main sequence, $\alpha = \frac{1}{2}$ may be more appropriate (Puls, Springmann, & Owocki 1998). Therefore, we shall consider both cases $\alpha = \frac{1}{2}$ and $\alpha = \frac{2}{3}$ to study the effect of α on the structure of disk winds.

Using equation (1), the CAK force from all lines can be written in a general way that is applicable for both geometries (e.g., Owocki & Puls 1996),

$$g_L = \kappa_0 v_{\rm th} \frac{\Gamma(\alpha)}{1-\alpha}\frac{1}{c^2}\int d\omega\, I_\gamma \hat{\gamma}\, \tau_\gamma^{-\alpha} , \qquad (2)$$

by means of the Sobolev approximation (Sobolev 1957). $\Gamma(\alpha)$ is the complete gamma function, c is the speed of light, $d\omega$ is the solid angle centered on $\hat{\gamma}$, and I_γ is the frequency-integrated intensity in this direction. The line optical depth in direction $\hat{\gamma}$ is given by

$$\tau_\gamma = \frac{\kappa_0 \; v_{\rm th} \; \rho}{\hat{\gamma} \cdot \nabla(\hat{\gamma} \cdot {\bf v})} , \qquad (3)$$

with gas density ρ, and $\hat{\gamma} \cdot \nabla(\hat{\gamma} \cdot {\bf v})$ being the gradient along $\hat{\gamma}$ of the velocity component in direction $\hat{\gamma}$. Note that $\kappa_0 \; v_{\rm th}$ is independent of the ion thermal speed $v_{\rm th}$ and so is the line force. Assuming spherical symmetry, and adopting the "radial streaming" approximation of CAK, i.e., $\tau_\gamma \equiv \tau_r$, equation (2) simplifies to

$$g_L = (\kappa_0 v_{\rm th})^{1-\alpha} \frac{\Gamma(\alpha)}{1-\alpha}\frac{F}{c^2}\left(\frac{dv/dr}{\rho}\right)^{\alpha} , \qquad (4)$$

with frequency-integrated, radial flux F.

2.2. *Stellar Euler Equation*

For an isothermal, spherically symmetric stellar wind, the stationary Euler equation in dimensionless form can be written as

$$\left(1 - \frac{A^2}{W}\right)W' = -1 - \frac{4A^2}{U} + EW'^{\alpha} , \qquad (5)$$

where, after CAK, we introduced a radial coordinate $U = -R_*/r$, with R_* being the stellar radius. The sound speed, A, and the flow speed, $V = W^{1/2}$, are normalized to the photospheric escape speed from the reduced stellar mass,

$M(1-\Gamma)$, where Γ is the Eddington factor. The normalized wind acceleration is given by $W' = dW/dU = r^2vv'/GM(1-\Gamma)$, with v the flow speed and $v' = dv/dr$. Note (1) the different meaning of the prime in W' and v' and (2) that the gravitational acceleration is normalized to -1, whereas CAK normalize it to $-\frac{1}{2}$. The constant E in equation (5) is given by

$$E = \frac{\Gamma(\alpha)}{1-\alpha}\left[\frac{\kappa_0\, v_{\rm th}}{4\pi GM(1-\Gamma)}\right]^{1-\alpha}\frac{L/c^2}{\dot{M}^\alpha}\,, \qquad (6)$$

where G is the gravitational constant, L is the stellar luminosity, and $\dot{M}$ is the mass-loss rate, $\dot{M} = 4\pi r^2 \rho v$. Global solutions to equation (5) exist only above a certain, critical $E_{\rm cr}$, called an eigenvalue of the problem, i.e., below a *maximum allowable* mass-loss rate. In the zero sound speed limit, $A = 0$, the differential equation (5) separates into an algebraic equation,

$$P \equiv W' + 1 - EW'^\alpha = 0\,, \qquad (7)$$

and a trivial differential equation $W' = {\rm const}$, which leads to the CAK velocity law, $v(r) = v_\infty(1 - R_*/r)^{1/2}$, where v_∞ is the flow terminal velocity. The Euler equation in the form given in equation (7) is particularly simple and its terms have a straightforward physical meaning, namely, inertia, gravity, and line force.

2.3. *The Stellar Wind Topology: Critical Point of the Flow*

We now consider solutions to equation (5) with finite A. According to CAK, for sufficiently large values of E, there are two solutions in the supersonic regime, $W > A^2$, termed "shallow" (small W') and "steep" (large W') solutions; whereas in the subsonic, photospheric regime, $W < A^2$, only the shallow solutions exist. On the other hand, only the steep solutions reach infinity. Namely, the term $-4A^2/U$ (the thermal pressure force caused by geometrical expansion) becomes infinite for $r \to \infty$ and must be balanced by $W' \to \infty$ along the branch of steep solutions. CAK concluded, therefore, that the true, unique wind solution has to switch from the shallow to the steep branch at a "critical" point (see Fig. 1). Of course, a nonzero pressure term at infinity is unphysical because it requires an infinite amount of energy in the flow and is purely a result of the imposed isothermal conditions in the wind.

We find that shallow solutions can always be extended to infinity, *if* one allows for a kink in the velocity law at large radii. At this kink, the wind switches to the branch of decelerating solutions, $W' < 0$. The latter are found after replacing W'^α in the line force by $|W'|^\alpha$. Since stellar winds essentially reach v_∞ at a few 100 R_*, the kink and subsequent deceleration hardly show up. For disk winds, the kink can be more pronounced; this is discussed further in Appendix B.

The subsonic region has an extent of a few percent of the stellar radius for O-star winds, while the pressure force $-4A^2/U$ becomes important only beyond a few 100 R_*. In the intermediate regime, i.e., almost everywhere, the simplified equation (7) with $A = 0$ holds to a good approximation, and therefore $W' = {\rm const}$. This happens because both gravity and line force are $\propto r^{-2}$. Solution curves in the (W', U)-plane are essentially straight lines, but the lines bend over because of thermal pressure both at $U = -1$ and 0. As a result, the critical point is a saddle point in the (W', U)-plane (Bjorkman 1995). The usual definition of a critical point in hydrodynamics refers, however, to the (W, U)-plane (a topologically equivalent plane).

For $A = 0$, the critical point lies on an extended ridge, and its position becomes ill-defined (Fig. 1*a*). In this limit, *every* point of the critical solution is a critical point. For $A > 0$, however, CAK find the critical point to lie at $r_{\rm cr} = 3/2R_*$ (Fig. 1*b*). Inclusion of further correction terms to the line force, especially owing to the finite size of the stellar disk, breaks the r^{-2} dependence of the line force, pushes the two almost degenerate critical solutions $W'(U)$ apart, and shifts the critical point toward the sonic point (Fig. 1*c*). Pauldrach et al. (1986) find then $r_{\rm cr} \lesssim 1.1R_*$.

A critical point is the information barrier for LDWs and plays a role similar to the sonic point in thermal winds or nozzle flows (Abbott 1980). How can the pressure mismatch of a shallow solution at $r \gtrsim 300R_*$ be communicated upstream to the critical point at $1.1R_*$? We speculate that it is not really the outer boundary mismatch that forces the flow through a critical point. Instead, the truly distinguishing property of the critical solution should be its correspondence to the *maximum* mass-loss rate in the wind. Work is underway to identify the feedback mechanism between the wind and the photosphere that drives the wind from any shallow solution to the unique critical solution. This issue will be addressed elsewhere. In the present paper, we *assume* that the true disk wind solution is the one with the maximal allowable mass-loss rate.

The flow critical point (subscript "cr") is defined by the singularity condition, $\partial P/\partial W'_{\rm cr} = 0$ (i.e., the merging of a shallow and a steep solution). Together with the Euler equation, $P = 0$, this implies

$$W'_{\rm cr} = \frac{\alpha}{1-\alpha}\,, \qquad (8a)$$

$$E_{\rm cr} = \frac{1}{\alpha^\alpha(1-\alpha)^{1-\alpha}}\,. \qquad (8b)$$

The eigenvalue $E_{\rm cr}$ determines the maximum mass-loss rate, and $W'_{\rm cr}$ determines the terminal speed. They are discussed further in Paper II. Furthermore, from the Euler equation, $dP/dU = 0$ must hold everywhere. This leads to the regularity condition, $\partial P/\partial U_{\rm cr} + W'_{\rm cr}\,\partial P/\partial W_{\rm cr} = 0$ (if $W''_{\rm cr} < \infty$), which determines the position of the critical point.

3. DISK WIND GEOMETRY AND RADIATION FIELD IN CVS

3.1. *Flow Geometry, Gravity, and Centrifugal Force*

The central assumption throughout this paper is that the helical streamline of a fluid parcel in the wind is contained within a *straight* cone. While this is certainly an idealization, and a major restriction of this model, justification comes first from the related kinematical model of Shlosman & Vitello (1993) and second from the numerical two-dimensional hydrodynamic simulations of PSD. The latter showed that the escaping mass loss carrying streamlines are well approximated by straight lines in the (r, z)-plane, with r and z being cylindrical coordinates. The rotational speed and the centrifugal forces in the wind depend on the cone opening angle that is calculated self-consistently here. The angular momentum is preserved along any streamline (see below) and, therefore, does *not* depend on its shape.

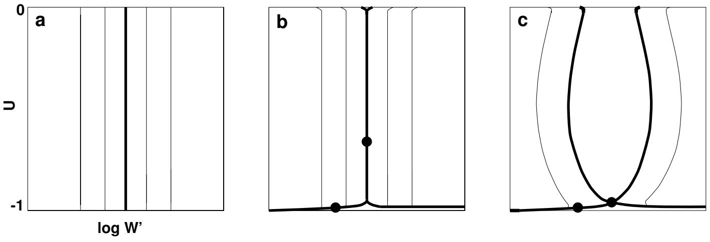

FIG. 1.—Saddle-point topology of stellar CAK winds in the (W', U)-plane, for (*a*) a point star and zero sound speed; (*b*) a point star and finite sound speed; (*c*) an extended star and finite sound speed. Filled dots mark the sonic points (at $U \simeq -1$) and the critical points.

We denote the angle between the wind cone and the radial direction in the disk plane by λ. This angle is calculated using the Euler equation and is not assumed a priori. The footpoint radius of a streamline in the disk is r_0, and x is the distance along the cone (see Fig. 2). We search for the solutions of the Euler equation in the $[\lambda(r_0), x]$-plane for a streamline starting at arbitrary r_0. The $\lambda(r_0)$ dependence leads to the appearance of a new eigenvalue problem for the disk wind, and derivation of this function is the focus of the present paper.

Since LDWs are highly supersonic, we neglect the pressure forces and furthermore assume that the azimuthal velocity is determined by angular momentum conservation above the disk and by Keplerian rotation in the disk plane. The tilt angle λ has to be a monotonically decreasing function of r_0 to avoid streamline crossing, which would violate the assumption of a pressure-free gas. The only remaining velocity component is v_x, which points upward along the cone. The dynamical problem has therefore been reduced to solving the Euler equation for v_x.

In a frame rotating with the angular velocity $\boldsymbol{\Omega}$ of a fluid parcel positioned at radius vector $\boldsymbol{s}$, there are three fictitious forces (e.g., Binney & Tremaine 1987, p. 664). The Coriolis acceleration, $-2\,\boldsymbol{\Omega} \times \dot{\boldsymbol{s}}$, has no component along $\hat{\boldsymbol{x}}$, and the same is true for the inertial force of rotation, $-\,\dot{\boldsymbol{\Omega}} \times \boldsymbol{s}$. We introduce the effective gravity function, which is the component of gravity minus centrifugal force along the straight line in direction $\hat{\boldsymbol{x}}$, and is given by $-(GM_{\rm wd}/r_0^2)\,g(X, \lambda)$, with $M_{\rm wd}$ being the mass of the white dwarf, and

$$g(X, \lambda) = \frac{X + \cos\lambda}{(1 + 2X\cos\lambda + X^2)^{3/2}} - \frac{\cos\lambda}{(1 + X\cos\lambda)^3}\,, \quad (9)$$

where $X \equiv x/r_0$. In the following, all lengths written in capital letters are normalized to the footpoint radius, r_0, in the disk. For disk winds, the variable X will play the role U played for stellar winds (cf. eq. [5]). Close to the disk, $X \ll 1$, and $g \simeq X$, while for $X \gg 1$, $g \simeq X^{-2}$. For a vertical ray, $\lambda = 90°$, g has its maximum at $X = 1/\sqrt{2}$, while for a horizontal ray, $\lambda = 0$, the maximum is at $X = \frac{1}{2}$.

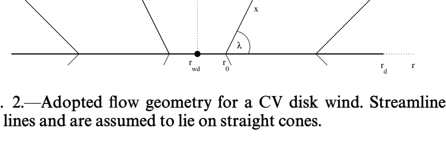

FIG. 2.—Adopted flow geometry for a CV disk wind. Streamlines are helical lines and are assumed to lie on straight cones.

Equation (9) shows an important difference between stellar and disk winds. The stellar gravity is always decreasing with distance, while for the disk an effective gravity "hill" must be overcome before the wind can escape. This effect of disk LDWs will be discussed in § 5.

3.2. *Radiation Field above the Disk*

Next, we evaluate the line force in equation (2). Besides the initial growth of effective gravity with height, the opacity-weighted flux integral is the central property that distinguishes disk winds from stellar winds. Pereyra, Kallman, & Blondin (1997) give an analytical approximation for this integral above an isothermal disk. Unfortunately, an error was introduced with a change of integration variable, which led to an artificial, linear dependence of the vertical flux on z, even as $z \rightarrow 0$. PSD solve this integral numerically (cf. Icke 1980), using approximately 2000 Gaussian integration points.

In the general spirit of the radial streaming approximation of CAK, we replace the integral in equation (2) by $\bar{\tau}^{-\alpha}\boldsymbol{F}$, thus introducing an *equivalent* optical depth, $\bar{\tau}$. We first calculate the frequency-integrated flux $d\boldsymbol{F}(r, z)$ at a location (r, z) in cylindrical coordinates, from a flat ring of radius q, radial width dq, and isotropic intensity $I(q, 0)$,

$$d\boldsymbol{F}(r, z) = \begin{pmatrix} dF_r \\ dF_z \end{pmatrix} = 2\pi I(q, 0)q\,dq\,\frac{z}{B^{3/2}}\begin{pmatrix} r[r^2 + z^2 - q^2] \\ z[r^2 + z^2 + q^2] \end{pmatrix}, \quad (10)$$

where

$$B = (r^2 + z^2 - q^2)^2 + 4z^2q^2\,. \quad (11)$$

For an *isothermal* disk with isotropic intensity, we integrate equation (10) over q, to obtain the disk flux

$$\boldsymbol{F}(r, z) = \frac{\pi I}{2}\,\frac{1}{\sqrt{B}}\begin{pmatrix} [z/r][r^2 + z^2 + q^2] \\ -r^2 - z^2 + q^2 \end{pmatrix}\Bigg|_{q=r_{\rm wd}}^{r_d}, \quad (12)$$

where r_d is the outer disk radius. For the nonmagnetic systems considered here, we identify the inner disk radius with $r_{\rm wd}$, the white dwarf radius. We do not include contributions to the radiative flux from the white dwarf and the boundary layer. Generally, of course, accretion disks are not isothermal. We, therefore, consider two complementary cases with $T(r_0) \propto r_0^{-1/2}$ (termed "Newtonian" disk in what follows) and $T(r_0) \propto r_0^{-3/4}[1 - (r_{\rm wd}/r_0)^{1/2}]^{1/4}$ (Shakura & Sunyaev 1973; hereafter SHS). Observations show that the brightness temperature stratification of CV disks is consis-

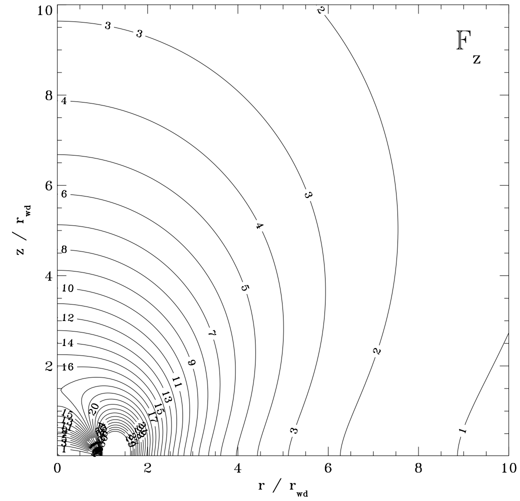

FIG. 3.—Isocontours of the frequency-integrated, vertical flux component F_z above a Newtonian disk. The disk extends from 1 to $30 r_{\rm wd}$. Normalization is $I(r_0 = 5 r_{\rm wd}, z = 0) = 1$.

tent with both distributions (Horne & Stiening 1985; Horne & Cook 1985; Rutten et al. 1993).

For the Newtonian disk, we find

$$\boldsymbol{F}(r, z) = \pi I(r, 0) r^2 \frac{z}{r^2 + z^2} \times \left. \begin{pmatrix} \dfrac{3r^2 - z^2 - q^2}{2r\sqrt{B}} - \dfrac{r}{z^2 + r^2} \ln C \\ \dfrac{3z^2 - r^2 + q^2}{2z\sqrt{B}} - \dfrac{z}{z^2 + r^2} \ln C \end{pmatrix} \right|_{q = r_{\rm wd}}^{r_d} , \tag{13}$$

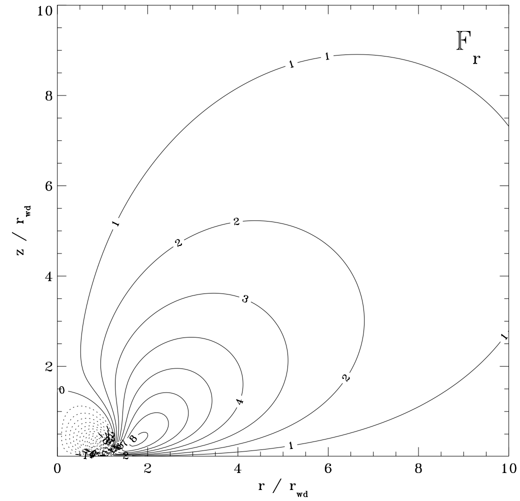

FIG. 4.—Same as Fig. 3 (including normalization), now for the radial flux component F_r. Dotted lines indicate an inward flux.

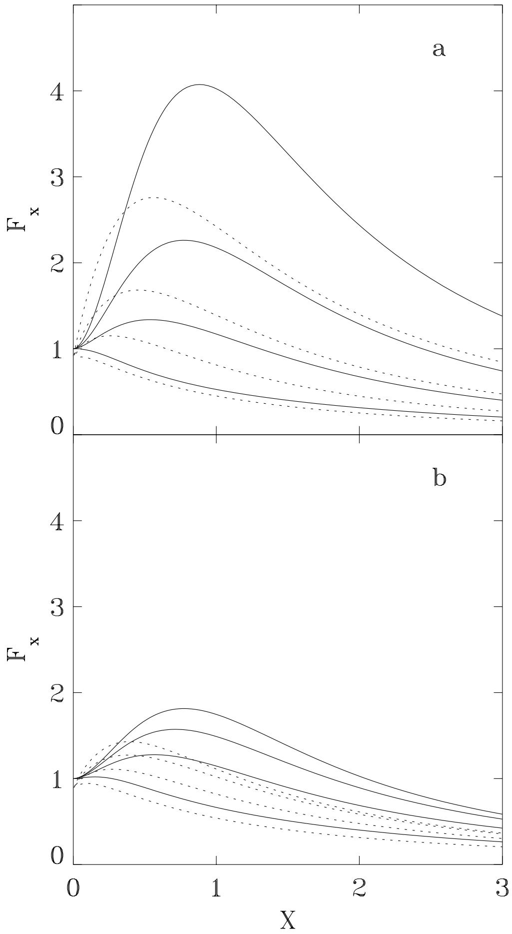

FIG. 5.—Normalized, projected flux $\tilde{F}_x(r_0, X)$ for SHS (*a*) and Newtonian (*b*) disks, at footpoint radii $r_0 = 20$, 10, 5, and $2 r_{\rm wd}$ (*top to bottom curves*). The tilt angle with the disk plane is 90° for full lines and 60° for dashed lines.

where

$$C = \frac{(z^2 - r^2) q^2 + (z^2 + r^2)^2 + (z^2 + r^2)\sqrt{B}}{q^2} . \tag{14}$$

The surface flux above the SHS disk can only be integrated numerically, using equation (10). Yet, this has the advantage that $\bar{\tau}$ can be introduced for each ring individually. More specifically, $\bar{\tau}$ is calculated along the flux direction of a given ring at the position of the wind parcel. If the flux in equation (13) is used instead, $\bar{\tau}$ is calculated along the disk flux direction. Typical differences in the resulting value for the tilt angle $\lambda_{\rm cr}$ (see below) are 5°–10° for the two approaches. Corrections owing to the $\tau^{-\alpha}$ weighting in the azimuthal integral are even smaller.

Figures 3 and 4 show isocontours for the z- and r-components of the flux in equation (13) above the Newtonian disk. For sufficiently large tilt angles, the flux along the streamlines has a maximum larger than $\pi I(r_0, 0)$ at some X. This is caused by the increasing visibility of the inner, hot disk regions. We denote this regime, where the flux has a maximum, the "panoramic" regime, to be distinguished from the planar "disk" regime, where $F_z \simeq \pi I$, and the "far field" regime, where $F \propto X^{-2}$.

We introduce the normalized flux, $\tilde{\boldsymbol{F}}(r, z) = \boldsymbol{F}(r, z)/\pi I(r_0, 0)$, along a streamline, which is independent of disk luminosity. To quantify the flux increase above the disk, Figure 5 shows the projected, normalized flux $\tilde{F}_x = \hat{x} \cdot \tilde{\boldsymbol{F}}$ as function of X, for different footpoint radii r_0 and for both types of nonisothermal disks. Note that the initial increase of $\tilde{F}_x$ with X caused by the wind's exposure to the central disk region is rather mild, a factor of a few only, because the central region has a small area. In § 5 we discuss how the maximum in $\tilde{F}_x$ controls the base extent of the wind above the disk, as well as the height of the wind critical point.

In deriving the above fluxes, the intensity was assumed to be isotropic. Using instead the Eddington limb darkening law, $I_\theta = 2/5 I_0[1 + (3/2) \cos \theta]$, with polar angle θ, the vertical flux in the planar disk regime above an isothermal disk becomes larger by a factor of 8/7, i.e., limb darkening should not significantly affect the wind properties. However, limb darkening can be more important in the UV spectral regime because of the Wien part of the spectrum, and the correction factors could become somewhat larger there (Diaz, Wade, & Hubeny 1996).

4. VERTICAL WIND ABOVE AN ISOTHERMAL DISK

As an analytically tractable case, we consider first a vertical (or cylindrical) wind with $\lambda = 90°$, or $\hat{x} = \hat{z}$, above an infinite, isothermal disk with flux $\boldsymbol{F} = \pi I \hat{z}$. We again adopt the "radial streaming" approximation in equation (2), i.e., $\bar{\tau} = \tau_z$. Note that τ_z has no contributions from either azimuthal velocity gradients, $\partial v_\phi / \partial r$, or from geometrical expansion terms, $\propto v_\phi$, the latter describing photon escape along the tangent to the helical streamline.

The density ρ that enters τ is replaced by introducing the mass-loss rate from one side of a disk annulus, $d\dot{M}$. Since the mass that streams upward between two cylinders is conserved,

$$d\dot{M}(r_0) = 2\pi r_0 \, dr_0 \, v_x(r_0, x) \rho(r_0, x) \; . \tag{15}$$

For simplicity, we apply the zero sound speed limit, $A = 0$, for the rest of this paper and neglect the force caused by electron scattering because of small Γ above the geometrically thin disk. The Euler equation becomes

$$0 = P(W', X) = W' + g - E W'^{\alpha} \; , \tag{16}$$

where $g = X/(1 + X^2)^{3/2}$ for $\lambda = 90°$, and $W' = dW/dX = 2V \, dV/dX$. Here $d/dX = r_0 \, d/dx$, and V is the flow speed along X, normalized to the *local* escape speed at the footpoint r_0 on the disk. Note the difference in the definition of W' as compared with that for stellar winds (cf. eq. [5]). Also, normalizing the velocity V instead to the escape speed from the white dwarf leads to unwanted, explicit appearances of r_0 in the Euler equation. The constant $E(r_0)$ for a streamline starting at r_0 on the disk is defined as (cf. eq. [6])

$$E(r_0) = \frac{\Gamma(\alpha)}{1 - \alpha} \left(\frac{\kappa_0 \; v_{\rm th}}{2\pi G \; M_{\rm wd}} \right)^{1-\alpha} \frac{2\pi r_0^2 \, F_z(r_0, z = 0)/c^2}{(r_0 \, d\dot{M}(r_0)/dr_0)^{\alpha}} \; . \tag{17}$$

Similarly to the stellar case, equation (16) for the disk wind has global solutions only above a critical value $E_{\rm cr}$, the eigenvalue of the problem, i.e., below a maximum allowable mass-loss rate. Unlike the point star case, however, P in equation (16) is a function of X even when $A = 0$. As a result, the degeneracy in the position of the critical point does not exist here, and one has a well-defined critical point, irrespective of A.

There exists an additional difference between the stellar and disk LDWs. In Figure 1*c*, the finite cone correction factor causes the critical point in the stellar wind to move upstream, and, for vanishing sound speed, both the critical point and the sonic point are found in the stellar photosphere. For the disk case, however, only the sonic point falls toward the photosphere, whereas the critical point stays at finite height. Namely, from the regularity condition $\partial P/\partial X = 0$ (P does not depend on W), the critical point of the disk wind lies at the location of maximal gravity, at $X_{\rm cr} = 1/2^{1/2}$.

This explains why Vitello & Shlosman (1988) find no critical point in the disk regime, $X \ll 1$, for a vertical wind with constant ionization. The variable wind ionization introduces additional gradients into the driving force, shifting the critical point toward the disk photosphere. For the solution discussed here, vertical ionization gradients are not mandatory.

Additional justification that the critical solution is the true wind solution comes from the fact that only the shallow solutions connect to the photosphere. However, terminal speeds of the shallow solutions are much smaller than the white dwarf escape speed, in sharp contrast to observed CV winds. The solution we are searching for should, therefore, switch to the steep branch (with large v_∞) at a critical point, i.e., there should be the solution of maximum mass-loss rate.

The conditions $P = 0$ and $\partial P/\partial W' = 0$ lead to

$$W'_{\rm cr} = \frac{\alpha}{1 - \alpha} \, g_{\rm cr} \; , \tag{18a}$$

$$E_{\rm cr} = \frac{1}{\alpha^{\alpha}(1 - \alpha)^{1-\alpha}} \, g_{\rm cr}^{1-\alpha} \; , \tag{18b}$$

where $g_{\rm cr} = 2/(3 \times 3^{1/2})$. This defines the wind solution of maximum allowable mass-loss rate. The effective gravity hill imposes a "bottleneck" on the flow, i.e., the maximum of $g(X)$ defines the minimum, constant eigenvalue $E_{\rm cr}$, or the maximum allowable $\dot{M}$, for the critical solution which extends from the disk photosphere to large X. Larger values of E correspond to shallow solutions and, hence, to smaller mass-loss rates. Smaller values of E correspond to stalling wind solutions, which become imaginary around the location of the gravity maximum. Note that $E_{\rm cr}$ in equation (18b) is independent of r_0, in accordance with equation (16).

5. TILTED DISK WINDS

With all prerequisites at hand, we can now solve the general eigenvalue problem for a tilted wind above a nonisothermal disk. The density ρ in equation (3) is replaced by the conserved mass-loss rate between two wind cones,

$$d\dot{M}(r_0) = 2\pi r_0 \, dr_0 \, (1 + X \cos \lambda) \times \left[1 - \frac{X r_0 \, (d\lambda/dr_0)}{\sin \lambda} \right] \sin \lambda v_x(r_0, x) \rho(r_0, x) \; . \tag{19}$$

The term $(1 + X \cos \lambda)$ describes the density drop caused by the increasing radius of the cone, and $[1 - Xr_0 (d\lambda/dr_0)/\sin \lambda]$ describes the density drop caused by the geometrical divergence of neighboring cones. The factor $\sin \lambda$ stems from the quenching of the flow at small λ.

5.1. *Disk Euler Equation*

The geometrical expansion term $\nabla \hat{y}$ in the directional derivative $\hat{y} \cdot \nabla(\hat{y} \cdot \mathbf{v})$ has contributions from the azimuthal curvature of helical streamlines and from the cone divergence $d\lambda/dr_0$. *Close* to the disk, where the mass-loss rate of the wind is established, both contributions are small. For azimuthal curvature terms, this is shown in Appendix A. With regard to cone divergence, the argument is a posteriori, i.e., we find below that $d\lambda/dr_0$ is small. Two neighboring wind rays launched at, e.g., $r_0 \sim 5r_{\rm wd}$ intersect at a normalized distance $X_i \sim -10$ below the disk. Generally, X_i is larger by a factor of 10 than $X_{\rm cr}$, the distance between the disk and the critical point. By analogy with spherically symmetric stellar winds, where $\hat{y} \cdot \nabla(\hat{y} \cdot \hat{r} v_r) = \mu^2\, dv_r/dr + (1 - \mu^2)v_r/r$, with $\mu = \hat{y} \cdot \hat{r}$, the geometrical expansion term $\propto v_x \nabla(\hat{y} \cdot \hat{x})$ for disk winds should be $\propto v_x/[r_0(X - X_i)]$. Whereas the geometrical expansion term for O-star winds, $(1 - \mu^2)v_r/r$, is of the same order as the gradient term, $\mu^2 dv_r/dr$, it is much smaller than the latter for disk winds. On the other hand, *far* from the disk, the expansion term may become important. However, we find from solving the Euler equation that it has only a marginal influence on the terminal wind velocity. Furthermore, azimuthal terms for helical streamlines are unimportant far from the disk, where the wind is essentially radial. We, therefore, neglect all geometrical expansion terms in the following. Appendix A also shows that *gradients* in the azimuthal velocity can be neglected in the line force. Finally, we assume that the gradient of v_x points in the $\hat{x}$-direction. This is a reasonable assumption since the velocity gradients develop roughly in the flux direction, as is shown below. The normalized Euler equation for a conical disk wind, and for vanishing sound speed, is then

$$0 = P(W', X) = W' + g - EfW'^{\alpha}\,, \tag{20}$$

with auxiliary function f,

$$f(r_0, X) \equiv \left[(1 + X \cos \lambda)\left(\sin \lambda - Xr_0 \frac{d\lambda}{dr_0}\right)\right]^{\alpha} \int_{r_{\rm wd}}^{r_d} d\tilde{F} \mu^{1+2\alpha}\,. \tag{21}$$

Here, $d\tilde{F} = |d\tilde{\boldsymbol{F}}|$ (see eq. [10]), and μ is the cosine of the angle between $d\tilde{\boldsymbol{F}}$ and the wind cone. Again, $W' = 2V\, dV/dX$, where the velocity V is normalized to the local escape speed; $E(r_0)$ is defined in equation (17). Note that the flux integral in equation (21) introduces a further dependence of f on r_0. Furthermore, because of the weighting with $\mu^{2\alpha}$ in the integral, the disk flux vector and the wind cone generally do not point in the same direction. For disk winds as considered here, good alignment between radiative flux and wind flow is expected, however. In cases where such an alignment is not possible, e.g., for atmospheres irradiated from above, *ablation* winds at large tilt angle with the radiative flux were recently suggested (Gayley, Owocki, & Cranmer 1999).

5.2. *Wind Tilt Angle as an Eigenvalue and Solution Topology*

The critical-point conditions for a specific streamline are, from equation (20)

$$W'_{\rm cr} = \frac{\alpha}{1 - \alpha}\, g_{\rm cr}\,, \tag{22a}$$

$$E_{\rm cr} = \frac{1}{\alpha^{\alpha}(1 - \alpha)^{1-\alpha}}\, \frac{g_{\rm cr}^{1-\alpha}}{f_{\rm cr}}\,, \tag{22b}$$

$$0 = (1 - \alpha)\, \frac{g'_{\rm cr}}{g_{\rm cr}} - \frac{f'_{\rm cr}}{f_{\rm cr}}\,, \tag{22c}$$

where $g' = \partial g/\partial X$ and $f' = \partial f/\partial X$. The tilted disk wind is essentially a two-dimensional phenomenon; hence, we expect two eigenvalues of the Euler equation with respect to E and λ. Finding the critical solution of maximum mass loss at a given footpoint r_0 implies minimizing E in equation (22b) with respect to the position of the "critical" point $(X_{\rm cr}, \lambda_{\rm cr})$. We show now that $(X_{\rm cr}, \lambda_{\rm cr})$ is a *saddle* point of $g^{1-\alpha}/f$. We consider first the X coordinate and recall from the analysis of the vertical disk wind that the maximum of $g^{1-\alpha}$ has determined the eigenvalue $E_{\rm cr}$. From equation (22b), the relevant function now is $g^{1-\alpha}/f$. This means that the maximum of $g^{1-\alpha}/f$ with respect to X for a fixed λ serves as a bottleneck of the flow, i.e., the most stringent condition on the wind between the photosphere and infinity. Therefore, it defines the maximum allowable mass-loss rate. Next, we analyze the mass-loss rate along a streamline by varying its tilt angle λ. To obtain the maximum mass-loss rate, we look for the minimum of $g^{1-\alpha}/f$ as a function of λ. This particular $\lambda_{\rm cr}$ plays the role of a second eigenvalue of the Euler equation, besides $E_{\rm cr}$. Note that because of the dependency of f on r_0, the wind tilt will change with r_0. The eigenvalue $E_{\rm cr}$ is thus given by

$$E_{\rm cr} = \frac{1}{\alpha^{\alpha}(1 - \alpha)^{1-\alpha}} \min_{\lambda} \max_{X} \frac{g^{1-\alpha}}{f}\,. \tag{23}$$

This is the definition of a saddle point of $g^{1-\alpha}/f$. Isocontours of this function are shown in Figure 6 for the SHS disk. The existence of the saddle point in $g^{1-\alpha}/f$ underlines the two-dimensional nature of disk LDWs. Because the saddle opens in the X-direction, the wind escapes to large X.

Furthermore, the critical solution of maximum mass loss passes also through a saddle point of the Euler function P in the (W', X)-plane, in complete analogy with O-star winds. (It may be an interesting task to consider the solution topology in the three-dimensional space spanned by $[\lambda, X, W']$.) The regularity condition, equation (22c), determines the loci $X_{\rm cr}$ of these critical points, as shown by the heavy lines in Figure 6. On the left branch of these curves, which also pass through the saddle point of $g^{1-\alpha}/f$ (if the latter exists), lie critical points of the saddle- or X-type. Here, $W'(X)$ can switch from a shallow (small W') to a steep (large W') solution. On the other hand, the right branch of the regularity curves, which pass through the minimum of $g^{1-\alpha}/f$, consists of critical points of the focal type (Holzer 1977; Mihalas & Mihalas 1984). They correspond to solutions that do not extend from the disk photosphere to large radii and are ignored in our discussion.

Figure 7 shows a good overall alignment of the wind ray of maximum mass-loss rate with the radiative flux vector from the disk, at least up to the critical point. This is (1)

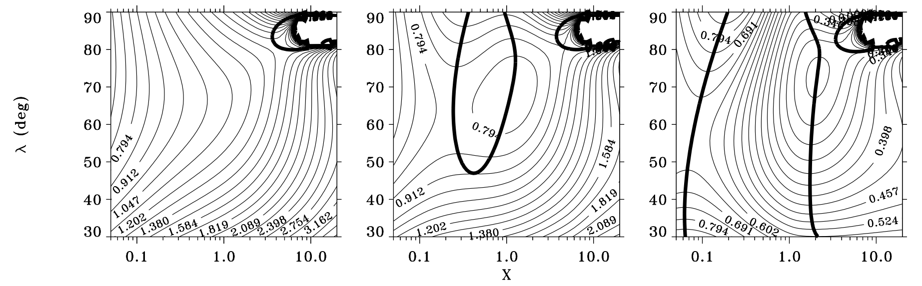

FIG. 6.—Isocontours of $g^{1-\alpha}/f$, normalized to $[2/(3 \times 3^{1/2})]^{1-\alpha}$, over the (X, λ)-plane. Footpoints of the wind are at $r_0 = 3$, 5, and $15 r_{\rm wd}$, respectively (*left to right panels*). The isocontours have logarithmic spacing. The temperature stratification is that of the SHS disk with $r_d = 30 r_{\rm wd}$, and $\alpha = \frac{2}{3}$ was used. Heavy lines are solutions to the regularity condition in eq. (22c).

because the eigenvalue $E_{\rm cr}$ depends linearly on f, but only with a small power of $1 - \alpha$ on g, and (2) because only $f(\lambda)$ has a maximum, whereas $g(\lambda)$ falls off monotonically.

The figure suggests that the wind should actually be launched vertically from the disk surface and then later bend over because of the increasing radial flux component. The latter is (mostly) caused by the radial temperature stratification of the disk, $T \propto r_0^{-n/4}$, with some number n. From a series expansion, one finds $F_r(z) \propto -nz \ln z$, for $z \ll r_0$. We expect streamline bending because of this initial increase in F_r to be more important than bending caused by the higher gas pressure at smaller radii (for a disk with radial temperature fall-off). Furthermore, streamline bending caused by centrifugal forces occurs only on a much larger length scale, r_0. Since the true bent trajectory is expected to follow the flux vector rather closely, a somewhat larger mass-loss rate is expected than along straight wind cones. However, the difference should be rather small. A clear benefit from this approximation is a dramatically reduced complexity of the wind treatment.

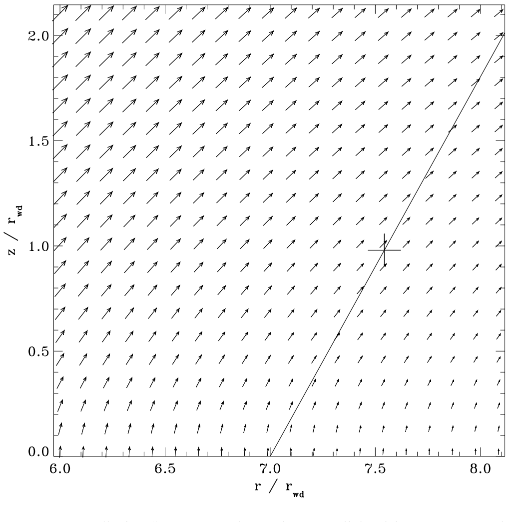

FIG. 7.—Radiative flux vector above the SHS disk with $r_d = 30 r_{\rm wd}$. The straight line indicates a wind cone at eigenvalue $\lambda = 61°$ (cf. Table 1). The plus sign marks the critical point.

5.3. *Inner and Outer Disk Winds*

Up to this point we ignored the possibility of multiple saddle points of $g^{1-\alpha}/f$. We now address this issue. As shown in Figure 6, for $r_0 \lesssim 4 r_{\rm wd}$ the function $g^{1-\alpha}/f$ has only one saddle at a large height, e.g., $X_{\rm cr} \simeq 4.4$ for $\alpha = \frac{2}{3}$. However, for $r_0 \gtrsim 4 r_{\rm wd}$, a second saddle exists at smaller $X_{\rm cr}$, which lies on a different branch of the regularity curve. We name these two types of saddles the *high* and *low* saddles, according to their height $X_{\rm cr}$ above the disk. The effective gravity "hill" separates the two saddle points.

From Figure 6, the low saddle corresponds to a larger mass-loss rate than does the high saddle. For $r_0 \gtrsim 4 r_{\rm wd}$, the solution of maximum mass loss is therefore determined by the low saddle. For smaller r_0, however, only the high saddle exists and determines the wind solution. These two cases define the *outer* and *inner* disk wind, respectively. Clearly, the assumption of straight streamlines is a severe one for the inner wind with high-lying critical points.

The tilt angle of the outer wind is around 60°, namely $\lambda_{\rm cr} = 65°$ at $r_0 = 4 r_{\rm wd}$, and 55° at 20 $r_{\rm wd}$. This is largely independent of α. For the inner wind, the tilt is larger, $\lambda_{\rm cr} = 80°$ for $\alpha = \frac{2}{3}$ and 70° for $\alpha = \frac{1}{2}$. Furthermore, the critical point, $X_{\rm cr}$, for the inner wind is much higher above the disk than the critical point for the outer wind. As mentioned above, these critical points fall on the opposite slopes of the effective gravity hill. For the outer disk wind, the position $X_{\rm cr}$ of the critical point is moving closer to the wind sonic point with increasing r_0. The reason for this is the larger gradient of the disk radiative flux in the x-direction for larger r_0. As a result, the line force can balance gravity at smaller X.

Figure 8 shows critical wind solutions $W'(X)$ above the SHS disk for different r_0. The decelerating solution branches, $W' < 0$, are discussed in Appendix B. The critical point topology of Figure 8 may be compared with that of the CAK stellar wind in Figure 1. (Note, that W' has a slightly different definition for the stellar and disk wind cases.) From Figure 8, we can also derive a condition for the *existence* of a stationary, outer wind solution, further clarifying the role of the effective gravity hill. The plus signs at the critical points in the figure indicate where the Euler function $P > 0$, i.e., where drag forces (gravity and inertia) overcome the driving forces (line and centrifugal force); this is correspondingly so for the minus signs. Hence, $\partial^2 P/\partial X_{\rm cr}^2 < 0$ at the low saddle, or, using equation (22a), (22b), and (22c), $(1 - \alpha)\, g''_{\rm cr}/g_{\rm cr} < f''_{\rm cr}/f_{\rm cr}$ (respectively, " > "

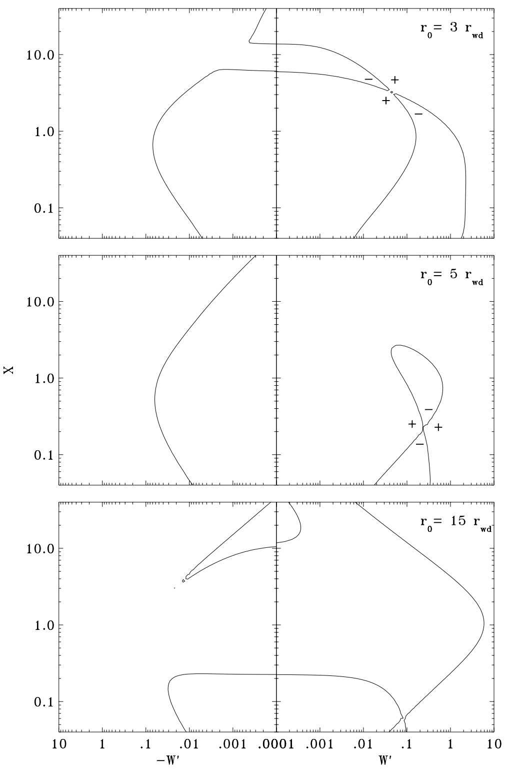

FIG. 8.—Critical wind solutions $W'(X)$ at zero sound speed above the SHS disk ($r_d = 30r_{wd}$, $\alpha = \frac{2}{3}$). At $r_0 = 3r_{wd}$: *high* saddle; at $r_0 = 5$ and $15r_{wd}$: *low* saddle. The branches $W' < 0$ are decelerating wind solutions and are discussed in Appendix B. Plus and minus signs refer to the sign of the Euler function P in eq. (20). For comparison with the critical-point topology of a spherically symmetric, stellar wind, see Fig. 1.

at the high saddle). This means, the maximum of f must be sufficiently broad to allow for a stationary solution with a low saddle. The critical point for a vertical wind above an infinite, isothermal disk, where $f = 1$, corresponds to a low saddle.

To understand the geometry of disk LDWs fully, we consider also the transition region between the inner and outer winds. As discussed above, the low saddle does not exist below $r_0 \lesssim 4r_{wd}$. Figure 9 shows $g^{1-\alpha}/f$ in the neighborhood of this footpoint radius. At $r_0 = 4r_{wd}$, only the high saddle exists and determines the wind solution. At $r_0 = 4.03r_{wd}$, an inner regularity curve of elliptical shape has formed but not yet the low saddle point of $g^{1-\alpha}/f$. The mass-loss rate is maximal at the smallest λ along the curve, i.e., at its lower tip, which determines the wind solution in this transition regime. By $r_0 = 4.15r_{wd}$, a low saddle has formed at $\lambda_{cr} = 65°$. Going to larger r_0, the wind tilt stays (roughly) at this value λ_{cr}, which corresponds to the maximum mass-loss rate. In total, the wind tilt switches continuously from the high to the low saddle over a narrow range of 0.1 r_{wd} in the footpoint radius.

5.4. *Overall Disk Wind Geometry*

Table 1 lists important parameters of the wind above SHS and Newtonian disks, i.e., the tilt angle, λ_{cr}, the normalized mass-loss rate from a disk annulus, $\dot{m}_{cr}$, and the critical point location, X_{cr}. The mass-loss rate $\dot{m}$ is normalized to a vertical wind above an isothermal disk. The shallow maxima of the function $\tilde{F}_x$ in Figure 5 are responsible for $\dot{m} = O(1)$. Implications of these mass-loss rates are discussed in Paper II. From the table, one finds the ray dispersion in the outer wind, at intermediate footpoint radii 4–10 r_{wd}, to be

$$\frac{d\lambda}{dr_0} \simeq -\frac{1°}{r_{wd}} . \qquad (24)$$

Farther in or out, the ray dispersion is even smaller. Since $d\lambda/dr_0$ also enters the Euler equation (20), the full wind problem can be solved only iteratively. However, the dependence of the eigenvalues E_{cr} and λ_{cr} on $d\lambda/dr_0$ is weak, and we assume throughout that equation (24) holds.

The overall geometry of the disk wind is shown in Figure 10. For $\alpha = \frac{2}{3}$, the critical points are at $x_{cr} \sim$ 10–20 r_{wd} for the inner wind, then move toward the disk photosphere and stay at $x_{cr} \simeq r_{wd}$, independent of footpoint radius r_0 in the outer wind. For $\alpha = \frac{1}{2}$, on the other hand, the critical points lie somewhat higher for the outer wind, at $x_{cr} \simeq 2r_{wd}$, but their location is again independent of radius r_0. While the division into an inner and outer wind persists (namely high-lying vs. low-lying saddle, or critical points on opposing

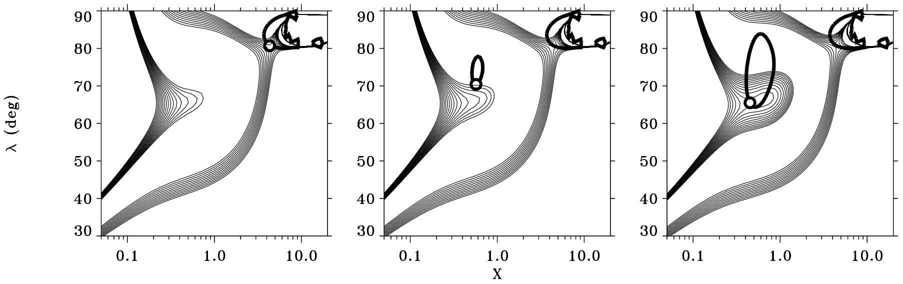

FIG. 9.—Isocontours of $g^{1-\alpha}/f$, normalized to $(2/3\sqrt{3})^{1-\alpha}$; from 0.855 to 0.885 in steps of 2×10^{-3} at the low saddle; from 1.05 to 1.15 in steps of 10^{-2} at the high saddle. At r_0 = 4, 4.03, and 4.15r_{wd}, respectively (*left to right panels*). Heavy lines are solutions to the regularity condition. Circles mark the critical wind solution of maximum mass-loss rate. Within the footpoint range from r_0 = 4 to 4.15r_{wd}, the wind switches from $\lambda_{cr} = 80°$ to $\lambda_{cr} = 65°$ via a growing regularity curve of ellipsoidal shape.

TABLE 1

TILT ANGLE $\lambda_{\rm cr}$, NORMALIZED MASS-LOSS RATE $\dot{m}_{\rm cr}$, AND POSITION $X_{\rm cr}$ OF THE CRITICAL POINT FOR DIFFERENT DISK WIND MODELS

	SHS DISK						NEWTONIAN DISK					
	$\alpha = \frac{2}{3}$			$\alpha = \frac{1}{2}$			$\alpha = \frac{2}{3}$			$\alpha = \frac{1}{2}$		
$r_0/r_{\rm wd}$	$\lambda_{\rm cr}$(°)	$\dot{m}_{\rm cr}$	$X_{\rm cr}$	$\lambda_{\rm cr}$	$\dot{m}_{\rm cr}$	$X_{\rm cr}$	$\lambda_{\rm cr}$	$\dot{m}_{\rm cr}$	$X_{\rm cr}$	$\lambda_{\rm cr}$	$\dot{m}_{\rm cr}$	$X_{\rm cr}$
2	80	0.42	4.4	68	0.62	1.9	78	0.64	4.3	65	0.94	1.2
3	80	0.60	4.4	72	1.02	2.3	78	0.90	$\underline{4.7}$	65	1.45	$\underline{0.82}$
4	80	0.86	$\underline{4.4}$	69	1.60	$\underline{1.7}$	65	1.23	0.32	63	1.78	0.58
5	64	1.37	0.26	63	2.23	0.52	64	1.32	0.26	62	2.10	0.43
6	62	1.48	0.19	61	2.69	0.35	63	1.37	0.23	61	2.23	0.38
7	61	1.60	0.16	60	3.08	0.27	63	1.37	0.21	61	2.37	0.34
10......	58	1.82	0.11	58	3.84	0.18	62	1.48	0.17	60	2.69	0.28
15......	57	2.10	0.08	55	5.41	0.12	61	1.54	0.15	58	3.08	0.23
20......	56	2.26	0.06	53	6.57	0.10	60	1.60	0.13	58	3.31	0.2
25......	55	2.45	0.05	52	8.16	0.08	60	1.67	0.13	57	3.31	0.3
28......	55	2.59	0.04	51	8.16	0.10	58	1.35	0.2	57	2.44	0.2

NOTE—.Underlined numbers indicate the transition from the inner to the outer wind.

sides of the gravity hill), the transition in λ between the two regions is smooth for $\alpha = \frac{1}{2}$, and the inner tilt reaches a maximum of $\lambda = 70°$ only.

The innermost disk region, from 1–$2r_{\rm wd}$, is left out of Figure 10. The details of the disk wind and its very existence here are subject to great uncertainties in the radiation field, which depends on the properties of the transition layer and the white dwarf itself. The outer boundary of the disk LDW, on the other hand, is set by the radius where the disk temperature falls below 10^4 K and UV line driving becomes inefficient, in analogy with stellar winds (Abbott 1982; Kudritzki et al. 1998). For the SHS disk with $L_d = 10\ L_\odot$, this should happen around $30r_{\rm wd}$.

6. DISCUSSION

Here we compare our theoretical model of LDWs from accretion disks in CVs with those available in the literature, both kinematical and dynamical models. We ignore the radial wind models, with the white dwarf being the wind base, because they are in a clear contradiction with current observations (e.g., review by Mauche & Raymond 1997). An alternative source of gas is the disk itself. Kinematical models that account for this source of material subject to the line-driving force successfully explained the observed bipolarity of the outflow and reproduced the inclination-dependent line profiles (Shlosman & Vitello 1993). Their weak point was the absence of a unique solution. The one-dimensional dynamical models in a simplified disk radiation field revealed some major differences between the stellar and disk winds, e.g., the bipolarity and the existence of a gravity hill (Vitello & Shlosman 1988).

More sophisticated two-dimensional kinematical models, supplemented with a three-dimensional radiation transfer in Sobolev approximation, showed the importance of rotation in shaping the lines (Vitello & Shlosman 1993; Shlosman et al. 1996). Finally, the two-dimensional hydrodynamical model of a disk wind in a realistic radiation field and with the line-force parameterized by the CAK approximation has addressed the issue of flow streamlines and mass-loss rates in the wind (PSD). Our comparison, therefore, is focused on these models.

Vitello & Shlosman (1993) set up a kinematical disk wind model assuming straight flow lines in order to fit the C IV P Cygni line profiles of three CVs observed with the *IUE* satellite. The fit parameters included the inner and outer terminating radius of the wind base and the corresponding tilt angles of the wind cone. The best fit appeared to be *indifferent* to the mass-loss rate, within the range of 10^{-1} to 10^{-2} of the accretion rate. In the present work, which accounts for wind dynamics, we find lower mass-loss rates

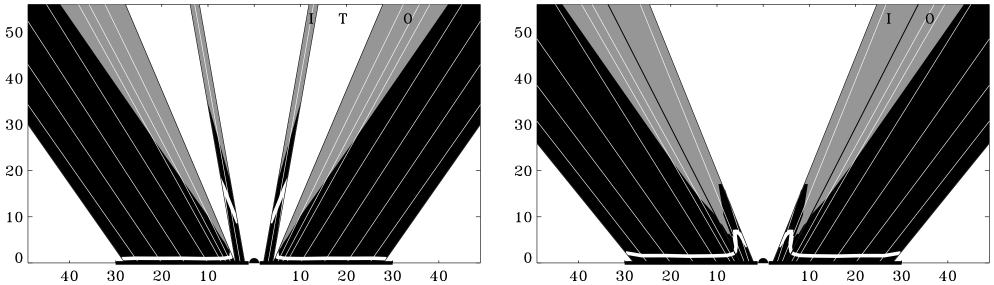

FIG. 10.—Wind geometry above the SHS disk ($r_d = 30r_{\rm wd}$) according to Table 1, for $\alpha = \frac{2}{3}$ (*left-hand panel*) and $\alpha = \frac{1}{2}$ (*right-hand panel*). Black regions indicate the accelerating LDW, and thin white lines show individual wind cones. Gray areas indicate decelerating wind (Appendix B) for a ray dispersion $d\lambda/dr_0 = -1°/r_{\rm wd}$. "I" and "O" mark the inner and outer wind; "T" is the transition region. Heavy white lines are locations of flow critical points. The innermost region of the disk, at $r_0 < 2r_{\rm wd}$, is not treated because of uncertainties in the radiation field.

more justified and discuss various implications of these rates on the wind models in Paper II. The tilt of the innermost wind cone in Vitello & Shlosman was rather steep, $\lambda = 80°$, while at the outer disk edge $\lambda = 25°$. A similar work by Knigge et al. (1995), but using Monte Carlo radiation transfer in the wind, gave similar results. In the present work, the tilt angle λ is calculated self-consistently from the Euler equation, resulting in a similar inner tilt as found in kinematical models, while the outer tilt differs by a factor of 2 between the two approaches.

The most advanced numerical modeling of CV winds from the SHS disk was performed by PSD using the time-dependent ZEUSS two-dimensional code. We find a number of similarities with PSD, but differences exist as well. Our comparison is limited to their models 2–5, i.e., those without a central luminous star. These models are in agreement with the overall wind geometry discussed here. This includes the streamline shape and the run of the wind opening angle with radius. The streamlines in PSD appear to form straight lines in the (r, z)-plane, in striking similarity with the previous kinematical models. In addition, the change in the wind opening angle with distance from the rotation axis seems to be weak in PSD. The mass-loss rates are consistent between both models, and so are the wind optical depths, which can approach unity even for very strong resonance lines (Paper II).

While PSD also find two markedly distinct flow regions, the inner and outer, their inner wind, at $r_0 \lesssim 4r_{\rm wd}$, appears as the only outflow. The outer disk region, at radii $\gtrsim 4r_{\rm wd}$, exhibits a time-dependent irregular flow, resulting in essentially no mass loss. On the other hand, in our model, mass loss from the SHS disk is dominated by the inner wind and the innermost part of the outer wind, as is discussed in Paper II. Interestingly, our outer wind seems to be more robust than the inner wind. For the inner wind, the balance of driving and drag forces that leads to a high saddle on the far side of the gravity hill is a rather delicate one. Setting, for example, the centrifugal force *arbitrarily* to zero causes the high saddle solution to vanish, whereas the low saddle remains almost unchanged.

PSD suggest that the irregular behavior of their outer flow is a consequence of the different X-dependence of gravity and disk flux, with the gravity preventing the wind from developing. This is similar to chocking a nozzle flow. However, we find here that at radii $r_0 \gtrsim 4r_{\rm wd}$, where a low saddle exists, the fast increase in the projected disk flux, $\tilde{F}_x(X)$, results in a sufficiently strong growth of the line force, which drives the wind past the gravity hill. For the inner wind regions, on the other hand, where no lower saddle branch exists, the wind indeed must overcome the gravity barrier without the appropriate radiation flux increase with X. In contrast to the findings of PSD, mass overloading seems therefore more likely for the inner wind. Indeed, from the simulations by PSD, it appears that wave-like perturbations originate at the base of the *inner* wind (D. Proga, 1999, private communication) and propagate to outer disk regions where they prevent a stationary solution from developing. Future work will have to clarify this issue.

Furthermore, we cannot confirm the dependence of λ on the disk luminosity as in the PSD model. We find that the eigenvalue $\lambda_{\rm cr}$ for each streamline is determined from the positions of the saddle points of the function $g^{1-\alpha}/f$. Both g and f are independent of the disk luminosity, f specifically so because it is normalized to the flux at the streamline footpoint (eq. [21]). Therefore, $\lambda_{\rm cr}$ depends only on the radial temperature stratification in the disk.

One important issue neglected in our modeling is the saturation of the line force when all the driving lines become optically thin. If this thick-to-thin transition occurs before the flow reaches its critical point, the wind solution is lost, since the drag forces overcome the driving forces. However, this still leaves the possibility that a more complicated wind dynamics is established, where the decelerating flow at some larger radius starts again to accelerate (i.e., jumps from a W'_- to a W'_+ solution). We leave this question open for future scrutiny and note here that the mass-loss rates derived from the present eigenvalues E are upper limits.

The present work is based on the CAK theory for stellar winds. Over the years, questions have been raised concerning the physical meaning of the CAK critical point (Thomas 1973; Lucy 1975; Cannon & Thomas 1977; Abbott 1980; Owocki & Rybicki 1986; Poe, Owocki, & Castor 1990). Most interesting for the present context is the inclusion of higher order corrections to the diffuse line force in the Sobolev approximation, which shift the critical point even closer to the sonic point (Owocki & Puls 1998; see also Fig. 1). This proximity of the sonic and critical points may not be coincidental, and one can speculate whether or not the *sonic* point determines the mass-loss rate instead of the critical point. In contrast, we find for the disk wind cases, where the sonic and critical points lie far apart, e.g., for a vertical wind above an isothermal disk or a tilted wind close to the rotation axis ("inner wind").

These fundamental issues impair our understanding of LDWs from stars and disks and therefore must be addressed in the future.

7. SUMMARY

We discuss an analytical model for two-dimensional stationary winds from accretion disks in cataclysmic variable stars. The parameters chosen are typical for high-accretion rate disks in nova-like CVs. We solve the Euler equation for the wind, accounting for a realistic radiation field above the disk, which drives the wind by means of radiation pressure in spectral lines. Some key assumptions are that each helical streamline lies on a straight cone; that the driving line force can be parameterized according to CAK theory; and that the thermal gas pressure in the supersonic wind can be neglected. Our results are summarized as follows.

The disk wind solutions are characterized by two eigenvalues, the mass-loss rate and the flow tilt angle, $\lambda_{\rm cr}$, with the disk. The additional eigenvalue $\lambda_{\rm cr}$ for each streamline reflects the two-dimensional nature of the model. We find that the wind exhibits a clear biconical geometry with a small ray dispersion. Specifically, two regions can be distinguished in the wind, launched from within and outside 4 $r_{\rm wd}$, respectively. The tilt angle for the outer wind is $\lambda \sim 60°$ with the disk. At these angles, the wind flow and radiative flux vectors from the disk are well aligned. For the inner wind, the tilt angle is larger, up to 80°. We emphasize that the disk wind tilt angle (i.e., the wind collimation) depends upon the radial temperature stratification in the disk solely, unless there is an additional degree of freedom such as central luminosity associated with nuclear burning on the surface of the white dwarf.

A major distinction between stellar and disk winds is the existence of maxima in both the gravity and the disk flux along each streamline. The flux maximum appears to be a crucial factor in allowing the wind to pass over the gravity "hill." The flux increase is more pronounced farther away from the rotation axis. As a result, the critical point of the outer wind lies close to the disk photosphere and to the sonic point. In fact, it lies upstream of the top of the gravity hill, and this proximity of the critical and sonic points is typical of LDWs from O stars as well. On the other hand, for the inner wind, the increase in radiation flux with height is smaller, and the critical point lies far away from the sonic point, beyond the top of the gravity hill.

Comparing our analytical models with the two-dimensional numerical simulations of Proga et al. (1998), we find an overall good agreement in the streamline shape, tilt angle, and mass-loss rate, but our wind baseline is wider.

We are grateful to Jon Bjorkman, Rolf Kudritzki, Chris Mauche, Norman Murray, Stan Owocki, Joachim Puls, and Peter Vitello for numerous discussions on various aspects of line-driven winds. I. S. acknowledges the hospitality of the IGPP/LLNL, where this work was initiated, and of its director, Charles Alcock. This work was supported in part by NASA grants NAG5-3841 and WKU-522762-98-06, and HST GO-06546.02-95A and AR-07982.01-96A.

APPENDIX A

LINE FORCE CAUSED BY GRADIENTS IN THE AZIMUTHAL VELOCITY

We estimate here the importance of azimuthal velocity terms for the line force in the x-direction. Assuming Keplerian rotation within the disk, and angular momentum conservation above the disk, one has (with r and z being cylindrical coordinates),

$$\begin{aligned}
\frac{\partial v_\phi/\partial z}{\partial v_x/\partial x} &= -\frac{1}{\sqrt{2}}\,\frac{1}{\tan\lambda}\,\frac{1}{1+X\cos\lambda}\,\frac{\sqrt{W}}{W'}\,,\\
\frac{\partial v_\phi/\partial r}{\partial v_x/\partial x} &= -\frac{1}{\sqrt{2}}\,\frac{1-X\cos\lambda}{(1+X\cos\lambda)^2}\,\frac{\sqrt{W}}{W'}\,,\\
-\frac{v_\phi/r}{\partial v_x/\partial x} &= -\frac{\sqrt{2}}{(1+X\cos\lambda)^2}\,\frac{\sqrt{W}}{W'}\,. \qquad \text{(A1)}
\end{aligned}$$

Here, the singularity of $\tan^{-1}\lambda$ at $\lambda = 0$ is a result of neglecting the pressure terms in the Euler equation. Note that $\partial v_\phi/\partial r$ changes sign at $X = 1/\cos\lambda$. From equation (A1), gradients in v_ϕ are comparable to gradients in v_x when $W^{1/2}/W' \sim 1$. The main question is their influence on the mass-loss rate. Because, in the CAK model, $\dot{M}$ is determined by the conditions at the critical point, we calculate $W^{1/2}/W'$ at the latter. We consider first a vertical wind from an isothermal disk. Since W' grows monotonically up to and somewhat beyond the critical point (see Fig. 8), and because $W = \int W' dX$, one has $(W_{\rm cr})^{1/2}/W'_{\rm cr} < (3/2)^{3/4} \times (1 - \alpha/\alpha)^{1/2} \sim 1$. Here, $X_{\rm cr} = 1/2^{1/2}$ and equation (18a) were used. Alternatively, the critical points of the outer wind above a nonisothermal disk typically lie close to the disk, where $g(X) \simeq X$. Using equation (22a), $(X_{\rm cr}/W'_{\rm cr})^{1/2} \sim (1 - \alpha/\alpha)^{1/2} \sim 1$. Both disk cases give, therefore, essentially the same result. We conclude that v_ϕ-terms can be important everywhere between the disk photosphere and the critical point and, hence, may modify $\dot{M}$.

To find their effect on $\dot{M}$, we include v_ϕ-terms in the evaluation of the line force, equation (2), in an approximate manner. Only the disk regime is considered, in which case the radiation intensity is roughly isotropic and the radiation flux has a z-component only. The azimuthal part of the solid angle integral in equation (2) is approximated by a four-point quadrature at angles $n\pi/2$ with $\hat{r}$, where $n = 0, 1, 2, 3$. This leads to a correction factor of the approximate form $1/4(2 + |1 + S|^\alpha + |1 - S|^\alpha)$ to the line force, EfW'^α. Here, S is a linear combination of the expressions in equation (A1), with coefficients <1 from angle integration. In the disk regime, $S_{\rm cr} \sim 1$ from equation (A1). This coincides with the borderline between an increase and a decrease in $\dot{M}$ due to the inclusion of v_ϕ-terms, which lies at $S_{\rm cr} = 1.25$ for $\alpha = \frac{1}{2}$ and at $S_{\rm cr} = 1.18$ for $\alpha = \frac{2}{3}$. Hence, a detailed, numerical calculation of the above angle integral is required to decide which of both cases actually occurs. Since $S_{\rm cr}$ is close to unity, the influence on the mass-loss rate is limited to a 30% effect. We, therefore, neglect v_ϕ-terms in calculating the line force.

APPENDIX B

DISK WIND DECELERATION

In Figure 6, isocontours that cross through the low saddle point *loop* into one another at some larger height, X_d. At $X > X_d$, one has $E > E_{\rm cr}$ from the figure, i.e., the allowed maximum mass-loss rate in this region is *smaller* than that at the saddle. At these distances, inertia and gravity overcome the line force plus centrifugal force, and the wind decelerates, $W' < 0$. As is shown in Paper II, the wind speed always exceeds the *local* escape speed at X_d, which implies that the decelerating wind reaches infinity at a positive speed.

Because of the deceleration, the velocity law becomes nonmonotonic, and the line transfer is no longer purely local, because global couplings occur between distant resonance locations. We neglect these couplings and simply replace W'^α in the line force by $|W'|^\alpha$. For a wind ray launched at $r_0 = 5r_{\rm wd}$, Figure 8 shows that a single, decelerating branch, $W'_- < 0$, accompanies the critical, accelerating solution W'_+ of maximum mass-loss rate. It is suggestive that at X_d the solution curve jumps from the W'_+ to the W'_- branch and extends thereupon to infinity.

The discontinuity in W' introduces a *kink* in the velocity law. Such kinks propagate at sound speed (Courant & Friedrichs 1948; actually, for LDWs, at some modified, radiative-acoustic speed—see Abbott 1980 and Cranmer & Owocki 1996) and are therefore inconsistent with the assumption of stationarity. It seems plausible, however, that the discontinuity in W' is an artifact of the Sobolev approximation, since the latter becomes invalid at small dv_x/dx, i.e., as $W' \rightarrow 0$. An exact line transfer should instead give a smooth transition from W'_+ to W'_-. We find indeed cases of "almost" smooth transitions, where both $dW'_{+,-}/dX_a \rightarrow -\infty$, e.g., in the top panel of Figure 8.

REFERENCES

Abbott, D. C. 1980, ApJ, 242, 1183
———. 1982, ApJ, 259, 282
Arav, N., Shlosman, I., & Weymann, R. J., eds. 1997, ASP Conf. Ser. 128, Mass Ejection from Active Galactic Nuclei (San Francisco: ASP)
Begelman, M. C., McKee, C. F., & Shields, G. A. 1983, ApJ, 271, 70
Binney, J., & Tremaine, S. 1987, Galactic Dynamics (Princeton: Princeton Univ. Press)
Bjorkman, J. E. 1995, ApJ, 453, 369
Blandford, R. D., & Payne, D. G. 1982, MNRAS, 199, 883
Cannon, C. J., & Thomas, R. N. 1977, ApJ, 211, 910
Cassinelli, J. P. 1979, ARA&A, 17, 275
Castor, J. I. 1974, MNRAS, 169, 279
Castor, J. I., Abbott, D. C., & Klein, R. I. 1975, ApJ, 195, 157 (CAK)
Córdova, F. A., & Mason, K. O. 1982, ApJ, 260, 716
———. 1985, ApJ, 290, 671
Courant, R., & Friedrichs, K. O. 1948, Supersonic Flow and Shock Waves (New York: Interscience)
Cranmer, S. R., & Owocki, S. P. 1996, ApJ, 462, 469
Diaz, M. P., Wade, R. A., & Hubeny, I. 1996, ApJ, 459, 236
Emmering, R. T., Blandford, R. D., & Shlosman, I. 1992, ApJ, 385, 460
Feldmeier, A., Shlosman, I., & Vitello, P. 1999, ApJ, 526, 357 (Paper II)
Gayley, K. G., Owocki, S. P., & Cranmer, S. R. 1999, ApJ, 513, 442
Heap, S. R., et al. 1978, Nature, 275, 385
Holzer, T. E. 1977, J. Geophys. Res., 82, 23
Horne, K., & Cook, M. C. 1985, MNRAS, 214, 307
Horne, K., & Stiening, R. F. 1985, MNRAS, 216, 933
Icke, V. 1980, AJ, 85, 329
Klare, G., Wolf, B., Stahl, O., Krautter, J., Vogt, N., Wargau, W., & Rahe, J. 1982, A&A, 113, 76
Knigge, C., Woods, J. A., & Drew, J. E. 1995, MNRAS, 273, 225
Krautter, J., Vogt, N., Klare, G., Wolf, B., Duerbeck, H. W., Rahe, J., & Wargau, W. 1981, A&A, 102, 337
Kudritzki, R. P., Springmann, U., Puls, J., Pauldrach, A., & Lennon, M. 1998, in ASP Conf. Ser. 131, Boulder-Munich II: Properties of Hot, Luminous Stars, ed. I. Howarth (San Francisco: ASP), 278
Lamers, H., & Cassinelli, J. P. 1999, Introduction to Stellar Winds (Cambridge: Cambridge Univ. Press)
Livio, M. 1997, in ASP Conf. Ser. 121, Accretion Phenomena and Related Outflows, ed. D. T. Wickramasinghe, G. V. Bicknell, & L. Ferrario (San Francisco: ASP), 8
Lucy, L. B. 1975, Mem. Soc. R. Sci. Liège, 8, 359
Lucy, L. B., & Solomon, P. M. 1970, ApJ, 159, 879
Mauche, C. W., & Raymond, J. C. 1997, in Cosmic Winds and the Heliosphere, ed. J. R. Jokipii, C. P. Sonett, & M. S. Giampapa (Tucson: Univ. of Arizona Press), 111
Mauche, C. W., et al. 1999, in preparation
Mihalas, D., & Mihalas, B. 1984, Foundations of Radiation Hydrodynamics (New York: Oxford Univ. Press)
Owocki, S. P., Castor, J. I., & Rybicki, G. B. 1988, ApJ, 335, 914
Owocki, S. P., & Puls, J. 1996, ApJ, 462, 894
———. 1998, ApJ, 510, 355
Owocki, S. P., & Rybicki, G. B. 1984, ApJ, 284, 337
———. 1985, ApJ, 299, 265
———. 1986, ApJ, 309, 127
Pauldrach, A. 1987, A&A, 183, 295
Pauldrach, A., Kudritzki, R. P., Puls, J., Butler, K., & Hunsinger, J. 1994, A&A, 283, 525
Pauldrach, A., Puls, J., & Kudritzki, R. P. 1986, A&A, 164, 86
Pereyra, N. A., Kallman, T. R., & Blondin, J. M. 1997, ApJ, 477, 368
Poe, C. H., Owocki, S. P., & Castor, J. I. 1990, ApJ, 358, 199
Proga, D., Stone, J. M., & Drew, J. E. 1998, MNRAS, 295, 595 (PSD)
Pudritz, R. E., & Norman, C. A. 1986, ApJ, 301, 571
Puls, J., Springmann, U., & Lennon, M. 1999, in preparation
Puls, J., Springmann, U., & Owocki, S. P. 1998, in Cyclical Variability in Stellar Winds, ed. L. Kaper & A. W. Fullerton (Berlin: Springer), 389
Rutten, R. G., Dhillon, V. S., Horne, K., Kuulkers, E., & Van Paradijs, J. 1993, Nature, 362, 518
Shakura, N. I., & Sunyaev, R. A. 1973, A&A, 24, 337 (SHS)
Shlosman, I., & Vitello, P. 1993, ApJ, 409, 372
Shlosman, I., Vitello, P., & Mauche, C. W. 1996, ApJ, 461, 377
Shlosman, I., Vitello, P., & Shaviv, G. 1985, ApJ, 294, 96
Sobolev, V. V. 1957, Soviet Astron., 1, 678
Thomas, R. N. 1973, A&A, 29, 297
Vitello, P., & Shlosman, I. 1988, ApJ, 327, 680
———. 1993, ApJ, 410, 815
Woods, D. T., Klein, R. I., Castor, J. I., McKee, C. F., & Bell, J. B. 1996, ApJ, 461, 767

THE ASTROPHYSICAL JOURNAL, 526:357–364, 1999 November 20

DYNAMICS OF LINE-DRIVEN WINDS FROM DISKS IN CATACLYSMIC VARIABLES.
II. MASS-LOSS RATES AND VELOCITY LAWS

ACHIM FELDMEIER AND ISAAC SHLOSMAN
Department of Physics and Astronomy, University of Kentucky, Lexington, KY 40506-0055; achim@pa.uky.edu, shlosman@pa.uky.edu

AND

PETER VITELLO
Lawrence Livermore National Laboratory, L-282, P.O. Box 808, Livermore, CA 94550; vitello@llnl.gov
Received 1999 February 9; accepted 1999 July 2

ABSTRACT

We analyze the dynamics of two-dimensional stationary, line-driven winds from accretion disks in cataclysmic variable (CV) stars by generalizing the formalism of Castor, Abbott, and Klein (CAK) for O stars. In Paper I, we solved the wind Euler equation, derived its two eigenvalues, and addressed the solution topology and wind geometry. Here, we focus on mass-loss rates and velocity laws of the wind. We find that disk winds, even in luminous nova-like variables, have low optical depth, even in the strongest driving lines. This suggests that thick-to-thin transitions in these lines occur in the wind. For disks with a realistic radial temperature law, the mass loss is dominated by gas emanating from the inner decade in radius. The total mass-loss rate associated with the wind from a disk of luminosity 10 $L_\odot$ is $\sim 10^{-12}$ $M_\odot$ yr^{-1}, or 10^{-4} of the mass accretion rate. This is 1 order of magnitude below the lower limit obtained from fitting P Cygni line profiles using kinematical wind models when the Lyman continuum is suppressed. The difficulties associated with such small mass-loss rates for line-driven winds from disks in CVs are principal and confirm our previous work on this subject. We conjecture that this issue may be resolved by detailed non-LTE calculations of the CAK line force within the context of CV disk winds and/or by better accounting for the disk energy distribution and wind ionization structure. We find that the wind velocity profile is well approximated by the empirical law used in kinematical modeling. The acceleration length scale is given by the footpoint radius of the wind streamline in the disk. This suggests an upper limit of $\sim 10 r_{\rm wd}$ to the acceleration scale, which is smaller by factor of a few as compared with values derived from line fitting.

Subject headings: accretion, accretion disks — novae, cataclysmic variables — stars: mass loss — stars: winds, outflows

1. INTRODUCTION

Line-driven winds (hereafter LDWs) are expected around luminous objects the spectra of which peak in the UV, such as OB stars and accretion disks, stellar and galactic (Vitello & Shlosman 1988). Feldmeier & Shlosman (1999, hereafter Paper I) have investigated a two-dimensional analytical model of LDWs from disks in cataclysmic variables (CVs) characterized by a large mass transfer rate from the secondary to the white dwarf. Such CVs, i.e., nova-like variables and dwarf novae in outburst, show clear signs of outflows driven by radiation pressure (Paper I and references therein).

Recent numerical simulations of time-dependent two-dimensional disk winds by Proga, Stone, & Drew (1998; hereafter PSD) largely confirmed the previous kinematical studies by Shlosman & Vitello (1993) and Knigge, Woods, & Drew (1995) and delineated a number of empirical relationships that require further physical explanation. Paper I has addressed the two-dimensional geometry of the wind streamlines and the topology of solutions to the wind momentum equation. In particular, a comparison with the PSD model was made as well as a comparison with the one-dimensional LDWs from OB stars.

The main results of Paper I are as follows. First, the solutions to the wind momentum equation are characterized by two eigenvalues, the mass-loss rate and the flow tilt angle with the disk, in the presence of a realistic radiation field above the disk. The existence of the second eigenvalue is a reflection of the multidimensional nature of a disk wind. The wind itself appears to be collimated to a certain degree, i.e., the wind collimation angle with the rotation axis (semi-opening angle) is about 10° for the wind launched within four white dwarf radii, and about 30° for the outer wind, for the Shakura & Sunyaev (1973, hereafter SHS) disk. Furthermore, the wind collimation solely depends on the radial temperature stratification in the disk, unless there is an additional degree of freedom such as a central luminosity associated with nuclear burning on the surface of the white dwarf or with a boundary layer. The above degree of collimation for disk winds in CVs should be taken with caution at large distances from the disk.

Second, a major distinction between stellar and disk LDWs is the existence of maxima in both the gravity and the radiation flux above the disk. This behavior of gravity and radiation flux results in profound topological differences in the solutions to the stellar and disk wind momentum equations. We find that two distinct regions of disk wind exist, the inner and outer winds. The critical point of the outer wind lies close to the disk photosphere and to the sonic point, upstream of the top of the gravity "hill." This proximity of the critical and sonic points is typical of LDWs from O stars as well. On the other hand, for the inner wind, the critical point lies far away from the sonic point, beyond the gravity hill.

Observationally, the mass-loss rates from CV disk winds are poorly constrained. This is mainly a consequence of uncertainties in the ionizing fluxes from different components in the system and, therefore, of the ionization stratification of the wind. Neglecting the boundary layer and assuming a local blackbody radiation from the disk, Vitello & Shlosman (1993) and Knigge et al. (1995) find wind mass-loss rates $\sim 1\%$ of the accretion rate by fitting observed P Cygni line profiles. For a system with luminosity $10\ L_\odot$, this corresponds to a mass-loss rate of about $2 \times 10^{-10}\ M_\odot\ \mathrm{yr}^{-1}$.

These mass-loss rates are *upper* limits for the following reason. The radiation field in the Lyman continuum is often found to be highly suppressed compared to blackbody emission or stellar photospheric fluxes, or it may even be absent (Polidan, Mauche, & Wade 1990; Long et al. 1991, 1994; van Teeseling, Verbunt, & Heise 1993; Knigge et al. 1997). This drastic reduction in ionizing flux allows a reduction in the electron density and, therefore, in the mass-loss rate from the disk, $\dot{M}$, while maintaining the same degree of ionization in the wind.

On the other hand, a reasonable *lower* limit to the wind mass-loss rate from luminous CV disks was found by Prinja & Rosen (1995). They argued that the product $\dot{M}q$, where q is the ionization fraction of C IV, lies between 5×10^{-13} and $1 \times 10^{-11}\ M_\odot\ \mathrm{yr}^{-1}$ for 10 dwarf novae and nova-like variables with high-resolution *IUE* spectra (see also Mauche & Raymond 1987; Hoare & Drew 1993). This results in a lower limit of $\dot{M} \sim 5 \times 10^{-13}\ M_\odot\ \mathrm{yr}^{-1}$. Note that this value is still model dependent to some degree, since Prinja & Rosen assumed a constant ionization fraction throughout the wind and a purely radial flow.

In this paper, we focus on the mass-loss rate and the velocity law of disk LDWs in CVs. We employ the main assumption of Paper I that the wind streamlines are contained in straight cones, the collimation angles of which are eigenvalues of the Euler equation. This approximation is acceptably close to the disk (e.g., as shown by PSD) and allows us to make a meaningful determination of the mass-loss rate (which is constrained close to the disk photosphere as well) and of the initial velocity law. A similar conclusion was reached from line fitting using two-dimensional wind kinematics (Vitello & Shlosman 1993; Knigge et al. 1995). On the other hand, we expect both the centrifugal forces and the polar component of the line force to bend the streamlines at large distances from the disk and to influence the terminal velocity of the flow.

This paper is organized as follows. Section 2 reviews the mass-loss rates derived from the theory of Castor, Abbott, & Klein (1975, hereafter CAK). Section 3 shows that CV disk winds are expected to have low optical depth even in strong lines. Sections 4 and 5 derive the mass-loss rates and velocity laws for the disk wind model. Sections 6 and 7 discuss and summarize our results.

2. CAK MASS-LOSS RATES FOR STARS AND CV DISKS

The CAK line force for stellar winds is fully determined by two parameters, the power exponent α and the mass absorption coefficient of the strongest driving line, κ_0 (Paper I; Puls, Springmann, & Lennon 1999). Instead of using κ_0 directly, CAK parameterize the line force per unit mass as $g_L = M(t)g_e$, where $M(t) \equiv kt^{-\alpha}$ (with $0 < \alpha < 1$) is the so-called force multiplier, and g_e is the force caused by electron scattering. The optical depth t refers to a line with $\kappa = \sigma_e$, where σ_e is the electron scattering coefficient. The parameter k is given in terms of κ_0 by

$$k = \frac{\Gamma(\alpha)}{1-\alpha} \frac{v_{\mathrm{th}}}{c} \left(\frac{\kappa_0}{\sigma_e}\right)^{1-\alpha} , \tag{1}$$

where $\Gamma(\alpha)$ is the complete gamma function, c is the speed of light, and v_{th} is the thermal speed of carbon ions (CAK) or hydrogen (Abbott 1982). The above parameterization for $M(t)$ as a power law, however, does not account correctly for optically thin winds, where the force multiplier saturates at some value $M_{\max}(t) \equiv Q \sim 2000$ for a gas of solar composition (Abbott 1982). Gayley (1995) noted that Q is essentially identical to the Q-value of a resonator and can be estimated as $Q \sim A\ \nu/\gamma$, where $A \sim 10^{-4}$ is the abundance of valence electrons, $\nu \sim 10^{15}\ \mathrm{s}^{-1}$ is the frequency of UV radiation, and $\gamma \sim 10^8\ \mathrm{s}^{-1}$ is the damping rate. Hence, $Q \sim 1000$ should be an appropriate value for O stars. However, for winds from B stars near the main sequence, modeling of X-ray spectra already suggests that appropriate Q-values differ from those for O stars. The mass-loss rates inferred from the standard theory can be substantially lower than the inferred ones (Cassinelli 1994; Cassinelli et al. 1994).

In terms of Q, κ_0 is given by (Gayley 1995)

$$\frac{\kappa_0 v_{\mathrm{th}}}{\sigma_e c} = \Gamma(\alpha)^{-[1/(1-\alpha)]} Q . \tag{2}$$

Inserting the eigenvalue E_{cr} from equation (8b) in Paper I into equation (6) thereof, the CAK mass-loss rate from O-star winds takes the compact form,

$$\dot{M} = \frac{\alpha}{1-\alpha} \left(\frac{Q\,\Gamma}{1-\Gamma}\right)^{(1-\alpha)/\alpha} \frac{L}{c^2} , \tag{3}$$

with luminosity L and the Eddington factor Γ. This expression is valid as long as $Q\ \Gamma/(1-\Gamma) > 1$. Otherwise, the gravity prevails and no wind solution exists. For the above value of Q, and assuming $\alpha = \frac{2}{3}$ and an Eddington factor $\Gamma = 0.5$ of an O supergiant, equation (3) gives $\dot{M} \sim 90L/c^2$. Thus, the mass-loss rate from the CAK theory agrees well with the estimate from the single scattering limit, $\dot{M} = (c/v_\infty)(L/c^2) \sim 100L/c^2$, for typical wind terminal speeds $v_\infty \sim 3000\ \mathrm{km\ s^{-1}}$. However, agreement between both mass-loss rates is solely the result of Γ being close to unity.

If, alternatively, $\Gamma \ll 1$, the CAK mass-loss rate falls well below the single scattering limit. As we show in § 3, the mass loss of a disk LDW is given again by equation (3), up to correction factors of order unity. Even for the brightest CVs, i.e., nova-like variables and dwarf novae in eruption, which experience LDWs, $Q\Gamma \sim 1$ (applying the O-star value of Q). Hence, $\dot{M} \sim L/c^2$ from equation (3), whereas the single scattering limit gives $\dot{M} \sim 60\ L/c^2$, for $v_\infty \sim 5000\ \mathrm{km\ s^{-1}}$. Since in thin LDWs the probability for a photon to be scattered by a line is less than unity, the estimate from the single scattering is way too high (see also Puls, Springmann, & Owocki 1998).

3. DISK WIND OPTICAL DEPTHS

A number of fundamental differences exist between stellar and disk LDWs in CVs, some of which have been discussed in Paper I. Here we show that optical depths for CV winds are more typical of thin winds, e.g., of B stars near the main sequence, than of more extensive supergiant winds.

3.1. *Disk Wind Geometry and Radiation Field*

The disk wind geometry is described in Paper I, and we repeat here only the essential assumptions and make necessary definitions. A flow streamline is a helix that is contained within a *straight* cone (Fig. 1). The footpoint radius of a streamline in the disk is r_0, the tilt of the cone with the disk is λ, and x is the distance along the cone. We neglect pressure forces and assume that the azimuthal velocity is determined by angular momentum conservation above the disk and by Keplerian rotation within the disk. The only remaining velocity component is v_x, which points upward along the cone. We introduce a normalized coordinate $X \equiv x/r_0$. The velocity V is normalized to the local escape speed, and the flow acceleration becomes $W' = dW/dX = 2V\,dV/dX$. Last, we introduce the radiation flux $\boldsymbol{F}$ above the disk and the flux $\tilde{\boldsymbol{F}}$ normalized to the footpoint flux of the streamline, as well as their projected counterparts F_x and $\tilde{F}_x$ along the wind cone (§ 3.2 of Paper I).

3.2. *Semitransparent Winds from CV Disks?*

In this section, we make use of a simplified Euler equation for the disk LDW to show explicitly that low Γ factors in CV disks imply low optical depths in the wind. By doing so, we neglect factors of order unity from the angle integration in equation (2) of Paper I, in replacing the optical depth, τ_γ, in arbitrary direction $\hat{\gamma}$ by the optical depth in flow direction, $\tau_\gamma = \tau_x$. For the sake of simplicity, only the disk with $F \propto r_0^{-2}$ (hereafter termed "Newtonian" disk) is considered. The line force per unit mass is then

$$g_L = \frac{\sigma_e F_x(r_0, X)}{c} M(t_x) = \frac{\sigma_e F_z(r_0, 0)}{c} \tilde{F}_x(r_0, X) M(t_x) . \tag{4}$$

The Euler equation for the disk wind, in the limit of zero sound speed, and neglecting the force caused by electron scattering because of small Γ above the disk, becomes (with gravitational constant G, white dwarf mass $M_{\rm wd}$, dimensional wind speed v_x, and $v_x' = dv_x/dx$),

$$v_x v_x' = -\frac{GM_{\rm wd}}{r_0^2} [g(X) - \Gamma(r_0) \tilde{F}_x(r_0, X) M(t_x)] , \tag{5}$$

where the effective gravity g was defined in equation (9) of Paper I, and we introduced

$$\Gamma(r_0) \equiv \frac{\sigma_e F_z(r_0, 0) r_0^2}{cGM_{\rm wd}} . \tag{6}$$

For the Newtonian disk, $\Gamma(r_0) = \sigma_e L_d/[4\pi cGM_{\rm wd} \ln(r_d/r_{\rm wd})]$ becomes *independent* of r_0. Here, L_d is the disk luminosity, and r_d and $r_{\rm wd}$ are the outer and inner disk radii, with $r_{\rm wd}$ being the white dwarf radius. Using typical parameters for nova-like CVs, $L_d = 10\ L_\odot$, $M_{\rm wd} = 0.7\ M_\odot$, and $r_d/r_{\rm wd} = 30$, one has that $\Gamma \simeq 10^{-4}$.

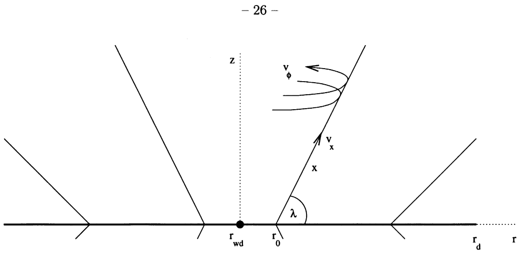

FIG. 1.—Adopted flow geometry for a CV disk wind. The streamlines are helical lines and are assumed to lie on straight cones.

For a stationary wind solution to exist, the right-hand side of equation (5) has to be positive. This poses a constraint on $M(t)$ and therefore on t. Namely, the maximum of reduced gravity g lies between $2/(3 \times 3^{1/2}) \simeq 0.38$ for $\lambda = 90°$ and $4/27 \simeq 0.15$ for $\lambda = 0°$. Since $\tilde{F}_x$ is of order unity (see Fig. 5 in Paper I), $M(t)$ approaches its maximum value, Q, in regions of large gravity and stays constant thereafter. In other words, because Γ is so small for CV disks, the wind solution barely "makes it" over the gravity hill.

This saturation effect in $M(t)$ happens when the strongest driving line in the wind becomes optically thin, at about $t \sim 10^{-7}$. If this thick-to-thin transition occurs before or at the critical point of the flow, the wind solution is lost. This possibility cannot be excluded in our model given the rapid change of the velocity gradient (and hence of t) in the vicinity of the critical point. The consequences of this effect on the feasibility of LDWs are discussed in § 6.

The situation is fundamentally different for dense winds of O stars, where the Euler equation for the radial wind speed, v_r, reads (with M being the stellar mass)

$$v_r v_r' = -\frac{GM}{r^2} \left(1 - \Gamma[M(t) + 1]\right) . \tag{7}$$

Assuming $\Gamma > 0.1$ for O stars, there is a wide range in $M(t)$ for a stationary solution to exist, namely $\sim$10–2000. The highest mass-loss rate solution (hence, the slowest wind) is characterized by the lowest allowable $M(t) \sim 10$. The permitted range in $M(t)$ corresponds to an even wider range in t (because $\alpha < 1$), $t \sim 10^{-7}$ to 10^{-3}. We further quantify these arguments in the Appendix.

Our estimate for t in CV winds contradicts the claim by Murray & Chiang (1996) that the optical depth parameter t is similar for CV disk and O-star winds.

4. DISK WIND MASS-LOSS RATES

4.1. *Vertical Disk Wind*

The mass-loss rate of the vertical wind above an isothermal disk is determined by the eigenvalue $E_{\rm cr}$ in equation (18b) in Paper I. From equation (17) in Paper I, one finds

$$\dot{M} = \frac{\alpha}{1-\alpha} \left(\frac{3\sqrt{3}c\sigma_e Q}{8\pi GM_{\rm wd}}\right)^{(1-\alpha)/\alpha} D \left(\frac{L_d}{c^2}\right)^{1/\alpha} . \tag{8}$$

The dimensionless constant D is given by

$$D = \int_{r_1}^{r_2} \frac{dr_0}{r_0} \left[\frac{4\pi r_0^2 F_z(r_0, 0)}{L_d}\right]^{1/\alpha} , \tag{9}$$

where r_1 and r_2 are the inner and outer radii of the wind base in the disk, respectively. Making the plausible assumptions that $r_d \gg r_{\rm wd}$, $r_2 \gg r_1$, and $r_2 \simeq r_d$ (both of the latter radii are determined essentially by the temperature dropping below 10^4 K), we estimate $D \simeq 1$ for $\alpha = \frac{1}{2}$ and $\alpha = \frac{2}{3}$. Introducing a new, global disk Eddington factor,

$$\Gamma_d = \frac{\sigma_e L_d}{4\pi cGM_{\rm wd}} , \tag{10}$$

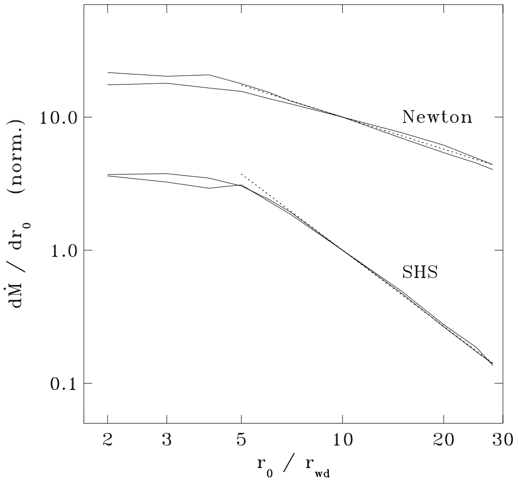

FIG. 2.—Mass-loss rate per disk annulus, $d\dot{M}/dr_0$, as function of footpoint radius, r_0. Table 1 and eq. (17) from Paper I were used for SHS and Newtonian disks with $\alpha = \frac{2}{3}$ and $\alpha = \frac{1}{2}$. Dotted lines are fits with $d\dot{M}/dr_0 \propto r_0^{-1.9}$ (SHS) and $\propto r_0^{-0.8}$ (Newtonian). The curves are normalized at $r_0/r_{wd} = 10$.

equation (8) becomes

$$\dot{M} \simeq \frac{\alpha}{1-\alpha}\left(\frac{3\sqrt{3}}{2}\,Q\Gamma_d\right)^{(1-\alpha)/\alpha}\frac{L_d}{c^2}\,. \tag{11}$$

Up to the correction factors caused by different gravity (and geometry), this equation is identical to the CAK mass-loss rate from a point star, equation (3). Note that a disk wind is more efficient in carrying mass loss than an O-star wind by a factor of $[(3 \times 3^{1/2})/2]^{(1-\alpha)/\alpha}$, owing to the lower gravity potential well. Rewriting equation (11) as $\dot{M} \equiv NL_d/c^2$ (where the coefficient N depends on L_d), and using the relevant parameters for nova-like CVs introduced above, gives $N \simeq 2$ and a disk mass-loss rate $\dot{M} \simeq 10^{-12}\ M_\odot\ \mathrm{yr}^{-1}$ for $Q = 2000$.

4.2. *Tilted Disk Winds*

A more realistic picture of disk mass loss consists of a tilted wind from a disk with radial temperature stratification. From equation (17) in Paper I, using equation (10),

$$\dot{M} = \frac{\alpha}{1-\alpha}\left(\frac{3\sqrt{3}}{2}\,Q\Gamma_d\right)^{(1-\alpha)/\alpha} D\langle\dot{m}\rangle\,\frac{L_d}{c^2}\,, \tag{12}$$

where

$$\langle\dot{m}\rangle \equiv \int_{r_1}^{r_2}\frac{dr_0}{r_0}\,\dot{m}(r_0)[r_0^2 F_z(r_0, 0)]^{1/\alpha}\bigg/\int_{r_1}^{r_2}\frac{dr_0}{r_0}\,[r_0^2 F_z(r_0, 0)]^{1/\alpha}, \tag{13}$$

and $\dot{m}(r_0)$ is normalized in units of mass loss from a vertical wind; $\langle\dot{m}\rangle$ is then a normalized mass-loss rate per dr_0, averaged over the wind base. Using values of $\dot{m}(r_0)$ from Table 1 in Paper I, we estimate $\langle\dot{m}\rangle = 1.2$ for $\alpha = \frac{2}{3}$, and $\langle\dot{m}\rangle = 2.2$ for $\alpha = \frac{1}{2}$, both for SHS and Newtonian disks. For the latter, one has $D = \ln(r_2/r_1)/[\ln(r_d/r_{wd})]^{1/\alpha}$. This expression is roughly correct also for the SHS disk, where D cannot be calculated analytically. Inserting the values for $\langle\dot{m}\rangle$ and D into equation (12), one finds, for $\alpha = \frac{1}{2}$ and $\alpha = \frac{2}{3}$, and for SHS and the Newtonian disks, assuming once again typical parameters for nova-like CVs and $Q = 2000$, that $N \simeq 2$ or $\dot{M} \simeq 10^{-12}\ M_\odot\ \mathrm{yr}^{-1}$.

Interestingly, the mass-loss rates for a vertical wind above an isothermal disk and for tilted winds above disks with temperature stratification are very similar. This means that the disk mass-loss rate is only a weak function of the tilt angle, *as long as* the latter is aligned with the radiation flux. For the disk types used in the present work, this range encompasses $\lambda \sim 50°$–$90°$, according to Table 1 in Paper I.

It is readily shown that the mass-loss rate for an LDW due to a single, optically thick line is roughly L_d/c^2. The above $N \simeq 2$, therefore, implies that only a few lines become optically thick in the present CV disk wind model. Unlike for disk winds, in O-star winds of the order of 100 lines become optically thick, according to equation (3).

Note that in Paper I, eigenvalues E were derived *without* including the saturation of the force multiplier at $M_{\max}(t) = Q$ (i.e., without applying the exponential line-list cutoff of Owocki, Castor, & Rybicki 1988). The above mass-loss rates are, therefore, upper limits.

Finally, we derive the dependence of the mass-loss rate $d\dot{M}$ on r_0. According to equation (17) in Paper I, this relation is determined by the disk temperature stratification and the run of E_{cr} with r_0. For an isothermal disk, E_{cr} was found to be independent of r_0, hence $d\dot{M}/dr_0 \propto r_0^{(2-\alpha)/\alpha}$. Such an unrealistic growth of $d\dot{M}/dr_0$ with radius is a consequence of the increase of radiation energy with r_0. For the Newtonian disk, Figure 2 shows $d\dot{M}/dr_0$ according to Table 1 and equation (17) in Paper I. A good power-law fit to the eigenvalues is given by $d\dot{M}/dr_0 \propto r_0^{-0.8}$ for $r_0 \gtrsim 5r_{\mathrm{wd}}$. The total disk mass-loss rate therefore scales roughly as $\dot{M} \propto \ln r_2$. For the SHS disk, Figure 2 gives approximately $d\dot{M}/dr_0 \propto r_0^{-1.9}$ for $r_0 \gtrsim 5r_{\mathrm{wd}}$; hence, the total $\dot{M}$ should depend on r_2 only very weakly. At $r_0 \lesssim 5r_{\mathrm{wd}}$, the radial dependency of $d\dot{M}/dr_0$ is weak for both types of disks. Therefore, the mass-loss rate $\dot{M}$ is centrally concentrated—and more so for SHS disks.

5. VELOCITY LAWS FOR DISK WINDS

We discuss the wind velocity law by solving the Euler equation, first neglecting, then accounting for ionization effects in the flow. Only the flow above the SHS disk is analyzed in this section.

5.1. *Solutions to the Algebraic Euler Equation*

The geometrical expansion terms, discussed in § 5.1 of Paper I, introduce a velocity dependency into the wind Euler equation. However, we find that these terms leave the mass-loss rates in the model practically unchanged and increase the wind velocity by at most 10%. The reason for this is the small angle dispersion in the wind streamlines. Therefore, we omit geometrical expansion terms here.

Without explicit dependence on velocity, the Euler equation becomes purely algebraic. Figure 8 of Paper I displays the solutions $W'(X)$ of the Euler equation (20) thereof for a tilted disk wind at different r_0. The velocity field above the disk is obtained by integrating W' and is displayed for a number of streamlines in Figure 3 for the SHS disk and $\alpha = \frac{2}{3}$. As shown in Paper I, the LDW velocity law is not necessarily a monotonic function of X. Clearly, the deceleration regime (marked with a cross in Fig. 3) is unimportant for streamlines starting at large r_0, because it lies at large X

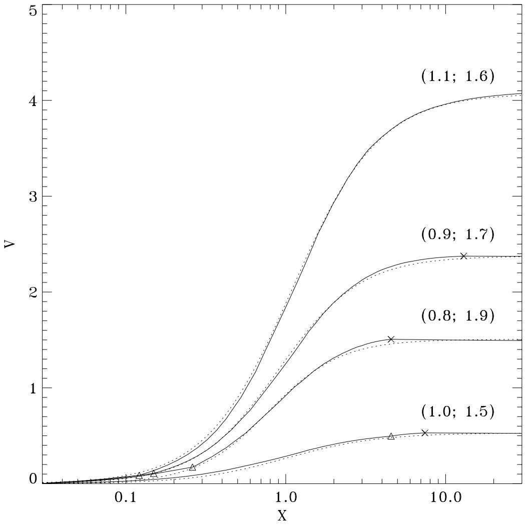

FIG. 3.—Velocity profiles for the SHS disk with $r_d = 30r_{\rm wd}$, for $\alpha = \frac{2}{3}$, and at footpoint radii 3, 7, 10, $15r_{\rm wd}$ (*from bottom to top*). The dotted lines are fits using the velocity law eq. (14), with the values of $(X_{\rm acc};\, \beta)$ given in brackets. The velocity V is in units of the local escape speed at r_0. For the tilt angles, eigenvalues $\lambda_{\rm cr}$ from Paper I were used. Triangles mark the critical point, and crosses mark the point where the wind starts to decelerate.

where the flow moves much faster than the local escape speed. The inner streamlines do show a more pronounced kink.

The wind terminal velocities are found to be independent of r_0, for $\alpha = \frac{1}{2}$, and linearly dependent on r_0 for $\alpha = \frac{2}{3}$, growing by a factor of 5 over the whole disk. However, this may be of academic interest only, since the wind is expected to go through an optically thick-to-thin transition beforehand. Hence the actual observable terminal velocities may be smaller.

The velocity profiles in Figure 3 are well approximated by the empirical velocity law used by Shlosman & Vitello (1993) in fitting the line profiles of nova-like CVs,

$$v = v_\infty \frac{(X/X_{\rm acc})^\beta}{1 + (X/X_{\rm acc})^\beta} . \tag{14}$$

Here, $X_{\rm acc}$ is the acceleration length scale along the wind cone. We find the best fits to Figure 3 for $\beta = 1.5$–1.9. Vitello & Shlosman quote rather similar values of $\beta = 1.3$–1.5. Furthermore, $X_{\rm acc} \approx 1$ in Figure 3, which means that the footpoint radius r_0 sets the acceleration length. The reason for this is that $X_{\rm acc}$ is determined by the effective gravity and disk radiation field, i.e., by the auxiliary functions g and f (Paper I), which change on length scales $\sim r_0$. For this reason, we do not expect $X_{\rm acc}$ to depend on α. The $X_{\rm acc}$ from observed P Cygni line profiles are usually found to be larger, namely, in the range 1–10 (Hoare & Drew 1993; Vitello & Shlosman 1993), depending on individual objects. We comment further on this in § 6.3.

5.2. *Effects of Ionization Stratification in the Wind*

The major concern of the present model is the small optical depth in the wind, making the latter semitransparent even in the strongest driving lines, when $Q = 2000$ is used. The resolution of this problem may be related to the ionization structure in the wind, which is expected to lead to a more shallow velocity law and smaller velocity gradients. We parameterize the ionization stratification in the simplest possible way by introducing the $\delta(>0)$ parameter customarily used in stellar wind theory (e.g., Abbott 1982), namely,

$$g_L \propto t^{-\alpha} \xi^{-\delta} , \tag{15}$$

where $\xi \equiv J/n_e$ is the ionization parameter, J is the frequency-integrated mean intensity, and n_e is the electron number density. Higher ionization stages typically harbor fewer lines than lower ionization stages and therefore lead to a smaller line force. Typical values for O stars are $\delta \lesssim 0.1$ (Abbott 1982; Puls 1987; Pauldrach et al. 1994), but values as large as $\delta = 0.7$ have been suggested recently for winds at low effective temperatures of 8000 K (Kudritzki et al. 1998).

To include the δ-correction term in the present model, we calculate first dJ from a disk annulus of radius q and width dq, using cylindrical coordinates r and z,

$$dJ(r, z) = 4I(q, 0) q\, dq z \frac{\sqrt{q^2 + r^2 + z^2 - 2rq}}{(q^2 + r^2 + z^2)^2 - (2rq)^2} \times E_2\left[-\frac{4rq}{(q - r)^2 + z^2} \right] , \tag{16}$$

where I is the isotropic, frequency-integrated intensity, and E_2 is the complete elliptical integral of the second kind (Abramowitz & Stegun 1965, p. 590). For the temperature stratifications of interest, this expression for dJ cannot be integrated analytically over q to give J. Resorting to a one-dimensional numerical integration, Figure 4 shows J and F as function of X for the SHS disk at a representative r_0. Importantly, for the outer wind, the critical point lies upstream of the maximum of both J and F. Since J increases along the streamline while the electron density drops, ξ *increases* all the way to the critical point, as in O-star winds. The line force at the critical point is, therefore,

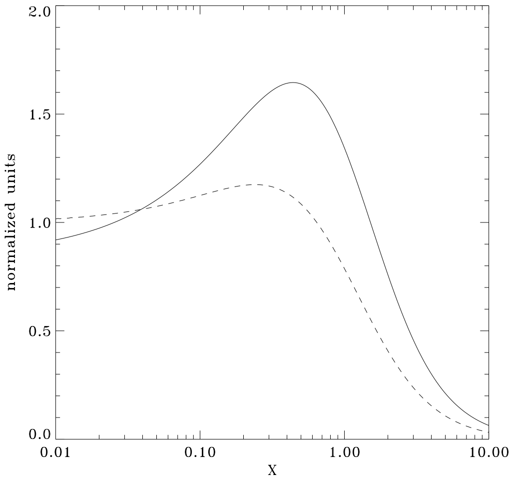

FIG. 4.—Normalized, projected flux (*solid line*) and mean intensity (*dashed line*) above the SHS disk ($r_d = 30r_{\rm wd}$) along a ray with footpoint $r_0 = 10r_{\rm wd}$ and $\lambda_{\rm cr} = 58°$.

smaller for $\delta > 0$ than for $\delta = 0$, and the same is true for the mass-loss rate. Alternatively, in the unlikely situation that the wind recombines along the streamline, the driving force as well as the mass loss would increase because of a larger number of metal transitions.

To understand the effect of ionization stratification on the wind velocity law, we include the δ-correction above the critical point but neglect it below the same, thereby leaving the mass-loss rate unaltered. Since the δ-term introduces a dependence of the line force on W besides that on W', the solution to the Euler equation has to be iterated until convergence is achieved.

We find that, assuming $\alpha = \frac{2}{3}$ and $\delta = 0.2$, terminal speeds decrease by a factor of ~ 2 for outer regions of the SHS disk, whereas the optical depth t increases by a factor of ~ 4, thereby pushing the solution further away from the cutoff at $t \sim 10^{-7}$. For inner disk regions, the effect of δ on v_∞ and t is less pronounced. The somewhat ambivalent conclusion is, therefore, that δ-terms may, as desired, raise t by a factor of a few but, at the same time, also lead to an unwanted reduction in terminal speeds.

6. DISCUSSION

In this section, we compare the mass-loss rates from our model with values quoted in the literature, which are typically estimated from P Cygni line fits or from dynamical wind modeling. We also mention briefly some processes neglected in this work that may have an effect on $\dot{M}$.

6.1. *Comparison with $\dot{M}$ from Kinematical Wind Modeling*

The most reliable estimates for mass-loss rates from CVs are, so far, from P Cygni line fits. For nova-like variables with parameters similar to those considered here, Vitello & Shlosman (1993) and Knigge et al. (1995) find a lower limit of $\sim 10^{-2}$ to the ratio of mass–loss to accretion rates. Below this value, the observed line profiles cannot be reproduced because the wind becomes overionized. This is about 2 orders of magnitude larger than $\dot{M}$ derived in § 4, when $Q = 2000$ is used as in O stars. It is important, however, that a highly idealized blackbody disk spectrum was used in the line fitting. This is a clear overestimate of the ionizing radiation in the Lyman continuum (Polidan et al. 1990; Long et al. 1991, 1994; van Teeseling et al. 1993; Knigge et al. 1997). For a more realistic radiation field that accounts for the Lyman cutoff, the wind mass-loss rate can be reduced while maintaining the same ionization parameter.

As is shown in Figure 5, we have been able to reproduce acceptable P Cygni line profiles down to $\dot{M} \sim 10^{-11}$ $M_\odot$ yr^{-1} for a generic wind model. We use the Lyman cutoff and a tail of high-energy X-rays to account for carbon ionization. Essentially, all the carbon is then in the form of C IV because of Auger ionization of C II by X-rays. For $\dot{M} \sim 10^{-12}$ $M_\odot$ yr^{-1}, on the other hand, the emission component in the calculated line profile is missing, which is in disagreement with observations (Fig. 5).

6.2. *Comparison with $\dot{M}$ from Dynamical Wind Modeling*

Next, we compare the mass-loss rates from our analytical wind model with those from dynamical simulations of disk winds. The only realistic dynamical modeling of CV disk winds attempted so far was performed by PSD. We have provided a general comparison between our model and theirs in Paper I and turn here to mass-loss rates.

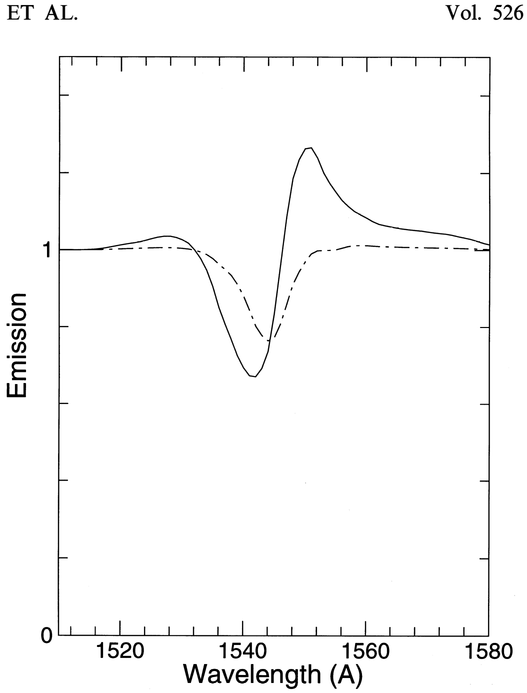

FIG. 5.—Synthetic P Cygni line profiles for an LDW from a disk with suppressed Lyman continuum. The wind mass-loss rate is $\sim 10^{-11}$ $M_\odot$ yr^{-1} (*solid line*) and $\sim 10^{-12}$ $M_\odot$ yr^{-1} (*dashed line*).

Using $k = 0.2$ and $\alpha = 0.6$, PSD find for the SHS disk mass-loss rates of $\dot{M} = 5 \times 10^{-14}$ $M_\odot$ yr^{-1} and $\dot{M} = 5 \times 10^{-12}$ $M_\odot$ yr^{-1}, corresponding to disk luminosities of $L_d = 8\,L_\odot$ and $L_d = 24\,L_\odot$, respectively. It is clear that such an increase by a factor of 100 in $\dot{M}$ cannot be understood from the simple CAK scaling, $\dot{M} \propto L^{1/\alpha}$. Instead, this strong dependence on L_d is a consequence of the optically thick-to-thin transition in the disk LDW when $Q\,\Gamma \sim 1$, as is also discussed by Proga (1999). Since PSD apply an exponential line-list cutoff (Owocki et al. 1988), the force multiplier $M(t)$ reaches a maximum in optically thin flow regions. This suppresses the mass-loss rate as compared with the case of a pure power-law force multiplier.

Even for a low-luminosity disk, PSD find that large $\dot{M}$ can be driven, namely when α is as large as 0.8. However, PSD assume the same value of $k = 0.2$ for *all* α. As is evident from Figure 4 of Gayley (1995), k drops by a factor of 10 when α is increased from 0.6 to 0.8, leading to a very similar $\dot{M}$ in both cases. This is a consequence of $Q\Gamma \sim 1$ for a disk wind (see eq. [12]). Contrary to this, for O-star winds, $Q\Gamma \gg 1$; hence, $\dot{M}$ depends strongly on α.

For a more luminous disk with $L_d = 24\,L_\odot$, we estimate $\dot{M} \simeq 4 \times 10^{-12}$ $M_\odot$ yr^{-1} from equation (12) when a value of D is used characteristic of the narrow wind base of PSD. The agreement with $\dot{M} = 5 \times 10^{-12}$ $M_\odot$ yr^{-1} as found by PSD is very good.

6.3. *The Mass-Loss Paradigm in Disk Winds from CVs*

Analysis of LDWs from O stars revealed $Q\Gamma$ to be the key parameter determining the mass-loss rate in the wind

(Gayley 1995). Namely, for $Q\Gamma < 1$, the wind ceases to exist. For O stars, $Q\Gamma > 100$, producing a kind of a "safety belt." The situation is different for winds from luminous CV disks, where $Q\Gamma \sim 1$, if the O-star value for Q is used (this work and PSD).

Taken at face value, the modified CAK theory of LDWs from CV disks predicts therefore surprisingly low mass-loss rates if $Q = 2000$. The calculated rates of $\dot{M} \sim 10^{-12}\ M_{\odot}$ yr^{-1} for $L_d = 10\ L_{\odot}$, or even lower, when the saturation of the force multiplier is accounted for, imply that LDWs will have a thick-to-thin transition in the strongest driving lines and will have difficulties in reproducing the observed line profiles. What are the possible solutions to this problem?

First, higher values of Q are the most obvious way to increase $\dot{M}$ in the wind. The value of Q is rather uncertain. It is especially unclear how the different spectral shape of the disk radiation field and its effect on the non-LTE occupation numbers will modify Q as compared with its O-star value. Such calculations have never been attempted and are clearly beyond the scope of this paper. Theoretically, the value of Q can be significantly larger than that for the O stars.

Second, a situation could arise in disk winds where the wind is driven by photons from a part of the disk that is UV bright, while the ionization is controlled by the central disk region, e.g., the boundary layer, which is X-ray bright. This, again, will be especially pronounced in the presence of a Lyman-continuum cutoff in the UV source. Under these circumstances, given the wind overionization, the line force will be reduced below its CAK value (MacGregor, Hartmann, & Raymond 1979; Fransson & Fabian 1980) and, hence, the velocity gradient will be small as well. A shallow velocity law will increase the overall optical depth in the wind and push the thick-to-thin transition downstream, away from the critical point. It is important in this context that the observed small changes in the P Cygni line profiles in eclipsing nova-like CVs *require* very shallow velocity profiles in the wind (Shlosman, Vitello, & Mauche 1996).

Additional factors can affect the mass-loss rates to a lesser degree. (1) Allowing for streamlines to bend will result in a better alignment with the radiative flux vector, which should increase the mass loss. (2) Pauldrach & Puls (1990) find a sudden increase in stellar mass-loss rates of B supergiants when the Lyman continuum becomes optically thick at the wind base, e.g., when the effective temperature drops below a certain threshold or if Γ reaches some critical value. This induces a shift to lower wind ionization, which, in turn, increases the mass loss (more driving lines), increases the Lyman jump even more, and so on, until a stable situation with high $\dot{M}$ and low wind ionization is reached. (3) Furthermore, Q depends linearly on the wind metallicity, and enhanced metal abundances could lead to a larger $Q\ \Gamma$, which governs the mass loss. This is particularly significant to the He abundance because of the efficient convection in the low-mass secondary stars but may be relevant to metals as well.

7. SUMMARY

The focus of this second paper on line-driven winds from accretion disks in cataclysmic variables is on theoretical estimates of mass-loss rates and wind velocity laws. Our results are as follows.

The mass-loss rates derived from applying the modified CAK formalism appear to be substantially smaller than those inferred from P Cygni line fits, even with a suppressed Lyman continuum, and are more so when the saturation effect in the line-force multiplier is included. Yet these rates are in good agreement with results from time-dependent, two-dimensional dynamical wind simulations by PSD. The reason for low mass-loss rates is that the key parameter controlling LDWs, $Q\Gamma \sim 100$ for O-star winds, is only ~ 1 for disk winds when O-star values for Q are used. Some potential resolutions to this problem were proposed.

We find that the mass loss is dominated by the inner decade in disk radii. For Shakura & Sunyaev and Newtonian disks, the mass loss per unit radius is roughly uniform out to five white dwarf radii and drops $\propto r_0^{-1.9}$ and $r_0^{-0.8}$ at larger r_0, respectively. Because of their low mass-loss rates, CV disk winds should experience a thick-to-thin transition even in the strongest driving lines. These winds should, therefore, resemble more closely winds of B stars near the main sequence than that of O supergiants.

The wind velocity profiles show a slowly accelerating flow, with a characteristic acceleration length given by the footpoint radius of the streamline in the disk. Fitting the observed line profiles using kinematical models suggests even slower accelerating winds. The observable terminal velocity of the wind is associated with the thick-to-thin transition in the driving lines. Given this latter fact, and given uncertainties in the ionization stratification and in the anticipated streamline bending at large radii, the actual wind terminal velocity is poorly constrained in our model.

We are grateful to Jon Bjorkman, Rolf Kudritzki, Chris Mauche, Norman Murray, Stan Owocki, and Joachim Puls for numerous discussions on various aspects of line-driven winds. I. S. acknowledges hospitality of the IGPP/LLNL, where this work was initiated, and of its director, Charles Alcock. This work was supported in part by NASA grants NAG 5-3841 and WKU-522762-98-06, and HST G0-06546.02-95A and AR-07982.01-96A (I. S.), and was performed under the auspices of the US Department of Energy by LLNL user contract number W-7405-ENG-48 (P. V.).

APPENDIX

DISK EDDINGTON FACTORS REQUIRED FOR LINE-DRIVEN WINDS

Using the eigenvalues $E_{\rm cr}$ from Paper I, one can further quantify the disk Eddington factors required to launch a line-driven wind that is optically thick at least up to the critical point. Consider first a vertical wind above an infinite, isothermal disk. The Euler equation (5) becomes, for $\tilde{F}_x = 1$ (the flux component along $\hat{x}$, normalized to the footpoint flux),

$$W' = -g + \Gamma(r_0)M(t_x)\ . \qquad \text{(A1)}$$

From equation (18) in Paper I, at the critical point,

$$\Gamma(r_0) = \frac{2/3\sqrt{3}}{(1-\alpha)M_{\rm cr}(t)} . \tag{A2}$$

Since the maximum of $M(t)$ for a gas of solar composition is ~ 2000 (Abbott 1982), one has that $\Gamma(r_0) \gtrsim 4 \times 10^{-4}$ for all r_0. Next, for the more realistic case of a tilted wind above a disk with radial temperature stratification, the simplified Euler equation (5) reads

$$W' = -g + \Gamma(r_0)\,\tilde{F}_x\,M(t_x) . \tag{A3}$$

Using $W'_{\rm cr} = (\alpha/1-\alpha)g_{\rm cr}$ and assuming $g_{\rm cr} \simeq X_{\rm cr}$ for critical points close to the disk,

$$\Gamma(r_0) = \frac{X_c}{(1-\alpha)\tilde{F}_x(r_0, X_{\rm cr})M_{\rm cr}(t)} . \tag{A4}$$

According to Figure 5 in Paper I, $\tilde{F} < 4$; hence, $\Gamma(r_0) \gtrsim 10^{-4}$ is required for the wind to be optically thick at the critical point.

REFERENCES

Abbott, D. C. 1982, ApJ, 259, 282
Abramowitz, M., & Stegun, I. A., ed. 1965, Handbook of Mathematical Functions (New York: Dover)
Cassinelli, J. P. 1994, Ap&SS, 221, 277
Cassinelli, J. P., Cohen, D. H., MacFarlane, J. J., Sanders, W. T., & Welsh, B. Y. 1994, ApJ, 421, 705
Castor, J. I., Abbott, D. C., & Klein, R. I. 1975, ApJ, 195, 157 (CAK)
Feldmeier, A., & Shlosman, I. 1999, ApJ, 526, 344 (Paper I)
Fransson, C., & Fabian, A. C. 1980, A&A, 87, 102
Gayley, K. G. 1995, ApJ, 454, 410
Hoare, M. G., & Drew, J. E. 1993, MNRAS, 260, 647
Knigge, C., Long, K. S., Blair, W. P., & Wade, R. A. 1997, ApJ, 476, 291
Knigge, C., Woods, J. A., & Drew, J. E. 1995, MNRAS, 273, 225
Kudritzki, R. P., Springmann, U., Puls, J., Pauldrach, A., & Lennon, M. 1998, in ASP Conf. Ser. 131, Boulder-Munich II: Properties of Hot, Luminous Stars, ed. I. Howarth (San Francisco: ASP), 278
Long, K. S., et al. 1991, ApJ, 381, L25
Long, K. S., Wade, R. A., Blair, W. P., Davidsen, A. F., & Hubeny, I. 1994, ApJ, 426, 704
MacGregor, K. B., Hartmann, L., & Raymond, J. C. 1979, ApJ, 231, 514
Mauche, C. W., & Raymond, J. C. 1987, ApJ, 323, 690
Murray, N., & Chiang, J. 1996, Nature, 382, 789
Owocki, S. P., Castor, J. I., & Rybicki, G. B. 1988, ApJ, 335, 914
Pauldrach, A., & Puls, J. 1990, A&A, 237, 409
Pauldrach, A., Kudritzki, R. P., Puls, J., Butler, K., & Hunsinger, J. 1994, A&A, 283, 525
Polidan, R. S., Mauche, C. W., & Wade, R. A. 1990, ApJ, 356, 211
Prinja, R. K., & Rosen, S. R. 1995, MNRAS, 273, 461
Proga, D. 1999, MNRAS, 304, 938
Proga, D., Stone, J. M., & Drew, J. E. 1998, MNRAS, 295, 595 (PSD)
Puls, J. 1987, A&A, 184, 227
Puls, J., Springmann, U., & Lennon, M. 1999, in preparation
Puls, J., Springmann, U., & Owocki, S. P. 1998, in Cyclical Variability in Stellar Winds, ed. L. Kaper & A. W. Fullerton (Berlin: Springer), 389
Shakura, N. I., & Sunyaev, R. A. 1973, A&A, 24, 337 (SHS)
Shlosman, I., & Vitello, P. 1993, ApJ, 409, 372
Shlosman, I., Vitello, P., & Mauche, C. W. 1996, ApJ, 461, 377
van Teeseling, A., Verbunt, F., & Heise, J. 1993, A&A, 270, 159
Vitello, P., & Shlosman, I. 1988, ApJ, 327, 680
———. 1993, ApJ, 410, 815

THE ASTROPHYSICAL JOURNAL, 532:L125–L128, 2000 April 1

RUNAWAY OF LINE-DRIVEN WINDS TOWARD CRITICAL AND OVERLOADED SOLUTIONS

ACHIM FELDMEIER
Imperial College of Science, Prince Consort Road, London SW7 2BZ, England, UK; a.feldmeier@ic.ac.uk
AND
ISAAC SHLOSMAN
University of Kentucky, Department of Physics and Astronomy, Lexington, KY 40506-0055; shlosman@pa.uky.edu
Received 1999 October 28; accepted 2000 February 15; published 2000 March 9

ABSTRACT

Line-driven winds from hot stars and accretion disks are thought to follow a unique, critical solution that corresponds to a maximum mass-loss rate and a particular velocity law. We show that in the presence of negative velocity gradients, radiative-acoustic (Abbott) waves can drive shallow wind solutions toward larger velocities and mass-loss rates. Perturbations that are introduced downstream from the critical point of the wind lead to a convergence toward the critical solution. By contrast, low-lying perturbations cause evolution toward a mass-overloaded solution, developing a broad deceleration region in the wind. Such a wind differs fundamentally from the critical solution. For sufficiently deep-seated perturbations, overloaded solutions become time-dependent and develop shocks and shells.

Subject headings: accretion, accretion disks — galaxies: active — hydrodynamics — novae, cataclysmic variables — stars: mass loss — stars: winds, outflows

1. INTRODUCTION

Atmospheres of hot luminous stars and accretion disks in active galactic nuclei and in cataclysmic variables form extensive outflows because of the super-Eddington radiation fluxes in UV resonance and subordinate lines. An understanding of these winds is hampered by the pathological dependence of the driving force on the flow velocity gradient. Castor, Abbott, & Klein (1975, hereafter CAK) found that line-driven winds (LDWs) from O stars should follow a unique, critical state that corresponds to a maximum mass-loss rate. The equation of motion for a one-dimensional, spherically symmetric, polytropic outflow that is subject to a Sobolev line force allows for two infinite families of so-called shallow and steep solutions. However, none of these families can provide for a *global* solution alone. Shallow solutions do not reach infinity, while steep solutions do not extend into the subsonic regime, including the photosphere. The critical wind starts then as the fastest shallow solution and switches at the critical point in a continuous and differentiable manner to the slowest steep solution. Hence, the critical point and not the sonic point determines the bottleneck in the wind. This description, in principle, applies equally to winds from stars and accretion disks.

A physical interpretation of the CAK critical point was given by Abbott (1980), who derived a new type of radiative-acoustic wave (hereafter Abbott waves). These waves can propagate inward, in the stellar rest frame, only from below the CAK critical point. Above the critical point, they are advected outward. Hence, the CAK critical point serves as an information barrier, much like the sonic or Alfvén points in thermal and hydromagnetic winds. Abbott's analysis was challenged by Owocki & Rybicki (1986), who found that for a pure absorption LDW, the signal speed is the sound speed and not the much faster Abbott speed. As noted already by these authors, this should be the consequence of assuming pure line absorption, which does not allow for any radiatively modified, inward-wave mode. Meanwhile, there is ample evidence for Abbott waves in time-dependent wind simulations (Owocki & Puls 1999).

Shallow solutions fail to reach infinity because they cannot perform the required spherical expansion work, implying that the flow starts to decelerate. Since this usually occurs very far out in the wind, the local wind speed is much larger than the local escape speed, and the wind escapes to infinity. Thus, a simple generalization of the CAK model, allowing for flow deceleration, renders shallow solutions globally admissible. This raises a fundamental question of why the wind would adopt the critical solution at all, and attain the critical mass-loss rate and velocity law, as proposed by CAK.

In this Letter, we analyze the physical mechanism that drives shallow solutions toward the critical solution, and we discuss under what conditions this evolution does not terminate at the CAK solution but continues into the realm of overloaded solutions. We find that, so far, simulations were affected by the numerical runaway toward the critical solution, by not accounting for Abbott waves in the Courant time step.

2. ABBOTT WAVES

Abbott waves are readily derived by bringing the wind equations into characteristic form. We consider a one-dimensional planar wind of velocity $v(z, t)$ and density $\rho(z, t)$, assuming zero sound speed. The continuity and Euler equations are, respectively, as follows:

$$\frac{\partial \rho}{\partial t} + v \frac{\partial \rho}{\partial z} + \rho \frac{\partial v}{\partial z} = 0, \qquad (1)$$

$$E \equiv \frac{\partial v}{\partial t} + v \frac{\partial v}{\partial z} + g(z) - CF(z) \left(\frac{\partial v/\partial z}{\rho} \right)^{\alpha} = 0. \qquad (2)$$

Here $g(z)$ and $F(z)$ are the gravity and the radiative flux, respectively. The CAK line force is given by $g_{\mathrm{l}} \equiv CF(z)(v'/\rho)^{\alpha}$ (with $v' \equiv \partial v/\partial z$), with constant C and exponent $0 < \alpha < 1$. The unique stationary CAK wind, $v_{\mathrm{cr}}(z)$, $\rho_{\mathrm{cr}}(z)$, is found by requiring a critical point at some z_{cr}. The number of solutions for $vv'(z)$ changes from 2 to 1 at z_{cr} (which is a saddle point); hence, $\partial E/\partial(vv')_{\mathrm{cr}} = 0$ holds. Writing C in terms of critical point quantities, the Euler equation becomes

$$\frac{\partial v}{\partial t} + v\frac{\partial v}{\partial z} + g(z) - \alpha^{-\alpha}(1-\alpha)^{-(1-\alpha)}\frac{F(z)}{F(z_{\rm cr})} \times g(z_{\rm cr})^{1-\alpha}(\rho_{\rm cr}v_{\rm cr})^{\alpha}\left(\frac{\partial v/\partial z}{\rho}\right)^{\alpha} = 0. \qquad (3)$$

Note that for stationary planar winds, ρv is constant. If, in addition, g and F are taken to be constant with height and if $\rho_{\rm cr}v_{\rm cr}v'/\rho$ is replaced by $vv'/\dot{m}$, with a normalized mass-loss rate $\dot{m} \equiv \rho v/\rho_{\rm cr}v_{\rm cr}$, one finds that E no longer depends explicitly on z for stationary solutions. Hence, vv' is independent of z, too. This implies that $z_{\rm cr}$ is ill-defined and that every point of the CAK solution is a critical point. CAK removed this degeneracy by introducing gas pressure terms. Here we take a different approach and assume $g = z/(1+z^2)$. A situation with roughly constant radiative flux and gravity showing a maximum at finite height could be encountered above isothermal disks around compact objects (see Feldmeier & Shlosman 1999). The critical point is determined by the regularity condition, $dE/dz_{\rm cr} = 0$; hence, $z_{\rm cr} = 1$, and the critical point coincides with the gravity maximum. For simplicity, we also choose $\alpha = \frac{1}{2}$ from now on, which is reasonably close to realistic values of $\alpha \leq \frac{2}{3}$ (Puls, Springmann, & Lennon 2000). None of our results should depend qualitatively on the assumptions made so far. The Euler equation is

$$\frac{\partial v}{\partial t} + v\frac{\partial v}{\partial z} + g(z) - 2\sqrt{g_{\rm cr}\rho_{\rm cr}v_{\rm cr}}\sqrt{\frac{\partial v/\partial z}{\rho}} = 0, \qquad (4)$$

where $g_{\rm cr} \equiv g(z_{\rm cr})$. The stationary solutions for wind acceleration are given by

$$vv'(z) = \frac{g_{\rm cr}}{\dot{m}}\left[1 \pm \sqrt{1 - \frac{\dot{m}g(z)}{g_{\rm cr}}}\right]^2, \qquad (5)$$

where the plus and minus signs refer to steep and shallow solutions, respectively. For $\dot{m} \leq 1$, shallow and steep solutions are globally (i.e., everywhere) defined. For $\dot{m} > 1$, solutions are called *overloaded*, and they become imaginary in the neighborhood of the gravity maximum. These winds carry mass-loss rates that are too large, and they eventually stagnate.

Next we put the Euler equation into quasi-linear form, which does *not* mean that we linearize it. Differentiating E with respect to z (Courant & Hilbert 1962; Abbott 1980) and introducing $f \equiv \partial v/\partial z$, equations (1) and (4) become, respectively,

$$\left(\frac{\partial}{\partial t} + v\frac{\partial}{\partial z}\right)\rho + \rho f = 0, \qquad (6)$$

$$\left[\frac{\partial}{\partial t} + (v + v_{\rm A})\frac{\partial}{\partial z}\right]\frac{f}{\rho} + \frac{1}{\rho}\frac{\partial g}{\partial z} = 0, \qquad (7)$$

with the inward Abbott speed in the rest frame, $v_{\rm A} \equiv -(g_{\rm cr}v/\dot{m}v')^{1/2}$. In the WKB approximation, individual spatial and temporal variations are much larger than the inhomogeneous term g'/ρ in equation (7), and so the term can be neglected. Consequently, v'/ρ is a Riemann invariant propagating at characteristic speed $v + v_{\rm A}$. Perturbations of v'/ρ correspond to the amplitude of a wave propagating at phase speed $v + v_{\rm A}$. Note that v'/ρ is proportional to the Sobolev line optical depth, indicating that this wave is a true radiative mode.

The second characteristic is determined by the continuity equation (6). In the advection operator in parentheses, v has to be read as $v + 0$ in the zero sound speed limit. This outward-propagating invariant corresponds to a sound wave, with amplitude ρ scaling with gas pressure.

At the critical point, $\dot{m} = 1$ and $vv'(z_{\rm cr}) = g(z_{\rm cr})$ after equation (5); hence, $v_{\rm A,\,cr} = -v_{\rm cr}$ [where we introduced $v_{\rm A,\,cr} \equiv v_{\rm A}(z_{\rm cr})$]. Abbott waves stagnate at the critical point, analogous to the sound waves at the sonic point. For shallow solutions, $\dot{m} < 1$ and $vv' < v_{\rm cr}v'_{\rm cr}$ from equation (5); hence, $v + v_{\rm A} < 0$. Shallow LDW solutions are therefore the subcritical analog to solar wind breezes.

Because, in the rest frame, the inward Abbott mode can propagate at larger absolute speeds than the outward sound mode, Abbott waves can determine the Courant time step in time-explicit hydrodynamic simulations. Violating the Courant step results in numerical instability. Despite this fact, Abbott waves along shallow solutions were never considered in the literature.

3. WIND CONVERGENCE TOWARD THE CRITICAL SOLUTION

We turn our attention to the physical mechanism that can drive LDWs away from shallow solutions and toward the critical one. Starting from an arbitrary shallow solution as the initial condition, we explicitly introduce perturbations at some fixed location in the wind and study their evolution. In order to keep *unperturbed* shallow solutions stable in numerical simulations, we fix one outer boundary condition, according to inward-propagating Abbott waves. A constant mass-loss rate at either the outer boundary condition or the nonreflecting boundary condition (Hedstrom 1979) serves this aim. At the inner, subcritical boundary, we also fix one boundary condition, according to incoming sound waves. Nonreflecting boundary conditions and $\rho = \text{const}$ give similar results.

Wind convergence toward the critical solution is then triggered by negative flow velocity gradients. Allowing for $v' < 0$ turns the inward Abbott mode of phase speed $v + v_{\rm A} < 0$ in the rest frame into an outward-propagating mode. This is readily seen for a line force that is zero for negative v', i.e., when all photons are absorbed at a resonance location between the photosphere and the wind point. The Euler equation is simplified to that for an ordinary gas, with characteristic speed $v - 0 > 0$ in the zero sound speed limit. At the other extreme, for a purely local line force in which the unattenuated stellar or disk radiation field reaches the wind point, $g_1 \propto (|v'|)^{1/2}$. Here the Abbott phase speed is found to be $v + v_{\rm A}$, with $v_{\rm A} = +(-g_{\rm cr}v/\dot{m}v')^{1/2}$ for $v' < 0$.

Consider then a sawtooth-like velocity perturbation (a sinusoidal perturbation leads to similar results). Slopes $v' > 0$ propagate inward, and slopes $v' < 0$ propagate outward. Hence, as a kinematical consequence, a sawtooth that is initially symmetric with respect to the underlying stationary velocity law evolves toward larger velocities. This is demonstrated in Figure 1, where, in the course of time, a periodic sawtooth perturbation is introduced at $z = 2$. The line force is assumed to be proportional to $(|v'|)^{1/2}$, and the initial shallow solution has $\dot{m} = 0.8$. The figure shows $2\frac{1}{2}$ perturbation cycles. For upward-pointing kinks, the slopes propagate apart, and a flat velocity law develops between them. At each time step dt, a new increment $dv = 4\,dt\,\delta v/T$ (δv and T being the amplitude and period of the sawtooth, respectively) is added at $z = 2$; hence, the flattening velocity law does not show up in region A of Figure 1. Overall, the wind speed at the perturbation site

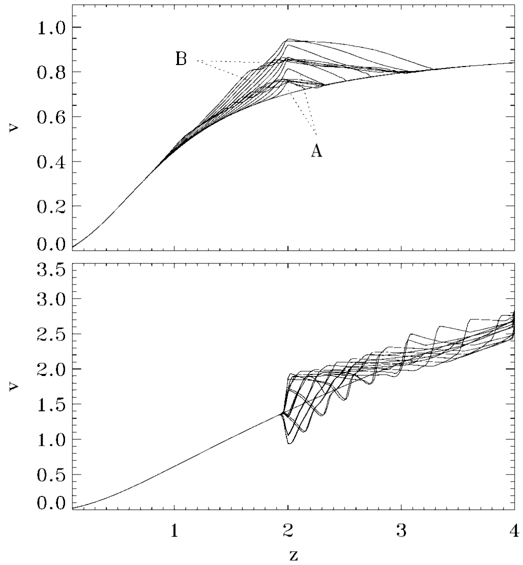

FIG. 1.—*Top*: Evolution of a shallow wind during $2\frac{1}{2}$ periods of a sawtooth perturbation of amplitude, with 10% being introduced at $z = 2$. Regions "A" and "B" correspond to phases in which upward- and downward-pointing kinks, respectively, are introduced into the flow. *Bottom*: Stable Abbott wave excitation in the critical wind, at 35% perturbation amplitude.

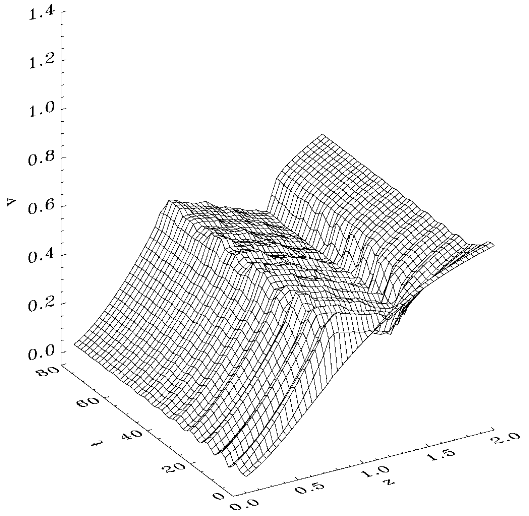

FIG. 2.—Wind evolution toward a stationary, overloaded solution showing an extended decelerating region. A periodic sawtooth perturbation is introduced into a shallow solution at $z = 0.8$, upstream from the critical point at $z_{\rm cr} = 1$.

evolves toward larger values during these phases. On the other hand, for downward-pointing kinks of the sawtooth, $-\delta v$, the two approaching slopes merge, and the wind speed evolves back toward its unperturbed value after each decrement $-dv = -4\,dt\,\delta v/T$. The wind velocity hardly evolves during these phases (see region B of Fig. 1). Over a full perturbation cycle, the wind speed clearly increases.

Essentially, any perturbation that introduces negative v' will accelerate the wind. The amplitude of the perturbation is rather irrelevant since, with decreasing perturbation wavelength, negative v' occur at ever smaller amplitudes. However, in more realistic winds, dissipative effects may smear out short-scale perturbations before they can grow. Details of the physical mechanism will be discussed elsewhere.

If the perturbation lies downstream from the critical point, the wind converges toward the critical solution. Namely, as soon as the perturbation site comes to lie on the supercritical part of the CAK solution during its evolution, positive velocity slopes propagate *outward* and combine with negative slopes to a full wave train. No information is propagated upstream. This unconditional stability of the outer CAK solution is shown in the bottom panel of Figure 1.

4. WIND CONVERGENCE TOWARD OVERLOADED SOLUTIONS

Wind runaway toward larger speeds, as caused by perturbations introduced *upstream* from the critical point, does not terminate at the critical CAK solution. For low-lying perturbations, communication with the wind base is still possible once the subcritical branch of the CAK solution is reached. The wind gets further accelerated into the domain of mass-overloaded solutions (where $vv' > v_{\rm cr}v'_{\rm cr}$, and hence $v > v_{\rm cr}$ for $z < z_{\rm cr}$ according to eq. [5]) until a generalized critical point develops, which prevents the inward propagation of Abbott waves and the adjustment of the mass-loss rate. Such generalized critical points are given by "termination" points z_t of overloaded solutions, where the velocity becomes imaginary. At z_t, the number of real solutions $vv'(r)$ changes from 2 (shallow and steep) to 0. Hence, termination points are defined by the same condition as the CAK critical point (at which the number of solutions changes from 2 via 1 to 2), $\partial E/\partial(vv')_t = 0$. From the stationary version of equation (4), $v_{\mathrm{A},t} = -v_t$; hence, Abbott waves stagnate at termination points, and the latter become generalized critical points.

The fact that perturbations with negative v' accelerate the wind to either a critical or an overloaded state can be cast into the black hole conjecture (Penrose 1965): an LDW avoids a "naked" base by enclosing it with a critical surface.

Since to each z_t there corresponds a unique, supercritical mass-loss rate, the latter is determined by the perturbation *location* alone. Using $v_{\mathrm{A},t} = -v_t$, one finds $\dot{m}_t = g_{\rm cr}/g_t > 1$ for a planar wind with constant radiative flux.

At a termination point, vv' jumps to the decelerating branch, $vv' < 0$. Beyond a well-defined location above the gravity maximum, the super-CAK mass-loss rate can again be lifted by the line force, and vv' jumps back to the accelerating branch. Hence, two stationary kinks occur in the velocity law. Figure 2 shows a hydrodynamic simulation of the evolution toward an overloaded solution. Sawtooth-type velocity perturbations were introduced at $z = 0.8$. Correspondingly, $\dot{m} = 1.025$ for the overloaded solution, using $g = z/(1 + z^2)$.

Future work has to clarify whether or not LDWs show deep-seated perturbations. It seems unlikely, however, that they would occur at a unique location. Hence, overloaded winds should be nonstationary and should show a *range* of supercritical mass-loss rates.

More fundamentally, time-dependent overloaded solutions occur already for single, unique perturbation sites once these sites lie below a certain height. For the present wind model, this is at $z \approx 0.66$. The overloading is then so severe and the decelerating region so broad that negative wind speeds result (see Poe, Owocki, & Castor 1990). The corresponding mass-loss rates are still only a few percent larger than the CAK value. The gas that falls back toward the photosphere collides with the outflowing gas, and a time-dependent situation develops. Within each perturbation period, a shock forms in the velocity law, supplemented by a dense shell. These shocks and shells propagate outward (A. Feldmeier & I. Shlosman 2000, in preparation).

Although strong perturbations introducing negative velocity gradients can appear already in O star winds, accretion disk winds are the prime suspects. The reasons for this are that accretion processes and their radiation fields in cataclysmic variables and galactic nuclei are intrinsically variable on a range of timescales (Frank, King, & Raine 1992) and that disk LDWs are driven by a combination of uncorrelated, local, and central radiation fluxes.

5. SUMMARY

We find that shallow solutions to line-driven winds are subcritical with respect to Abbott waves (sub-Abbottic). These waves cause shallow solutions to evolve toward larger speeds and mass-loss rates because of the asymmetry of the line force with regard to positive and negative velocity gradients and because perturbations with opposite signs of dv/dz propagate in opposite directions. Steep velocity slopes propagate toward the wind base, steepen the inner wind, and lift it to higher mass-loss rates. In the presence of enduring wind perturbations, this proceeds until a critical point forms and Abbott waves can no longer penetrate inward.

The resulting solution does not necessarily correspond to the CAK wind. For perturbations that originate below the critical point, the developing Abbott wave barrier is found to be the termination point of a mass-overloaded solution. The velocity law acquires a kink at the termination point, where the wind starts to decelerate. Whether the wind converges to a critical or an overloaded solution depends entirely on the *location* of perturbations and not, e.g., on the boundary conditions at the wind base.

If Abbott waves are not accounted for in the Courant time step of hydrodynamic simulations, we find that *numerical* runaway can drive the solution toward the critical CAK wind. A detailed discussion of this will be given elsewhere.

Future work has to clarify whether and where the perturbations causing the local flow deceleration, $dv/dz < 0$, can occur in LDWs. Overloaded winds may be detected observationally. While their mass-loss rates should still be close to CAK values, broad regions of decelerating flow could be identified in P Cygni line profiles. Furthermore, besides the shocks from the line-driven instability (Lucy 1982; Owocki, Castor, & Rybicki 1988), the shocks occurring in overloaded solutions with infalling gas may contribute to the X-ray emission from LDWs. Note that the present wind runaway occurs already in the lowest order Sobolev approximation and is therefore unrelated to the line-driven instability that depends on velocity curvature terms (Feldmeier 1998).

We thank R. Buchler, J. Drew, R. Kudritzki, C. Norman, S. Owocki, and J. Puls for intense blackboard discussions and the referee, Stan Owocki, for suggestions that improved the manuscript. This work was supported in part by PPA/G/S/1997/00285, NAG5-3841, WKU-522762-98-6, and HST GO-08123.01-97A.

REFERENCES

Abbott, D. C. 1980, ApJ, 242, 1183
Castor, J. I., Abbott, D. C., & Klein, R. I. 1975, ApJ, 195, 157 (CAK)
Courant, R., & Hilbert, D. 1962, Methods of Mathematical Physics (New York: Interscience)
Feldmeier, A. 1998, A&A, 332, 245
Feldmeier, A., & Shlosman, I. 1999, ApJ, 526, 344
Frank, J., King, A., & Raine, D. 1992, Accretion Power in Astrophysics (Cambridge: Cambridge Univ. Press)
Hedstrom, G. W. 1979, J. Comput. Phys., 30, 222
Lucy, L. B. 1982, ApJ, 255, 286
Owocki, S. P., Castor, J. I., & Rybicki, G. B. 1988, ApJ, 335, 914
Owocki, S. P., & Puls, J. 1999, ApJ, 510, 355
Owocki, S. P., & Rybicki, G. B. 1986, ApJ, 309, 127
Penrose, R. 1965, Phys. Rev. Lett., 14, 57
Poe, C. H., Owocki, S. P., & Castor, J. I. 1990, ApJ, 358, 199
Puls, J., Springmann, U., & Lennon, M. 2000, A&AS, 141, 23

THE ASTROPHYSICAL JOURNAL, 564:385–394, 2002 January 1

ABBOTT WAVE–TRIGGERED RUNAWAY IN LINE-DRIVEN WINDS FROM STARS AND ACCRETION DISKS

ACHIM FELDMEIER
Astrophysik, Institut für Physik, Universität Potsdam, Am Neuen Palais 10, 14469 Potsdam, Germany; afeld@astro.physik.uni-potsdam.de
AND
ISAAC SHLOSMAN[1,2]
Joint Institute for Laboratory Astrophysics, University of Colorado, Box 440, Boulder, CO 80309-440; shlosman@pa.uky.edu
Received 2001 June 7; accepted 2001 September 4

ABSTRACT

Line-driven winds from stars and accretion disks are accelerated by scattering in numerous line transitions. The wind is believed to adopt a unique critical solution out of the infinite variety of shallow and steep solutions. We study the inherent dynamics of the transition toward the critical wind. A new runaway wind mechanism is analyzed in terms of radiative acoustic (Abbott) waves, which are responsible for shaping the wind velocity law and fixing the mass loss. Three different flow types result depending on the location of perturbations. First, if the shallow solution is perturbed sufficiently far downstream, a single critical point forms in the flow, which is a barrier for Abbott waves, and the solution tends to the critical one. Second, if the shallow solution is perturbed upstream from this critical point, mass overloading results, and the critical point is shifted inward. This wind exhibits a broad, stationary region of decelerating flow, and its velocity law has kinks. Third, for perturbations even further upstream, the overloaded wind becomes time-dependent and develops shocks and dense shells.

Subject headings: accretion, accretion disks — hydrodynamics — instabilities — stars: mass loss — waves

1. INTRODUCTION

Radiation-driven winds that are accelerated by absorption and reemission of continuum photons in spectral lines form an interesting class of hydrodynamic flows, termed line-driven winds (LDWs). They occur in OB and Wolf-Rayet stars and cataclysmic variables and probably in active galactic nuclei and luminous young stellar objects. These winds are characterized by a unique dependence of line force on the velocity gradient in the flow. This causes a new, radiative wave type.

The nature of these waves (hereafter Abbott waves) was first discussed by Abbott (1980), who found two modes, a slow, acoustic one propagating downstream and a fast, radiative one propagating upstream. The critical point found by Castor, Abbott, & Klein (1975, hereafter CAK) from analysis of the stationary Euler equation is a barrier for these waves, the same as the sonic point is to sound waves. The intriguing property of Abbott waves is that they propagate downstream slower than the sound speed, while they propagate upstream at very large speeds, highly supersonically. The latter fact reflects essentially the radiative nature of Abbott waves.

No such upstream-propagating radiative mode was found by Owocki & Rybicki (1986), who calculated the Green's function for winds driven by pure line absorption. The explanation is that the pure absorption case suppresses the radiative upstream mode since photons can propagate only downstream. The radiative upstream mode returns when line scattering is included (Owocki & Puls 1999).

The question arises for the physical interpretation of Abbott waves. Do they represent a physical entity that is responsible for shaping the flow by communicating essential flow properties between different points in the wind? In particular, could Abbott waves be the prime cause for evolution of LDWs toward a CAK-type, steady state solution?

The analysis by CAK of the steady state Euler equation for LDWs has revealed an infinite family of mathematical solutions but only one, hereafter the "critical solution," that extends from the photosphere to arbitrary large radii. Other solutions do not reach either infinity or the photosphere. The former solutions are called shallow and the latter ones, steep. The unique, critical wind starts as the fastest shallow solution and switches smoothly to the slowest steep solution at the critical point.

The shallow wind solutions found by CAK are the analog to solar wind breezes in that they are sub-Abbottic everywhere. They were abandoned by CAK because they cannot provide the required spherical expansion work at large radii. This exclusion of shallow solutions can be criticized in different respects: (1) The breakdown happens only around 300 stellar radii, where basic assumptions of the model (fluid description, spherical symmetry, isothermality) may become invalid. (2) Shallow solutions could be extended to infinity by jumping at some large radius to a decelerating wind branch. The latter was excluded a priori by CAK. However, this jump can occur beyond a few stellar radii, where the wind has already reached its local escape speed. (3) For models of disk LDW, even the critical solution itself does not extend to infinity and becomes imaginary beyond a certain radius (Feldmeier & Shlosman 1999). Jumps to the decelerating branch are unavoidable then.

With shallow solutions being valid stationary solutions, the following question arises: what forces the wind to adopt the critical CAK solution? Numerical aspects of this question have been discussed by Feldmeier, Shlosman, & Hamann (2001), who noted that outer boundary conditions and a Courant time step that do not account for Abbott

---

[1] JILA Visiting Fellow.

[2] Permanent address: Department of Physics and Astronomy, University of Kentucky, Lexington, KY 40506-0055.

waves can set off numerical runaway, often toward the critical solution.

In the present paper, we focus on a physical interpretation of Abbott waves, extending our previous work on this subject (Feldmeier & Shlosman 2000). We show that these waves are the prime driver of evolution of LDWs toward a unique, steady state solution characterized by a specific velocity law and mass-loss rate. In particular, we find that since this is the case for solar wind breezes, shallow solutions can evolve because of waves that propagate upstream to the wind base (the photosphere). As a new effect in LDWs, Abbott waves "drag" the solution in one preferred direction, toward larger velocities. The wind becomes stable when a critical point forms, through which outer perturbations can no longer penetrate inward.

2. ABBOTT WAVES

2.1. *Wind Model*

Only wind acceleration due to a line force in Sobolev approximation for radiative transfer is considered in this paper. The large number of lines driving the wind is dealt with using a CAK line distribution function. The latter is characterized by a power-law index α, which lies between 0 and 1. The Sobolev force is proportional to

$$g_l \sim \int d\omega\, \boldsymbol{n} \boldsymbol{I}_{\boldsymbol{n}} \tau_{\boldsymbol{n}}^{-\alpha} , \tag{1}$$

where $\boldsymbol{n}$ is the unit vector pointing in the direction of the surface angle element $d\omega$, I is the frequency-integrated specific intensity, and τ is the Sobolev optical depth,

$$\tau_{\boldsymbol{n}} = \frac{\kappa \rho v_{\rm th}}{\boldsymbol{n} \cdot [\boldsymbol{n} \cdot (\nabla \boldsymbol{v})]} , \tag{2}$$

with rate-of-strain tensor $\nabla \boldsymbol{v}$, mass absorption coefficient κ, and ion thermal speed $v_{\rm th}$. The force proportionality constant is fixed later in terms of the critical solution. Through $\nabla \boldsymbol{v}$, the line force depends on the streamline geometry. To simplify, we take τ in equation (1) out of the integral and replace it by an average or *equivalent* optical depth in one direction. Specifically, the latter is assumed to be the flow direction. This approach corresponds to the CAK "radial streaming approximation." For a planar flow with height coordinate z, the line force becomes, assuming constant κ and $v_{\rm th}$,

$$g_l \sim F(v'/\rho)^{\alpha} , \tag{3}$$

where $v' = \partial v/\partial z$ and the radiative flux F is a function of z. Even this highly idealized line force depends in a nonlinear way on the hydrodynamic variables v' and ρ.

So far, the following assumptions were introduced: (1) the line force is calculated in Sobolev approximation using (2) a CAK line distribution function (without line overlap) and (3) applying the radial streaming approximation for (4) planar flow. To these, we add the following further assumptions: (5) The flux F is constant with z, but gravity g may depend arbitrarily on z. This can serve to model winds from thin, isothermal accretion disks, in which case g grows first linearly with z and at large distances drops off as z^{-2}. Alternatively, with F *and* g being constants, one can model the launch region of a stellar wind, but a well-known degeneracy occurs here (Poe, Owocki, & Castor 1990). (6) Zero sound speed is assumed, $a = 0$, and (7) we fix $\alpha = \frac{1}{2}$. Note that the Sobolev line force is independent of $v_{\rm th}$ and therefore of a. LDWs are hypersonic, and except near the photosphere, gas pressure plays no role. The one-dimensional continuity and Euler equations are

$$\frac{\partial \rho}{\partial t} + v \frac{\partial \rho}{\partial z} + \rho \frac{\partial v}{\partial z} = 0 , \tag{4}$$

$$E \equiv \frac{\partial v}{\partial t} + v \frac{\partial v}{\partial z} + g(z) - C_0 F \sqrt{\frac{\partial v/\partial z}{\rho}} = 0 , \tag{5}$$

with constant C_0. We consider first stationary solutions, $\rho v = \text{const}$. A normalized quantity $m = \rho v/\rho_c v_c$ is introduced, where $\rho_c(z)$ and $v_c(z)$ are the density and velocity law of the critical wind, respectively, which is defined below. Besides m, a second, new hydrodynamic variable, $w' = vv'$, is defined, and the Euler equation becomes

$$w' + g(z) - C\sqrt{w'/m} = 0 . \tag{6}$$

The flux F was absorbed into the constant C. At each z, equation (6) is a quadratic equation in $\sqrt{w'}$, with solutions

$$\sqrt{w'} = \frac{1}{2\sqrt{m}} (C \pm \sqrt{C^2 - 4gm}) . \tag{7}$$

The velocity law $v(z)$ is obtained from w' by quadrature. Solutions for which the minus (plus) sign applies are termed *shallow* (*steep*). If $m < 1$ (see below), shallow and steep solutions exist from $z = 0$ to ∞. If $m > 1$, shallow and steep solutions become imaginary in a certain z interval. In this region, the line force $\sim C/\sqrt{m}$ cannot balance gravity g.

Within the family of shallow wind solutions, the mass flux ρv increases monotonically with terminal speed, while for steep solutions, the trend is opposite. The largest mass flux that keeps the solution everywhere real defines the critical wind $m_c = 1$. Setting the square root in equation (7) to 0 implies for C

$$C = 2\sqrt{g_c} , \tag{8}$$

where $g_c = g(z_c)$ means gravity at the critical point of the critical solution. How is z_c found? Differentiating the stationary Euler equation $E[z, w'(z)] = 0$ with respect to z and using $\partial E/\partial w'_c = 0$ at the critical point (crossing of solutions), one finds

$$0 = \frac{dE}{dz_c} = \frac{dg}{dz_c} . \tag{9}$$

Hence, the critical point coincides with the gravity maximum. This is not an accident but expresses that the critical point lies at the bottleneck of the flow, as for a Laval nozzle (Abbott 1980). If the flux F varies with z, the generalized area function depends also on F, and the critical point no longer coincides with the gravity maximum (see Feldmeier & Shlosman 1999 for examples). If $g = \text{const}$, the critical point degenerates, and every point in the flow becomes critical. In stellar wind calculations, the correct critical point location is found by including the finite cone correction factor for the stellar disk as an "area" function (Pauldrach, Puls, & Kudritzki 1986; Friend & Abbott 1986).

The wind solution becomes

$$w' = \frac{g_c}{m} \left(1 \pm \sqrt{1 - \frac{mg}{g_c}} \right)^2 . \tag{10}$$

At the critical point, shallow and steep solutions with $m = 1$ merge in such a way that the slope in passing from one to the other is continuous. Staying instead on either shallow or steep solutions introduces a discontinuity in $v''(z_c)$. Discontinuities in derivatives of hydrodynamic variables, termed weak discontinuities, lie on flow characteristics (Courant & Hilbert 1968). Characteristics are the space-time trajectories of wave phases. Indeed, we find below that the critical point is a barrier for Abbott waves.

It is at this point that the following question arises: which solution does the wind adopt—a shallow, steep, or critical one? This issue will be resolved by discussing *runaway* of shallow solutions. We shall find that Abbott waves are the prime driver of this evolution.

2.2. *Green's Function*

We derive the Green's function for Abbott waves in Sobolev approximation. The Green's function gives the response of a medium to a localized delta function perturbation in space and time and is complementary to the harmonic dispersion analysis of Abbott (1980) and Owocki & Rybicki (1984). Since localized perturbations contain many harmonics, a Green's function describes wave interference. This is clearly seen for surface water waves, whose Green's function is known from Fresnel diffraction in optics (Lamb 1932, p. 386). For simplicity, we consider only a single, optically thick line, with Sobolev force ($\alpha \equiv 1$),

$$g_1 = A\,\frac{\partial v}{\partial z}\,. \tag{11}$$

Density ρ was absorbed into the constant A. We assume WKB approximation to hold (slowly varying background flow) and consider velocity perturbations only. The characteristic analysis in the next section will show that the Abbott wave amplitude is v'/ρ; hence, Abbott waves are not annihilated by this restriction to velocity perturbations. The linearized Euler equation for small perturbations is

$$\frac{\partial}{\partial t}\,\delta v(z, t) = \delta g_1(z, t) = A\delta v'(z, t)\,. \tag{12}$$

The Green's function problem is posed by specifying as initial conditions

$$\delta v(z, 0) = \delta(z - z_0)\,. \tag{13}$$

Multiplying equation (12) by e^{-ikz} and integrating over z, we get

$$\frac{\partial}{\partial t}\,\overline{\delta v}(k, t) = ikA\overline{\delta v}(k, t)\,, \tag{14}$$

where a bar indicates Fourier transforms, $\overline{\delta v} = \int \delta v e^{-ikz}\,dz$. The right-hand side was obtained by integration by parts, assuming $\delta v(-\infty, t) = \delta v(\infty, t) = 0$. This is shown a posteriori. The solution of equation (14) is

$$\overline{\delta v}(k, t) = be^{ikAt}\,, \tag{15}$$

with constant b. Fourier transforming equation (13) from z to k space,

$$\overline{\delta v}(k, 0) = e^{-ikz_0} = b\,, \tag{16}$$

and

$$\overline{\delta v}(k, t) = e^{ik(At - z_0)}\,. \tag{17}$$

Fourier transforming back to z space, we get

$$\delta v(z, t) = \frac{1}{2\pi}\int_{-\infty}^{\infty} dk\, e^{ikz} e^{ik(At - z_0)} = \delta(z - z_0 + At)\,. \tag{18}$$

Therefore, the initial delta function propagates without dispersion toward smaller z at an Abbott speed $-A$. Furthermore, $\delta v = 0$ at $z = \pm\infty$, as assumed. Since no wave dispersion occurs, the same Abbott speed A is also obtained by considering *harmonic* perturbations. Inserting $\delta v = \overline{\delta v} e^{i(kz - \omega t)}$ in equation (12) gives as phase and group speed

$$\frac{\omega}{k} = \frac{d\omega}{dk} = -A\,. \tag{19}$$

The Green's function G is defined by (F an arbitrary function)

$$F(z, t) = \int_{-\infty}^{\infty} dz' G(z - z', t) F(z', 0)\,. \tag{20}$$

From equations (13) and (18),

$$G(z, t) = \delta(z + At)\,, \tag{21}$$

a result first obtained by Owocki & Rybicki (1986).

The present case of optically thick lines only corresponds to $\alpha = 1$. An explicit expression for the Abbott speed is not relevant then: opposed to all cases $\alpha < 1$, $\alpha = 1$ poses *no* eigenvalue problem for m. We return therefore to $\alpha = \frac{1}{2}$.

2.3. *Abbott Wave Characteristics*

Besides a harmonic and Green's function analysis, a characteristic analysis can be given for Abbott waves. The latter, especially, is not restricted to linear waves. Inserting C from equation (8), the equations of motion (eqs. [4] and [5]) become (dots indicate time derivatives)

$$\dot\rho + v\rho' + \rho v' = 0\,, \tag{22}$$

$$\dot v + vv' + g(z) - 2\Gamma\sqrt{\frac{v'}{\rho}} = 0\,, \tag{23}$$

where we introduced the constant

$$\Gamma = \sqrt{g_c \rho_c v_c}\,. \tag{24}$$

To bring these equations into characteristic form, we first write the continuity equation formally as $K(\rho, v) = 0$ and the Euler equation as $E(\rho, v) = 0$. For nonlinear, first-order systems of partial differential equations, $K = 0$ and $E = 0$, in two unknown variables ρ and v, the latter being functions of coordinates t and z, the characteristic directions or speeds a are determined by (Courant & Hilbert 1968, p. 304)

$$\begin{vmatrix} -aK_{\dot\rho} + K_{\rho'} & -aK_{\dot v} + K_{v'} \\ -aE_{\dot\rho} + E_{\rho'} & -aE_{\dot v} + E_{v'} \end{vmatrix} = 0\,, \tag{25}$$

where $K_{\rho'} = \partial K/\partial \rho'$, $E_{\dot v} = \partial E/\partial \dot v$, etc. We use the symbol a, hitherto reserved for the sound speed, also for characteristic speeds. The meaning should be clear from the context. Inserting K and E in equation (25), we get

$$\begin{vmatrix} -a + v & \rho \\ 0 & -a + v - \dfrac{\Gamma}{\sqrt{\rho v'}} \end{vmatrix} = 0\,; \tag{26}$$

hence,

$$a_+ = v, \quad a_- \equiv A = v - \frac{\Gamma}{\sqrt{\rho v'}}\,, \tag{27}$$

in the observers frame. The Abbott speed is again denoted A. In the comoving frame, $a_+ = 0$ and $a_- = -\Gamma/(\rho v')^{1/2}$. The downstream (positive) slow wave mode corresponds to sound waves. The upstream (negative) fast mode is of radiative origin.

A simple, heuristic argument can be given for the occurrence of Abbott waves. Consider a long-scale perturbation of a stationary velocity law. At the node where the velocity gradient gets steepened, the Sobolev line force increases. The gas is accelerated to larger speeds; hence, the node shifts inward. Similarly, the node where the velocity law becomes shallower shifts inward. The node shift corresponds to phase propagation of a harmonic wave.

Next, we bring the equations of motion into characteristic form. To this end, the Euler equation is quasi-linearized by differentiating it with respect to z (Courant & Hilbert 1968), introducing a new, fundamental variable $f = v'$,

$$\dot{f} + vf' + f^2 - \frac{\Gamma}{\sqrt{f\rho}}\left(f' - f\frac{\rho'}{\rho}\right) + g' = 0\,. \tag{28}$$

Rebracketing and multiplying with ρ,

$$\rho\dot{f} + \rho A f' + \rho f^2 + \frac{\Gamma}{\sqrt{f\rho}} f\rho' + \rho g' = 0\,. \tag{29}$$

Using the continuity equation,

$$\begin{aligned} 0 &= \rho\dot{f} + \rho A f' - f\dot{\rho} - \left(v - \frac{\Gamma}{\sqrt{f\rho}}\right) f\rho' + \rho g' \\ &= \rho\dot{f} + \rho A f' - f\dot{\rho} - A f\rho' + \rho g' \\ &= \rho^2(\partial_t + A\partial_z)\frac{f}{\rho} + \rho g'\,. \end{aligned} \tag{30}$$

The Euler equation in characteristic form is therefore

$$(\partial_t + A\partial_z)\frac{v'}{\rho} = -\frac{g'}{\rho}\,, \tag{31}$$

with A from equation (27). We assume that WKB approximation applies, i.e., that the temporal and spatial derivatives on the left-hand side are individually much larger than the right-hand side; hence, the latter can be neglected. In a frame moving at speed $-A$, the function v'/ρ is constant and can be interpreted as a wave amplitude. Note that v'/ρ is inversely proportional to the Sobolev line optical depth, indicating that Abbott waves are indeed a radiative mode.

Introducing f in the continuity equation puts it into characteristic form,

$$(\partial_t + v\partial_z)\rho = -f\rho\,. \tag{32}$$

Here, $f\rho$ is an inhomogeneous term. WKB approximation cannot be assumed here since f may vary on short scales. The wave amplitude ρ is no longer constant along v characteristics but changes according to this (ordinary) differential equation. Since gas pressure p scales with density, this equation shows that the outward mode corresponds to sound.

For *stationary* winds, the Abbott speed in the observers frame becomes ($\alpha = \frac{1}{2}$),

$$A = v\left(1 - \sqrt{\frac{g_c}{mw'}}\right) = v\left(1 - \frac{1}{\sqrt{mw'/w'_c}}\right) \tag{33}$$

since $w'_c = g_c$ from equations (7) and (8). With $A_c = 0$, the critical point is a stagnation point for Abbott waves. For shallow winds, $m < 1$ and $w'/w'_c < 1$; hence, $A < 0$ and Abbott waves propagate upstream from any z to the photosphere located at $z = 0$. Shallow solutions are, therefore, sub-Abbottic and are the analog to solar wind breezes. For steep solutions, $(mw'/w'_c)^{1/2} > 1$ from equation (10). Hence, $A > 0$, and steep solutions are super-Abbottic. Once the wind has adopted a steep solution, the flow can no longer communicate with the wind base: steep solutions cannot evolve by means of Abbott waves.

2.4. *Negative Velocity Gradients*

A surprising result occurs when we allow for *negative* velocity gradients, $v' < 0$, somewhere in the wind. This corresponds to flow deceleration, not necessarily to accretion instead of wind. The Sobolev force is blind to the sign of the velocity gradient. All that is important is the presence of a velocity gradient to Doppler-shift ions out of the absorption shadow of intervening ions. Hence, a natural generalization of the Sobolev line force is

$$g_1 = 2\Gamma\sqrt{\frac{|v'|}{\rho}}\,. \tag{34}$$

This holds for a purely local force. However, if $v' < 0$, the velocity law is nonmonotonic, and multiple resonance locations occur. Radiative transfer is no longer local since photons are absorbed and scattered at different locations. The incident flux is no longer determined by the photospheric flux F alone, but forward and backward scattering has to be accounted for. The constant C becomes frequency- and velocity-dependent. Rybicki & Hummer (1978) introduced a generalized Sobolev method for nonmonotonic velocity laws in which the radiation field is found by iteration. This introduces interesting, nonlocal effects into Abbott wave propagation (action at a distance). We postpone such an analysis to a future paper and proceed here in a simpler fashion. Together with $g_1 \sim |v'|^{1/2}$, the opposite extreme $g_1 \sim [\max(v', 0)]^{1/2}$ is treated. In the latter force, all radiation is assumed to be absorbed at the first resonance location, where necessarily $v' > 0$. The line force according to Rybicki & Hummer (1978) lies in between these two extremes.

Repeating the above steps for these generalized line forces, the Euler equation maintains its characteristic form,

$$(\partial_t + A\partial_z)\frac{v'}{\rho} = -\frac{g'}{\rho}\,,$$

with Abbott speed $A = v - \Gamma/(1/2\rho v')$ for $v' > 0$ and

$$A = \begin{cases} v + \dfrac{\Gamma}{\sqrt{-\rho v'}}\,, & \text{if } g_1 \sim \sqrt{|v'|}\,, \\ v\,, & \text{if } g_1 \sim \sqrt{\max(v', 0)} \end{cases} \tag{35}$$

for $v' < 0$. Therefore, if the velocity gradient is negative, Abbott waves propagate downstream, with a positive (or zero) comoving frame velocity along all solution types, whether shallow, steep, or critical. This is peculiar since

Abbott waves appeared so far as *upstream* mode. (Note that, for $g_1 \sim [\max(v', 0)]^{1/2}$, the line force drops out of the Euler equation if $v' < 0$. Both wave modes become ordinary sound then.) We conclude that regions with $v' < 0$ cannot communicate with the wind base.

3. ABBOTT WAVE RUNAWAY

3.1. *Method*

In the remainder of the paper, we study wave propagation in LDWs numerically using a standard time-explicit Eulerian grid code (van Leer advection on staggered grids). Nonreflecting Riemann boundary conditions for Abbott waves are used (Feldmeier et al. 2001). As an inner boundary, $z = 0.1$ is chosen to avoid negative speeds when Abbott waves leave the mesh at the wind base; numerical artifacts may result when the v characteristic changes its direction. For gravity, we assume $g = z/(1 + z^2)$, with a maximum at $z = 1$. Since g and z are normalized, so are v and t. Steep solutions are of no further interest here since they are super-Abbottic and, therefore, numerically stable. Furthermore, since they start supersonically at the wind base, they are unphysical. We are left with shallow winds, which can evolve toward the critical solution by means of Abbott waves. Shallow solutions are numerically unstable if pure outflow boundary conditions are used. The mechanism of this runaway is not easy to analyze because of numerical complications in the vicinity of the boundary, where the nature of the difference scheme changes.

To clearly separate effects of boundary conditions from wave dynamics, we introduce controlled, explicit perturbations in the *middle* of the calculational domain.

3.2. *Mechanism of the Runaway*

Figure 1 demonstrates the result derived above, that positive and negative velocity slopes propagate in opposite directions. The initial conditions are a shallow velocity law that is perturbed by a triangular wave train. The subsequent evolution of this wave train follows from the kinematics of the velocity slopes. In strictly mathematical terms, the plateaus that form in Figure 1 correspond to centered rarefaction waves. We postpone such an analysis to a forthcoming paper. The essential result from the figure is that the wind speed in the sawtooth evolves asymmetrically, toward larger values.

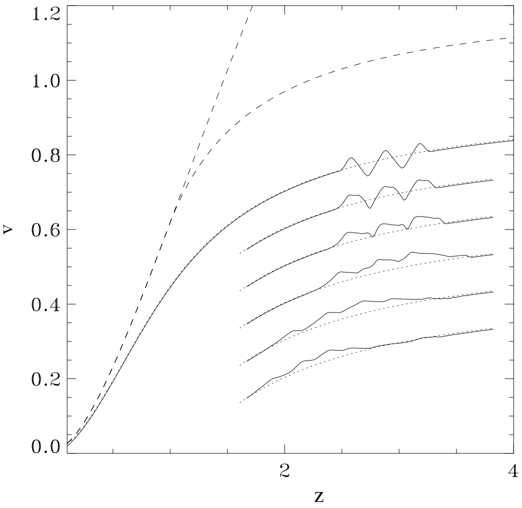

FIG. 1.—Evolution of a triangular wave train in a shallow wind (*dotted line*). For clarity, the velocity law is plotted with a negative, vertical offset that increases with time. The dashed lines show the shallow solution with $m = 1$ and the critical solution.

The whole sawtooth pattern moves upstream as an Abbott wave. This is of a prime importance for our understanding of the observed runaway.

Namely, if a perturbation is fed into the wind continuously over time, the whole inner wind is eventually lifted toward larger speeds and mass-loss rates. The same is true for the outer wind, first directly by the runaway and, second, as a consequence of the accelerated inner gas propagating outward.

We consider a *coherent* sinusoidal velocity perturbation of period P and maximum amplitude S, which is fed into the flow at a fixed location z. The fundamental hydrodynamic variables used in the code are ρ and ρv. After each time step δt, perturbations

$$\rho v \to \rho v + \rho \delta v, \qquad \rho \to \rho(1 - \delta v/|A|)\,, \tag{36}$$

with

$$\delta v = \delta t \, \frac{2\pi S}{P} \cos\left(\frac{2\pi t}{P}\right) \tag{37}$$

are applied to ρv and ρ on a single mesh point. The density fluctuations follow from the continuity equation $\delta\rho/\rho \approx -\delta v/|A|$. For linear waves, the observers frame Abbott speed is $A \approx -1.05$ at $z_e = 2$ for $m = 0.8$.

For sufficiently small amplitudes S, v' remains positive, and Abbott waves propagate in a stable fashion toward the wind base. This is shown in the left-hand panel of Figure 2 for $P = 1$ and $S = 0.04$. Doubling the perturbation amplitude to $S = 0.08$ implies wind runaway toward the critical solution, as is shown in the right-hand panel of Figure 2. The wind converges to $m = 1$ everywhere (not shown). Instead of adopting the critical, accelerating branch, the velocity law jumps at $z > z_e$ to the decelerating branch. This is even true for the converged, stationary solution as $t \to \infty$. (The velocity slope is so mildly negative for $t \to \infty$ that the wind speed is almost constant above $z_e = 2$.) We add some further remarks on this issue below.

The runaway results from the occurrence of negative velocity gradients. During excitation phases during which $v' < 0$, the resulting line force perturbations are *not sufficiently negative* to compensate for positive line force perturbations during phases where $v' > 0$. Net acceleration of the wind results over a full excitation cycle as a consequence.

Figure 3 shows again the runaway time series of Figure 2, with subsequent snapshots displaced vertically for clarity. During the negative perturbation half-cycle, $-\delta v(z_e)$, negative velocity slopes propagate outward from below z_e and merge with positive slopes propagating inward from above z_e. The merging slopes mutually annihilate. After a time $P/2$, the velocity law is left largely unaltered in presence of the perturbation. This causes the dense spacing of curves in Figure 2, especially at $z > z_e$, once every perturbation cycle. On this rather flat velocity law, a positive perturbation $+\delta v$ is added during the next half-cycle. Here, inner, positive slopes propagate inward and separate from outer, negative

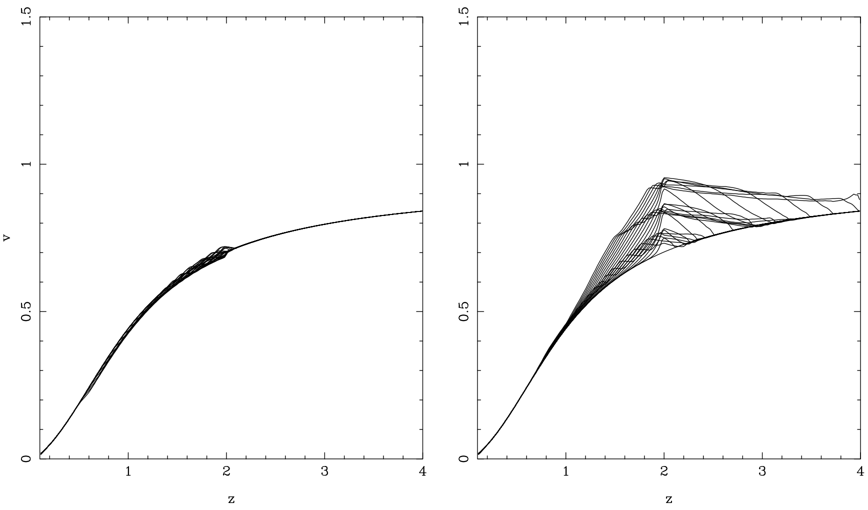

FIG. 2.—*Left:* Stable Abbott wave propagation along a shallow velocity law. A sinusoidal perturbation with amplitude $S = 0.04$ and period $P = 1$ is applied at $z_e = 2$. *Right:* Abbott wave runaway if the amplitude is doubled to $S = 0.08$.

slopes, which propagate outward. Obviously, runaway is caused by positive perturbations, but its deeper origin is that negative perturbations are self-annihilating and cannot balance positive ones.

The runaway terminates when z_e comes to lie on the critical solution and Abbott waves can no longer propagate inward.

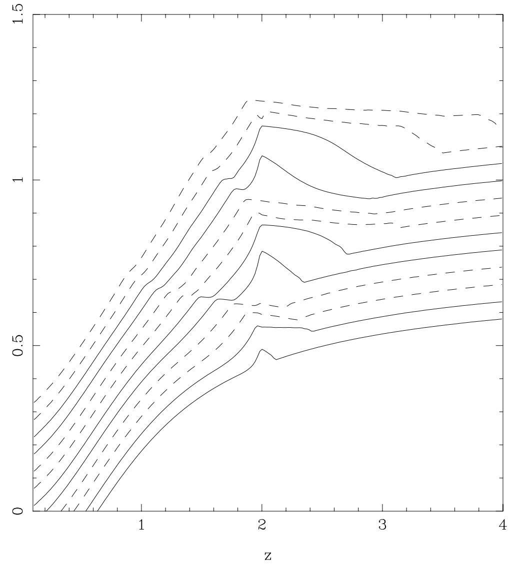

FIG. 3.—Runaway time series from Fig. 2, shown with a constant vertical displacement between snapshots. The dashed lines show phases where negative velocity perturbations are applied at z_e, leading to self-annihilating slopes.

The velocity gradient at $z > z_e$ is then still negative and in most of our simulations remains negative at all times: at z_e, the wind jumps to the decelerating branch with $m = 1$, which causes a kink in $v(z)$. Runaway perturbations above z_e would be required to establish a critical, accelerating velocity law in the outer wind. For certain combinations of model parameters, we find instead a critical solution with $v' > 0$ over the whole mesh. The near plateau above z_A evolves then toward larger speeds, and the velocity kink propagates outward, eventually leaving the mesh. We believe that this is an artifact caused by boundary-induced numerical runaway (Feldmeier & Shlosman 2000). The latter can even occur when nonreflecting Abbott boundary conditions are used, via *non-WKB* (standing?) waves; our Riemann boundary conditions were formulated to annihilate WKB waves only. We prefer the situation $v' < 0$ for $z > z_e$ over any numerical runaway that would assist the present, physical runaway in reaching the critical solution. A future analysis of outer boundary conditions has to clarify this issue of the outer wind velocity law.

We can still test the stability of the full, critical solution, as is done in Figure 4. Above the critical point, perturbation phases with $v' > 0$ and $v' < 0$ combine here and propagate outward as a smooth, marginally stable Abbott wave.

3.3. *Stationary Overloaded Winds*

So far, we assumed that wind perturbations are located above the critical point. We consider now the opposite case, $z_e < z_c$.

Figure 5 shows the wind velocity law resulting from a perturbation location $z_e = 0.8$ on the critical solution. A period $P = 0.3$ was chosen. A stationary wind with a broad deceleration region $v' < 0$ develops. Abbott waves propagate *outward* from z_e through the decelerating wind. Since the CAK critical point, which is the bottleneck of the flow, lies in the deceleration regime, the present solution should be overloaded. Indeed, the mass-loss rate is found to be $m = 1.05$.

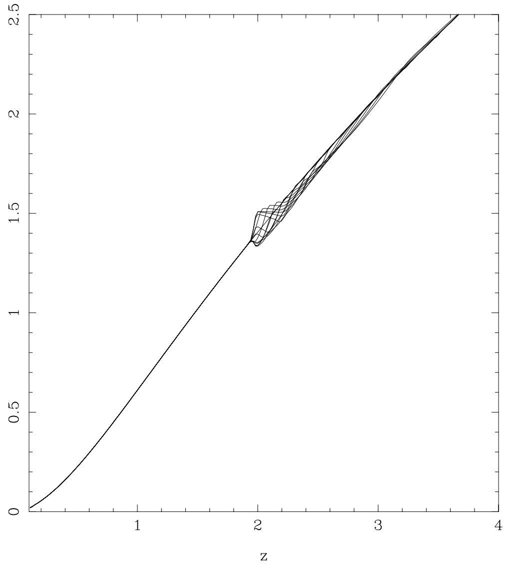

FIG. 4.—Critical CAK solution, stable with respect to Abbott waves excited above the critical point. Perturbation phases with positive and negative v' combine to an outward propagating, harmonic Abbott wave.

This result is readily understood. The flow at z_e is still sub-Abbottic because $z_e < z_c$. Runaway to larger v occurs until inward propagation from z_e becomes impossible. The velocity at $z < z_e$ is then everywhere *larger* than the critical speed. The runaway stops when the inward Abbott speed becomes zero in the observers frame. We are interested in a stationary solution; hence, $A = 0$ in equation (33), implying $mw' = g_c$. The square root in equation (10) has to vanish then, hence $m = g_c/g$.

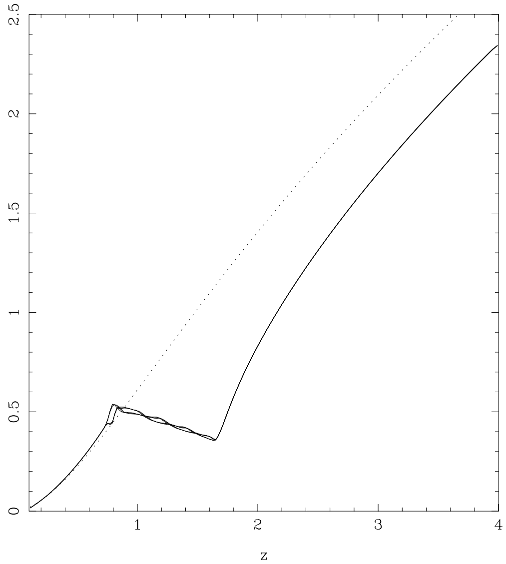

FIG. 5.—Velocity law for a wind with harmonic perturbation at $z_e =$ 0.8, below the critical point $z_c = 1$. The wind converges to a stationary, overloaded solution. The dotted line shows the initial conditions, the critical CAK solution.

So far, we restricted ourselves to $g = g_c$ and $m = 1$, but critical points can also occur along overloaded solutions. In this case, $m = g_c/g(z_c) > 1$, and the square root in equation (10) becomes imaginary at $z > z_e$. Remember that g_c refers to gravity at the critical point of the *critical* solution, which is the maximum of g. Hence, $g(z_c) < g_c$ for any other possible critical point. The perturbation site z_e stops communicating with the wind base only when it becomes a critical point itself. At z_e, the overloaded wind jumps to the decelerating branch, resulting in a kink in the velocity law. This kink has all the attributes of a critical point. Especially, as an Abbott wave barrier, it shuts off communication with the wind base.

It is easily seen that a critical point at $z < z_e$ would imply that z_e is already super-Abbottic, which cannot happen during runaway. Since $g(z)$ is a monotonically growing function with a maximum g_c, the perturbation site $z_e < z_c$ is the first one that becomes critical to Abbott waves on the evolving overloaded solution. We emphasize that the amount of overloading is solely determined by z_e.

At some height above the gravity maximum, the decelerating solution jumps back to the accelerating branch, giving a second kink: the wind has overcome the bottleneck and starts to accelerate again. In the present wind model, the (imaginary, overloaded) solution becomes real again at $z = 1/z_e$ (z_e being the location where the solution becomes first imaginary). For $z_e = 0.8$, the overloading is $m = 1.025$, and the wind can start accelerating again at $z = 1.25$. In the simulation, however, $m = 1.05$, and the second kink occurs at $z = 1.6$. The discrepancy in m can be attributed to mesh resolution, which blurs out z_e. This leaves still unanswered why the wind "waits" so long before it starts accelerating again.

Furthermore, starting with a shallow wind as initial conditions instead of a critical wind, the simulation converges again to an overloaded solution. However, the jump from the decelerating back to the accelerating branch does not terminate on the steep but already on the shallow overloaded solution with $m = 1.05$. This is a numerical artifact caused by nonreflecting, outer boundary conditions, which try to maintain shallow solutions. As above, we prefer this situation over any boundary-induced, numerical runaway.

A third kink may occur. For realistic radiative fluxes above accretion disks, we find that at still larger distances from the disk, the line force drops below absolute gravity for *all* solution types (Feldmeier & Shlosman 1999). Another jump to the decelerating branch is unavoidable. Since the local wind speed is much larger than the local escape speed, the velocity law stays essentially flat above this kink.

3.4. *Time-dependent Overloaded Winds*

Already a minor increase in the mass-loss rate causes a broad deceleration region. This is a consequence of $g(z)$ having a broad maximum at z_c. Integrating $w'(z) = vv'$ numerically, we find that $v(1/z_e) = 0$ for $z_e = 0.660$. If z_e is still smaller, the gas starts to fall back toward the photosphere before it reaches $1/z_e$ and collides with upward-streaming gas. A stationary solution is no longer possible. Figure 6 shows, for $z_e = 0.5$, that an outward propagating

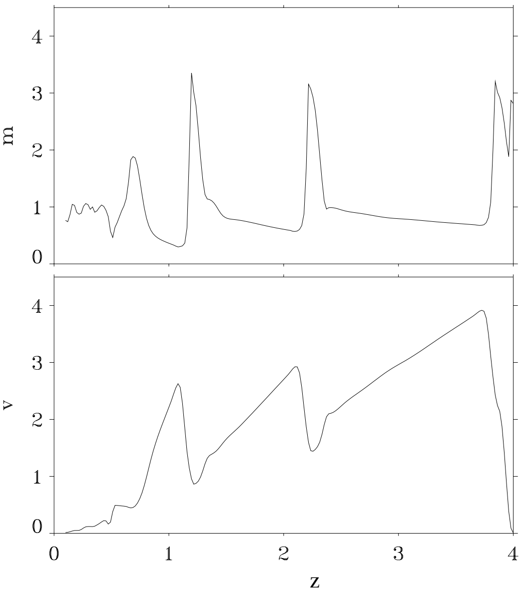

FIG. 6.—Velocity v and mass flux m of a wind perturbed at $z_e = 0.5$. During each perturbation cycle, gas falls back toward the photosphere and collides with upward-streaming gas. Shocks form and propagate outward.

sequence of shocks and dense shells form. The shock spacing is determined by the perturbation period.

As a technical comment, we add that the latter simulation tends to develop extremely strong rarefactions and, correspondingly, very large velocities. The latter cause the Courant time step to approach zero. This is a well-known artifact of the power-law form of the CAK line force, $g_1 \propto (v'/\rho)^\alpha$, implying $g_1 \to \infty$ as $\rho \to 0$. The true line force reaches instead a finite maximum in a flow that is optically thin even in very strong lines (Abbott 1982). This is achieved by truncating the line distribution function (Owocki, Castor, & Rybicki 1988). Using a simpler approach that suffices for the present purposes, we simply truncate m at large values.

Even for $z_e = 0.660$ implying negative speeds, overloading is small, only 9% above the critical CAK value ($m = 1.088$). This shows that the CAK mass-loss rate is a significant upper limit for mass-loss rates in LDWs, with or without mass overloading. If overloading occurs, it should be detectable only via broad, decelerating flow regions.

It is important to distinguish the present runaway from the well-known line-driven instability (Lucy & Solomon 1970; Owocki & Rybicki 1984; Lucy 1984), which leads to strong shocks and dense, narrow shells in the wind. For perturbations longer than the Sobolev scale, the instability can be understood as a linear process in second-order Sobolev approximation, including curvature terms v''. By contrast, runaway occurs already in first-order Sobolev approximation, yet finite perturbations are required to achieve $v' < 0$.

3.5. *Triggering Perturbations*

We discuss the following topics related to triggering:

Amplitudes.—Still, even perturbations with small amplitudes can lead to runaway if their wavelength is sufficiently short to cause negative v'. One expects, however, that dissipative processes like heat conduction prevent runaway for short wavelength perturbations.

Coherence.—In a hydrodynamic instability, a feedback cycle amplifies small initial perturbations. Even perturbations of short duration trigger unstable growth. By contrast, the present wind runaway requires a continuously maintained perturbation seed. No feedback occurs. The runaway is a pure wave feature caused by the peculiar v' asymmetry of the line force.Perturbations of short duration lead to a localized runaway. The wind is shifted toward larger v and m within a small z interval. If the perturbation ceases, so does the runaway. The region of increased v and m propagates upstream as an Abbott wave and eventually lifts the wind base to a *stable* shallow solution with slightly higher m. Successive Abbott waves lift the wind until the critical or an overloaded solution is reached.

Surrounding medium.—One expects that mismatches at the outer boundary, where the wind propagates into a medium of given properties, create perturbations that can trigger runaway. This is supported by the fact that at large z the velocity law is almost flat, and even small-amplitude perturbations can cause $v' < 0$. The Abbott speed is large at large z since $A \sim 1/(v')^{1/2}$; hence, perturbations propagate inward quickly. We performed tests with the outer boundary at $z = 40$. Inherent interpolation errors are sufficient then to set off boundary runaway.

Other sources.—Inner wind perturbations could occur because of prevalent shocks from the line-driven instability (Owocki et al. 1988). The critical point usually lies close to the sonic point (Owocki & Puls 1999; Feldmeier & Shlosman 1999), and it is therefore not easy to contemplate strong shocks below the critical point. This means that perturbations at large and not at small z dominate the runaway and drive the wind to a critical solution. Hence, overloaded winds formed by internally generated perturbations should be rare.

3.6. *Critical Points and Mass-Loss Rate*

We discuss here some general issues related to critical points and mass-loss rates in different types of stellar winds.

Holzer's wind laws.—The idea that upstream, inward propagating waves adapt the wind base to outer (boundary) conditions is fundamental to solar wind theory. From this grew the recognition that an outward force that is applied above the sonic (critical) point does not affect the mass-loss rate but only accelerates the flow, whereas a force applied below the sonic point increases the mass-loss rate but has a vanishing effect on terminal wind speeds (Leer & Holzer 1980; Holzer 1987). These "wind laws" have proven to be of interest for cases far beyond the coronal winds for which they were first applied. We refer to Lamers & Cassinelli (1999) for a detailed discussion.

Most relevant to us is the case of a force applied in the subcritical wind region, causing enhanced mass loss. For coronal winds, the subsonic region has essentially a barometric density stratification. Any extra force assisting the pressure gradient helps to establish a larger scale height. From the continuity equation, a shallower velocity gradient results, although the terminal speed is hardly affected. The corresponding situation, analyzed by us for LDWs, is even simpler. No outward force occurs besides line driving. Our choice of zero sound speed emphasizes that the barometric stratification plays no role for mass-loss runaway or for establishing an overloaded solution. Overloaded LDW solutions have a *steeper* velocity gradient than the critical solution, as can be seen from equation (7). Physically, a steeper velocity gradient is required to create a generalized critical point below the CAK critical point. In LDWs, a critical *acceleration* $w' = vv'$, not a critical speed v, is adopted at the critical point and prevents further Abbott wave runaway.

Physical relevance of critical points.—The physical relevance of the CAK critical point was questioned by Lucy (1975, 1998), arguing that it may be an artifact of Sobolev approximation. Holzer (1987, p. 296) doubts that critical points, i.e., singularities of the flow equations, generally coincide with those points beyond which "information relevant to the acceleration of the wind" can no longer be transported upstream. We have tried in the present paper to reestablish a more traditional viewpoint (Courant & Friedrichs 1948; Courant & Hilbert 1968), namely, that a critical point as a mathematical singularity leaves certain derivatives of flow quantities undetermined. This is only possible along characteristics, which are the space-time trajectories of the specific *waves* in the problem. This establishes the transonic (or trans-Abbottic, etc.) nature of the critical point. Similarly, one can argue that the critical point is a singularity because different solution branches cross there. Hence, by passing continuously from one branch to another (actually, by staying on a certain branch), higher order or weak discontinuities appear in the flow properties, for LDWs, in v''. Again, weak discontinuities propagate at characteristic wave speed, making the critical point transonic.

Mass-loss rate as an eigenvalue.—We remind the reader of a deep difference between coronal and line-driven winds. For coronal winds, the mass-loss rate is a free parameter within wide margins and is determined by the base density. For LDWs, on the other hand, the mass-loss rate is a unique, discrete eigenvalue (CAK). This is a consequence of the line *acceleration* depending on ρ; see Lamers & Cassinelli (1999).

Abbott speed and speed of light.—In the literature, the propagation speed of radiative waves is occasionally identified with the speed of light. This is not true in general: the Abbott speed and, in magnetized flows, the Alfvén speed are smaller than the speed of light. To make the point totally obvious, note that the diffusion speed of photons through stellar interiors is much smaller than the speed of light. The basic cause is here the same as for Abbott waves: optical depths larger than unity.

3.7. *Deep-seated X-Rays, Infall, and Mass Overloading*

Besides adapting the wind base to outer flow conditions, we find that Abbott waves can even lead to mass inflow. This seems like a novel feature of these waves, and it leads to interesting observational consequences, like explaining the formation of hard X-rays anomalously close to the surfaces of hot stars. Formation depths of $r \approx 1.1\ R_*$ are deduced from X-ray emission lines observed with the *Chandra* satellite (for ζ Ori, see Waldron & Cassinelli 2001; for ζ Pup, see Cassinelli et al. 2001). The favored model for X-ray emission from hot stars is via strong shocks (Lucy 1982) from the deshadowing instability (Lucy & Solomon 1970; Owocki & Rybicki 1984). The shocks become strongest in collisions of fast clouds with dense gas shells (Feldmeier, Puls, & Pauldrach 1997). From theoretical arguments (line drag effect; Lucy 1984) and numerical simulations, it appears that this shock scenario cannot explain X-rays originating from the small heights mentioned above.

Howk et al. (2000) suggest gas infall as possible origin of X-rays from near the photosphere. They consider a ballistic model of stalled wind clouds falling back toward the star to explain the hard X-rays observed from τ Sco (Cassinelli et al. 1994). At any instant, $\approx 10\%$ of the mass flux from the star resides in numerous, $\gtrsim 1000$, clouds that barely reach distances of $r = 2\ R_*$ before falling back inward. The overall resemblance of this cloud model with time-dependent wind overloading as shown in Figure 6 is striking. In the latter case, the overloading is sufficiently mild that upstreaming gas can push downfalling clumps outward (which corresponds to the drag force of ambient wind gas in Howk et al.). Stronger overloading is achieved by shifting the Abbott wave source farther inward but cannot be addressed using our simple numerical approach. Clearly, two-dimensional simulations are required to model true infall. A systematic study relating the Howk et al. approach with ours is in preparation.

Note that the critical point in stellar wind models accounting for the finite cone effect lies at $r \lesssim 1.1\ R_*$ (Pauldrach et al. 1986). An overloaded wind starts to decelerate below the critical point and may already reach negative or infall speeds at similarly small heights. This shows the relevance of overloading in understanding the *Chandra* observations mentioned above. The topic of stalling and backfalling gas has acquired some general attention in recent papers on LDWs and is discussed in different contexts by Friend & Abbott (1986), Poe et al. (1990), Koninx (1992), Proga, Stone, & Drew (1998), and Porter & Skouza (1999).

We finally mention another idea related to overloaded flows, which has played some role in sharpening our understanding of coronal winds. Cannon & Thomas (1977) and Thomas (1982) challenged Parker's (1958, 1960) theory of the solar wind. They postulated an outward-directed, subphotospheric mass flux. In analogy with a Laval nozzle (see, e.g., Chapman 2000, p. 127) into which a too strong mass or energy influx is fed (Cannon & Thomas 1977 use the terminology "imperfect nozzle" instead of "overloading"), the solar outflow should choke, creating shocks below the nozzle throat or the critical point of the smooth (perfect nozzle) flow. The shocks are responsible for heating the chromosphere and corona, making the latter a consequence, not the origin, of outflow from the Sun. This model was ruled out by Parker (1981) and Wolfson & Holzer (1982).

Still, it leads to another interesting difference between coronal and Laval nozzle flows on the one side and LDWs on the other: the former two do not allow for continuous, overloaded solutions; instead, overloaded flows have shocks in the vr plane where the critical point resides. By contrast, overloaded LDWs show jumps in the critical vv'-r plane, i.e., jumps in the wind acceleration, which correspond to *kinks* in a continuous velocity law.

4. SUMMARY

We have studied the stability of shallow and steep solutions for accretion-disk– and stellar line-driven winds. This was done by introducing flow perturbations into the wind at a fixed height. For sufficiently large perturbation amplitudes, negative velocity gradients occur in the wind and cause runaway toward the critical solution. The origin of this runaway is an asymmetry in the line force: negative velocity gradients cause a force decrease that cannot balance the force increase during phases in which the velocity law gets steepened. Net acceleration results over a full perturbation cycle.

A new type of waves, termed Abbott waves, are exited by the perturbations. They provide a communication channel between different parts of the wind and define an additional critical point in the flow, downstream from the sonic point. Shallow solutions are subcritical everywhere; steep solutions are supercritical. Along shallow solutions, Abbott waves propagate upstream toward the photosphere at a high speed as a radiative mode and creep downstream at a fraction of the sonic speed as an acoustic mode. The critical solution is the one that switches continuously from the shallow to the steep branch at the critical point.

Inward-propagating Abbott waves turn the local, asymmetric response to velocity perturbations into a global runaway toward the critical solution. The converged, steady wind solution depends on the location of seed perturbations. Three spatial domains can be distinguished: (1) If perturbations are prevalent in outer wind regions, above the critical point, the wind settles on the critical solution. (2) If perturbations occur just below the critical point, runaway proceeds to a stationary, so-called overloaded solution. Such a flow is characterized by a broad deceleration domain. The line force cannot balance gravity in the vicinity of the critical point (the bottleneck of the flow) because of a supercritical mass-loss rate. (3) Perturbations close to the photosphere result in the wind being decelerated to negative speeds. Gas falls back toward the photosphere and collides with upward-streaming gas. A time-dependent, overloaded wind results with a train of shocks and shells propagating outward.

The runaway mechanism discussed here depends solely on the asymmetry of the line force with respect to velocity perturbations that cause local flow deceleration, $dv/dr < 0$. It should, therefore, be a robust feature and not depend on Sobolev approximation.

We thank Mark Bottorff, Wolf-Rainer Hamann, Colin Norman, Stan Owocki, and Joachim Puls for illuminating discussions. We thank the referee, Joe Cassinelli, for suggestions toward a more detailed discussion of critical points and gas infall. This work was supported in part by NASA grants NAG 5-10823, NAG 5-3841, WKU 522762-98-6, and HST GO-08123.01-97A to I. S., which are gratefully acknowledged.

REFERENCES

Abbott, D. C. 1980, ApJ, 242, 1183
———. 1982, ApJ, 259, 282
Cannon, C. J., & Thomas, R. N. 1977, ApJ, 211, 910
Cassinelli, J. P., Cohen, D. H., MacFarlane, J. J., Sanders, W. T., & Welsh, B. Y. 1994, ApJ, 421, 705
Cassinelli, J. P., Miller, N. A., Waldron, W. L., MacFarlane, J. J., & Cohen, D. H. 2001, ApJ, 554, L55
Castor, J. I., Abbott, D. C., & Klein, R. I. 1975, ApJ, 195, 157 (CAK)
Chapman, C. J. 2000, High Speed Flow (Cambridge: Cambridge Univ. Press)
Courant, R., & Friedrichs, K. O. 1948, Supersonic Flow and Shock Waves (New York: Interscience)
Courant, R., & Hilbert, D. 1968, Methoden der Mathematischen Physik (Berlin: Springer)
Feldmeier, A., Puls, J., & Pauldrach, A. 1997, A&A, 322, 878
Feldmeier, A., & Shlosman, I. 1999, ApJ, 526, 344
———. 2000, ApJ, 532, L125
Feldmeier, A., Shlosman, I., & Hamann, W.-R. 2001, ApJ, submitted
Friend, D. B., & Abbott, D. C. 1986, ApJ, 311, 701
Holzer, T. E. 1987, in IAU Symp. 122, Circumstellar Matter, ed. I. Appenzeller & C. Jordan (Dordrecht: Reidel), 289
Howk, J. C., Cassinelli, J. P., Bjorkman, J. E., & Lamers, H. J. G. L. M. 2000, ApJ, 534, 348
Koninx, J.-P. 1992, Ph. D. thesis, Utrecht Univ.
Lamb, H. 1932, Hydrodynamics (New York: Dover)
Lamers, H. J. G. L. M., & Cassinelli, J. P. 1999, Introduction to Stellar Winds (Cambridge: Cambridge Univ. Press)
Leer, E., & Holzer, T. E. 1980, J. Geophys. Res., 85, 4681
Lucy, L. B. 1975, Mem. Soc. R. Sci. Liège, 8, 359
———. 1982, ApJ, 255, 286
———. 1984, ApJ, 284, 351
———. 1998, in Cyclical Variability in Stellar Winds, ed. L. Kaper & A. W. Fullerton (Berlin: Springer), 16
Lucy, L. B., & Solomon, P. M. 1970, ApJ, 159, 879
Owocki, S. P., Castor, J. I., & Rybicki, G. B. 1988, ApJ, 335, 914
Owocki, S. P., & Puls, J. 1999, ApJ, 510, 355
Owocki, S. P., & Rybicki, G. B. 1984, ApJ, 284, 337
———. 1986, ApJ, 309, 127
Parker, E. N. 1958, ApJ, 128, 664
———. 1960, ApJ, 132, 175
———. 1981, ApJ, 251, 266
Pauldrach, A., Puls, J., & Kudritzki, R. P. 1986, A&A, 164, 86
Poe, C. H., Owocki, S. P., & Castor, J. I. 1990, ApJ, 358, 199
Porter, J. M., & Skouza, B. A. 1999, A&A, 344, 205
Proga, D., Stone, J. M., & Drew, J. E. 1998, MNRAS, 295, 595
Rybicki, G. B., & Hummer, D. G. 1978, ApJ, 219, 654
Thomas, R. N. 1982, ApJ, 263, 870
Waldron, W. L., & Cassinelli, J. P. 2001, ApJ, 548, L45
Wolfson C. J., & Holzer, T. E. 1982, ApJ, 255, 610

The Astrophysical Journal, 566:392–398, 2002 February 10

RUNAWAY ACCELERATION OF LINE-DRIVEN WINDS: THE ROLE OF THE OUTER BOUNDARY

Achim Feldmeier
Astrophysik, Institut für Physik, Universität Potsdam, Am Neuen Palais 10, 14469 Potsdam, Germany; afeld@astro.physik.uni-potsdam.de
Isaac Shlosman[1,2]
JILA, University of Colorado, Box 440, Boulder, CO 80309-0440; shlosman@pa.uky.edu
and
Wolf-Rainer Hamann
Astrophysik, Institut für Physik, Universität Potsdam, Am Neuen Palais 10, 14469 Potsdam, Germany; wrh@astro.physik.uni-potsdam.de
Received 2001 May 4; accepted 2001 October 11

ABSTRACT

Observations and theory suggest that line-driven winds from hot stars and luminous accretion disks adopt a unique, critical solution that corresponds to maximum mass-loss rate. We analyze the numerical stability of the infinite family of shallow wind solutions, which resemble solar wind breezes, and their transition to the critical wind. Shallow solutions are subcritical with respect to radiative (or Abbott) waves. These waves can propagate upstream through shallow winds at high speeds. If the waves are not accounted for in the Courant time step, numerical runaway results. The outer boundary condition is equally important for wind stability. Pure outflow conditions, as assumed in the literature, trigger runaway of shallow winds to the critical solution or to accretion flow.

Subject headings: accretion, accretion disks — hydrodynamics — instabilities — stars: mass loss — waves

1. INTRODUCTION

Line-driven winds (LDWs) occur in various astronomical objects, such as OB and Wolf-Rayet stars, in accretion disks in cataclysmic variables, and, probably, in active galactic nuclei and luminous young stellar objects. These winds are powered by absorption and re-emission of photospheric continuum flux in numerous spectral transitions of C, N, O, and Fe, among other ions.

Castor, Abbott, & Klein (1975, hereafter CAK) analyzed the steady state Euler equation for LDWs. They found an infinite family of mathematical solutions, but only one, hereafter the "critical solution," that extends from the photosphere to arbitrarily large radii. Other solutions either do not reach infinity or do not reach the photosphere. The former solutions are called shallow and the latter ones steep. The unique, critical wind starts on the fastest shallow solution and switches smoothly to the slowest steep solution at the critical point.

Observational support that LDWs adopt the critical solution comes from measured terminal speeds (Abbott 1982). Furthermore, mass-loss rates of supergiant winds are in general agreement with modified CAK theory (Lamers & Leitherer 1993; Puls et al. 1996). These measurements were recently extended to include Galactic and extragalactic OB and A stars and central stars of planetary nebula (Kudritzki et al. 1999).

Abbott (1980) interpreted CAK theory as a complete analogy to the solar wind and nozzle flows. The existence of a sonic point defines the unique, transonic solutions for these flows, whereas the existence of a critical point for Abbott waves defines the unique, CAK solution for LDWs. Only from below this critical point can Abbott waves propagate upstream toward the photosphere. Above the critical point, they are advected outward. Because Abbott waves generally propagate highly supersonically, the critical point of LDWs lies at much higher speeds than the sonic point.

Abbott's (1980) analysis was challenged by Owocki & Rybicki (1986), who derived the Green's function for a pure absorption LDW. The Green's function yields correct signal speeds in the presence of hydrodynamic instabilities. The inward signal speed in a pure absorption line wind is the sound speed, and not the much higher Abbott speed, because photons propagate outward only. Owocki & Rybicki (1986) showed that a fiducial upstream signal, which still propagates inward at Abbott speed, must be interpreted as *purely local* Taylor series reconstruction. For a flow driven by scattering lines, however, Owocki & Puls (1999) find *physically relevant* Abbott waves for a numerical Green's function.

In the present paper, we further analyze the properties of Abbott waves. We show that they are crucial for our understanding of stability of LDWs and must be included in the Courant time step. So far, time-dependent numerical simulations of LDWs from stars and accretion disks have ignored the ability of Abbott waves to communicate in the supersonic regime, which results in a numerical runaway. In particular, this runaway can lift the wind to the critical solution.

The critical solution is also enforced by applying pure outflow boundary conditions. It is often argued that outflow boundary conditions are appropriate because LDWs are highly supersonic. Instead, they have to be *superabbottic*. We show that shallow wind solutions, which correspond to solar wind breezes, are everywhere subabbottic. Hence, these solutions are numerically destabilized by applying outflow boundary conditions.

We formulate boundary conditions that render shallow solutions numerically stable. Those include nonreflecting Riemann conditions for Abbott waves. By allowing for

---

[1] JILA Visiting Fellow.

[2] Permanent address: Department of Physics and Astronomy, University of Kentucky, Lexington, KY 40506-0055.

kinks in the velocity law, shallow solutions can be made globally admissible.

2. THE WIND MODEL

In the CAK model for LDWs, both gravity and line force scale with r^{-2}. If the sound speed and, hence, the pressure forces are set to zero, this leads to a degeneracy of the critical-point condition, which is satisfied formally at every radius (Poe, Owocki, & Castor 1990). Thus, in this case, Abbott waves cannot propagate inward from any location in the wind. For finite sound speed, they creep inward at low speed. Inclusion of the finite disk correction factor is much more relevant for LDWs than inclusion of pressure forces. With the finite disk included, the inward speed of Abbott waves below the critical point is significantly higher than the wind speed. Unfortunately, the finite-disk correction factor depends on the (unknown) velocity law of the wind, preventing a simple analysis of the wind dynamics.

We consider, therefore, a wind model that is analytically feasible and yet prevents the (near-)degeneracy of the CAK point star wind. (Especially, this degeneracy leads to poor convergence of time-dependent numerical schemes.) As a prototype, a vertical LDW from an isothermal, geometrically thin, non-self–gravitating accretion disk is assumed. The sound speed is set to zero. Keplerian rotation is assumed within the disk and angular momentum conservation above the disk. This reduces the flow problem to a one-dimensional, planar one. The radiative flux above an isothermal disk is roughly constant at small heights. On the other hand, the vertical gravity component along the wind cylinder is zero in the disk midplane, grows linearly with z if $z \ll R$ (with R the footpoint radius in the disk), reaches a maximum, and drops off at large z. To model the launch region of the wind and the gravity maximum, we choose $g(z) = z/(1 + z^2)$, with normalization $GM = 1$ and $R = 1$, where G is gravitational constant and M is the mass of the central object. The differing spatial dependences of flux and gravity result in a well-defined critical point in the flow.

For constant radiative flux, the CAK line force becomes $g_l = C(\rho^{-1} dv/dz)^{\alpha}$, where ρ and v are the density and velocity and α and C are constants. We choose $\alpha = 1/2$. Typical values of α from non–LTE calculations (Pauldrach 1987) and Kramers' law (Puls, Springmann, & Lennon 2000) are $\alpha = 0.4$ to 0.7. The constant C can be expressed in terms of the unique, critical CAK mass-loss rate. This is the maximum allowed mass-loss rate for a stationary wind. We introduce new fluid variables m and w,

$$m = \frac{\rho v}{\rho_c v_c} \, , \quad w = \frac{1}{2} v^2 \, , \tag{1}$$

where subscript c refers to the critical CAK solution. For stationary, plane-parallel winds, the continuity equation becomes $\rho v = \text{const}$, and m is a constant. In the following, the quantity $w' = dw/dz = v \, dv/dz$ will play a central role. The velocity law, $v(z)$, is obtained by quadrature of the wind "solution" $w'(z)$. For $\alpha = 1/2$, the stationary Euler equation becomes

$$E = w' + g(z) - 2(g_c w'/m)^{1/2} = 0 \, , \tag{2}$$

where we multiplied the nominator and denominator in the line force by v, and introduced $g_c = g(z_c)$, the gravity at the location of the CAK critical point. The dependence of w' on z is suppressed in the equation. The constant C is determined as follows. Equation (2) is a quadratic equation in $\sqrt{w'}$. Consider the $\sqrt{w'}E$-plane. For arbitrary z and sufficiently small m, the crossings $E = 0$ of the parabola $E(\sqrt{w'})$ with the abscissa determine two wind solutions $w'(z)$, termed shallow and steep. When m increases, the crossings approach each other, and merge at some maximum $m \geq 1$, beyond which no further solutions exist. Hence, the *singularity condition* $\partial E/\partial w' = 0$ holds when two solutions merge, as is the case at the critical point. Together with $E = 0$, this yields $w'_c = g_c$ and $C = 2(g_c \rho_c v_c)^{1/2}$.

We add a comment that is important for what follows. At every location $z \neq z_c$, $m > 1$ for the parabola that meets the abscissa in just one point. The minimum, $m = 1$, is reached at the unique critical point, z_c, which is the flow *nozzle* and determines the maximum mass loss that can be driven from the photosphere to infinity. Solutions (actually, pairs of shallow and steep solutions) with $m > 1$ are called *overloaded*. They correspond to a *choked* Laval nozzle flow. These solutions become imaginary in the neighborhood of the critical point. We have shown elsewhere (Feldmeier & Shlosman 2000) how overloaded LDW solutions can be defined globally, by letting them decelerate, $dv/dz < 0$, around the critical point.

The *position* of the critical point is determined by the *regularity* condition, which is derived next. Because $E = 0$ everywhere, $dE/dz = 0$ holds, too. Because $\partial E/\partial w'_c = 0$, it follows that $\partial E/\partial z_c = 0$, if $| w''_c| < \infty$. This latter condition singles out the unique critical point, because overloaded winds have kinks at the merging point of two solutions, $| w'' | \equiv \infty$. Hence, the critical point lies at the gravity maximum, $dg/dz_c = 0$. For $g(z) = z/(1 + z^2)$, $z_c = 1$ and $g_c = 1/2$. The line force in equation (2) becomes $(2w'/m)^{1/2}$. This holds for any solution, whether shallow or steep. Solving equation (2) for $\sqrt{w'}$,

$$q(z) \equiv [2mw'(z)]^{1/2} = 1 \pm [1 - 2mg(z)]^{1/2} \, , \tag{3}$$

where we introduced a new variable, q. The signs refer to steep (plus) and shallow (minus) solutions. For $m = 1$, the square root in equation (3) vanishes at the critical point. For $m > 1$, the root becomes imaginary in the neighborhood of the critical point. The solutions $w'(z)$ of equation (3) have a saddle topology in the zw'-plane when m is varied from $m < 1$ to $m > 1$. The critical point—$z_c = 1$, $w'_c = 1/2$—is the saddle point. A variable radiative flux above a nonisothermal accretion disk leads instead to two different values of z_c, above and below the gravity maximum (Feldmeier & Shlosman 1999). The lower is a saddle, the upper an extremum.

Note that the CAK critical point of LDWs is a saddle in the z-vv' plane, whereas the sonic point of the solar wind is a saddle in the zv-plane. In all other respects, we find a deep analogy between LDWs and the solar wind. Only the notion of a critical speed is replaced by a critical acceleration. Shallow solutions are the analogs to solar wind breezes.

According to equation (3), shallow and steep solutions with $m \leq 1$ extend from $z = 0$ to ∞ for the present model with zero sound speed. CAK found that steep solutions start supersonically at the wind base $z = 0$, which seems unphysical. In a spherically symmetric wind, shallow solutions do not extend to arbitrarily large z, because they cannot provide the required expansion work. These two results and the requirement for a continuous and differentiable solution imply that the wind has to pass through the critical point. It starts on the fastest shallow solution and ends on the slowest steep one.

Figure 1 (which is adapted from Fig. 4 in Abbott 1980 and Fig. 8.13 in Lamers & Cassinelli 1999) shows the LDW solution topology in the *rv*-plane for a finite sound speed. In region II (regions defined in CAK), which is spatially the most extended in real LDWs, shallow and steep solutions exist at each point (r, v). If $z \neq z_c$, these solution pairs may be overloaded. In the subsonic region I, only shallow solutions (possibly overloaded) exist; steep solutions are necessarily supersonic. Correspondingly, only steep solutions (possibly overloaded) exist in region III. No solutions exist in regions IV and V. Note that the gap in overloaded solutions around z_c can be bridged by an extended decelerating region, $dv/dr < 0$.

The argument by CAK ruling out global, steep solutions is stringent, but the exclusion of shallow solutions seems too restrictive. The pressure force due to spherical expansion becomes important only at very large distances from the wind base. According to CAK, shallow solutions break down around 300 stellar radii for realistic O star wind parameters. Most shallow solutions have by then overcome the local escape speed. Shallow solutions can be globally defined by a slight generalization of the CAK approach, allowing for negative $v' = dv/dz$ in the line force $\sim \sqrt{v'}$. This can be done by replacing v' with $|v'|$ or with $\max(v', 0)$. The former expresses the "blindness" of purely local line driving to flow acceleration or deceleration. The latter accounts for the nonlocal effect of shadowing in nonmonotonic velocity laws, creating a resonance coupling. All radiation is assumed to be absorbed at the first resonance location. Realistically, the value of the line force lies between these extremes. The decelerating wind solution, $w' < 0$, is unique and does not split into shallow and steep branches.

Hyperbolic differential equations allow for weak discontinuities, which are represented in the *zw*′-plane by jumps between different solution branches. Hence, a shallow solution may jump onto the decelerating branch. Even an overloaded solution can avoid becoming imaginary by jumping onto the decelerating branch in the vicinity of the critical point. This opens the possibility that global solutions can be composed in a piecewise manner.

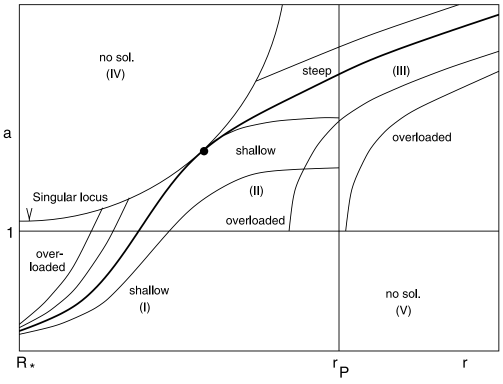

FIG. 1.—Solution topology of line-driven winds, showing shallow, steep, and overloaded solutions. The circle marks the CAK critical point. Roman numerals refer to cases I–V of CAK. Regions I–III and V are mutually separated by straight lines (sound speed $v = a$; Parker point $r = r_P$); regions II and IV are separated by the single locus.

Jumps in w' introduce *kinks* in $v(z)$. Such kinks have been found on various occasions in time-dependent LDW simulations. They may play a central role in the observed *discrete absorption components* in nonsaturated P Cygni line profiles (Cranmer & Owocki 1996). In LDWs from accretion disks in cataclysmic variables, a jump onto the decelerating branch even occurs for the critical solution, which would elsewhere not extend to infinity (Feldmeier & Shlosman 1999). Hence, the smoothness argument of CAK cannot be used to disqualify shallow solutions.

3. ABBOTT WAVES

3.1. *Linear Dispersion Analysis*

The time-dependent continuity and Euler equations for the present wind model are

$$\frac{\partial \rho}{\partial t} + \frac{\partial(\rho v)}{\partial z} = 0 , \tag{4}$$

$$\frac{\partial v}{\partial t} + v \frac{\partial v}{\partial z} = -\frac{z}{1+z^2} + \left(2\rho_c v_c \frac{\partial v/\partial z}{\rho}\right)^{1/2} . \tag{5}$$

In the Euler equation, $v' > 0$ is assumed. The case $v' < 0$ will be discussed below. To derive Abbott waves, small perturbations are applied, $v = v_0 + v_1 \exp[i(kz - \omega t)]$ and $\rho = \rho_0 + \rho_1 \exp[i(kz - \omega t)]$. The subscript 0 refers to a stationary solution, subscript 1 to the perturbation. Linearizing yields

$$\left[-i\frac{\omega}{v_0'} + i\chi + 1\right]\frac{\rho_1}{\rho_0} + (i\chi - 1)\frac{v_1}{v_0} = 0 , \tag{6}$$

$$\frac{1}{q_0}\frac{\rho_1}{\rho_0} + \left[-i\frac{\omega}{v_0'} + 1 + i\chi\left(1 - \frac{1}{q_0}\right)\right]\frac{v_1}{v_0} = 0 , \tag{7}$$

with nondimensional $\chi \equiv k\ v_0/v_0'$ and $q_0 = (2m_0 w_0')^{1/2}$. Setting the determinant of the system to zero yields the dispersion relation $\omega(k)$. In a WKB approximation, $\chi \gg 1$, one finds for the phase speed A_0 and the growth rate of the inward (minus) mode,

$$A_0 = \mathrm{Re}(\omega_-)/k = v_0[1 - (1/q_0)],\ \mathrm{Im}(\omega_-) = 0 , \tag{8}$$

in the observer's frame, and for the outward (plus) mode,

$$A_0 = \mathrm{Re}(\omega_+)/k = v_0,\ \mathrm{Im}(\omega_+) = -\epsilon , \tag{9}$$

with $-\epsilon$ a small damping term of no further consequence. Along a shallow solution $q_0 < 1$, and along a steep solution $q_0 > 1$. For shallow solutions with small m_0 and w_0', q_0 is small, and the inward mode can propagate at arbitrarily large phase speed from *every* location z. This result is new, because so far Abbott waves along shallow solutions were not considered ("a LDW has no analog to a solar breeze"; Abbott 1980). Because for the CAK point star model every point is critical, $q_0 = 1$, and the inward mode is stagnating everywhere. Stability of *non*–WKB waves, $\chi = O(1)$, is found from a numerical solution.

Integrating equation (3), the velocity of the critical solution at $z_c = 1$ (the "critical speed") is $v \approx 0.61$. On the other hand, a shallow solution with $m_0 = 0.8$ has $v > 0.61$ for $z > 1.51$. This is no contradiction to the fact that the shallow solution is subabbottic.

3.2. *Characteristic Analysis*

The above analysis holds for linear waves, and the wave speed is determined by the underlying stationary solution. General, nonlinear waves can be derived from a characteristic analysis. The characteristic form of the above equations is, without further approximations,

$$\left[\frac{\partial}{\partial t} + v\,\frac{\partial}{\partial z}\right]\rho = -\rho\,\frac{\partial v}{\partial z}\,, \tag{10}$$

$$\left[\frac{\partial}{\partial t} + A\,\frac{\partial}{\partial z}\right]\left(\frac{1}{\rho}\,\frac{\partial v}{\partial z}\right) = -\frac{1}{\rho}\,\frac{\partial g}{\partial z} \tag{11}$$

(Feldmeier & Shlosman 2000), where the Abbott speed, A, in the observer's frame is

$$A = v\left(1 - \frac{1}{q}\right) = v - \left(\frac{\rho_c v_c}{2\rho\partial v/\partial z}\right)^{1/2}\,. \tag{12}$$

The interpretation of equation (11) is unconventional, in that v' should now be considered the fundamental hydrodynamic field, instead of v. This happens because of the nonlinear dependence of E on v' (Courant & Hilbert 1968).

Hence, $-\rho v'$ in the continuity equation and $-g'/\rho$ in the Euler equation are inhomogenous terms, because they do not contain derivatives of the hydrodynamic fields ρ and v'. The advection operators are $\partial/\partial t + v\partial/\partial z$ and $\partial/\partial t + A\partial/\partial z$, with characteristic speeds v and A. The former should be read as $v + a$ in zero sound speed approximation. The Riemann invariants ρ and v'/ρ correspond to wave amplitudes. In a frame moving at v, the amplitude ρ is constant, except for sources and sinks $-\rho v'$. In an isothermal gas $p \sim \rho$, and the wave amplitude is indeed that of a pressure wave. In a frame moving at A, the amplitude v'/ρ is constant, except for sources and sinks $-g'/\rho$. The Sobolev optical depth is $\sim(v'/\rho)^{-1}$, indicating that the inward mode is a radiative wave.

Even for waves of infinitesimal amplitude, v' may deviate strongly from v'_0, if the wavelength λ is short. Because $A \sim (v')^{-1/2}$, short-scale Abbott waves are highly dispersive. For sufficiently small λ, v' becomes negative at certain wave phases. The characteristic equations (10) and (11) hold also for $v' < 0$, but A has different meaning then. For a line force $\sim|\,v'\,|^{1/2}$, the general A is

$$A = v[1 \mp (1/q_\pm)]\,, \tag{13}$$

where the lower sign applies for $v' < 0$ and in q_- one has to use $-v'$. Trivially, Abbott waves are advected *outward* in superabbottic flow. But that Abbott waves propagate *downstream* as an outward mode in regions where $v' < 0$ is probably their single most unique property.

For a line force $\sim[\max(0, v')\,]^{1/2}$, then, $A = v$ if $v' < 0$. This is because the line force drops out of the Euler equation, and both wave modes become ordinary sound. (Actually, $A = v - a$ for upstream-propagating sound.) In this case one has, along a characteristic curve with coordinate s,

$$\frac{\rho(s)}{\rho(0)} = \frac{v'(s)}{v'(0)} = \frac{1}{1 + v'(0)s} \tag{14}$$

as the WKB wave solution of equations (10) and (11). This describes gasdynamical *simple* waves. Because $v'(0) < 0$, they steepen and break ($v' = -\infty$). The derivation of simple *Abbott* waves is beyond the scope of this paper.

4. BOUNDARY CONDITIONS FOR LINE-DRIVEN WINDS

We discuss now the outer boundary conditions for shallow solutions. Abbott waves can enter through the outer boundary; hence, pure outflow boundary conditions are not appropriate for shallow solutions.

As hydrocode we use a standard Eulerian scheme on a staggered mesh. Advection is solved in the conservative control volume approach, using monotonic van Leer (1977) interpolation. The sound speed is set exactly to zero, and a small amount of artificial viscosity is added to handle occasional shock fronts. Details of the scheme can be found in Reile & Gehren (1991) and Feldmeier (1995).

In a first step, we consider simple boundary conditions for ρ and v that still preserve essential features of Abbott waves. These boundary conditions render shallow solutions stable and allow small perturbations to leave the grid. They are

$$\begin{aligned}\rho(0) &= \text{const}, \quad v(0) = v(1)\,,\\ \rho(I) &= \rho(I-1), \quad v(I) = \text{const}\,,\end{aligned} \tag{15}$$

where 0 and I are the mesh indices of the inner and outer boundary, respectively. The conditions (eq. [15]) are motivated as follows. (The reader may jump to the end of this paragraph.) On a characteristic curve $[z(s), t(s)]$ that leaves the mesh through a boundary, the characteristic equation is solved on the boundary via *extrapolation*, using one-sided, interior differentials. Such an *upwinded* scheme is stable (Steger & Warming 1981). For shallow winds, the ρ wave leaves through the outer boundary if $v > 0$; hence, ρ is extrapolated from the interior in (15). Zeroth-order extrapolation is used for stability reasons. Abbott waves enter the mesh through the outer boundary; hence, a boundary condition must be applied. We choose $v(I) = \text{const}$. [To prevent standing waves, $v(I) = m_0/\rho(I)$ is often more appropriate, but is also more susceptible to runaway than $v(I) = \text{const}$.] At the *inner* boundary, the argument proceeds correspondingly, with interchanged roles of the waves. We find that using $\rho(0) = \rho(1)$ and $v(0) = \text{const}$ instead destabilizes shallow solutions.

4.1. *The Courant Time Step*

In time-dependent hydrodynamic simulations published so far, it is customary to insert the *sound* speed in the Courant time step,

$$\Delta t = \sigma\,\min(\Delta z/|\,v \pm a\,|)\,, \tag{16}$$

with Courant number $\sigma \leq 1$, and the minimum has to be taken over the mesh. We see now that Abbott waves, as the characteristic inward wave mode, have to be included in the Courant time step,

$$\Delta t = \sigma\,\min\left(\frac{\Delta z}{|\,v - A\,|}\,, \frac{\Delta z}{v + a}\right), \tag{17}$$

where A is in the fluid frame now. Note that A changes sign with v'. For sufficiently small $v' > 0$ and for arbitrary $v' < 0$, Abbott waves determine the time step. At velocity plateaus where the wind velocity is more or less constant, $A \to -\infty$, from equation (11), and the Courant time step $\to 0$. This is an artifact of Sobolev approximation, in which the line radiation force tends to zero in the absence of velocity gradients. In practice, in calculating the Courant time step we do not allow q to drop below a certain minimum value, usually 10^{-4}. This corresponds to $\sigma \approx 10^{-4}$ for an ordinary Courant time step, not including Abbott waves. Our results are not sensitive to the value of this minimum q, if the latter is sufficiently small. Furthermore, velocity plateaus quickly acquire a tilt and propagate at finite speed.

4.2. *Nonreflecting Boundary Conditions*

We can then formulate *nonreflecting* boundary conditions for the Riemann invariants ρ and v'/ρ, which annihilate incoming waves. This prevents boundary reflection of waves that originate on the interior mesh. To annihilate a wave, its amplitude (the Riemann invariant) is kept constant in time at the boundaries, $\partial(v'/\rho)/\partial t = 0$ and $\partial\rho/\partial t = 0$ for Abbott and sound waves, respectively (Hedstrom 1979; Thompson 1987). One may say that nonreflecting boundary conditions drive the numerical solution toward a neighboring, stationary solution without waves. The technical details of implementing these boundary conditions are discussed in Appendix A.

5. STABILITY OF SOLUTIONS

We discuss here the numerical stability of shallow and steep solutions, depending on the appropriate Courant time step and boundary conditions.

5.1. *Stability of Steep Solutions*

We start with steep solutions and show that they are unconditionally stable, even when simplified boundary conditions analogous to equation (15) are used. According to equation (3), $q > 1$ everywhere for steep solutions, and Abbott waves can propagate only toward larger z. At the outer boundary, the extrapolations $\rho(I) = \rho(I-1)$ and $v(I) = v(I-1)$ are therefore appropriate. At the inner boundary, two conditions have to be specified. The obvious choices are either ($\rho = \text{const}$, $v = \text{const}$) or ($\rho = \text{const}$, $v' = \text{const}$). The first set fixes the mass-loss rate, whereas the second establishes nonreflecting boundary conditions by keeping the wave amplitudes ρ and v'/ρ constant in time, which means that there are no waves.

We find that steep solutions are stable for both types of boundary conditions. Even when the initial conditions differ profoundly from those of a steep wind, the numerical code converges to a steep solution. Furthermore, we performed tests with an explicit, harmonic perturbation at a fixed Eulerian position in the wind. Even if the perturbation amplitude reached 100%, the wind remained on average on a steep solution, which can therefore be considered as unconditionally stable.

5.2. *Stability and Runaway of Shallow Solutions*

A physically more relevant question is the stability of shallow solutions. In a first step, we use an analytic, shallow wind as initial conditions. Table 1 shows the *runaway* of this shallow solution to the critical velocity law. Abbott waves are *not* accounted for in the Courant time step, and pure outflow boundary conditions, $\rho(I) = \rho(I-1)$ and $v(I) = v(I-1)$, are applied. This corresponds to the typical procedure adopted in the literature. The runaway starts at the outer boundary and generates inward-propagating Abbott waves. The velocity law evolves toward higher speeds, until the critical solution is reached.

TABLE 1

NUMERICAL RUNAWAY OF A SHALLOW VELOCITY LAW

z	$t = 0$	$t = 3$	$t = 6$	$t = 9$	$t = 20$	$t = \infty$
0.1……	**0.0**	**0.0**	**0.0**	**0.0**	**0.0**	**0.0**
0.5……	**0.2**	**0.2**	**0.2**	**0.2**	**0.2**	**0.2**
1.0……	0.5	0.4	**0.6**	**0.6**	**0.6**	**0.6**
1.5……	0.6	0.6	0.9	**1.0**	**1.0**	**1.0**
2.0……	*0.7*	0.8	*1.2*	1.4	**1.4**	**1.4**
2.5……	*0.8*	0.9	*1.3*	*1.5*	**1.8**	**1.8**
3.0……	*0.8*	*1.1*	*1.3*	*1.5*	**2.1**	**2.1**
3.5……	*0.8*	*1.1*	*1.4*	*1.6*	*2.2*	**2.4**
4.0……	*0.8*	*1.2*	*1.4*	*1.6*	*2.3*	**2.7**

The mechanism of the runaway seems to be as follows. The Courant condition for Abbott waves is violated in the outer wind, where the velocity law is flat and the Abbott speed is high. This causes numerical runaway. In contrast to standard gas dynamics, the LDW runaway does not crash the simulation. We speculate that exponential growth in v creates high $|v'|$, which implies low Abbott speeds. The Courant condition is no longer violated, and runaway stops. Abbott waves are also excited at the outer boundary, by switching from the interior to the boundary scheme. Upstream-propagating Abbott waves are inconsistent with the assumed outflow boundary conditions. The waves propagate to the wind base and drive the inner wind toward the critical solution, which is indeed consistent with outflow boundary conditions.

Note in Table 1 that Abbott waves can propagate inward from the outer boundary, $z_M = 4$, until the critical velocity law is reached (indicated by bold numbers in the table). This is no contradiction to the critical point being located at $z_c = 1$: the outer, shallow portion of the velocity law (the numbers in italics) is subabbottic, even when the inner, steep velocity law is already superabbottic.

To *prevent numerical runaway* of shallow solutions, we apply nonreflecting Riemann boundary conditions and include Abbott waves in the Courant time step. As initial conditions, an arbitrary (for example, linear) velocity law is used. Abbott waves are again excited at the outer boundary and propagate inward. However, the simulation relaxes quickly to a shallow solution. The m-value depends on the initial data. Even for an initial model with height-dependent mass flux, we find quick convergence to a shallow solution.

Further details on the stability of shallow solutions are given in Appendix B. To summarize this section, both improper outer boundary conditions and Courant conditions that do not account for Abbott waves are responsible for numerical runaway.

6. SUMMARY

We present a simplified model for line-driven winds from stars and accretion disks that avoids the r^{-2} degeneracy of the CAK model. Radiative, or Abbott, waves are derived from both a dispersion and a characteristic analysis and for all possible solutions to the Euler equation, i.e., shallow, critical, steep, and overloaded ones.

We find that Abbott waves can propagate upstream, toward the photosphere, from any position along a shallow wind solution. Hence, for shallow winds, Abbott waves can

TABLE 2

Runaway in Simulations Applying Different Boundary Conditions and Courant Time Steps

Run	z_M	Grid Points	Line Force	Abbott Time	Courant Number	Boundary Condition	Result
1	4	200	abs(v')	No	0.5	Outflow	Runaway
2	4	200	abs(v')	No	0.1	Outflow	$m_0 = 0.7$; oscillating
3	4	200	abs(v')	No	0.5	Shallow	Runaway
4	4	200	abs(v')	No	0.1	Shallow	Runaway
5	10	200	abs(v')	No	0.1	Outflow	Runaway
6	4	200	abs(v')	Yes	0.5	Outflow	$m_0 = 0.5$; oscillating
7	10	200	abs(v')	Yes	0.5	Outflow	Slow runaway
8	10	500	abs(v')	Yes	0.5	Outflow	Slow runaway
9	4	80	abs(v')	Yes	0.5	Outflow	$m_0 = 0.5$; oscillating
10......	4	200	abs(v')	Yes	0.5	Shallow	Stable
11......	4	200	max(0, v')	No	0.5	Outflow	Accretion
12......	4	200	max(0, v')	No	0.1	Outflow	Accretion
13......	4	200	max(0, v')	No	0.5	Shallow	Stable, oscillating
14......	4	200	max(0, v')	No	0.1	Shallow	Stable, oscillating
15......	10	200	max(0, v')	No	0.1	Outflow	Accretion
16......	4	200	max(0, v')	Yes	0.5	Outflow	Accretion
17......	10	200	max(0, v')	Yes	0.5	Outflow	Accretion
18......	10	500	max(0, v')	Yes	0.5	Outflow	Accretion
19......	4	80	max(0, v')	Yes	0.5	Outflow	Accretion
20......	4	200	max(0, v')	Yes	0.5	Shallow	Stable

enter the calculational grid through the outer boundary. The wave propagation speed depends on the velocity slope of the wind. Abbott's (1980) result that these waves are creeping, i.e., have only slightly negative inward speeds, holds globally only for the almost degenerate CAK point star model. In more realistic wind models, Abbott waves can limit the Courant time step.

The neglect of Abbott waves in either the Courant time step or the boundary conditions leads to numerical runaway toward the critical wind solution of maximum mass-loss rate or to accretion flow. If, instead, incoming waves are annihilated at the outer boundary and the correct Courant time step is used, shallow solutions are stable.

It is a pleasure to thank Janet Drew, Leon Lucy, Stan Owocki, and Joachim Puls for frequent discussions. This work was supported in part by NASA grants NAG 5-10823, NAG 5-3841, WKU-522762-98-6, and HST GO-08123.01-97A to I. S., which are gratefully acknowledged.

APPENDIX A

NONREFLECTING BOUNDARY CONDITIONS

We adopt the following procedure to calculate ρ and v on a boundary. (1) If the ρ wave leaves the grid, $\dot{\rho} = -(\rho v)'$ is calculated using one-sided, interior differentials. (2) If the ρ wave enters the grid, $\dot{\rho} = 0$ is set (wave annihilation; see § 4.2). (3) If the v'/ρ wave leaves the grid, $\dot{v}'/v'$ is calculated from the Euler equation (eq. [11]) in characteristic form, using one-sided, interior differentials. Note that v'' appears here. (4) If the v'/ρ wave enters the grid, $\dot{v}'/v' = \dot{\rho}/\rho$ is set, assuming WKB waves. (5) The new values for ρ and v on the boundary are found by integrating $\dot{\rho}$ and $\dot{v}'$ using a time-explicit scheme.

In step 5, one actually needs $\dot{v}$, not $\dot{v}'$. To integrate from time step $n - 1$ to n at the outer boundary using $\dot{v}'$, we write

$$v'^{n} = v'^{n-1} + \dot{v}'\Delta t \; . \tag{A1}$$

Using $v'^{n} = (v_I^n - v_{I-1}^n)/\Delta z$, and similarly for v'^{n-1}, this becomes

$$v_I^n = v_I^{n-1} + v_{I-1}^n - v_{I-1}^{n-1} + \dot{v}'\Delta z \Delta t \; , \tag{A2}$$

whence v_n^I depends on v_{I-1}^{n-1}. Because of frequent variable updating in an operator splitting scheme during the time step, v_{I-1}^{n-1} would have to be stored as an extra variable. This seems undesirable, and indeed it causes numerical runaway of shallow solutions. Fortunately, a simple approximation to equation (A2) yields satisfactory results, namely, setting $v_{I-1}^{n-1} \equiv v_{I-1}^n$, or

$$v_I^n = v_I^{n-1} + \dot{v}'\Delta z \Delta t \; . \tag{A3}$$

APPENDIX B

NUMERICAL STABILITY OF SHALLOW SOLUTIONS

For numerical stability tests, we assume the following parameters, if not otherwise stated: 200 equidistant grid points from $z = 0.1$ to $z = 4$. Below $z = 0.1$, the stationary wind speed is very small. Because $\delta v/A_0 = \delta\rho/\rho_0$, one has $v_0 \ll A_0$ for an inner boundary $z_m \rightarrow 0$. Even small perturbations, $\delta\rho$, then cause negative speeds at z_m. This alters the direction of the ρ characteristic and often causes numerical problems. A shallow solution with $m = 0.8$ serves as start model. The sound speed is set to zero. The flow time from $z = 0.1$ to $z = 4$ is 12.4 for a shallow solution with $m = 0.8$, and 9.1 for the critical solution (in the units specified in the main text). For $m = 0.8$, linear Abbott waves propagate from $z = 4$ to $z = 0.1$ in a time of 6.0. All simulations are evolved to time of 50. Table 2 lists results from simulations using different outer boundary conditions and Courant time steps. On the inner boundary, conditions (eq. [15]) were used.

Consider first the line force $\sim |v'|^{1/2}$. The table shows that inclusion of Abbott waves in the Courant time is mandatory to prevent runaway (runs 1–5; " shallow " in the column for the outer boundary conditions refers to eq. [15]). For small Courant numbers, Abbott waves are, to a degree, already accounted for by an ordinary time step. Runaway may then be prevented, as in run 2, though the solution does oscillate at all times. If the outer boundary is shifted outward, the runaway occurs again (run 5). If Abbott waves are accounted for in the time step, outflow boundary conditions (extrapolation of ρ and v) do not necessarily lead to runaway. Instead, a stable, shallow solution may be maintained (runs 6 and 9; also run 2). However, the solution oscillates at all times. Shallow solutions become more unstable when the outer boundary is shifted outward, into the shallow part of the velocity curve where Abbott waves are easily excited. Finally, the control run 10 shows that the initial shallow solution is numerically stable if Abbott waves are included in the time step and boundary conditions of equation (15) are used.

For a line force $\sim [\max(0, v')]^{1/2}$, the scheme is even more susceptible to numerical runaway. All cases with outflow boundary conditions undergo runaway. However, for the boundary condition $v(I) = v(I - 1)$, the solution no longer tends toward the critical solution. Instead, $v(I)$ drops to zero and with it the interior wind velocity. The outcome of the simulation is not clear, because we have not formulated appropriate line-driven *accretion* boundary conditions. The reason for the drop in $v(I)$ is that an accidental $v' < 0$ at the outer boundary implies zero line force. This causes further velocity drop, and v' becomes more negative. Abbott waves carry this wind breakdown to the interior mesh. It is not clear whether this type of line force should actually be applied in the proximity of the outer boundary.

REFERENCES

Abbott, D. C. 1980, ApJ, 242, 1183
———. 1982, ApJ, 259, 282
Castor, J. I., Abbott, D. C., & Klein, R. I. 1975, ApJ, 195, 157 (CAK)
Courant, R., & Hilbert, D. 1968, Methoden der Mathematischen Physik (Berlin: Springer)
Cranmer, S. R., & Owocki, S. P. 1996, ApJ, 462, 469
Feldmeier, A. 1995, A&A, 299, 523
Feldmeier, A., & Shlosman, I. 1999, ApJ, 526, 344
———. 2000, ApJ, 532, L125
Hedstrom, G. W. 1979, J. Comput. Phys., 30, 222
Kudritzki, R.-P., Puls, J., Lennon, D. J., Venn, K. A., Reetz, J., Najarro, F., McCarthy, J. K., & Herrero, A. 1999, A&A, 350, 970
Lamers, H. J. G. L. M., & Cassinelli, J. P. 1999, Introduction to Stellar Winds (Cambridge: Cambridge Univ. Press)
Lamers, H. J. G. L. M., & Leitherer, C. 1993, ApJ, 412, 771
Owocki, S. P., & Puls, J. 1999, ApJ, 510, 355
Owocki, S. P., & Rybicki, G. B. 1986, ApJ, 309, 127
Pauldrach, A. 1987, A&A, 183, 295
Poe, C. H., Owocki, S. P., & Castor, J. I. 1990, ApJ, 358, 199
Puls, J., et al. 1996, A&A, 305, 171
Puls, J., Springmann, U., & Lennon, M. 2000, A&AS, 141, 23
Reile, C., & Gehren, T. 1991, A&A, 242, 142
Steger J. L., & Warming, R. F. 1981, J. Comput. Phys., 40, 263
Thompson, K. W. 1987, J. Comput. Phys., 68, 1
van Leer, B. 1977, J. Comput. Phys., 23, 276